The Human Body Antenna: Characteristics and its Application

Behailu Mulatu KIBRET

A thesis by publication submitted in fulfilment of the requirements

for the degree of

DOCTOR OF PHILOSOPHY

College of Engineering and Science

Victoria University

January 2016

Abstract

The human body has antenna characteristics that are not explored in detail to explain some phenomena involving the interaction of electromagnetic fields and the human body. Moreover, the characterization of the human body as antenna unlocks new applications in body area networks for low-power wireless communications by utilizing the human body itself as an antenna.

This thesis presents a new theory for explaining the antenna characteristics of the human body in transmission and reception mode. The theory is applied to two areas of study, namely, Human Body Communication (HBC) and whole-body radio-frequency (RF) dosimetry. Based on this, the thesis proposes a new concept where the human body is utilized as an antenna for wireless implant communication.

When a high frequency alternating current is applied to the human body, the human body acts like an antenna in transmission mode by radiating part of the energy and dissipating the rest as heat. Within the human body resonance region (<200 MHz), one of the study areas that involves the application of RF current into the human body is HBC. HBC is a relatively new wireless communication technique that uses the human body as a communication channel to connect wearable electronic devices. Specifically, in this thesis, we study both types of HBC, which are the galvanic and capacitive coupled HBC.

The galvanic coupled HBC involves low frequency coupling of electric currents (<10 MHz) to the human body for the purpose of wireless communication of wearable electronic devices. Several HBC studies have attempted to describe the mechanism of signal propagation in the human body; however, some major gaps remain. For example, the effect of various tissues, the electrode–skin contact impedance and user anthropometry on signal quality have not been explained. In this thesis, the effect of these factors explained by a new circuit model of the human arm. It is found that the dielectric properties of muscle tissue primarily affect the spectral content of the received signal close to the transmitter whereas the skin affects the signal received farther down the arm. Moreover, it is found that the electrode-skin contact impedance acts like a high pass filter affecting low frequency components of the signal.

In HBC, the impact of the human body antenna is little understood; consequently, there are uncertainties regarding the signal propagation and interference mechanisms due to human body antenna effects. Moreover, there are some experimental phenomena that are still not satisfactorily explained in the literature. For example, there are no analyses on why the maximum HBC gain occurs near 50 MHz. This thesis demonstrates that such problems can be explained by considering the antenna characteristics of the human body for higher frequencies (<200 MHz) in capacitive coupled HBC. In this case, it is demonstrated that the frequency where the maximum gain occurs aligns with the resonance frequency of the human body when treated as a radiating antenna. A semi-analytic cylindrical antenna model of the human body is proposed, which is applied to analyze the antenna effect of the human body on HBC. From the analysis, the mechanism of electromagnetic interference due to the human body antenna is explained, which is also supported by experimental results. It is shown that the magnitude of induced interference currents inside the human body due to external electromagnetic fields are also maximum at the resonance frequency of the human body.

It is known that when the human body is exposed to radio-frequency (RF) electromagnetic fields, it acts like an antenna by absorbing part of the incident energy and scattering the rest. The problem of quantifying the absorbed power has been the subject of a large number of studies in the area of RF dosimetry. Unfortunately, in these studies, little can be found on the analysis of the human body antenna characteristics from the antenna theory perspective. This thesis proposes the analysis of whole-body RF dosimetry for far-field exposure of a grounded human body in the frequency range of 1-150 MHz based on a semi-analytic cylindrical antenna model of the human body. For the first time, an explicit model for the resonance frequency of a grounded human body is proposed. The model captures the effects of the human body weight, height and the dielectric properties of tissues. It also addresses the effect of shoes on whole-body RF dosimetry. It is found that the resonance frequency with subjects wearing shoes is higher than reported from using the bare-footed models, as confirmed by theory and measurement

Even though a large number of studies on the interaction of the electromagnetic fields and the human body exist, little is known on the antenna nature of the human body let alone applying it as an antenna. In this work, the human body is characterized as a monopole antenna theoretically and experimentally, in the frequency range of 10 - 110

MHz to investigate the efficacy of a human body antenna. The reflection coefficient is measured using a human subject as a monopole antenna. It is found that the human body resonates between 40 - 60 MHz depending on the posture of the body when it is fed by a 50 Ω impedance system at the base of the foot. A minimum reflection coefficient of -12 dB is measured shows that the human body can be potentially used as an antenna. Theoretically, the human body is predicted to be an efficient antenna with a maximum radiation efficiency reaching 70 %, which is supported by measurement results found in the literature.

Lastly, the thesis discusses the feasibility of using the human body as an antenna for wireless implant communication by injecting an RF current into the tissues within the frequency range of 1-70 MHz. In particular, the thesis describes a scenario where the RF current is fed by a tiny toriodal inductor clamped around soft tissues in the ankle. The theoretical results show that the system exhibit broadband characteristics with a maximum gain of -25 dB between 20 to 40 MHz, assuming isotropic radiation from the human body. However, the very small radiation resistance of the system increases the power consumption of implants. Consequently, it is found that by reducing the parasitic capacitance of the inductor and the magnetic core loss, the radiation resistance of the system can be increased. This can be done by choosing a magnetic core with high permeability and low loss, as well as, optimising the number of turns to reduce the parasitic capacitance to obtain a usable magnetizing inductance.

Declaration

"I, Behailu Mulatu KIBRET, declare that the PhD thesis by Publication entitled, 'The Human Body Antenna: Characteristics and its Application' is no more than 100,000 words in length including quotes and exclusive of tables, figures, appendices, bibliography, references and footnotes. This thesis contains no material that has been submitted previously, in whole or in part, for the award of any other academic degree or diploma. Except where otherwise indicated, this thesis is my own work."

Signed:

Date: 03/03/2016

"Oh, the depth of the riches and wisdom and knowledge of God! How unsearchable are his judgments and how inscrutable his ways!"

Romans 11:33

Acknowledgements

First and for most, praise to the Lord Jesus Christ for the light shining in me.

Next, I would like to express my sincere gratitude to my supervisor Dr. Daniel Lai for the continuous mentoring, immense patience, inspiration and encouragement throughout the period of my PhD study. I would also like to thank Prof. Mike Faulkner for the feedbacks, suggestions and comments on some ideas of my research.

I would like to thank Hojjat, Clement, Kim, Zibo, Angela, Johannis, and Rebecca for being friendly colleagues. In particular, I am grateful to Assefa for the friendship, motivations, and discussions we had.

Lastly, but not the least, my deepest gratitude goes to my wife Yodith for the love, patience, and encouragement.

List of Published/Submitted Papers

Journal Articles

1. MirHojjat Seyedi, **Behailu Kibret**, and Daniel T H Lai, Michael Faulkner, 'A survey on intrabody communication for body area network applications', *IEEE Transaction on Biomedical Engineering*, Vol. 60, No. 8, 2067-2079, 2013

2. **Behailu Kibret**, MirHojjat Seyedi, Daniel T H Lai, and Michael Faulkner, 'Investigation of galvanic coupled intrabody communication using human body circuit model', *IEEE Journal of Biomedical and Health Informatics*, Vol. 18, No. 4, 1196-1206, 2014

3. **Behailu Kibret**, Assefa K Teshome, and Daniel T H Lai, 'Human body as antenna and its effect on human body communications', *Progress in Electromagnetics Research*, Vol. 148, 193-207, 2014

4. **Behailu Kibret**, Assefa K Teshome, and Daniel T H Lai, 'Analysis of the whole-body averaged apecific absorption rate (SAR) for far-field exposure of an isolated human body using cylindrical antenna theory', *Progress in Electromagnetics Research M*, Vol. 38, 103–112, 2014

5. **Behailu Kibret**, Assefa K Teshome, and Daniel T H Lai, 'Characterizing of the human body as a monopole antenna', *IEEE Transactions on Antennas and Propagation*, Vol. 63, No. 10, 4384-4392, 2015

6. **Behailu Kibret**, Assefa K Teshome, and Daniel T H Lai, 'Cylindrical antenna theory for the analysis of whole body averaged specific absorption rate', *IEEE Transactions on Antennas and Propagation*, Vol. 63, No. 11, 5224 - 5229, 2015

7. **Behailu Kibret**, Assefa K Teshome, and Daniel T H Lai, 'Analysis of the Human Body as an Antenna for Wireless Implant Communication', *IEEE Transactions on Antennas and Propagation*, accepted, January 2016

8. **Behailu Kibret**, Assefa K Teshome, and Daniel T H Lai, 'A New Perspective on the Cylindrical Antenna Theory', *IEEE Transactions on Antennas and Propagation*, submitted, Sep 2015

9. Assefa K Teshome, **Behailu Kibret**, and Daniel T H Lai, 'Galvanically Coupled Intra-body Communications for Medical Implants: A Unified Analytic Model', *IEEE Transactions on Antennas and Propagation*, submitted, Aug 2015

Book Chapter

1. MirHojjat Seyedi, **Behailu Kibret**, Sravanreddy Salibindla, and Daniel T H Lai, 'An overview of intra-body communication transceivers for biomedical applications', *IGI Global Encyclopaedia of Information Science and Technology*, Vol. 3, 469-478, 2014

Conference Articles

1. **Behailu Kibret**, MirHojjat Seyedi, Daniel T H Lai, and Michael Faulkner, 'The effect of tissues in galvanic coupled intrabody communication', *IEEE Eighth International Conference on Intelligent Sensors, Sensor Networks and Information Processing*, 318-323, 2013

2. MirHojjat Seyedi, **Behailu Kibret**, Daniel T H Lai, Michael Faulkner, 'An Empirical Comparison of Limb Joint Effects on Capacitive and Galvanic Coupled Intra-Body Communications', *IEEE Eighth International Conference on Intelligent Sensors, Sensor Networks and Information Processing*, 213-218, 2013

Contents

List of Figures

List of Tables

Abbreviations

IBC	**I**ntra-**B**ody **C**ommunication
HBC	**H**uman **B**ody **C**ommunication
PAN	**P**ersonal **A**rea **N**etwork
FDTD	**F**inite **D**ifference **F**inite **T**ime
VNA	**V**ector **N**etwork **A**nalyzer
ICNIRP	**I**nternational **C**ommission for **N**on-**I**onising **R**adiation **P**rotection
HF	**H**igh **F**requency
VHF	**V**ery **H**igh **F**requency
WBAN	**W**ireless **B**ody **A**rea **N**etwork
EMI	**E**lectro**m**agnetic **I**interference
RF	**R**adio **F**requency
SIR	**S**ignals to **I**nterference **R**atio
FSBT	**F**requency **S**elective **B**aseband **T**ransmission
FM	**F**requency **M**odulation
SAR	**S**pecific **A**bsorption **R**ate
WBA-SAR	**W**hole **B**ody **A**veraged **S**pecific **A**bsorption **R**ate
VED	**V**ertical **E**lectric **D**ipole
EMC	**E**lectromagnetic **C**ompatibility
MoM	**M**ethod of **M**oments
ISM	**I**ndustrial **S**cientific and **M**edical
dB	**d**eci-**B**ell
IEEE	**I**nstitute of **E**lectrical and **E**lectronic **E**ngineers
BAN	**B**ody **A**rea **N**etwork
MICS	**M**edical **I**mplants **C**ommunication **S**ystem
ETSI	**E**uropean **T**elecommunications **S**tandards **I**nstitute

ERP	**E**quivalent **R**adiated **P**ower
EIRP	**E**quivalent **I**sotopically **R**adiated **P**ower
LTCC	**L**ow **T**emprature **C**o-fired **C**eramic
AWG	**A**merican **W**ire **G**auge

Physical Constants

Speed of Light	c	$=$	$2.997\ 924\ 58 \times 10^8$ ms^{-1}
Permeability of Free Space	μ_0	$=$	$4\pi \times 10^7$ Hm^{-1}
Permittivity of Free Space	ϵ_0	$=$	$8.854\ 187\ 817 \times 10^{-12}$ Fm^{-1}
Impedance of Free Space	ς_0	$=$	$120\pi\ \Omega$

Symbols

E	electric field intensity vector	Vm^{-1}
H	magnetic field intensity vector	Am^{-1}
D	electric field flux density	Cm^{-2}
B	magnetic field flux density	T
A	magnetic vector potential	Tm^{-1}
φ	scalar electric potential	V
J	volume current density vector	Am^{-2}
ρ	volume charge density	Cm^{-3}
ϵ_r	relative permittivity	
μ_r	relative permeability	Fm^{-1}
σ	conductivity	Sm^{-1}
ω	angular frequency	rads^{-1}
γ	complex propagation constant	
β	phase constant	
α	propagation constant	
I	current	A
k_2	free space wave number	m^{-1}
V_0	electromotive force	V
Z	impedance	Ω
Y	admittance	S
Z_A	antenna impedance	Ω
Z_L	load impedance	Ω
z^i	surface impedance per unit length	Ωm^{-1}
E_0, E^{inc}	incident electric field	Vm^{-1}
R	distance	m

P_{diss}	power dissipated	W
P_{rad}	power radiated	W
W	weight of human body	kg
H	height of human body	m
h	height of cylinder	m
a	radius of cylinder	m
ρ_m	average density of human body	kgm^{-3}
f_{res}	resonance frequency	Hz
η	radiation efficiency	
Γ	reflection coefficient	
R_w	winding resistance	Ω
L_{AC}	internal inductance	H
C_{sh}	parasitic capacitance	F

Dedicated to my wife Yodith

Chapter 1

Introduction

1.1 Research Background and Motivation

The interaction of biological entities and the electromagnetic field has been the focus of interest since the discovery of 'animal electricity' by the Italian physician and physicist Liugi Galavni in the late eighteenth century. Galvani coined the term 'animal electricity' to describe the phenomenon he observed when the legs of a dead frog twitched in response to the application of electrostatic potential difference from two separate metallic objects [1]. Unfortunately, he believed the cause of 'animal electricity' was ions that were released from the nerves to the muscle when an electric loop was formed by the contact of metallic objects. But the fact is the phenomenon occurred due to the electrostatic charge established from rubbing the frogs skin with metallic object, which was explained by Volta - a peer scientist of the time. Shortly afterwards, Volat's investigation on this area led to the invention of an early battery. Consequently, Galvani pioneered the broad field of bioelectromagnetics, which studies the interaction of electromagnetic fields and biological materials. Bioelectromagnetics includes the study of the electromagnetic fields generated by living cells; it also studies the effects of man-made electromagnetic fields on biological entities.

The constituents of biological tissues, such as, water, ions and cell membranes, determine the response of tissues when an electrical stimulus is applied. These constituents contribute the dipoles and free charges present in the tissues that are responsible for the electrical nature of tissues. When an external alternating electric field is applied to

tissues, it suffers loss in magnitude due to the power dissipated in transporting the free charges and the 'friction' caused by dipole displacement. It also suffers phase lag due to the delayed response from rotating the dipoles. In other words, the free charges and the dipoles determine the effective conductivity of tissues, whereas the dipoles determine the permittivity of tissues. Due to the presence of various constituents in tissues, the values of the effective conductivity and permittivity of tissues depend on the frequency of the applied alternating electric field. For example, in the kHz region, the transport of ions mainly determines the dielectric properties of tissues while the dipoles due to water molecules are primarily responsible for the dielectric properties in the GHz region.

Some studies in the area of bioelectromagnetics focus on the electromagnetic phenomena on the cellular level, such as, the study of action potential in excitable cells including neurons and muscle cells. Other studies apply the techniques in electrophysiology to study the phenomena in body organs; for example, electrocardiography, which is the process of recording the electrical activity of the heart. Also, further studies take the whole human body into consideration, such as, in the characterization of the effect of the human body on wearable antennas. In this category of study, the whole human body is taken as a single electrical entity without the need to focus on the details of the phenomena in the cellular level. The main theme of this thesis belongs to the third category where the focus is on whole human body as an antenna in the frequency range lower than 200 MHz (whole body-resonance frequency region).

An antenna converts electrical power into electromagnetic energy, and vice versa. In transmission mode, when an alternating current is applied to an antenna, it radiates part of the energy in the current as electromagnetic waves; a portion of the energy also oscillates as the near-field in the vicinity of the antenna and the remaining energy dissipates as heat in the antenna. Similarly, in reception mode, when an electromagnetic wave impinges on an antenna, part of the electromagnetic wave is converted into an alternating current flowing inside the antenna and a portion of the electromagnetic wave gets scattered by the antenna. A fraction of the energy in the induced alternating current dissipates as heat and the remaining energy is stored as a potential energy in the electromotive force setup at the antenna terminals.
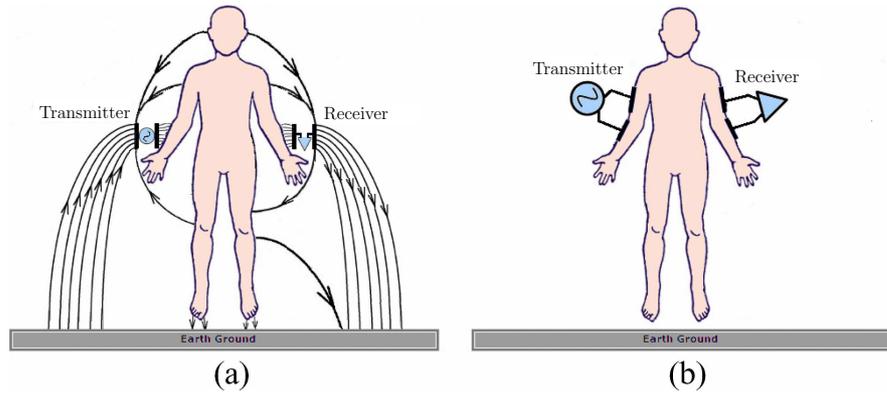
FIGURE 1.1: The two types of HBC. (a) is capacitive coupled and (b) is galvanic coupled

1.1.1 Human Body Antenna in Transmission mode

When an alternating current is applied to the human body, the human body tends to act like an antenna in transmission mode. Similar phenomena occur when an alternating current is applied to the human body, the applied energy undergoes three different phenomena, depending on the frequency of the current: it radiates as radio waves, dissipates as heat in the tissues and oscillates as near-field in the vicinity of the human body. The heat generated in the tissues due to the dissipated energy, when a radio-frequency (RF) current is applied to the body, has medical applications, such as, in the treatment of cancer by heating tumor cells and in cutting, shrinking or sculpting soft tissues [2]. The near-field generated in the vicinity of the human body, when an RF current is applied to the human body, is utilized to connect wearable electronic devices in the wireless communication technique known as Human Body Communication (HBC). HBC, also known as Intrabody Communication (IBC) or Body Channel Communication (BCC), uses the human body as part of the communication channel to connect wearable electronic devices.

The IEEE 802.15.6 is the first standard for wireless body area networks (WBAN) that is intended for low-power, short-range, and reliable wireless communication of electronic devices placed on the surface, inside or in the vicinity of the human body [3]. The standard supports three different types of physical (PHY) layers, which are, the Ultra-wideband (UWB) PHY, Narrowband (NB) PHY, and Human Body Communication (HBC) PHY. The UWB and NB PHYs are designed for high data rate wireless communications with most of their allocated frequency bands located in the Industrial,

Scientific, and Medical (ISM) bands; thus, they are prone to interference from the well-established wireless protocols, such as, the Wi-Fi, Bluetooth and Zigbee. In addition to this, UWB PHY channel is affected by human body-shadowing effects [4]. The first part of this thesis is dedicated to investigate the mechanism of signal propagation in HBC in the frequency range of 0.2 - 200 MHz. The frequency range considered in this thesis includes the center frequency proposed for the IEEE 802.15.6 HBC PHY, which is 21 MHz.

The signals in HBC are coupled to the body using electrodes that generate electromagnetic fields inside, on the surface or in the vicinity of the human body. Since the size of the electrodes are much smaller compared to the wavelength of the RF signals generated, they can be considered as electrically small antennas. It is known that these type of antennas have low radiation efficiency; thus, the electrodes used have high reactive antenna impedance. Consequently, the reactive near-field generated from the electrodes is utilized to connect wearable electronic devices. Since the human body has higher conductivity than air, the generated near-field has the tendency to be confined to the human body. Due to these characteristics, HBC promises a low-power at the expense of lower date communication channel. Moreover, since HBC is intended for low-power wireless communication, the effects on living tissue due to power dissipated are usually ignored. This risky assumption might lead to unsafe practice in carrying out experiments that involve the application of high power electric currents into the body.

Generally, HBC is classified as galvanic coupled and capacitive coupled as shown in Fig. 1.1. In galvanic coupled HBC, the human body is utilized as a medium of signal transmission by differentially injecting a low-power and low-frequency ($\leq$ 10 MHz) electric current into the body using a pair of electrodes. The electric potential difference on a pair of receiver electrodes, which are placed on the body, is used to detect the transmitted signal. In capacitive coupled HBC, the transmitter generates a reactive near-field from a single electrode attached or placed close to the surface of the human body, while the transmitter circuit ground-plane serves as the ground electrode. The receiver detects the transmitted signal from the potential difference between two receiver electrodes or between a single receiver electrode and its circuit ground-plane. In capacitive coupled HBC, the frequency range lower than 150 MHz is often thought to be suitable since it is believed that the signals are confined as near-fields in this frequency range.

Several HBC studies have attempted to describe the mechanism of signal propagation in the human body [5–12]; however, some major knowledge deficiencies remain. For example, the effect of various tissues on signal propagation in galvanic coupled HBC has not been analyzed in detail. Also, some of these models did not include the effect of the electrode–skin contact impedance and, in other models, the electrode-skin impedance was not clearly presented. In addition to these, the models do not take into account subject-specific anatomical parameters, i.e., the anthropometry. For these reasons, present galvanic coupled HBC models do not accurately describe or predict signal propagation through human subjects. For example, in the model proposed in [10], a constant bias was added on the theoretical model in order to match empirical results without clear and reasonable justification.

In order to investigate galvanic coupled HBC, in this thesis, an electric circuit model of the human arm for the frequency range of 200 kHz to 10 MHz is proposed. At this frequency range, the wavelength of the signals is much larger than the dimension of the human body; therefore, a quasistatic approximation using discrete circuit elements is applied. Under these approximations, it is assumed that the human body poorly radiate at this frequency range. The circuit model is used to investigate how the dielectric properties of tissues affect the electric current coupled to the human body. Using the proposed circuit model and experimental results, it is known that the dielectric properties of the muscle tissue affect the electric signals that were detected very close to the transmitting electrodes and the skin affects the signals that were detected farther. In this thesis, a model for the skin-electrode contact impedance is also proposed for the first time. It is found that the skin-electrode contact impedance is one of the factors of discrepancies in the experimental results reported by other authors. The proposed model helps to analyse the effect of surface electrodes in galvanic coupled HBC.

Due to the higher frequency of operation and the orientation of the electrodes, the near-field generated from capacitive coupled HBC can couple to nearby objects. Consequently, the characteristics of the channel alter depending on the presence of objects in the vicinity of the human subject, such as, the earth ground. In other words, this is equivalent to saying that the power consumption of the transmitter and the characteristics of the channel vary due to the impedance of the immediate surroundings. For example, it is expected that the presence of conductors close to the human body changes the channel characteristics, which is also affected by the movement and posture of the

human body. For these reasons, the design of HBC transceiver demands efficient, robust and channel-aware communication techniques that can adapt to the dynamic nature of the HBC channel.

There have been uncertainties on the mechanism of electromagnetic propagation in the capacitive coupled HBC. One of the common misconceptions is the view that the signals are physically guarded by the human body and electromagnetic radiation is low. Thus, it was concluded that the signals are less prone to electromagnetic interference [5, 13, 14]. This thought had its origin from the fact that the electrodes used in HBC can be considered as electrically small antennas, which are known to be inefficient at radiating and receiving electromagnetic fields. The misconception also has its base from the fact that, at the frequency of operation of HBC ($\leq$ 150 MHz), the human body tends to be a good electric conductor. Therefore, this led to the belief that HBC devices are less affected by interference; as well as, it led to the misconception that they are less likely to interfere with other nearby electronic devices. However, while experimenting on capacitive coupled HBC, we were able to measure strong electromagnetic signals that were radiated from a human subject wearing an HBC transmitter. Also, at the same distance, a much smaller signal was measured when the HBC device was transmitting by itself without being attached to the human subject. Additional experiments showed that the human subject acted like an antenna with radiating signals having a maximum magnitude near the resonance frequency of a quarter-wave monopole antenna of the same height. The near-field generated by the capacitive coupled HBC electrodes induces an RF current inside the human subject, which acted like a monopole antenna by radiating some of the energy as radio waves.

Based on the observations stated previously, in this thesis, the human body was modeled as an imperfectly conducting cylindrical monopole antenna, which is analysed based on the three-term approximation technique. The three-term approximation is a semi-analytic expression of the RF current in cylindrical antennas using three sinusoidal functions. The sinusoidal functions have amplitude and phase that are defined from the geometry and dielectric properties of the antenna. The use of the proposed cylindrical antenna model is also based on the results of some studies that have demonstrated that the total axial induced RF current in a standing human subject when irradiated by vertically polarized plane wave, is less affected by the change in cross-sectional size of the body [15–17]. Moreover, these studies reported that the induced RF current behaves

more like the axial current distribution in a cylindrical monopole antenna. Applying the reciprocity principle, such properties of the human body apply when it is considered as a transmitting antenna. Supporting this, we also found that the cylindrical antenna model of the human body is sufficient to describe the whole body antenna effect of a human body in standing position, as described later in the thesis.

The antenna effect of the human body and the mechanism of electromagnetic interference, in the context of HBC, is discussed thoroughly. A comprehensive study of HBC from the electromagnetic perspective is also presented. A prior popular article published by other authors attempted to explain the electromagnetics in HBC based on a well-known theory that was devised to analyse the propagation of electromagnetic fields from a dipole source over an infinite and conductive plane [18]. This approach fails to explain important phenomena in HBC, such as, the reason for empirical results showing maximum gain occurring near 50 MHz. Our proposed cylindrical antenna model demonstrates that that this frequency matches to the resonance frequency of the human body behaving as a monopole antenna.

1.1.2 Human Body Antenna in Reception Mode

The study of the human body as an antenna in the reception mode involves the quantification of the alternating current induced inside the body when exposed to incident electromagnetic waves. Knowledge of this current can be used to determine the amount of dissipated power inside the whole body; for example, the value of the dissipated power can be applied to determine the safe level of electromagnetic exposure. In relation to this, a branch of bioelectromagnetics that is concerned with the quantification of the power dissipated by the human body when it is exposed to radio waves is known as RF dosimetry. RF dosimetry not only deals with the power dissipated in the whole human body but also is concerned with quantifying the amount of power absorbed in specific body parts due to whole body or partial exposure.

Excessive whole-body exposure to RF electromagnetic fields raises the core temperature of the human body due to the heat generated from the dissipated power. In whole-body RF dosimetry, whole-body averaged specific absorption rate (WBA-SAR) is used as a surrogate metric to quantify the temperature rise in the body. It is defined as the ratio of the total average electromagnetic power dissipated inside the human body

to the weight of the human body. Since it is not convenient to measure WBA-SAR inside the human body, computational techniques are often used to relate WBA-SAR to external measurable quantities, such as, the incident electric field. The common trend is to employ computational electromagnetics tools, such as, the finite-difference-finite-time (FDTD) and using high resolution realistic 3D numerical models of the human body.

To date, there have been a large number of studies on whole-body RF dosimetry. Surprisingly enough, aside from briefly highlighting the analogy between human body in standing position and a quarter-wave monopole antenna, little has progressed in the analysis of the computational results from antenna theory perspective. For example, a notable attempt to analyse the WBA-SAR values of a human subject standing on a highly conductive ground, obtained from FDTD computations on realistic numerical models, was reported in [16] based on antenna theory. Nevertheless, there were technical contradictions in the interpretation of the results reported in the paper. The analysis holds valid for highly conductive wire antennas; therefore, it was concluded in the paper that the human body has a radiation resistance of approximately 292 Ω. This is equivalent to saying that the human body is highly efficient antenna with negligible loss, which is unrealistic compared to the 37 Ω radiation resistance of a perfectly conducting quarter-wave monopole antenna. In this thesis, an in-depth analysis of WBA-SAR based on the cylindrical monopole antenna model of a human subject standing on a highly conductive ground is provided. The presented analysis shows how the dielectric properties of the tissues, anthropometry of human subjects, and the shoes affect the WBA-SAR. Moreover, an accurate formula for the resonance frequency of the human body as a function of the weight and height is proposed for the first time. The resonance frequencies and the corresponding resonance WBA-SAR computed by other authors, using FDTD and realistic numerical models representing human subjects of different age group, gender, and race are predicted accurately by the proposed models. Moreover, in most RF dosimetry articles, the realistic numerical models used represent bare-footed human subjects; thus, the effect of shoes on WBA-SAR was not studied thoroughly. In this thesis, the effect of shoes on WBA-SAR is further analyzed based on antenna theory, which shows that resonance frequency increases with shoes.

1.1.3 Human Body Antenna in Transmission and Reception Mode

The natural questions that come next are: 'How good is the human body as an antenna?' and 'Can the human body work reliably as an antenna for wireless applications?'. To answer these questions, the human body has to be characterized with the intention of applying as an antenna and to determine its performance in comparison to other traditional metallic antennas. In the literature, despite the presence of a large number of studies on the interaction of electromagnetic fields and the human body, little is known of the human body antenna characteristics, especially, in the context of applying the human body as an antenna device for wireless communication purposes.

In RF dosimetry, the problem of quantifying the absorbed RF energy inside the whole human body has been exhaustively studied. For example, early studies have identified that the absorbed RF power depends on the polarization of the incident electromagnetic field, its frequency, the presence of reflectors in the environment, and the posture of the human body [19]. In these studies, important antenna characteristics of the human body were identified, such as, the frequency at which maximum RF power is absorbed when a vertically polarized plane wave illuminates a man in free space or standing on perfectly conducting ground. It was also reported that this frequency is close to the resonance frequency of a half wave dipole or quarter wave monopole antenna of the same height, respectively. Even though these studies focused on quantifying the amount of RF power absorbed inside the human body; little has been reported about the characterization of the human body with the objective of utilizing it as an antenna.

A remarkable historical attempt to use the human body as an antenna goes back to the 1970s, in a research undertaken by the US army, in an effort to design camouflaged and wearable radio transmitters that use the human body as antenna [20]. The objective was to replace the traditional infantry whip antennas, which were not suitable to be used in a jungle environment - being physical obstacles to the radio operator. Since the application was a long-range communication, a high-power transmitter was used with a coil of wire wound around the chest to couple the electric signal into the body. It was reported that for a transmitter output power of 1 Watt, a radio signal was transmitted at 4.2 MHz for a distance of more than 1.5 km. The power used for the experiment was too much considering human safety. At that time, there were no standards or guidelines that set limitations on the safe amount of electromagnetic power coupled to the body.

The rationale for using 1 Watt of power was based on comparisons to the amount of radio-frequency power used in some medical applications of the time, such as, a device for cauterization that used a peak power of 600 Watt.

Also, an early and noteworthy experiment, in order to characterize the human body as an antenna, was carried out by Andersen *et al.* [21]. In this study, based on the measurement of the admittance of the human body, it was concluded that the human body has no significant resonance within this frequency range. This contradicts the large number of RF dosimetry studies that demonstrated the human body resonates within the 10-70 MHz frequency range. In addition to this, reproducing their experimental setting, we found that the significant admittance peak occurred near 80 MHz, which was out of the range considered in the prior study of Andersen *et al.*. Though, the human body resonance is within 35-70 MHz, the shift in the peak admittance to 80 MHz was due to the parasitic impedance between the foot and the ground. In the experimental setting, the human subject was standing on a conductive plate that was excited by an RF signal in similar manner to feeding a monopole antenna. It was found that the capacitive impedance due to the potential difference between the conductive plate and the ground shifts the peak admittance to higher frequencies.

In this thesis, it is shown that the human body exhibits very interesting antenna characteristics, which have not been reported in the literature before. The antenna characteristics of the human body are assessed based on the antenna performance indicators, which are, the radiation efficiency and the reflection coefficient. It is found that the human body can act like a monopole antenna with a theoretical radiation efficiency reaching up to 70 % (compared to the amount of power dissipated inside the human body) when an RF voltage is applied at the sole of the feet. This is in good agreement with a measurement result found in the literature, based on the comparison of the human body measurements with that of different whip antennas. Moreover, an experiment was carried out to measure the reflection coefficient of the human body using a human subject of height 1.76 m and weight 73 kg. From the experiment, a minimum reflection coefficient of -12 dB was measured at the resonance frequency, which occurred between 35-70 MHz depending on the posture of the subject. This experiment was carried out based on the safety standards set by the International Commission for Non-ionising Radiation Protection (ICNIRP) [22].

These results indicate that the human body is indeed a good antenna. Therefore, this leads to the next question, 'Can the human body be applied as an antenna for other wireless applications?' To answer this question, we assess the feasibility of applying the human body as an antenna for wireless implant communication.

Implants can be used for physiological monitoring in a clinical or research setting, which is, the continual monitoring of vital signs, such as, cardiac, body temperature, or blood glucose. The wireless communication with implants is usually accomplished using magnetic induction or radio-waves.

The wireless implant communication using magnetic induction is affected by the orientation of the magnetic coils used, which should also be placed very close to or in contact to the surface of the body. Moreover, magnetic induction usually operates in the low-MHz frequency that requires large coils for efficient communication. This puts a design challenge since implants are required to be very small in order to be implanted inside the body safely. Usually, most implants that use magnetic induction cannot initiate communication since they are powered by the external coil.

The small size requirement of implants leads to the use of very small antennas for the purpose of radio-wave wireless telemetry. It is known that very high frequency is needed for an efficient operation of small antennas in free space. Unfortunately, the human body is a hostile environment for wireless communication at high frequency [23]; it absorbs the power carried by radio waves. It is also known that as frequency increases the penetration depth of radio waves into the human body decreases. Moreover, an antenna designed for free space operation has different characteristics when operated inside the body. This is due to the dielectric properties of the tissues that modify the antenna parameters, such as, the resonance frequency and the radiation pattern. In addition to this, at high frequencies the body movement affects signal propagation in the vicinity of the body due to shadowing [4].

Currently, wireless RF telemetry using radio-waves employs Medical Implant Communication Service (MICS), a standard developed by European Telecommunications Standards Institute (ETSI) for implant wireless communication [24]. MICS uses the frequency band between 402 and 405 MHz with claims that the signals at this frequency band are less affected by the human body with little supporting evidence. Within this

context, we propose a novel wireless communication technique using the human body itself as an antenna at lower frequencies (<100 MHz), which can be used as an alternative wireless implant communication technique.

The study is based on previous results about the antenna characteristics of the human body and well-known results in the field of RF dosimetry. It is known that the electric current induced inside the human body when exposed to electromagnetic field gets large near the foot for frequencies less than 100 MHz [16]. This is because the distribution of the induced current is similar to that of a monopole antenna, where the current is not uniform along its length. Thus, the axial electric current density in the cross-section of the ankles is very large. Moreover, the transverse cross-sectional areas of the conductive tissues in the ankle are relatively very small. As a result, the viability of using a very small toroidal inductor as a means to induce an RF current inside the ankle for the purpose of wireless implant communications was investigated. It is hypothesised that the induced current dissipates inside the tissues as well as radiates out using the human body as an antenna. The objective is to determine the efficacy of applying this scheme to connect implant devices with external monitoring devices that are located close to the human body. Our analysis showed that the system performance was affected by several factors including, the number of turns of the winding in the inductor and the magnetic core loss. The theoretical results indicate that there is potential for using the human body itself as a radiating antenna for implants, if the implant can be safely anchored to a tissue.

1.2 Research Aims

This research primarily focuses on investigating the human body antenna effects on HBC and the whole-body RF dosimetry. It also addresses the application of the human body antenna for wireless implant communications. The specific objectives of the thesis are as follows:

1. Investigate the effect of the dielectric properties of tissues, electrode-skin contact impedance, anthropometry, and electrodes configuration on galvanic coupled HBC, using the circuit model of the human body in the frequency range of 0.2 - 10 MHz

2. Analyze the signal propagation mechanism and interference in HBC using the imperfectly conducting cylindrical antenna model of the human body in the frequency range of 1 - 200 MHz

3. Analyze the effects of anthropometry, dielectric properties of tissues, and environmental factors on the whole-body RF dosimetry in the frequency range of 1 - 150 MHz

4. Characterize the human body as a monopole antenna using the antenna performance indicator quantities, such as, the reflection coefficient and the radiation efficiency, in the frequency range of 1 - 110 MHz

5. Investigate the viability of using the human body as an antenna for wireless implant communication

1.3 Research Methodology

In the study of the galvanic coupled HBC, a quasistatic approximation is applied to mathematically model the human arm with the attached electrodes using a two-port circuit network of discrete circuit elements. Four different tissues in the arm, namely, skin, fat, muscle and bone, are taken into account. The arm was approximated as a layered cylinder with each tissue layer represented by a parallel RC circuit. The resistance and capacitance values of the circuit elements are calculated from the geometry of the arm and the dielectric spectrum of tissues. The dielectric spectrum of the tissues, which are the conductivity and the permittivity, are taken from the Cole-Cole dispersion model of tissues that were parameterized by Gabriel *et al* [25]. The current flow paths in the tissues are approximated as longitudinal and transverse paths. The two-port network circuit is analyzed using Kirchhoff's circuit laws with the resulting linear equations solved applying matrix algebra.

In order to analyze the antenna characteristics of the human body, the human body standing on a highly conductive ground plane is represented by an imperfectly conducting cylindrical antenna. This is based on the results of some studies that reported that the axial current distribution inside the human body when exposed to plane electromagnetic wave is similar to that of a monopole cylindrical antenna. The equivalent

cylindrical antenna is analyzed by applying the three-term approximation method to express the axial current. The three-term approximation technique involves the numerical computation of some integrals that are solved using Matlab. Since the effect of the shoes on the human body antenna characteristics is taken into account, the cylindrical antenna model is assumed to have a load at its base. Thus, a general expression of the current, which applies for a loaded and imperfectly conducting cylindrical antenna, is derived based on the approaches found in the literature. The expression of the axial current in the cylindrical antenna model helps to analyze the near-field distribution of fields in the vicinity of the human body. For example, it is implemented to understand the distribution of the scalar electric potential on the surface of the human body when a vertical dipole source on the surface of the body is assumed to represent an HBC transmitter. The scalar electric potential distribution is used to predict the measured HBC voltage. Consequently, it explains why the gain has a maximum value near 50 MHz, which aligns with the resonance frequency of the human body antenna.

The FDTD computed WBA-SAR of high resolution realistic voxel models of a human male adult, a female adult and a child, are used to define the corresponding parameters of cylindrical antenna models. The defined parameters of the cylindrical antenna are the radius, height, and the complex conductivity. Based on these models, accurate formula for the resonance frequency of the human body antenna is proposed. Also, the defined model also helps to predict measured experimental values, such as, the reflection coefficient and radiation efficiency of the human body antenna. The experimental setup for the measurement of the reflection coefficient was carried based on the safety guidelines proposed by ICNIRP; the VNA used runs on battery and generates output power much less the safety limit.

The author's perspective on the cylindrical antenna theory is included in Appendix A. Also, the application of a cylindrical dipole antenna for the analysis of the WAB-SAR of a human body in free space is also given in Appendix B.

1.4 Thesis Organization and Contributions

The chapters in this thesis are arranged in chronological order reflecting the time they were submitted for publication.

Chapter 2 This chapter introduces the theoretical background necessary to review the electromagnetic concepts and theories used in the thesis. In particular, it introduces the dielectric properties of tissues, and the spectral models used to represent the measured values of conductivity and permittivity of different tissues. In addition to this, the chapter also introduces cylindrical antenna theory, which is used to mathematically model the human body as an antenna. A three-term representation of the axial current in an imperfectly conducting cylindrical antenna is derived starting from a general expression of the current in infinite cylindrical antennas.

Chapter 3 This chapter contains the copy of the paper "Investigation of galvanic-coupled intrabody communication using the human body circuit model" that was published in *IEEE Journal of Biomedical and Health Informatics*, in 2014. In this chapter, a novel electric circuit model of the human arm is proposed that is applied to explain galvanic coupled HBC. The model is used to analyze how the dielectric properties of tissues affect the electric current coupled to the human body. It was discovered that the dielectric properties of the muscle tissue affect the electric signals that are detected very close to the transmitting source while skin properties affect the signals that are detected farther. This model also explains skin-electrode contact impedance and suggests a new approach to measure it. This impedance is shown to be one of the reasons for the major discrepancies between experimental measurements and theoretical predictions by previous authors. The common trend of applying electric signals to the human body, in the HBC experimental setting, is using pre-gelled medical electrodes. The proposed model helps to analyse the effect of electrodes by indicating that the electrode-skin contact has a high-pass filter effect on the signal coupled to the body.

Chapter 4 This chapter contains the copy of the paper "Human body as antenna and its effect in human body communication" published in *Progress in Electromagnetics Research*, in 2014. In this chapter, a mathematical cylindrical antenna model of the human body is proposed based on the three-term approximation technique. For the first time, the antenna effect of the human body, in the context of HBC, is discussed thoroughly; and the model is used to explain the observed phenomenon of the human body antenna effect. Also a comprehensive study of HBC from the electromagnetic perspective is presented.

Chapter 5 This chapter contains the copy of the paper "Cylindrical antenna theory

for the analysis of whole-body averaged specific absorption rate", which was submitted to *IEEE Transactions on Antennas and Propagation* in March 2015, revised and resubmitted in June, 2014. This chapter provides an in-depth analysis of the WBA-SAR by demonstrating on how the dielectric properties of the tissues, the anthropometry and the shoes affect it. Moreover, an accurate formula for the resonant frequency of the human body as a function of the weight and height was proposed for the first time. The resonant frequencies computed, by other authors, using FDTD and realistic numerical models representing human subjects of different age group, gender, and race, are predicted accurately using the proposed formula. In most RF dosimetry studies, the realistic numerical models used represent bare-footed human subjects; thus, the effect of shoes on WBA-SAR was not studied thoroughly. This chapter analyzes the effect of shoes on WBA-SAR based on antenna theory. It is shown that the resonance frequency increases due to the shoes.

Chapter 6 This chapter contains the copy of the paper "Characterizing the human body as a monopole antenna", which was submitted to *IEEE Transactions on Antennas and Propagation* in April, 2015 and accepted for publication in July, 2015. In this chapter, it is found that the human body acts like an efficient monopole antenna with a radiation efficiency reaching 70 % when an RF electric current is applied at the sole of the feet. Also, it is found that the human body as a monopole antenna has a minimum reflection coefficient of -12 dB. This is based on experimental results that are predicted accurately using the mathematical cylindrical antenna model of the human body. The chapter reports very important findings that open up new prospective applications that use the human body as an antenna. Since it is not ethical and safe to couple large RF power into the body, such potential applications should involve very low power signals. For example, one such application that uses low power is wireless implant communication. The results in this chapter laid the foundations of the next chapter, which is a theoretical exploration of the human body antenna characteristics for wireless implant communications.

Chapter 7 This chapter contains the copy of the paper "Analysis of the Human Body as an Antenna for Wireless Implant Communication", which is submitted to *IEEE Transactions on Antennas and Propagation* in June, 2015. The basis of this study is the previous results about the antenna characteristics of the human body and also the well-known results in the field of RF dosimetry. In this chapter, the feasibility of using a tiny toroidal inductor to induce an RF current at the cross-section of the ankle, for the

purpose of wireless implant communications, is investigated for the frequency range of 1- 70 MHz. The high frequency loss introduced from the inductor winding and the magnetic core are taken into account. From the results, crucial factors are identified that determine the performance of the system, which are, the parasitic capacitance and the magnetic core loss of the inductor. Among other factors, we found out that the number of turns of the wire and the way it is wound around the iron core have crucial effect on the performance of the whole system. The theoretical results indicate the proposed technique has the potential to be implemented in wireless implant communications.

Chapter 2

Background Theory

The study of the human body antenna characteristics involve the interaction of electromagnetic fields with the body, which is determined by the dielectric properties of the tissues. More specifically, the constituents of tissues, which are, the cell membrane, intracellular and extracellular fluids, characterize the dielectric properties of tissues. The ions and polar molecules inside the intra- and extracellular fluids and the capacitive nature of the cell membranes determine the response of the human body when an external electric field is applied. Since the function and structure of tissues are different, their corresponding dielectric properties are also different. Usually, the dielectric properties of tissues are represented by the macroscopic parameters of conductivity and permittivity.

Studies on the RF dosimetry have reported that the human body in standing position has similar characteristics as a quarter wave monopole antenna. Therefore, in this thesis, the human body antenna characteristics are studied based on a cylindrical antenna model of the human body that is analyzed using the three-term approximation method. The three-term approximation method is a semi-analytic approach of representing the induced current in a cylindrical antenna using three sinusoidal functions. In this chapter, the dielectric properties of tissues are introduced followed by the overview of the cylindrical antenna theory, which are important to understand the proposed equivalent cylindrical antenna model of the human body.

2.1   The Dielectric Properties of Tissues

The interaction of electromagnetic fields with biological tissues can be described using Maxwell's equations. Maxwell's equations describe how electric and magnetic fields are generated; and they also govern the interaction of currents and charges. In other words, Maxwell's equation are used to define the electromagnetic fields [26]. Assuming, a harmonic time dependence $e^{j\omega t}$ for angular frequency ω, the Maxwell's equations in point form are given as

$$\nabla \times \mathbf{H} = \mathbf{J_c} + j\omega \mathbf{D}, \tag{2.1}$$

$$\nabla \cdot \mathbf{B} = \mathbf{0}, \tag{2.2}$$

$$\nabla \times \mathbf{E} = -j\omega \mathbf{B}, \tag{2.3}$$

$$\nabla \cdot \mathbf{D} = \rho, \tag{2.4}$$

where $\mathbf{E}$ is the electric field intensity vector in volts per meter (V/m); $\mathbf{H}$ is the magnetic field intensity in ampere per meter [A/m]; $\mathbf{D}$ is the electric flux density in coulomb per square meter (C/m^2); $\mathbf{B}$ the magnetic flux density vector in tesla (T); $\mathbf{J_c}$ is the volume conduction current density vector in amperes per square meter (A/m^2); and ρ is the volume charge density in coulombs per cubic meter (C/m^3). The charge and current densities (ρ and $\mathbf{J_c}$) can be thought as the sources of the electromagnetic fields. These densities are localized in space; for example, they are restricted to flow on an antenna. The generated electric and magnetic fields are radiated away from these sources and can propagate to large distances to the receiving antennas.

Assuming the human body tissues are macroscopically homogenous, their dielectric properties can be described by the permittivity and conductivity. The permittivity represents the tissue's ability to store electric energy; whereas the conductivity determines the tissue's ability to transport charge as response to applied electric field. The tissues are dispersive since they have frequency dependent dielectric properties. Therefore, the electric field components can be related as

$$\mathbf{D} = \epsilon_0 \left[\epsilon'(\omega) - j\epsilon''(\omega) \right] \mathbf{E} \tag{2.5}$$

where $\epsilon_0 = 8.854 \times 10^{-14}$ farads per meter (F/m) is the permeability of free space; $\epsilon'(\omega)$

is the real part of the complex relative permittivity that represents the displacement current; and $\epsilon''(\omega)$ is the imaginary part of the complex relative permittivity that represents the dielectric loss due to the displacement of bound charges. Moreover, tissues of the human body are nonmagnetic; so that the magnetic field components of the Maxwell's equation can be related as

$$\mathbf{B} = \mu_0 \mathbf{H} \tag{2.6}$$

where $\mu_0 = 4\pi \times 10^7$ henries per meter (H/m) is the permeability of free space. The conduction current density $\mathbf{J_c}$ and the applied electric field $\mathbf{E}$ can be related as

$$\mathbf{J_c} = \sigma_i \mathbf{E} \tag{2.7}$$

where σ_i is the static ionic conductivity.

The Maxwell's equation in (2.1) can be written as

$$\nabla \times \mathbf{H} = \mathbf{J_c} + j\omega \mathbf{D} = \mathbf{J_c} + \mathbf{J_d} = \mathbf{J} \tag{2.8}$$

where $\mathbf{J_d} = j\omega \mathbf{D} = \omega \epsilon_0 \left[\epsilon''(\omega) + j\epsilon'(\omega) \right] \mathbf{E}$ is the displacement current density and $\mathbf{J}$ is the total current density. Therefore, from (2.8), the total current density can be expressed as

$$\mathbf{J} = j\omega \epsilon_0 \epsilon_r^*(\omega) \mathbf{E} \tag{2.9}$$

where $\epsilon_r^*(\omega)$ is defined as

$$\epsilon_r^*(\omega) = \left[\epsilon'(\omega) - j\epsilon''(\omega) \right] - j\frac{\sigma_i}{\omega \epsilon_0} \tag{2.10}$$

Similarly, the expression in (2.9) can be rewritten using the complex conductivity σ_ω^* of tissues as

$$\mathbf{J} = \sigma_\omega^* \mathbf{E} \tag{2.11}$$

where

$$\sigma_\omega^* = j\omega \epsilon_0 \epsilon_r^*(\omega) = \sigma_i + \omega \epsilon_0 \epsilon''(\omega) + j\omega \epsilon_0 \epsilon'(\omega) = \sigma_{eff}(\omega) + j\omega \epsilon_0 \epsilon'(\omega) \tag{2.12}$$

where $\sigma_{eff}(\omega) = \sigma_i + \omega \epsilon_0 \epsilon''(\omega)$ is the effective conductivity or the AC conductivity.

Measured values of the relative permittivity $\epsilon'(\omega)$ and the AC conductivity $\sigma_{eff}(\omega)$ of

tissues exhibit different distinctive steps as frequency increases [27]. These transitions from one step to another is called dispersion, which is defined as the manifestations of the polarization and motion of charge carriers in tissues. Most tissues have three dispersion regions, namely, the α, β and γ dispersions. The transport of ions across a biological membrane is related to the low frequency α dispersion. The α dispersion can be found in the frequency range between 1 Hz up to 100 kHz. An increase in tissue conductivity is rarely evident in the α dispersion and the permittivity shows a significant decrease. The polarization of cellular membranes is an obstacle for an ion to flow in or out of the cell and leads to the β dispersion. This region lies within hundreds of kilohertz to tens of megahertz range. The polarization of protein is another contributing factor to the β dispersion trend. The polarization of water molecules creates the γ distribution in the gigahertz region (microwave frequencies). The γ dispersion is not strong and it has minimal effect on the electrical properties of body tissues which carry protein bound water.

An attempt to provide a mathematical model for the dielectric properties of tissues, circuit models that include capacitor and resistor have been used to reproduce the measured values of the permittivity and conductivity of tissues. One of such approaches is the Cole-Cole dispersion model that was successfully parameterized by Gabriel *et al* [28]. The Cole–Cole equation presents the change of dielectric properties of a tissue over a broad frequency range as

$$\epsilon_r^* (\omega) = \epsilon_\infty + \sum_n \frac{\Delta\epsilon_n}{1 + (j\omega\tau_n)^{(1-\alpha_n)}} - j\frac{\sigma_i}{\omega\epsilon_0} \tag{2.13}$$

where ϵ_∞ is the permittivity at terahertz frequency; n is the dispersion identifier; and $\Delta\epsilon_n$, τ_n and α_n are tissue parameters for each dispersion region. The dielectric performance of biological tissues is predicted by this summation through proper parameter selection for each tissue. In [28], four different dispersions were used to fit the measured data of different tissues in the frequency range of 10 Hz-20 GHz. The conductivity and permittivity of tissues obtained from this model are used in this thesis.

2.2 Overview of Cylindrical Antenna Theory

The methodology of this thesis makes use of the cylindrical antenna theory, which requires the solution of the total induced axial current inside a cylindrical antenna when illuminated by a vertically polarized electric field. Even though it is possible to determine the total induced axial current in a cylindrical antenna from the vertically polarized electric field at the surface of the antenna, it is much simpler to use auxiliary vector potential functions in the solution. In the antenna analysis problems, vector potentials are often introduced in order to simplify the solutions of the problems. Vector potentials are mathematical tools that are used as auxiliary functions in the analysis of electromagnetic radiation problems. Unlike electric field intensity $\mathbf{E}$ and magnetic field intensity $\mathbf{H}$, they are not measurable physical quantities. An example of vector potential includes the magnetic vector potential, $\mathbf{A}$, which is important in the analysis of the cylindrical antennas applied in this thesis.

Considering a circular conducting cylinder of radius a and complex conductivity σ_ω^* that extends along the z-axis of a system of cylindrical coordinates (ρ, ϕ, z) with a time harmonic $(e^{j\omega t})$ and rotationally symmetric axial magnetic vector potential $\mathbf{A}_1(\rho, z) = A_{1z}(\rho, z)\,\hat{\mathbf{z}}$ maintained inside it, the general equation for the vector potential, assuming a simple medium, can be written as

$$\nabla^2 \mathbf{A}_1(\rho, z) + k_1^2 \mathbf{A}_1(\rho, z) = 0 \tag{2.14}$$

where $k_1 = \sqrt{-j\omega\mu_0\sigma_\omega^*}$. Expanding the vector identity $\nabla^2 \mathbf{A}_1 = \nabla\nabla \cdot \mathbf{A}_1 - \nabla \times \nabla \times \mathbf{A}_1$ in cylindrical coordinates and substituting it into (2.14) gives

$$\frac{\partial^2 A_{1z}(\rho, z)}{\partial z^2} + \frac{1}{\rho}\frac{\partial}{\partial\rho}\rho\frac{\partial A_{1z}(\rho, z)}{\partial\rho} + k_1^2 A_{1z}(\rho, z) = 0. \tag{2.15}$$

The solution for (2.15) can be obtained by the method of separation of variables, such that $A_{1z}(\rho, z)$ can be written as

$$A_{1z}(\rho, z) = f(z)F(\rho). \tag{2.16}$$

Substituting (2.16) in (2.15) yields the equation

$$\frac{1}{f(z)}\frac{\partial^2 f(z)}{\partial z^2} + k_1^2 = -\frac{1}{F(\rho)}\frac{1}{\rho}\frac{\partial}{\partial \rho}\rho\frac{\partial F(\rho)}{\partial \rho}.$$ (2.17)

It can be seen that the left side of the above equation is a function of z and the right side is a function of ρ; thus, the two sides can be equal if both of them are equal to a constant. Denoting the constant by κ^2 and expressing it as $\kappa^2 = k_1^2 - \gamma^2$ so that

$$\frac{\partial^2 f(z)}{\partial z^2} + \gamma^2 f(z) = 0$$ (2.18)

and

$$\frac{1}{\rho}\frac{\partial}{\partial \rho}\rho\frac{\partial F(\rho)}{\partial \rho} + \kappa^2 F(\rho) = 0.$$ (2.19)

The expression in (2.18) is the well known one dimensional wave equation that has a solution of a traveling wave in a lossy medium given as $f(z) = C_1 e^{\pm j\gamma z}$ or the standing wave representation as $f(z) = C_2\cos(\gamma z) + C_3\sin(\gamma z)$, where C_1, C_2 and C_3 are arbitrary constants. The first expression of $f(z)$ represents a wave that originates from the origin and propagates along the length of the cylinder on the z-axis while being attenuated by the lossy medium. γ is the complex propagation constant that can be described as $\gamma = \beta - j\alpha$, where β is the phase constant and α is the attenuation constant. *(Please note that the common notations used for the complex propagation constant γ, the phase constant β and the attenuation constant α coincide with the notation used for the three dispersion regions of the dielectric spectrum of tissues discussed perviously. Though the notations are similar, their representations are different.)* In this thesis, since we are utilizing the infinite length cylinder to describe a finite length cylindrical antenna, the second solution of $f(z)$ is more appropriate.

Equation (2.19) can be written in terms of a new independent variable $x = \kappa\rho$ as

$$\frac{\partial^2 F\left(\frac{x}{\kappa}\right)}{\partial x^2} + \frac{1}{x}\frac{\partial F\left(\frac{x}{\kappa}\right)}{\partial x} + F\left(\frac{x}{\kappa}\right) = 0,$$ (2.20)

which is a Bessel equation with known solutions. One of the solution for the expression in (2.20) is $F(\rho) = C_4 J_0(\kappa\rho)$, where J_0 is the zeroth-order Bessel function and C_4 is an arbitrary constant. The Bessel function was chosen so that the vector potential is non-zero at the center of the cylinder. Therefore, the magnetic vector potential can be

written as

$$A_{1z}(\rho, z) = F(\rho) f(z) = C_4 J_0(\kappa\rho) [C_1 \cos(\gamma z) + C_2 \sin(\gamma z)] \qquad (2.21)$$

Assuming the axial electric field in the cylinder causes a total axial current $I(z)$, from Ampere's law, the magnetic flux density $B_{2\phi}(a, z)$ on the surface of the cylinder can be written as

$$B_{2\phi}(a, z) = \frac{\mu_0 I(z)}{2\pi a}. \qquad (2.22)$$

From the expression of the magnetic vector potential, the magnetic flux density inside the cylinder can also be expressed as

$$B_{1\phi}(\rho, z) = -\frac{\partial A_{1z}(\rho, z)}{\partial \rho} = C_4 \kappa J_1(\kappa\rho) [C_1 \cos(\gamma z) + C_2 \sin(\gamma z)] \qquad (2.23)$$

where J_1 is the first-order Bessel function. Defining the arbitrary constant C_4 as

$$C_4 = \frac{\mu_0}{2\pi a \kappa J_1(\kappa a)} \qquad (2.24)$$

and applying the magnetic field boundary condition at the surface of the cylinder, the magnetic flux density at the surface of the cylinder can be written as

$$B_{1\phi}(a, z) = B_{2\phi}(a, z) = \frac{\mu_0}{2\pi a} [C_1 \cos(\gamma z) + C_2 \sin(\gamma z)] = \frac{\mu_0 I(z)}{2\pi a} \qquad (2.25)$$

assuming the permeability of the cylinder is the same as that of the free space. From (2.25), the total axial current $I(z)$ can be expressed as

$$I(z) = C_1 \cos(\gamma z) + C_2 \sin(\gamma z). \qquad (2.26)$$

Equation (2.26) expresses a current that propagates as a standing wave and attenuates along the z-axis. When we adapt similar expressions to describe a finite length cylinder, the current at the ends of the cylinder has to be zero. Therefore, the total axial current in finite cylinders or cylindrical antennas has a general form similar to (2.26) with additional terms to compensate for the edge effects. Additionally, if the finite cylindrical dipole antenna is center-fed, we expect the current to have similar distribution on both direction

of the z-axis, having the general form:

$$I\left(z\right) = C_1 \cos\left(\gamma z\right) + C_2 \sin\left(\gamma|z|\right). \tag{2.27}$$

The electric field inside the cylinder can be found from the vector magnetic potential using their relationship in a simple media as

$$\mathbf{E_1} = \frac{-j\omega}{k_1^2}\left(\nabla\nabla \cdot \mathbf{A_1} + k_1^2\mathbf{A_1}\right). \tag{2.28}$$

From (2.28), the axial component of the electric field can be derived as

$$E_{1z}\left(\rho, z\right) = \frac{j\omega}{k_1^2}\frac{1}{\rho}\frac{\partial}{\partial\rho}\rho\left(\frac{\partial A_{1z}\left(\rho, z\right)}{\partial\rho}\right) = -j\omega\frac{\kappa^2}{k_1^2}A_{1z}\left(\rho, z\right) = \frac{I\left(z\right)\kappa}{2\pi a\sigma_\omega^*}\frac{J_0\left(\kappa\rho\right)}{J_1\left(\kappa a\right)}. \tag{2.29}$$

And the volume current density can be derived as

$$J_{1z}\left(\rho, z\right) = \sigma_\omega^* E_{1z}\left(\rho, z\right) = \frac{I\left(z\right)\kappa}{2\pi a}\frac{J_0\left(\kappa\rho\right)}{J_1\left(\kappa a\right)}. \tag{2.30}$$

In order to characterize the circuit properties per unit length of the cylinder, the surface impedance per unit length of the cylinder z^i was defined as

$$z^i = \frac{E_{1z}\left(a, z\right)}{I\left(z\right)} = \frac{\kappa}{2\pi a\sigma_\omega^*}\frac{J_0\left(\kappa a\right)}{J_1\left(\kappa a\right)}. \tag{2.31}$$

The cylindrical antenna was analysed by considering a finite size cylindrical dipole antenna of length $2h$ and radius a with axis aligned along the z-axis that was illuminated by a time-harmonic $(e^{j\omega t})$ vertically polarized electric field. It was assumed that the incident electric field induced a rotationally symmetric volume current density inside the cylinder. Based on the boundary conditions, the electric field at the surface can be related as

$$E_0 + E_{2z}\left(a, z\right) = E_{in}\left(a, z\right) \tag{2.32}$$

where E_0 is the incident electric field on the surface of the cylinder, $E_{2z}\left(a, z\right)$ is the scattered electric field at the surface of the cylinder, and $E_{in}\left(a, z\right)$ is the internal electric field at the surface of the cylinder. Assuming an infinitesimal transversal dielectric gap

is present at $z = 0$, the internal electric field can be described as

$$E_{in}(a, z) = E_{1z}(a, z) - V_0^e \delta(z) \tag{2.33}$$

where $E_{1z}(a, z)$ is the axial electric field obtained from (2.29) and V_0^e represents the voltage drop across the dielectric gap. The electric field across the dielectric gap was modeled using the *delta-gap* model as $E_g(a, 0) = -V_0^e \delta(z)$. Denoting the total axial current induced inside the finite cylinder as $I_{1z}(z)$, the $E_{1z}(a, z)$ can be written as

$$E_{1z}(a, z) = z^i I_{1z}(z). \tag{2.34}$$

The scattered axial electric field at the surface of the cylinder $E_{2z}(a, z)$ can be related to the axial magnetic vector potential on the surface of the cylinder $A_{2z}(a, z)$ due to the current density inside cylinder $J_{1z}(\rho, z)$ as

$$E_{2z}(a, z) = \frac{-j\omega}{k_2^2} \left(\frac{\partial^2}{\partial z^2} + k_2^2 \right) A_{2z}(a, z) \tag{2.35}$$

where $k_2 = \omega \sqrt{\epsilon_0 \mu_0}$ is the free space wave number. Also, the scattered vector magnetic potential $\mathbf{A}_2$ can be related to the source current density j_1 as

$$\mathbf{A}_2(\mathbf{r}) = \frac{\mu_0}{4\pi} \int_{V'} \mathbf{J}_1(\mathbf{r}') \frac{e^{-jk_2 R}}{R} dv' \tag{2.36}$$

where $R = \mathbf{r} - \mathbf{r}'$ is the distance between the source and observation point and V' indicates the integration is carried out in the domain of the cylinder volume. Assuming the condition $k_2 a \ll 1$ and $h \gg a$ is satisfied and the axial current density in the cylinder is similar to the expression in (2.30) as

$$J_{1z}(\rho, z) = \frac{I_{1z}(z) \kappa}{2\pi a} \frac{J_0(\kappa \rho)}{J_1(\kappa a)}, \tag{2.37}$$

the scattered axial vector magnetic potential on the surface of the cylinder can be approximated as

$$A_{2z}(a, z) = \frac{\mu_0}{4\pi} \int_{-h}^{h} \int_0^a 2\pi J_{1z}(\rho', z') \frac{e^{-jk_2 R_1}}{R_1} \rho' d\rho' dz' = \frac{\mu_0}{4\pi} \int_{-h}^{h} I_{1z}(z') \frac{e^{-jk_2 R_1}}{R_1} dz' \tag{2.38}$$

where $R_1 = \sqrt{(z - z')^2 + a^2}$. Therefore, the electric field boundary condition in (2.32) can be re-written as

$$\left(\frac{\partial^2}{\partial z^2} + k_2^2 \right) \int_{-h}^{h} I_{1z}\left(z'\right) \frac{e^{-jk_2 R_1}}{R_1} dz' = \frac{j4\pi k_2^2}{\omega\mu_0} \left(I_{1z}\left(z\right) z^i - V_0^e \delta\left(z\right) - E_0 \right). \qquad (2.39)$$

The expression in (2.39) does not have a closed form solution for the axial current; but it can be approximated using numerical approaches, such as, the Method-of-Moments. It can also be approximately solved by the semi-analytic approach, namely, the three-term approximation method, which is the approach used in this thesis. Thus, we derived an expression for the total axial current $I_{1z}\left(z\right)$ based on the approach used for imperfectly conducting transmitting cylindrical antenna [29] and for resistive receiving antenna [30]. The expression in (2.39) describes an imperfectly conducting and loaded receiving cylindrical antenna that requires a solution different from those reported in [29, 30]; but it was derived using similar methodology discussed in the papers. The technique used to solve the equation is well documented in the two articles [29, 30]; therefore, it was not repeated here. Consequently, the approximate semi-analytic solution for the total axial current is

$$I_{1z}\left(z\right) = V_0^e v\left(z\right) + \frac{E_0}{k_2} u\left(z\right) \qquad (2.40)$$

where

$$v\left(z\right) = \frac{j2\pi k_2}{\zeta_0 \gamma \Psi_{dR} \cos(\gamma h)} \left[\sin\gamma(h - |z|) + T_U(\cos\gamma z - \cos\gamma h) \right.$$
$$\left. + T_D(\cos\tfrac{1}{2}k_2 z - \cos\tfrac{1}{2}k_2 h) \right] \qquad (2.41)$$

$$u\left(z\right) = \frac{j4\pi}{\zeta_0} \left[H_U(\cos\gamma z - \cos\gamma h) + H_D(\cos\tfrac{1}{2}k_2 z - \cos\tfrac{1}{2}k_2 h) \right] \qquad (2.42)$$

where $\zeta_0 = 120\pi$ Ω is free space impedance. The functions $v\left(z\right)$ and $u\left(z\right)$ have a from similar to the current defined for the infinite cylinder in (2.26). The coefficients in (2.41) and (2.42) involve integrals that are computed numerically by applying the recursive adaptive Simpson quadrature function on Matlab

$$T_U = \frac{C_V E_D - C_D E_V}{C_U E_D - C_D E_U} \qquad T_D = \frac{C_U E_V - C_V E_U}{C_U E_D - C_D E_U} \qquad (2.43a)$$

$$H_U = \frac{C_D - E_D}{C_U E_D - C_D E_U} \qquad H_D = \frac{E_U - C_U}{C_U E_D - C_D E_U} \tag{2.43b}$$

where

$$C_U = \left(1 - \frac{\gamma^2}{k_2^2}\right)(\Psi_{dUR} - \Psi_{dR})(1 - \cos\gamma h) - \frac{\gamma^2}{k_2^2}\Psi_{dUR}\cos\gamma h$$
$$+ j\Psi_{dUI}\left(\frac{3}{4} - \cos\tfrac{1}{2}k_2 h\right) + \Psi_U(h) \tag{2.44a}$$

$$C_D = \Psi_{dD}\left(\frac{3}{4} - \cos\tfrac{1}{2}k_2 h\right) - \left(1 - \frac{\gamma^2}{k_2^2}\right)\Psi_{dR}\left(1 - \cos\tfrac{1}{2}k_2 h\right) + \Psi_D(h) \tag{2.44b}$$

$$C_V = -\left[j\Psi_{dI}\left(\frac{3}{4} - \cos\tfrac{1}{2}k_2 h\right) + \Psi_V(h)\right] \tag{2.44c}$$

$$E_U = -\frac{\gamma^2}{k_2^2}\Psi_{dUR}\cos\gamma h - j\tfrac{1}{4}\Psi_{dUI}\cos\tfrac{1}{2}k_2 h + \Psi_U(h) \tag{2.44d}$$

$$E_D = -\tfrac{1}{4}\Psi_{dD}\cos\tfrac{1}{2}k_2 h + \Psi_D(h) \qquad E_V = j\tfrac{1}{4}\Psi_{dI}\cos\tfrac{1}{2}k_2 h - \Psi_V(h) \tag{2.44e}$$

$$\Psi_V(h) = \int_{-h}^{h} \sin\gamma(h - |z'|)\frac{e^{-jk_2 R_h}}{R_h}dz' \tag{2.45a}$$

$$\Psi_U(h) = \int_{-h}^{h} \left(\cos\gamma z' - \cos\gamma h\right)\frac{e^{-jk_2 R_h}}{R_h}dz' \tag{2.45b}$$

$$\Psi_D(h) = \int_{-h}^{h} \left(\cos\tfrac{1}{2}k_2 z' - \cos\tfrac{1}{2}k_2 h\right)\frac{e^{-jk_2 R_h}}{R_h}dz' \tag{2.45c}$$

$$\Psi_{dR} = \Psi_{dR}(z_m), \quad \begin{cases} z_m = 0, & k_2 h \leq \pi/2 \\ z_m = h - \lambda/4, & k_2 h > \pi/2 \end{cases} \tag{2.46a}$$

$$\Psi_{dR}(z) = \csc\gamma(h - |z|)\int_{-h}^{h} \sin\gamma(h - |z'|)\left[\frac{\cos k_2 R}{R} - \frac{\cos k_2 R_h}{R_h}\right]dz' \tag{2.46b}$$

$$\Psi_{dUR} = [1 - \cos\gamma h]^{-1}\int_{-h}^{h} \left[\cos\gamma z' - \cos\gamma h\right]\left[\frac{\cos k_2 R_0}{R_0} - \frac{\cos k_2 R_h}{R_h}\right]dz' \tag{2.46c}$$

$$\Psi_{dD} = \left[1 - \cos\tfrac{1}{2}k_2 h\right]^{-1} \int\limits_{-h}^{h} \left[\cos\tfrac{1}{2}k_2 z' - \cos\tfrac{1}{2}k_2 h\right]\left[\frac{e^{-jk_2 R_0}}{R_0} - \frac{e^{-jk_2 R_h}}{R_h}\right] dz' \quad (2.46\text{d})$$

$$\Psi_{dI} = -\left[1 - \cos\tfrac{1}{2}k_2 h\right]^{-1} \int\limits_{-h}^{h} \sin\gamma(h - |z'|)\left[\frac{\sin k_2 R_0}{R_0} - \frac{\sin k_2 R_h}{R_h}\right] dz' \quad (2.46\text{e})$$

$$\Psi_{dUI} = -\left[1 - \cos\tfrac{1}{2}k_2 h\right]^{-1} \int\limits_{-h}^{h} \left[\cos\gamma z' - \cos\gamma h\right]\left[\frac{\sin k_2 R_0}{R_0} - \frac{\sin k_2 R_h}{R_h}\right] dz' \quad (2.46\text{f})$$

$$R_0 = \left[z'^2 + a^2\right]^{\frac{1}{2}} \qquad R_h = \left[(h - z')^2 + a^2\right]^{\frac{1}{2}} \quad (2.46\text{g})$$

The complex propagation constant $\gamma = \beta - j\alpha$ was defined as

$$\gamma^2 = k_2^2\left(1 - \frac{j4\pi z^i}{k_2\zeta_0\Psi_{dR}}\right). \quad (2.47)$$

The value of γ is calculated by the process of iteration that is initialised by $\gamma = k_2$ to calculate z^i and Ψ_{dR}, which are in turn used to calculate γ. The iteration is found to be highly convergent; thus, the results after several iteration steps suffice to provide an accurate approximation. It should be noted that for perfect conducting antennas $z^i = 0$, which reduces the expression in (2.47) to $\gamma = k_2$ resulting in the propagation constant is equal to the free space wave number. This also reduces the expression of of the current to the expression of the axial current in a perfectly conducting dipole antenna as shown in [29].

The cylindrical antenna considered here is a center-loaded dipole antenna with the dielectric gap taken as the load. Moreover, it is known that a receiving antenna can be represented by Thevenin's equivalent circuit using the antenna input impedance Z_A and the equivalent source voltage V_{eq}. From [29], the input impedance of the cylindrical dipole antenna can be defined as

$$Z_A = \frac{1}{v(0)}. \quad (2.48)$$

The equivalent source voltage can be calculated from the short-circuit current $I_{sc}(0)$, which is the current when there is no load or dielectric gap, and the input impedance as

$$V_{eq} = I_{sc}(0)Z_A = \frac{E_0}{k_2}u(0)Z_A. \quad (2.49)$$

Therefore, the voltage drop across the dielectric gap can be calculated as

$$V_0^e = -\frac{E_0}{k_2} u(0) \frac{Z_A Z_L}{Z_A + Z_L} \tag{2.50}$$

where Z_L is the impedance of the dielectric gap. Assuming the dielectric gap has a permittivity ϵ_g and thickness t, its capacitance C_L can be calculated as

$$C_L = \epsilon_g \frac{\pi a^2}{t}; \tag{2.51}$$

thus, its impedance can be expressed as

$$Z_L = \frac{-j}{\omega C_L}. \tag{2.52}$$

Therefore, the total axial current expressed in (2.40) can be re-written as

$$I_{1z}(z) = \frac{E_0}{k_2} \left(u(z) - \frac{Z_L u(0)}{1 + Z_L v(0)} v(z) \right). \tag{2.53}$$

In this thesis, the cylindrical monopole antenna is used to describe the antenna effect of a human subject standing on a perfectly conductive ground. Under this assumption, the expressions derived for the dipole cylindrical antenna can be easily adapted for the monopole antenna by applying the image theory. From image theory, the total axial current in the monopole cylindrical antenna is the same as that of the dipole. The reflection from the perfectly conducting ground has the same effect as if there was an image cylinder in the ground along the negative z-axis. It can also be assumed that half of the cylinder in the negative z-axis is the image of the monopole antenna grounded on the highly conductive ground. As a result, the input impedance for the monopole Z_A^m becomes half of that of the dipole, which is $Z_A^m = Z_A/2$. Thus, the expression of the total axial current in the case of the monopole cylindrical antenna on a perfectly conducting ground can be defined as

$$I_{1z}(z) = \frac{E_0}{k_2} \left(u(z) - \frac{2Z_A^m Z_L u(0)}{2Z_A^m + Z_L} v(z) \right). \tag{2.54}$$

In relation to this, a new perspective on the cylindrical antenna theory is given in Appendix A.

Chapter 3

Investigation of Galvanic Coupled Intrabody Communication using Human Body Circuit Model

BEHAILU KIBRET, MIRHOJJAT SEYEDI, DANIEL T H LAI, AND MICHEAL FAULKNER

3.1   Abstract

Intrabody Communication (IBC) is a technique that uses the human body as a transmission medium for electrical signals to connect wearable electronic sensors and devices. Understanding the human body as the transmission medium in IBC paves way for practical implementation of IBC in body sensor networks. In this study, we propose a model for galvanic coupling type IBC based on a simplified equivalent circuit representation of the human upper arm. We propose a new way to calculate the electrode–skin contact impedance. Based on the model and human experimental results, we discuss important characteristics of galvanic coupling-type IBC, namely, the effect of tissues,anthropometry of subjects, and electrode configuration on signal propagation. We found that the dielectric properties of the muscle primarily characterize the received signal when receiver electrodes are located close to transmitter electrodes. When receiver and transmitter electrodes are far apart, the skin dielectric property affects the received signal.

3.2   Introduction

The accomplishments in telemedicine technology and body sensor networks contribute to the fulfillment of the pervasive healthcare visions [31]. In body sensor networks, short range wireless communication between biomedical sensors is achieved using commonly used radio frequency based wireless links, e.g., Bluetooth and Zigbee. These protocols are designed for communications at distances of several tens of meters by radiating electromagnetic energy into the air; hence, they intrinsically require more power [32, 33]. As an alternative, a new method of wireless data transmission that uses the human body as transmission medium, or Intrabody Communication (IBC), was first proposed for Personal Area Networks (PAN) by Zimmerman [34]. This technique uses near-field and electrostatic coupling of signals; consequently, low frequency communication without electromagnetic radiation can be achieved that potentially leads to reduced power consumption.

Generally, there are two approaches of IBC, namely, capacitive coupling and galvanic coupling. In capacitive coupling, the signal is transmitted through the human body; and a return path is formed by the capacitive coupling between the transmitter electrodes and receiver electrodes through the external environment, e.g., air. In this approach,

the transmission quality is affected by the noisy environment and the size of the receiver ground planes [35]. In galvanic coupling, which is the focus of this study, the signal is applied differentially between two transmitter electrodes and received differentially by two receiver electrodes [36]. The signal in the galvanic coupling approach is confined within the body as it is transmitted from a pair of transmitter electrodes to a pair of receiver electrodes, and therefore, is less prone to noise from the external environment [37].

Several groups have attempted to investigate the propagation mechanism in IBC [38]; and models based on finite-element methods [5, 6], finite difference time-domain (FDTD) [7], quasi-static electromagnetic principles [8, 9], and equivalent electrical circuits [10–12] have been proposed. Recently, a more comprehensive model of signal transmission on the human body surface for capacitive coupling IBC was proposed by [18], based on electromagnetic theory. However, there are still some gaps in knowledge. For example, the effect of various tissues on signal propagation in galvanic IBC has not been analysed in detail. Some of the proposed models did not include the effect of electrode-skin contact impedance [5, 18] and in other models the impedance was not clearly presented [6, 10]. In addition, the models do not take into account subject specific anatomical parameters, i.e., anthropometry. For these reasons, current IBC models do not accurately describe or predict the empirical measurements of signal propagation through human subjects.

In this work, we propose a new circuit model of the transmission medium in galvanic coupling type IBC based on simplified equivalent circuit representation of the human upper arm. We propose a new way to calculate electrode-skin contact impedance from the human body input impedance measurement, which has not been previously emphasized. Moreover, we analyse the effect of tissues and electrode configuration on galvanic coupling IBC. We demonstrate that the proposed model successfully predicts gain and phase shift measurements over 6 human subjects with various anthropometric measures.

The paper is organized as follows. In Section A.3, the dielectric spectrum of biological tissues based on a single Cole-Cole dispersion and a macroscopic circuit model of tissues are discussed. This is followed by the construction and discussion of a simplified equivalent circuit model of the human upper arm in Section 3.4. In this section, the component impedances of the simplified circuit are analysed taking into consideration the new proposed approach of calculating electrode-skin impedance. Section **??** presents

the measurement set-up and calculation procedures, followed by the discussion of the experimental and calculation results in section 3.6.

3.3 Model for Dielectric Spectrum of Tissues

In our work, the frequency range selected for the investigation of the transmission medium in galvanic coupled IBC is from 200 kHz to 10 MHz. We set the lower bound of the frequency range, which is well above the spectrum of biological signals, based on the low frequency limitation of the measuring devices we used. At the upper frequency bound, 10 MHz, the dimension of the upper arm is smaller compared to the wavelength of the signal; therefore, the signal propagating within the arm can still be considered to be in the near-field region of the electromagnetic field. This region can be modeled by static circuit models, which our study is based upon. Moreover, at higher frequencies, it is thought that the human body radiates the signals to the air as electromagnetic waves and the signals are no longer confined within the body due to the human body antenna effects [14].

For the given frequency range, the dielectric spectrum of tissues can be approximated by the second Cole-Cole dispersion of Gabriel's parametric relation [25]. For a single dispersion, the expression for complex relative permittivity (ε_r^*) as a function of angular excitation frequency (ω) is given as

$$
\begin{aligned}
\epsilon_r^*(\omega) &= \epsilon_r^{'}(\omega) - j\epsilon_r^{''}(\omega) \\
&= \epsilon_\infty + \frac{\Delta\epsilon_n}{1 + (j\omega\tau_n)^{1-\alpha_n}} + \frac{\sigma_i}{j\omega\epsilon_0}
\end{aligned}
\tag{3.1}
$$

where $n = 2$ represents the second dispersion region in the Gabriel dispersion relation, $\epsilon_r^{'}$ and $\epsilon_r^{''}$ are the real and imaginary parts of ϵ_r^*, $\Delta\epsilon_n$ refers to the strength of the dispersion, ϵ_∞ is permittivity at infinite frequency, τ_n is the relaxation time constant, α_n is distribution parameter that controls the width of the dispersion, σ_i is the static ionic conductivity, and ϵ_0 is permittivity of vacuum.

The complex conductivity can be calculated from (1) as

$$
\sigma^*(\omega) = \sigma^{'}(\omega) + j\sigma^{''}(\omega) = j\omega\epsilon_0\epsilon_r^*(\omega)
\tag{3.2}
$$

where $\sigma^{'}$ and $\sigma^{''}$ are the real and imaginary parts of σ^{*}.

Since the fundamental processes of charge build up and conduction in tissue occur in parallel [39], we propose a simple two-component equivalent circuit that represents the admittance Y of tissues, which is a parallel combination of conductance G and susceptance B, as shown in (3). For this model, we assumed homogenous dielectric properties of tissue; thus, the admittance can be represented in terms of specific conductivity and relative permittivity, which are estimated by (1) and (2), respectively, as

$$Y(\omega) = G(\omega) + jB(\omega) \tag{3.3}$$

and frequency dependant conductance and susceptance for uniform cross-section of tissues are defined as

$$G(\omega) = K\sigma^{'}(\omega) = K\omega\epsilon_0\epsilon_r^{''} \tag{3.4}$$

$$B(\omega) = K\sigma^{''}(\omega) = K\omega\epsilon_0\epsilon_r^{'}(\omega) \tag{3.5}$$

where K is the ratio of cross-sectional area to length of tissues. This definition is based on the implicit assumption that current density is uniform throughout the cross-section. For the frequency range we used, the skin-depth of all tissues is large compared to the radius of the upper arm; therefore the assumption of uniform current density is justified.

3.4 Human Body Equivalent Circuit Model

Since our study of galvanic signal coupling focuses on the near-field region of electromagnetic field, where the signals exhibit dipole type field behaviour, we used the electric field intensity (current density) vectors of the electric dipole to represent the current flow paths in galvanic coupling as shown in Fig. 3.1.

We assumed the upper arm is composed of concentric layers of skin, subcutaneous fat, muscle, and cortical bone. In this study, we investigated these tissues based on their dielectric and anatomical characteristics to calculate their impedances and thus their contributions to the pathways of current flow in galvanic current coupling. Based on the
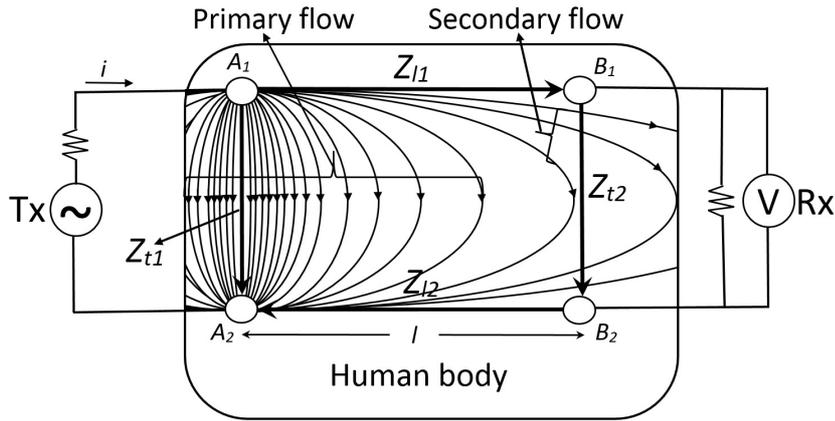
FIGURE 3.1: Current flow paths in galvanic coupling. The primary flow is the current flowing between the Tx electrodes, which does not contribute to the potential difference detected by Rx electrodes. The secondary flow is the current that induces potential difference on Rx electrodes. Z_{t1} represents the impedance of the primary flow path; Z_{l1} and Z_{l2} refer to the impedance of the longitudinal forward and return path of the secondary flow, respectively; and Z_{t2} refers to the transverse path of the secondary flow. l is the distance between transmitter and receiver electrode pairs. The distance between transmitter electrodes A_1 and A_2 is d_{ts} and between receiver electrodes B_1 and B_2 is d_{rs}.

current paths defined, each of the four tissues in the upper arm can be represented by four distinctive impedances characterising a unique galvanic coupled set-up as shown in Fig. 3.1. The set-up depends on the geometry and location of the electrodes, namely, the separation between transmitter and receiver electrodes, which is depicted as l in Fig. 3.1, the distance between the transmitter electrode pair (d_{ts}), and the distance between receiver electrode pair (d_{rs}).

The impedances are calculated using,

$$Z(\omega) = \frac{1}{Y(\omega)} = \frac{1}{K\omega\epsilon_0(\epsilon_r''(\omega) + j\epsilon_r'(\omega))} \tag{3.6}$$

where $Y(\omega)$ is the complex admittance characterising a single homogenous tissue and calculated based on (3); and K is the ratio of effective cross-sectional area to length of a tissue. The effective cross-sectional area and length depends on electrode configurations, width and depth of current distribution, and subject specific anatomical parameters such as tissue thickness.

We compared the impedance characteristics of each tissue in order to investigate their contributions to current flow in the upper arm. For simplicity, we considered a unit cell volume (i.e., cube of side 1 cm) of each tissue; and as a result, the value of K is equal
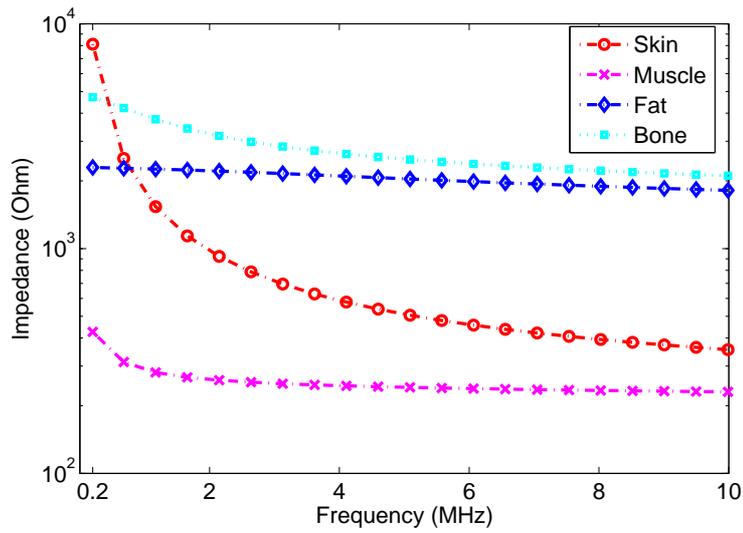
FIGURE 3.2: Impedance magnitude $|Z|$, in Ω, of tissues in the upper arm.
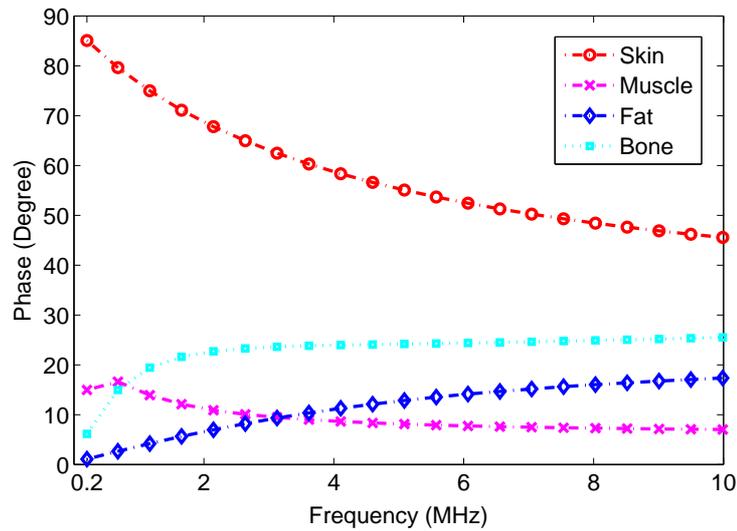
FIGURE 3.3: Impedance phase angle (degree) as function of frequency for tissues in the upper arm.

to 1 cm. Fig. 3.2 and Fig. 3.3 show impedance modulus and the corresponding phase angle, respectively, of each tissue calculated using (6).

Based on the impedance of tissues and human body anatomy, we propose the simplified equivalent circuit shown in Fig. 3.4. From Fig. 3.2, bone and fat have large impedance values. As a result, we assumed their contribution to longitudinal and transverse flow path is very small; and modelled their effects as open circuit. Muscle remains a potential current flow path in both longitudinal and transverse direction due to its small impedance over frequency. Therefore, its effect is included in the circuit as Z_{mtt} and
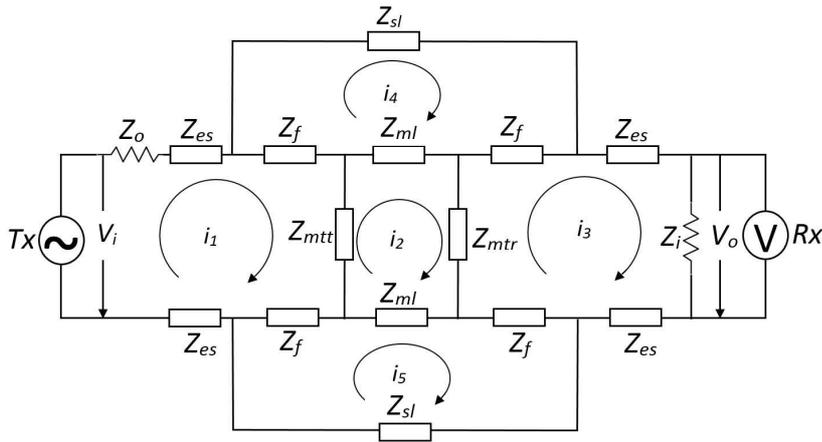
FIGURE 3.4: A simplified equivalent circuit representation of the upper arm for galvanic coupling type IBC, for the case of gelled electrodes, where Z_o is output impedance of the transmitter; Z_i is input impedance of receiver and the i_1 to i_5 are the mesh currents

Z_{mtr}, representing the transverse impedance of muscle at transmitter and receiver side, respectively; and Z_{ml}, the longitudinal impedance. Moreover, skin is located in direct contact with the coupling electrodes; and its impedance decreases as frequency increases. Z_{sl} thus represents the longitudinal impedance of skin.

Another current flow path we took into account is the path perpendicular to the surface of the coupling electrodes. In our abstraction of the upper arm, fat is located between skin and muscle; and thickness of fat can be large enough that it can impede the current flowing from skin to muscle. Therefore, the impedance of fat tissue underneath the location of electrodes is represented by the series fat impedance, Z_f.

Another factor that we considered for simplification of the equivalent circuit is the condition of the coupling electrodes. We modelled the pregelled Ag/AgCl electrodes used in this work. The impedance of skin at lower frequencies gets smaller in areas where the gel is applied; as a result, more current can be injected into the lower tissues compared to using dry electrodes [39]. We combined the individual impedances of the contacts among skin, gel and electrode as a single electrode-skin contact impedance, Z_{es}. In addition to this, we observed that the calculated transverse impedance of ungelled skin is very large compared to the measured electrode-skin contact impedance due to the small cross-sectional area to length ratio of the ungelled skin and its smaller conductivity. Consequently, we approximated the transverse impedance of the skin as open in the simplified equivalent circuit model.
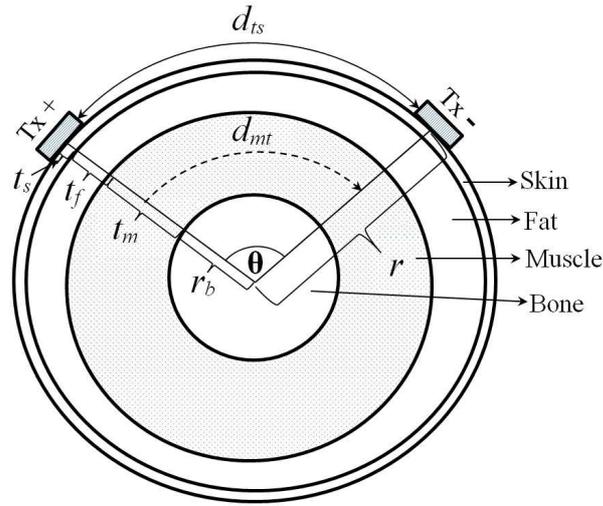
FIGURE 3.5: Cross-section of the upper arm abstraction along the transverse axis at the transmitter location. t_s is skin thickness, t_f fat thickness, t_m muscle thickness, r_b bone radius, r radius of the arm, d_{ts} inter-electrode distance, d_{mt} transverse path length of muscle, and θ radian angle formed by the two electrodes of the transmitter .

3.4.1 Transverse Impedances, Z_{mtt} and Z_{mtr}

The transverse impedances depend on the location and shape of electrode, such as inter-electrode distance, electrode pair separation, and electrode area. They also depend on anatomical parameters, such as muscle thickness. Fig. 3.5 shows the cross-section of the upper arm along transverse axis at the transmitter side.

To determine some of the anatomical parameters, we measured anthropometry of the upper arm that includes perimeter and skinfold measurements at location where electrodes are attached. We approximated the cross-section of the upper arm to a circle so that the measured perimeter of the arm at the transmitter side is equal to the circumference, c_t, of the circular cross-section of the arm. The radius of the arm at the transmitter side is calculated using,

$$r = c_t/(2\pi) \tag{3.7}$$

and the radian angle θ in Fig. 3.5 can be calculated by,

$$\theta = d_{ts}/r. \tag{3.8}$$

Accurate measurement of tissue thickness is a complicated task and *in vivo* measurement requires imaging modalities like MRI [40]. We assumed skin thickness t_s=0.2 cm and bone radius r_b=1 cm for all the human subjects we used (that are described in section 3.5) based on statistical measurements of skin thickness [41] and humerus radii [42]. In addition to this, we approximated thickness of fat, t_f, to half of skinfold thickness less skin thickness. We measured skinfold thickness on locations of the upper arm where electrodes are attached. For the measurement, we used Harpenden skinfold caliper, which has measuring range of up to 80 mm, dial graduation 0.2 mm, and accuracy 99.00 %. Averages of three measurements were used.

Muscle thickness is then:

$$t_m = r - (t_s + t_f + r_b). \tag{3.9}$$

The geometry of muscle tissue considered is similar to the portion of a cylindrical shell. Since the cylindrical shell has unequal interior and exterior arc lengths, the average arc length was used. For muscle, this average length depicted (Fig. 3.5) as d_{mt} is calculated as

$$d_{mt} = \theta(r - t_s - t_f - t_m/2). \tag{3.10}$$

Let w_{mt} be the width of the transverse flow path at the transmitter side. Along the longitudinal axis, the cross-sectional area of a cylindrical shell is rectangular and its value can be calculated as width multiplied by height. According to our definition, the secondary current that is responsible for the potential difference across the receiver electrodes is the current flowing within the tissues located under the surface of the receiver electrodes. Therefore, we assumed the width of the secondary transverse current path at the receiver side is equal to the diameter of the receiver electrodes. This implies that the remaining transverse current distribution belongs to the primary current. Therefore, we approximate w_{mt} equal to the distance between transmitter and receiver electrodes, l.

The ratio of cross-sectional area to length, K_{mtt}, for Z_{mtt} is calculated as
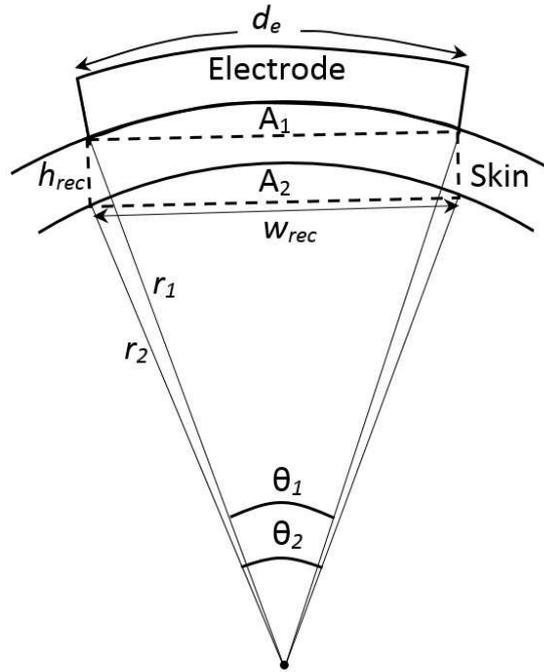
FIGURE 3.6: The cross-section of the arm where electrode is attached. r_1 is radius of upper arc, r_2 radius of lower arc, θ_1 central angle for the upper arc in radian, θ_2 central angle for the lower arc in radian, A_1 is area of the upper circular segment, A_2 is area of the lower circular segment, h_{rec} height of the rectangle, w_{rec} width of the rectangle and d_e electrode diameter.

$$K_{mtt} = \frac{t_m w_{mt}}{d_{mt}}. \tag{3.11}$$

The transverse impedance Z_{mtr} at the receiver was similarly calculated.

3.4.2 Longitudinal Impedances, Z_{ml} and Z_{sl}

The longitudinal impedances represent the impedance of the longitudinal current path of the secondary current. For symmetrical electrodes located along the longitudinal axis of the arm, the forward and return secondary flow path impedances are equal. The longitudinal impedances also depend on the electrode configuration and anatomical parameters.

In the previous subsection, we approximated the width of the transverse secondary current to the diameter of receiver electrodes. Since the longitudinal impedances represent the longitudinal secondary current flow path, we assumed the path width equal

to the electrode diameter. From Fig. 3.6, the cross-sectional area of skin, A_{sl}, which contributes to the longitudinal skin impedance is calculated as

$$A_{sl} = A_{rec} + A_1 - A_2 \tag{3.12}$$

where $A_{rec} = h_{rec} w_{rec}$ is the area of the rectangle formed by the broken line. The area of the upper circular segment, A_1 is calculated as

$$A_1 = \frac{1}{2} r_1 (\theta_1 r_1 - w_{rec} \cos(\frac{\theta_1}{2})) \tag{3.13}$$

and area of the lower circular segment, A_2, is calculated as

$$A_2 = \frac{1}{2} r_2 (\theta_2 r_2 - w_{rec} \cos(\frac{\theta_2}{2})) \tag{3.14}$$

where $r_1 = r$, which is radius of the arm calculated from (3.7), $r_2 = r_1 - t_s$, θ_1 is calculated as

$$\theta_1 = \frac{d_e}{r_1}. \tag{3.15}$$

height of the rectangle, h_{rec}

$$h_{rec} = \frac{t_s}{\cos(\frac{\theta_1}{2})}, \tag{3.16}$$

width of the rectangle, w_{rec}

$$w_{rec} = 2 r_1 \sin(\frac{\theta_1}{2}), \tag{3.17}$$

and θ_2 is calculated as

$$\theta_2 = 2 \sin^{-1}(\frac{w_{rec}}{2 r_2}). \tag{3.18}$$

We set the length of skin contributing to the longitudinal impedance of skin to the distance of transmitter and receiver electrode pair separation, which is l. Therefore, the ratio of cross-sectional area to length of the longitudinal skin impedance Z_{sl}, K_{sl}, is

$$K_{sl} = \frac{A_{sl}}{l} \tag{3.19}$$

Using a similar approach the cross-sectional area of muscle longitudinal path can be calculated. The known terms in this calculation are

$$r_1 = r - \frac{SFT}{2} \tag{3.20}$$

where r is radius of the arm from (3.7), SFT is measured skinfold thickness.

$$r_2 = r_b \tag{3.21}$$

where r_b is radius of bone. And w_{rec}, width of the rectangle is the same as that of skin. From these

$$\theta_1 = 2\sin^{-1}(\frac{w_{rec}}{2r_1}), \tag{3.22}$$

$$\theta_2 = 2\sin^{-1}(\frac{w_{rec}}{2r_2}), \tag{3.23}$$

and

$$h_{rec} = \frac{r_1 - r_2}{\cos(\frac{\theta_1}{2})}. \tag{3.24}$$

Using (3.12), (3.13) and (3.14), the area for longitudinal muscle impedance can be calculated.

3.4.3 Fat Series Impedance, Z_f

The current from electrodes and through gelled skin, suffers attenuation by fat tissue before entering muscle tissue. The effect of fat is represented by a series impedance, Z_f. We assumed that the cross-sectional area of fat where current flows to be equal to area of the electrodes. Fat thickness was approximated by measuring the skinfold thickness at the locations of electrodes attachments. Therefore, the cross-sectional area to length ratio, K_f, in the calculation of Z_f is given by

$$K_f = \frac{\pi d_e^2}{4t_f} \tag{3.25}$$
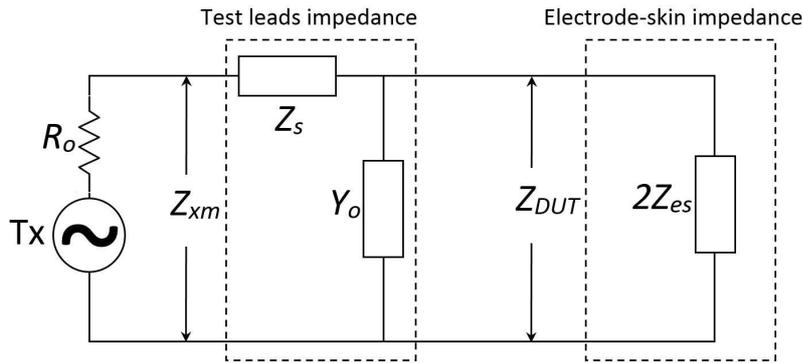
FIGURE 3.7: The circuit diagram proposed to calculate the electrode-skin impedance. Z_{xm} is impedance seen by the VNA port, Z_s and Y_o are series residual impedance and stray admittance of test leads; Z_{DUT} is input impedance of the arm with electrodes attached; Z_{es} is electrode-skin impedance; and R_o is the output impedance of the VNA.

where d_e is diameter of electrode and t_f is thickness of fat, which is calculated from measured skinfold thickness (SFT) and skin thickness, t_s as

$$t_f = \frac{SFT}{2} - t_s. \tag{3.26}$$

3.4.4 Electrode-Skin Impedance, Z_{es}

The electrode-skin impedance, Z_{es}, is composed of skin impedance underneath the electrode, electrode impedance and gel applied. In the literature, the electrode-skin impedance data are limited to the lower frequency range, due to the focus on the application of biomedical electrodes in detection of biologically generated signals. For IBC application, bulk impedance measurements of the arm with electrodes attached were carried out in [36], [37]; and the impedance was referred as contact impedance, which other authors took these measurement values for electrode or electrode-skin impedance. The bulk impedance does not represent the impedance of the skin, electrode or their combination; rather it is the input impedance of the arm with electrodes attached. Within this context, we propose a new approach to calculate electrode-skin impedance based on impedance measurements using a vector network analyser (VNA). The circuit diagram of the proposed electrode-skin impedance measurement system is shown in Fig. 3.7.

On the surface of the upper arm, we attached two round pregelled Ag/AgCl electrodes (diameter 1 cm) side by side and close to each other, and ensuring no contact between the electrolytic gel to avoid short circuit. In this configuration, most of the current
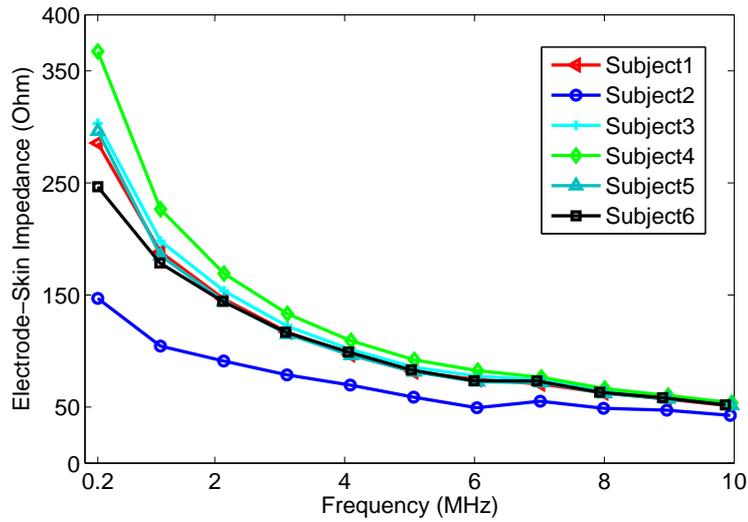
FIGURE 3.8: Normalized electrode-skin impedance modulus (for electrode area of 1 cm^2), in Ω, as a function of frequency, calculated based on impedance measurements on six subjects. The electrodes used are pregelled Ag/AgCl electrodes.

is flowing in the primary current flow path formed by gelled skin so that the effect of the inner tissues is negligible. The complex reflection coefficients of the attached electrodes was measured using VNA. It was found that the measurement values do not vary significantly for electrode separations as much as 3 mm. The impedance seen by the VNA, Z_{xm}, is calculated by

$$Z_{xm} = R_o \frac{1 + \Gamma}{1 - \Gamma} \tag{3.27}$$

where R_o is the output impedance of the VNA; and Γ is the complex reflection coefficient.

Since the known load available for calibration does not fit with the test lead connectors, we adapted the alternative technique of measuring their effect directly. The effect of the test leads is considered by measuring the series residual impedance, Z_s, and the stray admittance, Y_o, of the test leads, by applying an open-short compensation technique. Z_s is measured by shorting the test leads; and Y_o is measured leaving the test leads open with the same separation as when the test leads were attached to the electrodes. Since the series residual impedance, Z_s, is very small ($Z_s << 1/Y_o$), the open measurement is approximated to Y_o.

The impedance formed by the two electrodes, gel and skin, Z_{DUT}, is calculated as

$$Z_{DUT} = \frac{Z_{xm} - Z_s}{1 - (Z_{xm} - Z_s)Y_o}. \tag{3.28}$$

And from (3.28) and Fig. 3.7, electrode-skin impedance, Z_{es}, is calculated as

$$Z_{es} = (Z_{DUT})/2. \tag{3.29}$$

The electrode-skin impedance, Z_{es}, calculated based on (3.29), for six subjects is shown in Fig. 3.8; the measurement set-up is discussed in the next section. The impedance was normalized to 1 cm^2 electrode area.

3.5 Measurement Set-up and Calculation Procedure

The proposed simplified equivalent circuit was empirically compared by carrying out gain and phase shift measurements of galvanic coupling IBC system using the human upper arm as transmission medium. The measurement set-up, shown in Fig. 3.9, is composed of a battery powered VNA (miniVNA Pro, output impedance Z_o= 50 Ω and input impedance Z_i= 50 Ω, frequency range 100 kHz to 200 MHz, manufactured by Mini Radio Solutions), baluns (Coaxial RF transformers, FTB-1-1+, turns ratio of one, manufactured by Mini-Circuits), and round pre-gelled self-adhesive Ag/AgCl snap single electrodes (1cm diameter, manufactured by Noraxon). The VNA is set to sweep constant interval frequency of range 200 kHz to 10 MHz in 800 points with 0 dBm output power, which is well below the safety limit set by International Commission on Non-Ionizing Radiation Protection (ICNIRP) [43]. The signal is coupled to the upper arm by electrodes A_1 and A_2 via Tx of VNA; and at Rx, the VNA detects the potential difference across electrodes B_1 and B_2. The VNA is connected with laptop, where VNA manufacturer provided software calculated the gain in decibels and phase shift in degrees based on the measured potential difference and the input voltage. The block diagram of the measurement set-up is shown in Fig. 3.10. To minimise the uncertainties associated with measurement, gain measurements were repeated every 30 seconds for five times and their average was taken. Factors that contributed to the slight variations in measurements include cable and body movements, hence cable lengths were minimized and subjects asked to keep still.
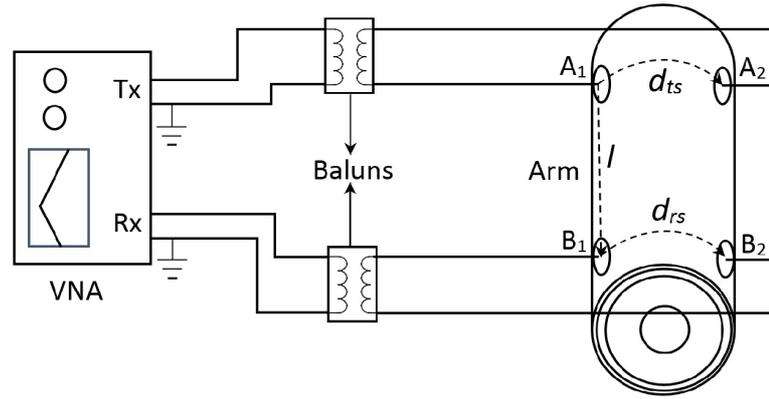
FIGURE 3.9: Measurement set-up for galvanic coupling IBC using the human upper arm as transmission path.
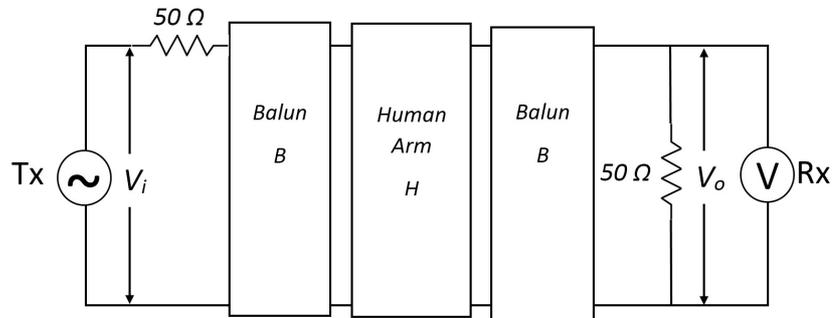
FIGURE 3.10: Block diagram of the measurement set-up. B is half of the measured insertion loss of the baluns and cables; and H is gain (in dB) of human arm and electrodes. V_i is the input voltage and V_o is the potential difference detected.

We used baluns to isolate the common ground return paths of the VNA to achieve galvanic coupled IBC system represented by our simplified equivalent circuit. The baluns are connected to the VNA ports, as shown in Fig. 3.9, using coaxial cables allowing sufficient separation between them, so that parasitic coupling impedance between the baluns was much higher compared to the longitudinal impedances of the system. Even though the effect of baluns can be eliminated by calibration of the VNA, the shape of the test leads does not allow the use of the available known loads that are needed for calibration. Therefore, we measured the insertion loss of the two baluns and the test leads, which is 4 dB at 200 kHz and decreases to 1 dB at 10 MHz, which matches to the measurement data provided by the manufacturer. The measured phase shift also decreases from 45 degrees at 200 kHz to -10 degrees at 10 MHz.

Let G_A be the gain calculated by the VNA. From Fig. 3.10, assuming the 50 Ω output impedance of the VNA is transformed across the balun and included in H, then

$$
\begin{bmatrix} V_i \\ 0 \\ 0 \\ 0 \\ 0 \end{bmatrix} = \begin{bmatrix} 2Z_{es} + Z_0 + 2Z_f + Z_{mtt} & -Z_{mtt} & 0 \\ -Z_{mtt} & Z_{mtt} + 2Z_{ml} + Z_{mtr} & -Z_{mtr} \\ 0 & -Z_{mtr} & Z_{mtr} + 2Z_{fm} + 2Z_{es} + Z_{in} \\ -Z_f & -Z_{ml} & -Z_f \\ -Z_f & -Z_{ml} & -Z_f \end{bmatrix}
$$

(3.32)

$$
\begin{bmatrix} -Z_f & -Z_f \\ -Z_{ml} & -Z_{ml} \\ -Z_f & -Z_f \\ 2Z_f + Z_{ml} + Z_{sl} & 0 \\ 0 & 2Z_f + Z_{ml} + Z_{sl} \end{bmatrix} \times \begin{bmatrix} i_1 \\ i_2 \\ i_3 \\ i_4 \\ i_5 \end{bmatrix}
$$

$$
G_A = 20\log_{10}(\frac{|V_o|}{|V_i|})dB
$$

(3.30)

and it can be written as $G_A = 2B + H$, where B is half of the measured insertion loss. It follows that the measured gain due to the human arm, electrodes, and impedances of the VNA is $H = G_A - 2B$.

From the simplified circuit shown in Fig. 3.4, let $H1$ be the calculated gain in dB due to human arm, electrodes, and impedances of the VNA; and it is calculated as

$$
H1 = 20\log_{10}(\frac{|V_o|}{|V_i|})dB.
$$

(3.31)

Note that the output impedance (Z_o=50 Ω) in Fig. 3.4 is included as part of the simplified circuit when computing $H1$; therefore, the assumption in (3.30) to include the output impedance of the VNA with H is validated.

Since the simplified equivalent circuit in Fig. 3.4 is system of linear equations, the voltage ratio in (3.31) does not change for any value of input voltage, V_i. And the output voltage is calculated by applying mesh current law to the simplified circuit and solving the linear equations with five unknowns using Matlab. The five linear equations for a single frequency are shown in (3.32) in a matrix form, which can also be represented in matrix multiplication form

$$
\mathbf{V} = \mathbf{ZI}
$$

(3.33)

where $\mathbf{V}$ is column vector holding the voltage across independent voltage sources in each mesh, $\mathbf{Z}$ is a 5×5 matrix holding the impedances seen by each mesh current, and $\mathbf{I}$ is column vector holding the mesh currents. Therefore, the current can solved by the multiplication of the impedance inverse matrix with the voltage vector

$$\mathbf{I} = \mathbf{Z}^{-1}\mathbf{V} \tag{3.34}$$

so that the output voltage, V_o, can be calculated as

$$V_o = Z_i i_3 \tag{3.35}$$

and the phase shift is calculated as

$$\Theta_{rad} = \tan^{-1}(\frac{imag(V_o)}{real(V_o)}) \tag{3.36}$$

$$\Theta_{deg} = \frac{\Theta_{rad}360}{2\pi}. \tag{3.37}$$

We assumed the phase angle of the input voltage, V_i, is zero; therefore, the phase shift is equal to the phase angle of the output voltage, V_o and calculated in radians using (3.36) and in degrees using (3.37). Also we subtracted the phase shift due to baluns and cables from the measured phase shift in a similar fashion we did for the gain calculation. Fig. 3.11 shows the measured gain H; and Fig. 3.12 shows the corresponding phase shifts.

For measurement, five male and one female subject participated. The subjects' ages were in late twenties and the anatomical parameters are shown in Table 3.1. Subject 4 is the female volunteer. During the measurement, the subjects were asked to stand in a relaxed manner arms by the side to ensure the current is confined within the arm by avoiding external physical contacts with the arm. We placed the electrode pair $A1$-$A2$ (see Fig. 3.9) at location of deltoid muscle and near the upper head of bicep brachii, respectively; and electrode pair $B1$-$B2$ at location of brachialis and the lower head of the triceps brachii, respectively.

TABLE 3.1: Anatomical and measurement set-up parameters of the subjects

	d_{ts} (cm)	d_{rs} (cm)	l (cm)	C_t (cm)	C_r (cm)	$Skinfold$ (cm)	BMI
Subject 1	10.0	11.5	11.0	28.0	26.0	1.00	24.49
Subject 2	8.5	10.0	9.0	25.5	23.0	0.32	22.72
Subject 3	9.5	12.0	10.0	27.5	26.0	2.02	22.64
Subject 4	9.5	9.0	10.5	26.0	24.0	2.50	22.37
Subject 5	13.5	13.5	8.0	32.0	32.0	3.10	28.73
Subject 6	9.5	9.5	7.5	31.0	29.0	2.70	26.12
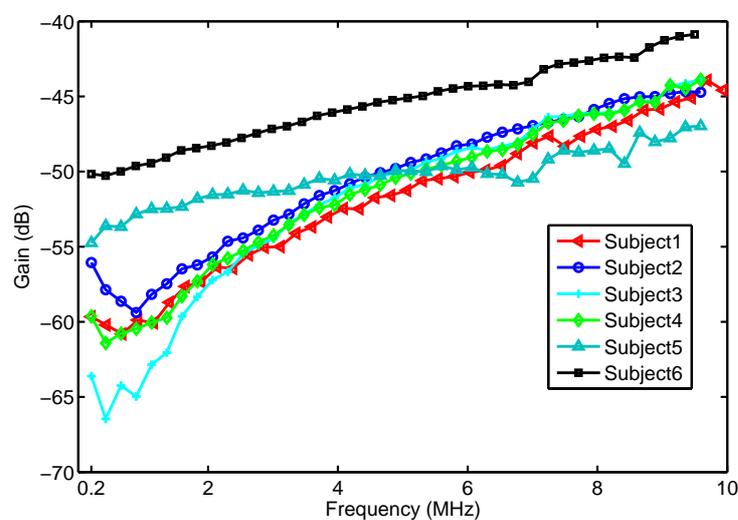
FIGURE 3.11: Measured gain (dB) as a function of frequency for six subjects.
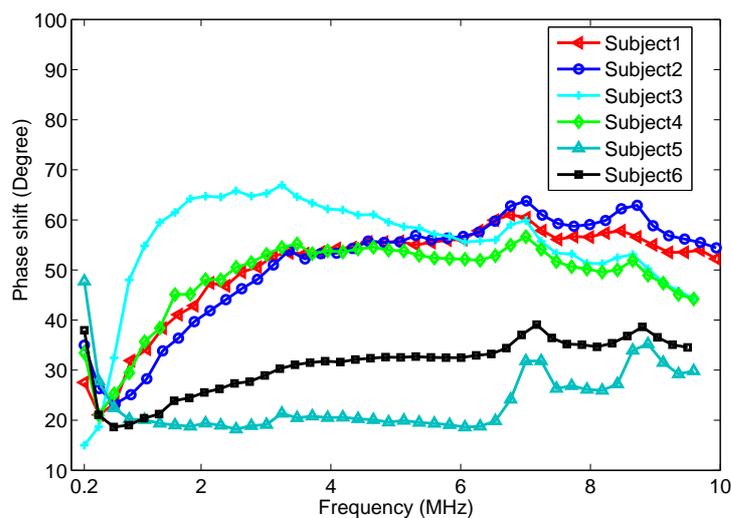
FIGURE 3.12: Measured phase shift (degree) as a function of frequency for six subjects.

3.6 Results and Discussion

The calculated electrode-skin contact impedance, as shown in Fig. 3.8, decreases with an increase in frequency, similar in manner to the impedance of skin shown in Fig. 3.2. At lower frequencies, the dielectric property of skin is dominated by the outermost layer of skin called stratum corneum (SC), which is composed of dead and flat skin cells. The dielectric property of SC depends on the state of the superficial layers and the water content of the surrounding air in contact with skin [39]. The effect of SC vanishes as frequency increases; this phenomenon is manifested by the decreasing skin impedance. The value and pattern of the calculated electrode-skin impedance agree well with the low frequency impedance data found in the literature [44], where impedance of electrode and gelled skin was measured for frequencies up to 1 MHz.

As shown in the graph of Fig. 3.8, all subjects, excluding subject 2 and 4, have similar impedances for most part of the frequency range, but with small variation at low frequencies that could be due to the variations in the degree of individual skin hydration. The impedance of subject 2 is smaller compared to that of the other subjects; furthermore, repeated impedance measurement on this subject confirmed the small impedance value. The anthropometry measurement of subject 2 reveals that he has exceptionally small skinfold thickness (0.32 mm), which could be the cause of the small impedance value. On the other hand, the anthropometry measurement of subject 4 does not support the larger impedance value, except this subject is the only female. But, we did not hasten to the conclusion that gender could affect impedance value; larger number of subjects are required for detailed analysis which we have differed to future work.

Generally, measured gain increases with frequency, as shown in Fig. 3.11, which is similar to galvanic coupled IBC gain measurements reported by other authors. From careful investigation of the relationship between the anthropometry and measurement setup parameters of subjects with their corresponding gain measurement, we found out there is a direct link between transmitter and receiver separation distance (l) and the measured gain, for most part of the frequency range. But, no clear link is shown between the parameters and the measured phase shift, except the distribution of l is reflected on the distribution of phase shifts. Subject 6 has the shortest distance, whereas subject 1 has the longest distance, which the gain measurement reflects for most part of the frequency range. The electrode distances (l) of subject 1, 2, 3 and 4 are relatively close
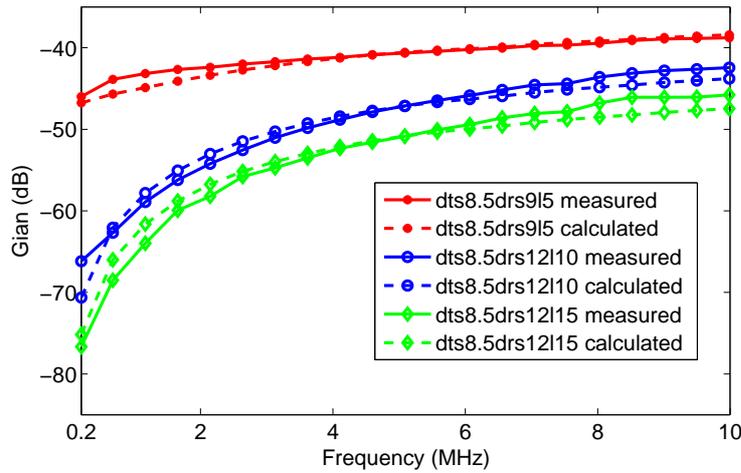
FIGURE 3.13: Gain measurement (solid lines) and corresponding calculation results (broken lines) on subject 1. The electrodes are placed on different location highlighting the relationship among different measurement parameters. The plot **dts8.5drs9l5** is measured gain for the case that $d_{ts} > l$, which is d_{ts}=8.5 cm, d_{rs}=9 cm and l= 5 cm. The plot **dts8.5drs12l10** is gain for the case of d_{ts}=8.5 cm, d_{rs}=12 cm and l=10 cm. And the plot **dts8.5drs12l15** is gain for the case of d_{ts}=8.5 cm, d_{rs}=12 cm, and l=15 cm.

and similar behaviour is shown on their gain and phase measurement for most part of the frequency range. An exception to the general gain pattern, Subject 3 has different gain and phase shift patterns at low frequency, which could arise from the variability of skin admittance at low frequency due to the state of skin hydration and other physiological factors [39]. The gain of subject 5 also exhibit a different pattern; the relationship between gain and l is no longer followed at higher frequency. Moreover, gain and phase shift for subjects 5 and 6 show larger difference compared to that of the remaining subjects; but similar large difference is not reflected in l. These discrepancies led us to see additional relationships among the parameters of subject 5 and 6, which show that l is smaller than the transmitter inter-electrode distance, d_{ts}, for both subjects. These observations initiated further measurements to investigate how l and its relationship with other parameters, such as d_{ts} and d_{rs}, affect gain and phase shift measurements. So far, our proposed equivalent circuit supports the observation.

We carried out additional measurements on subject 1. Fig. 3.13 shows the measured gain of subject 1 for different electrode configuration by varying the parameters l, d_{ts} and d_{rs}. Fig. 3.14 and Fig. 3.15 show the corresponding phase shift measurements with additional plots of muscle and skin impedance phase angles. Though the other subject specific parameters, such as skinfold thickness and circumference of the arm are
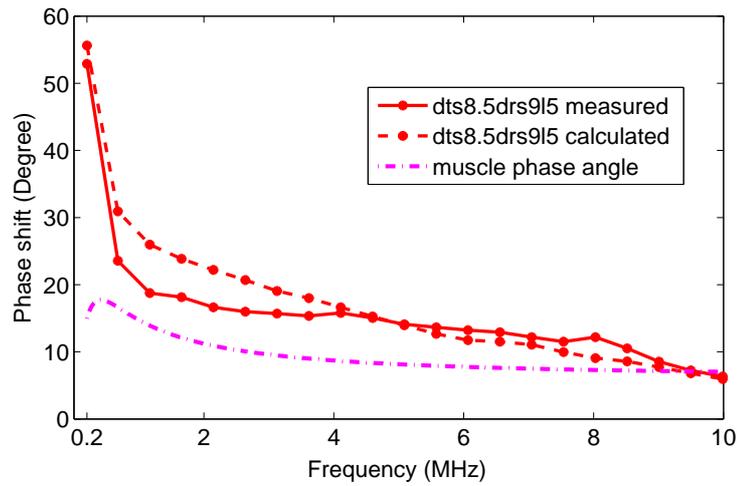
FIGURE 3.14: Phase shift measurement and corresponding calculation results on subject 1 for the case **dts8.5drs9l5**, $d_{ts} > l$, which is d_{ts}=8.5 cm, d_{rs}=9 cm and l= 5 cm. And the plot in broken line is impedance phase angle for muscle.
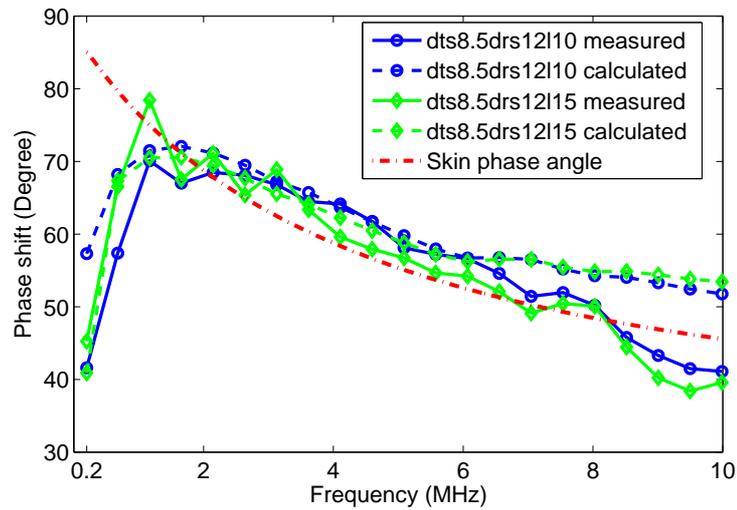
FIGURE 3.15: Phase shift measurement and corresponding calculation results on subject 1. The electrodes are placed on different location highlighting the relationship among different measurement parameters. The plot **dts8.5drs12l10** is phase shift for the case of d_{ts}=8.5 cm, d_{rs}=12 cm and l=10 cm. And the plot **dts8.5drs12l15** is phase shift for the case of d_{ts}=8.5 cm, d_{rs}=12 cm, and l=15 cm. The plot in broken line is impedance phase angle of skin.

important in the calculation of impedance elements, they can not be varied to investigate their effect on the measured gain and phase shift.

In order to demonstrate the relationship between l and gain (phase shift), we first considered the case $l > d_{ts}$ by varying l to 10 cm and 15 cm while holding other parameters constant, which are d_{ts}= 8.5 cm and d_{rs}= 12 cm. The measurement results are shown on Fig. 3.13 for gain and Fig. 3.15 for phase shift with the plots of **dts8.5drs12l10**

and **dts8.5drs12l15** and their corresponding calculation results. For 5 cm increase of l, the gain reduced by 3 dB and the phase shift rose slightly to 4 degrees; the same changes are predicted by our model. Though the calculation results predict the changes in gain and phase shift, they do not fit the measured results at higher frequencies. For frequencies greater than 6 MHz, the normal course of the measured gain and phase shift changes with a more pronounced divergence at approximately 8 MHz. We also observed similar frequency characteristics in the measured electrode-skin impedance. But, these frequency characteristics were not observed at the measured insertion loss of baluns and cables, dismissing the possibility that it is introduced by measuring devices. The dielectric properties of tissues also do not show changes at these frequencies. This suggests that the cause could be due to intrinsic characteristics of the electrode, its contact to skin or the possibility of propagation mechanism in the form of electromagnetic radiation. Additional work is required to clarify this problem.

Moreover, we investigated this electrode configuration based on calculation results from the equivalent circuit. From our calculation result, as l increases, the value of longitudinal impedances Z_{sl} and Z_{ml} increase, which lead to a decrease in the current flowing through them. For the case $l > d_{ts}$, a more closer look revealed that, as l increases, the current in fat impedance at the receiver side (Z_f), reduces significantly. In other words, the small current from Z_{ml} gets more attenuated by Z_f so that a negligible amount of current from Z_{ml} passes through Z_f to reach the receiver electrodes. This implies that the current at the receiver, i_3 (Fig. 3.4), is dominated by the current in Z_{sl}, i_4, indicating the frequency characteristics of the potential difference detected by the receiver is primarily influenced by skin impedance.

This observation is also supported by the impedance characteristics of skin. Among all circuit elements within the equivalent circuit, only skin admittance and electrode-skin contact admittance exhibit similar frequency characteristics with the measured gain. As shown in Fig. 3.2, the impedance of skin decreases with frequency. This implies that the admittance increases with frequency in a similar fashion to the measured gain. We also found that the measured phase shift is similar to the impedance phase angle of skin as shown in Fig. 3.3 and Fig. 3.15 plotted for comparison. This also suggests that, for the case $l > d_{ts}$, the dielectric properties of skin dominates the gain and phase shift characteristics.

The other case we studied is when $d_{ts} > l$. We took different measurements for this case by varying the value of the parameters accordingly and similar results were observed. One of our measurement results for the case d_{ts}= 8. 5 cm, d_{rs}=9 cm and l= 5 cm, is shown in Fig. 3.13 for gain and Fig. 3.14 for phase shift with the plot **dts8.5drs9l5**. As shown in the graphs, the gain and phase shift measurement results for this electrode configuration have different characteristics similar to the measurement results of subject 5 and 6. The gain is larger, about -45 dB at low frequencies, and rises slowly to -40 dB as frequency increases, unlike for the other case where gain appreciably increases with frequency. The phase shift is larger at low frequencies, about 50 degrees, but quickly falls to 20 degrees at around 1 MHz and decreases slowly to 10 degrees at 10 MHz.

We also studied this case of electrode configuration using the equivalent circuit. Since the value of l is relatively smaller compared to d_{ts}, more current flows in the longitudinal impedances of skin (Z_{sl}) and muscle (Z_{ml}) when compared to that of the previous case. As a result, the current in Z_{ml} is no longer attenuated by Z_f to a negligible level. The impedance of fat, as shown in Fig. 3.2, is constant for the frequency range; thus, all frequency components of the current flowing in Z_f are attenuated equally. This implies that the frequency characteristics of the current flowing in Z_f is not altered much, except for constant attenuation with respect to frequency. From the calculation results, we saw that the current in Z_f is larger than the current flowing in Z_{sl}. This suggests that the output current, i_3, is dominated by the current flowing through the muscle longitudinal impedance (Z_{ml}) and passing via Z_f. Hence, the potential difference detected is more influenced by muscle tissue. This observation is also supported by the comparison of muscle impedance characteristics to the measured gain and phase shift for this case. Based on Fig. 3.2, the muscle admittance has similar frequency characteristics to the measured gain for the case $d_{ts} > l$. The measured phase shift also shows similarity to the phase angle of muscle impedance as shown in Fig. 3.3 and also in Fig. 3.14 plotted for purpose of comparison with the measured phase shift. The comparison of muscle impedance phase angle to the measured phase shift show similarity for most part of the frequency range, but large differences at low frequencies. The large phase shift at low frequency could be due to the insertion of balun that has similar large phase shift at the same low frequencies. Though we subtracted the phase shift due to baluns from the measured phase shift, no other component of the system shows such phase shift characteristics at low frequencies.

Another electrode configuration we investigated is the case when $d_{rs} < l$ and $l > d_{ts}$. For changes of d_{rs} from 12 cm to 4.5 cm while keeping the other parameters constant, which is $d_{ts} = 8.5$ cm and $l = 10$ cm, the gain decreases by 3 dB and phase increases by 3 degrees. Gain and phase shift plots for this specific case overlaps with the plot of **dts85drs12l15**. The calculation result and impedance characteristics again show that the dielectric properties of skin mainly affect the detected potential difference similar to the first case discussed.

3.7 Conclusion

We have proposed a simplified equivalent circuit model of the upper arm for galvanic coupling type IBC of frequency range 200 kHz to 10 MHz. We addressed a new way of calculating electrode-skin contact impedance based on measured impedance of the arm. Based on the equivalent circuit, we also investigated the effect of tissues, anthropometry of subjects and electrode configuration on the measured gain and phase shift. With the aid of the equivalent circuit we saw that, for the case $l > d_{ts}$, the secondary current on skin is important in characterising the detected potential difference. On the other hand, for the case $l < d_{ts}$, the current distribution on muscle is more important in characterising the measured gain and phase shift. Our future work will focus on the possible applications of these findings to medical tissue diagnosis.

Chapter 4

Human Body as Antenna and its Effect on Human Body Communication

BEHAILU KIBRET, ASSEFA K TESHOME, AND DANIEL T H LAI

4.1 Abstract

Human body communication (HBC) is a promising wireless technology that uses the human body as part of the communication channel. HBC operates in the near-field of the high frequency (HF) band and in the lower frequencies of the very high frequency (VHF) band, where the electromagnetic field has the tendency to be confined inside the human body. Electromagnetic interference poses a serious reliability issue in HBC; consequently, it has been given increasing attention in regard to adapting techniques to curtail its degrading effect. Nevertheless, there is a gap in knowledge on the mechanism of HBC interference that is prompted when the human body is exposed to electromagnetic fields as well as the effect of the human body as an antenna on HBC. This paper narrows the gap by introducing the mechanisms of HBC interference caused by electromagnetic field exposure of human body. We derived analytic expressions for induced total axial current in the body and associated fields in the vicinity of the body when an imperfectly conducting cylindrical antenna model of the human body is illuminated by a vertically polarized plane wave within the 1-200 MHz frequency range. Also, fields in the vicinity of the human body model from an on-body HBC transmitter are calculated. Furthermore, conducted electromagnetic interference on externally embedded HBC receivers is also addressed. The results show that the maximum HBC gain near 50 MHz is due to whole-body resonance, and the maximum at 80 MHz is due to the resonance of the arm. Similarly, the results also suggest that the magnitude of induced axial current in the body due to electromagnetic field exposure of human body is higher near 50 MHz.

4.2 Introduction

Human body communication (HBC)/Intrabody communication (IBC)/Body channel communication (BCC) is an emerging wireless communication technique that uses the human body as a transmission medium to connect wearable biomedical sensor nodes and electronic devices in a wireless body area network (WBAN). The human body acts as a waveguide in the frequency range of hundreds of kHz to dozens of MHz, which is considered suitable for HBC operation. More specifically, IEEE 802.15.6 defines 21 MHz as center frequency for HBC. HBC uses near-field coupling that leads to low radiation to free space; as a result, it promises a secured low data rate communication. Due to

the low propagation loss, it also promises higher communication performance compared to other body area communication techniques, such as ultra wideband (UWB) [13].

In the literature, two approaches of HBC are widely discussed [38]. In the first approach, the transmitter uses two electrodes, which are attached to the body, to differentially couple modulated current into the body, resulting in gradient of electric potential around it. The receiver detects the signal from the potential difference between another pair of electrodes attached to the body. This type of approach is commonly called galvanic coupling HBC. In the second approach, the transmitter couples electric current into the body using a single on-body electrode and the receiver also detects the signal using a single on-body electrode. A return path is established through the vicinity of the human body with near-field coupling of the transmitter and receiver circuit ground planes. This type of approach is usually referred to as capacitive or near-field coupling HBC.

There is a prevalent claim that HBC provides secure and interference immune channel, which is hypothesised, based on the assumption that the signal is physically guarded by the human body and electromagnetic radiation is low [5, 13, 14]. But this view is not always valid. For efficient low power and high frequency operation, one of the constraints in HBC transceiver design is ensuring most of the signal is coupled to the body as electric current or confined to the vicinity of human body as reactive near-field, leading to reduction of power lost due to radiation into free space and due to mutual coupling with nearby objects. The natural approach to achieve this is through the use of coupling electrodes that are in direct contact with the body instead of using a traditional RF antenna. It can also be further improved by scaling the HBC circuit to a dimension that is very small compared to wavelength of the signal coupled to the body, and at the same time optimizing the size of circuit ground planes for good near-field coupling. This implies that properly designed HBC devices might not be good RF radiation sources, which in turn means that they might not also be good receiving antennas for external electromagnetic disturbances within HBC operation frequency. Such notion of HBC seemingly classify it as a wireless technique that is less sensitive to RF interference. Even though HBC devices are poor RF antennas, there is another mechanism of electromagnetic interference (EMI) that threatens the operation of HBC. Since HBC operates on the surface of the human body, the current induced in the body due to RF exposure may interfere with body-worn devices. In other words, the human body can act like receiving antenna, which indirectly affects the HBC channel. From

reciprocity, the reverse is also true - the human body can also act as transmitting antenna due to the HBC induced current inside the body - this could have impact on security.

In the literature, there are only a few studies that addressed interference problems posed by the human body acting as an antenna. The seriousness of reliability issue in HBC arising from interference caused by human body as a receiving antenna is discussed in [45]. From measured RF interference power, a specific case was reported that showed the signal-to-interference ratio (SIR) of HBC degrades to -22 dB. Based on this, the paper proposed an adaptive frequency hopping technique to improve the SIR. In a similar work [14], with an effort to investigate the proper HBC frequency range that has minimised effect on nearby RF devices, the electric field strength around the human subject with on-body HBC transmitter was measured using an antenna located at 3 m away from the subject. The study reported irregular radiation patterns and unpredictable directivity at different frequencies, which are typical near-field phenomena possibly affected by mutual coupling of the subject, the measuring antenna and nearby objects. Another study [46] investigated the effect of EMI on implanted medical devices, specifically cardiac pacemakers, due to electromagnetic field from on-body HBC transmitter. Park *et al.* [47] proposed the digital communication technique of frequency selective baseband transmission (FSBT) for HBC in order to cope with the reliability issue posed by interference. Anguera *et al.* showed that the human body can act as an efficient FM (100 MHz) antenna showing that the efficiency of an electrically small antenna is in some cases can be improved up to 10 dB, approximately [48–51]. Overall, little has been reported in the literature on the mechanism of human body antenna effect in the context of HBC.

In this paper, we present theoretical insights on the mechanism of HBC interference when the human body exposed to RF electromagnetic plane wave in conjunction with investigation of the antenna effect of the human body on HBC operation. Expressions for the total induced axial current and the associated near-fields are derived for cylindrical model of human body standing on a highly conductive infinite plane that is illuminated by vertically polarised RF plane wave as shown in Fig. 4.1. Moreover, fields in the vicinity of the cylindrical model are calculated when there is HBC transmitter attached on the surface of the model. Finally, theoretical results are validated by empirical measurement and important results are discussed. Source points inside the cylinder
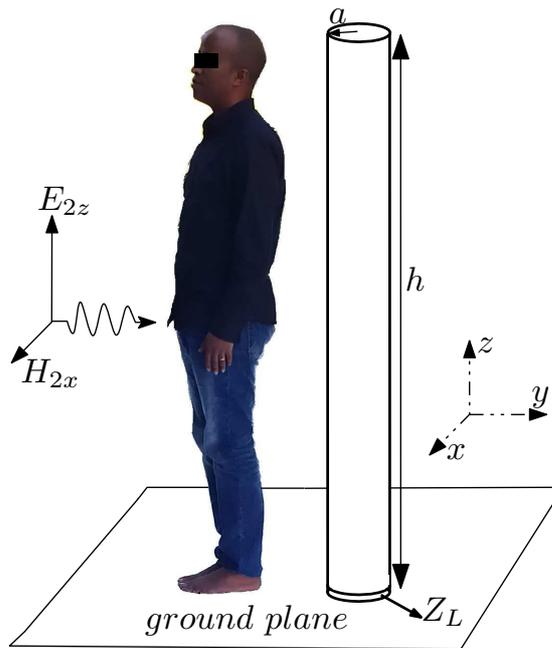
FIGURE 4.1: Cylindrical antenna model of the human body exposed to vertically polarised plane wave [53].

model are identified with coordinates with prime symbol; and also, quantities inside and outside of the cylinder are identified with subscripts 1 and 2, respectively.

4.3 Theory

4.3.1 Cylindrical Model of the Human Body

When the human body is illuminated by an electromagnetic plane wave, the total induced axial current in the body is less affected by the change in cross-sectional size and shape of the body provided that the tissue material is mainly conductive [52]. This explains the relatively higher specific absorption rate (SAR) in areas of the body where there is small conductive tissue mass or small cross-section area, such as the knee and ankle. Consequently, we used a homogenous cylindrical model of the body that comprises muscle tissue, which is the predominant tissue in the human body. The cylindrical human body model represents a standing posture with arms in contact with sides as shown in Fig. 4.1.

The dielectric properties of biological tissues are frequency dependent that arise from dielectric dispersion due to the constituents of tissues at cellular and molecular levels

[27]. The dielectric property of muscle can be approximated by Cole-Cole dispersions with parameters defined by Gabriel *et al.* [28]. The expression for the complex relative permittivity ϵ_ω^* as a function of excitation angular frequency ω is given as

$$\epsilon_\omega^* = \epsilon_\infty + \sum_{n=1}^{4} \frac{\Delta\epsilon_n}{1 + (j\omega\tau_n)^{1-\alpha_n}} + \frac{\sigma_i}{j\omega\epsilon_0} \tag{4.1}$$

where n is the dispersion region identifier, ϵ_∞ is permittivity at very large frequency, $\Delta\epsilon_n$ refers to strength of the dispersion, τ_n is the relaxation time constant, α_n is distribution parameter that controls width of the dispersion, σ_i is the static ionic conductivity, and ϵ_0 is the permittivity of free space. The complex conductivity σ_ω^* is calculated from (4.1) as

$$\sigma_\omega^* = j\omega\epsilon_0\epsilon_\omega^* = \sigma + j\omega\epsilon_0\epsilon \tag{4.2}$$

where σ is the conductivity and ϵ is the relative permittivity.

Skin effect is taken into account by considering a time harmonic $(e^{j\omega t})$ and rotationally symmetric magnetic vector potential $A_{1z}(\rho, z)\hat{\mathbf{z}}$ maintained inside a very long and circular homogenous conducting cylinder of radius a that extends along the z-axis of a system of cylindrical coordinates (ρ, ϕ, z). Solving the wave equation in the Lorenz gauge, the magnetic vector potential can be expressed as [54]

$$A_{1z}(\rho, z) = DJ_0(\kappa\rho)\left(C_1\cos\gamma z + C_2\sin\gamma z\right) \tag{4.3}$$

where D, C_1, and C_2 are constants; J_0 is zeroth-order Bessel function, $\kappa^2 = k_1^2 - \gamma^2$, $k_1 = \sqrt{j\omega\mu_0\sigma_\omega^*}$ and $\gamma = \beta$ - $j\alpha$ is the propagation constant along z-axis. The magnetic field inside the cylinder $B_{1\phi}$ is calculated as

$$B_{1\phi}(\rho, z) = -\frac{\partial A_{1z}(\rho, z)}{\partial\rho} = D\kappa J_1(\kappa\rho)\left(C_1\cos\gamma z + C_2\sin\gamma z\right). \tag{4.4}$$

If we assume the cylinder dimension satisfies the condition $k_2a \ll 1$ ($k_2 = \omega\sqrt{\mu_0\epsilon_0}$ is free space wave number) and it carries total axial current $I(z)$ that varies very slowly along the z-axis, then the magnetic field on the surface can be approximated as [55]

$$B_{2\phi}(a, z) \simeq \frac{\mu_0 I(z)}{2\pi a}. \tag{4.5}$$

Enforcing the boundary condition of tangential magnetic field on the surface of the cylinder,

$$B_{1\phi}(\rho, z) \simeq \frac{\mu_0 I(z)}{2\pi a} \frac{J_1(\kappa\rho)}{J_1(\kappa a)} \tag{4.6}$$

provided that permeability of the cylinder is equal to that of the free space surrounding it, where J_1 is first-order Bessel function. Equation (4.6) implies that

$$I(z) = C_1 \cos \gamma z + C_2 \sin \gamma z. \tag{4.7}$$

For the case of the proposed human body cylindrical model that has finite length h, when it is totally illuminated by a vertically polarized plane wave, the total axial current should have a form similar to (4.7) with some modifications to compensate for the finite length.

The axial electric field inside the conductor can be calculated as

$$E_{1z}(\rho, z) = -j\omega \frac{\kappa^2}{k_1^2} A_{1z}(\rho, z) \simeq \frac{I(z)\kappa}{2\pi a \sigma_\omega^*} \frac{J_0(\kappa\rho)}{J_1(\kappa a)} \tag{4.8}$$

the impedance per unit length z^i of the cylinder is [54]

$$z^i = \frac{E_{1z}(a, z)}{I(z)} = \frac{\kappa}{2\pi a \sigma_\omega^*} \frac{J_0(\kappa a)}{J_1(\kappa a)} \tag{4.9}$$

and the volume current density $J_{1z}(\rho, z)$

$$J_{1z}(\rho, z) = \sigma_\omega^* E_{1z}(\rho, z) \simeq \frac{I(z)\kappa}{2\pi a} \frac{J_0(\kappa\rho)}{J_1(\kappa a)}. \tag{4.10}$$

The above expressions for field quantities of a very long cylinder are the basis for the analysis of the finite length cylindrical model of human body, which is treated in the next subsections.

4.3.2   Induced Axial Current in the Cylindrical Model

For our particular case, a time-harmonic ($e^{j\omega t}$) incident plane wave with electric field parallel to the axis of the z-directed cylinder of height h and radius a induces a current density distribution $\mathbf{J}_1(\mathbf{r})$ inside the cylinder. If the current density is known, the

scattered magnetic vector potential outside the cylinder $\mathbf{A}_2(\mathbf{r})$ can be calculated in the Lorenz gauge as

$$\mathbf{A}_2(\mathbf{r}) = \frac{\mu_0}{4\pi} \int\limits_{V'} \frac{\mathbf{J}_1(\mathbf{r}')e^{-jk_2R}}{R} dv' \tag{4.11}$$

where $R = |\mathbf{r} - \mathbf{r}'|$ is the distance between observation and source points. We assumed that the current density $\mathbf{J}_1(\mathbf{r})$ is rotationally symmetric in the cylindrical coordinate system (ρ, ϕ, z); and, based on (4.10), it is approximated by the induced total axial current $I_{1z}(z)$ in the finite cylinder as

$$\mathbf{J}_1(\mathbf{r}) \simeq J_{1z}(\rho, z)\hat{\mathbf{z}} = \frac{I_{1z}(z)\kappa}{2\pi a} \frac{J_0(\kappa\rho)}{J_1(\kappa a)}\hat{\mathbf{z}}. \tag{4.12}$$

The dimension of the cylinder model loosely satisfies the *thin-wire antenna approximation* condition ($k_2a \ll 1$ and $h \gg a$) for the frequency range of 1-200 MHz; thus, when the observation point is on the surface of the cylinder, the expression for R simplifies to

$$R \simeq \sqrt{(z - z')^2 + a^2}. \tag{4.13}$$

Therefore, the vector potential on the surface of the cylinder has only z-component,

$$A_{2z}(a, z) = \frac{\mu_0}{4\pi} \int\limits_{-h}^{h} \int\limits_{0}^{a} 2\pi J_{1z}(\rho', z') \frac{e^{-jk_2R}}{R} \rho' d\rho' dz' = \frac{\mu_0}{4\pi} \int\limits_{-h}^{h} I_{1z}(z') \frac{e^{-jk_2R}}{R} dz' \tag{4.14}$$

where the integration is carried out taking into account the cylinder image in the highly conductive ground. By enforcing boundary condition, the electric fields on the surface of the cylinder can be related as

$$\left(\frac{\partial^2}{\partial z^2} + k_2^2\right) A_{2z}(a, z) = \frac{jk_2^2}{\omega}\left(I_{1z}(z)z^i - V_0^e\delta(z) - E_0\right) \tag{4.15}$$

where V_0^e is the potential difference on the load between the foot and the image in the ground with the electric field approximated by *delta-gap* model; and E_0 is the incident electric field at the surface of the cylinder.

From (4.14) and (4.15), we derived approximate analytic expressions for the total axial current based on the King's three-term approximation for imperfectly conducting and

loaded receiving cylindrical antenna as [29, 30]

$$I_{1z}(z) = V_0^e v(z) + U_0 u(z) \tag{4.16}$$

V_0^e and U_0 are defined as

$$V_0^e = -I_{sc}(0)\frac{Z_A Z_L}{Z_A + Z_L} \qquad U_0 = \frac{E_0}{k_2} \tag{4.17}$$

where $Z_A = 1/v(0)$ is driving-point impedance of the same cylinder when base driven, Z_L is the load impedance, and $I_{sc}(0) = U_0 u(0)$ is current at the base when there is no load.

$$v(z) = \frac{j2\pi k_2}{\zeta_0 \gamma \Psi_{dR} \cos(\gamma h)} \left[\sin\gamma(h - |z|) + T_U(\cos\gamma z - \cos\gamma h) \right.$$
$$\left. + T_D(\cos\tfrac{1}{2}k_2 z - \cos\tfrac{1}{2}k_2 h) \right] \tag{4.18}$$

$$u(z) = \frac{j4\pi}{\zeta_0} \left[H_U(\cos\gamma z - \cos\gamma h) + H_D(\cos\tfrac{1}{2}k_2 z - \cos\tfrac{1}{2}k_2 h) \right] \tag{4.19}$$

where $\zeta_0 = 120\pi \ \Omega$ is free space impedance. Both $v(z)$ and $u(z)$ have a form similar to the current in the long cylinder (4.7). The imperfectly conducting nature of the cylinder model is characterized by the parameter $\gamma = \beta - j\alpha$,

$$\gamma^2 = k_2^2 \left(1 - \frac{j4\pi z^i}{k_2 \zeta_0 \Psi_{dR}} \right). \tag{4.20}$$

The coefficients in (4.18) and (4.19) involve integrals that are computed numerically,

$$T_U = \frac{C_V E_D - C_D E_V}{C_U E_D - C_D E_U} \qquad T_D = \frac{C_U E_V - C_V E_U}{C_U E_D - C_D E_U} \tag{4.21a}$$

$$H_U = \frac{C_D - E_D}{C_U E_D - C_D E_U} \qquad H_D = \frac{E_U - C_U}{C_U E_D - C_D E_U} \tag{4.21b}$$

where

$$C_U = \left(1 - \frac{\gamma^2}{k_2^2}\right)(\Psi_{dUR} - \Psi_{dR})(1 - \cos\gamma h) - \frac{\gamma^2}{k_2^2}\Psi_{dUR}\cos\gamma h$$
$$+ j\Psi_{dUI}\left(\tfrac{3}{4} - \cos\tfrac{1}{2}k_2 h\right) + \Psi_U(h) \tag{4.22a}$$

$$C_D = \Psi_{dD}\left(\frac{3}{4} - \cos\frac{1}{2}k_2h\right) - \left(1 - \frac{\gamma^2}{k_2^2}\right)\Psi_{dR}\left(1 - \cos\frac{1}{2}k_2h\right) + \Psi_D(h) \qquad (4.22b)$$

$$C_V = -\left[j\Psi_{dI}\left(\frac{3}{4} - \cos\frac{1}{2}k_2h\right) + \Psi_V(h)\right] \qquad (4.22c)$$

$$E_U = -\frac{\gamma^2}{k_2^2}\Psi_{dUR}\cos\gamma h - j\frac{1}{4}\Psi_{dUI}\cos\frac{1}{2}k_2h + \Psi_U(h) \qquad (4.22d)$$

$$E_D = -\frac{1}{4}\Psi_{dD}\cos\frac{1}{2}k_2h + \Psi_D(h) \qquad E_V = j\frac{1}{4}\Psi_{dI}\cos\frac{1}{2}k_2h - \Psi_V(h) \qquad (4.22e)$$

$$\Psi_V(h) = \int_{-h}^{h} \sin\gamma(h - |z'|)\frac{e^{-jk_2R_h}}{R_h}dz' \qquad (4.23a)$$

$$\Psi_U(h) = \int_{-h}^{h} \left(\cos\gamma z' - \cos\gamma h\right)\frac{e^{-jk_2R_h}}{R_h}dz' \qquad (4.23b)$$

$$\Psi_D(h) = \int_{-h}^{h} \left(\cos\frac{1}{2}k_2z' - \cos\frac{1}{2}k_2h\right)\frac{e^{-jk_2R_h}}{R_h}dz' \qquad (4.23c)$$

$$\Psi_{dR} = \Psi_{dR}(z_m), \quad \begin{cases} z_m = 0, & k_2h \le \pi/2 \\ z_m = h - \lambda/4, & k_2h > \pi/2 \end{cases} \qquad (4.24a)$$

$$\Psi_{dR}(z) = \csc\gamma(h - |z|)\int_{-h}^{h} \sin\gamma(h - |z'|)\left[\frac{\cos k_2R}{R} - \frac{\cos k_2R_h}{R_h}\right]dz' \qquad (4.24b)$$

$$\Psi_{dUR} = [1 - \cos\gamma h]^{-1}\int_{-h}^{h} \left[\cos\gamma z' - \cos\gamma h\right]\left[\frac{\cos k_2R_0}{R_0} - \frac{\cos k_2R_h}{R_h}\right]dz' \qquad (4.24c)$$

$$\Psi_{dD} = \left[1 - \cos\frac{1}{2}k_2h\right]^{-1}\int_{-h}^{h} \left[\cos\frac{1}{2}k_2z' - \cos\frac{1}{2}k_2h\right]\left[\frac{e^{-jk_2R_0}}{R_0} - \frac{e^{-jk_2R_h}}{R_h}\right]dz' \qquad (4.24d)$$

$$\Psi_{dI} = -\left[1 - \cos\frac{1}{2}k_2h\right]^{-1}\int_{-h}^{h} \sin\gamma(h - |z'|)\left[\frac{\sin k_2R_0}{R_0} - \frac{\sin k_2R_h}{R_h}\right]dz' \qquad (4.24e)$$

$$\Psi_{dUI} = -\left[1 - \cos\frac{1}{2}k_2h\right]^{-1}\int_{-h}^{h} \left[\cos\gamma z' - \cos\gamma h\right]\left[\frac{\sin k_2R_0}{R_0} - \frac{\sin k_2R_h}{R_h}\right]dz' \qquad (4.24f)$$

$$R_0 = \left[z'^2 + a^2\right]^{\frac{1}{2}} \qquad R_h = \left[(h - z')^2 + a^2\right]^{\frac{1}{2}} \tag{4.24g}$$

The value of γ is calculated by the process of iteration that is initialised by $\gamma = k_2$ to calculate z^i and Ψ_{dR}, which are in turn used to calculate γ. The iteration is found to be highly convergent; thus, the results after several iteration steps suffice to provide accurate approximation.

4.3.3 Fields due to Antenna Effect of the Cylindrical Model

The essence of HBC operation is transmission of signal by maintaining electric potential distribution in the vicinity of the human body, where receiving units detect the signal from potential difference between two points located on the surface of the body or very close to the body. Therefore, it is relevant to introduce the fields produced in the vicinity of the human body due to electromagnetic field exposure, in this case a vertically polarized plane wave.

The magnitude of the volume charge density $\varrho_{1v}(\rho, z)$ inside the cylinder can be related to the current density $J_{1z}(\rho, z)$ via continuity equation as

$$\nabla.J_{1z}(\rho, z)\hat{\mathbf{z}} = \nabla.\frac{I_{1z}(z)\kappa}{2\pi a}\frac{J_0(\kappa\rho)}{J_1(\kappa a)}\hat{\mathbf{z}} = -j\omega\varrho_{1v}(\rho, z). \tag{4.25}$$

Enforcing the thin-wire approximation, fields very close to the cylinder can be approximately calculated by replacing the volume charge distribution with the total charge line density located on the axis of the cylinder [56]. Therefore, the radial electric field $E_{2z}(\rho, z)$ very close to the cylinder is approximated as

$$E_{2\rho}(\rho, z) \simeq \frac{1}{2\pi\epsilon_0\rho}\int\limits_0^a \varrho_{1v}(\rho', z)\rho'd\rho'\int\limits_0^{2\pi} d\phi' = \frac{j\zeta_0 I'_{1z}(z)}{2\pi k_2\rho} \tag{4.26}$$

where $I'_{1z}(z)$ is first derivative of the current. Also, applying the thin-wire approximation, the magnetic field very close to the cylinder can be calculated replacing the volume current density distribution with the total axial current in a current filament located on the axis of the cylinder. Therefore,

$$B_{2\phi}(\rho, z) \simeq \frac{\mu_0 I_{1z}(z)}{2\pi\rho}. \tag{4.27}$$

The radial electric field inside the cylinder $E_{1\rho}(\rho, z)$ and the magnetic field inside the cylinder $B_{1\phi}(\rho, z)$ can be calculated from the vector magnetic potential maintained inside the cylinder $A_{1z}(\rho, z)$, which is approximated as

$$A_{1z}(\rho, z) \simeq -\frac{\mu_0 I_{1z}(z)}{2\pi a\kappa} \frac{J_0(\kappa\rho)}{J_1(\kappa a)}. \tag{4.28}$$

Therefore,

$$E_{1\rho}(\rho, z) = -\frac{j\omega}{k_1^2} \frac{\partial}{\partial\rho} \left(\frac{\partial A_{1z}(\rho, z)}{\partial z} \right) \simeq \frac{I'_{1z}(z)}{2\pi a\sigma_\omega^*} \frac{J_1(\kappa\rho)}{J_1(\kappa a)} \tag{4.29}$$

$$B_{1\phi}(\rho, z) = -\frac{\partial A_{1z}(\rho, z)}{\partial\rho} \simeq \frac{\mu_0 I_{1z}(z)}{2\pi a} \frac{J_1(\kappa\rho)}{J_1(\kappa a)}. \tag{4.30}$$

Using the thin-wire approximation, the external magnetic field in (4.27) represents the average total magnetic field close to the cylinder; therefore, the total axial electric field very close to the cylinder $E_{2z}(\rho, z)$ can be calculated from Faraday's law as

$$\frac{\partial E_{2z}(\rho, z)}{\partial\rho} = \frac{\partial E_{2\rho}(\rho, z)}{\partial z} + j\omega B_{2\phi}(\rho, z) \tag{4.31}$$

and the axial electric field inside the cylinder $E_{1z}(\rho, z)$ can be calculated as

$$E_{1z}(\rho, z) = \frac{J_{1z}(\rho, z)}{\sigma_\omega^*}. \tag{4.32}$$

Taking the value of axial electric field on the surface equal to $E_{1z}(a, z)$ from (4.32), the external total axial electric field simplifies to

$$E_{2z}(\rho, z) \simeq I_{1z}(z)z^i + \frac{j\zeta_0}{2\pi k_2} \left[I''_{1z}(z) + k_2^2 I_{1z}(z) \right] \ln(\frac{\rho}{a}) \tag{4.33}$$

where $I''_{1z}(z)$ is second derivative of the current. The scalar potential distribution very close to the surface of the cylinder can be calculated from the radial electric field as

$$\varphi_2(\rho, z) = \varphi_2(a, z) - \int_a^\rho E_{2\rho}(\rho, z)d\rho. \tag{4.34}$$

The scalar potential at the surface of the cylinder $\varphi_2(a, z)$ can be estimated from the internal axial vector potential $A_{1z}(\rho, z)$ using the Lorenz condition,

$$\varphi_2(a, z) = \varphi_1(a, z) \simeq -\frac{j\omega}{k_1^2} \frac{\partial A_{1z}(\rho, z)}{\partial z}\bigg|_{\rho=a} = \frac{I'_{1z}(z)}{2\pi a\sigma_\omega^*\kappa} \frac{J_0(\kappa a)}{J_1(\kappa a)} \tag{4.35}$$

Therefore,

$$\varphi_2(\rho, z) \simeq \frac{I'_{1z}(z)}{2\pi} \left(\frac{1}{a\kappa\sigma^*_\omega} \frac{J_0(\kappa a)}{J_1(\kappa a)} - \frac{j\zeta_0}{k_2} \ln \frac{\rho}{a} \right). \tag{4.36}$$

4.3.4 Fields from HBC Transmitter Located on the Surface of the Cylindrical Model

The electromagnetic field produced by HBC transmitter situated on the surface of the body can be approximately analysed using the classic theory of electromagnetic fields from an elementary dipole source located above a plane conducting half-space. In particular, we considered a vertical electric dipole (VED) located at the surface of a homogenous, conducting, and semi-infinite media that has similar dielectric property as the cylinder model. It is well known that there are no suitable closed form solutions to the Sommerfeld integrals involved to evaluate fields near a dipole source. Thus, we adapted the approach of a finitely conducting half-space image theory to calculate the quasi-static fields within the limit of distance much less than the free space wavelength [57, 58]. Basically, the idea of the finitely conducting half-space image theory technique is to replace the imperfectly conducting half-space with a perfectly conducting half-space located at a complex depth $d/2$, where $d \simeq 2/k_1$. For the given frequency range of HBC operation, the domain of the quasi-static approach is appropriate for short distances on the vicinity of the body.

The charge oscillation between the body surface electrode and the circuit ground plane of HBC transceiver can be represented by VED with the vertical orientation defined with respect to the axis of the cylinder model. We assumed that there is a fictitious current filament forming VED of moment Il at the center of the transmitter, where I is the current fed to the surface electrode and l is the small separation between the electrode and the ground plane.

Defining a new set of cylindrical coordinate with origin on the surface of the cylindrical model (assuming the cylindrical model is part of the half-space), the quasi-static fields at points not very close to the VED but at distances much less than the free space wavelength are approximated in [59] as

$$E_z(\rho, z) \simeq \frac{jIl\zeta_0}{2\pi} \left(\frac{1}{R_1^3} - \frac{3z^2}{R_1^5} \right) \tag{4.37a}$$

$$H_\phi(\rho, z) \simeq \frac{Il}{2\pi} \frac{\rho}{R_1^3} \tag{4.37b}$$

$$E_\rho(\rho, z) \simeq \frac{jIl\zeta_0\rho}{4\pi} \left[\frac{6z}{R_1^5} \left(1 - \frac{k_2^2}{k_1^2} \right) - \frac{k_2^2}{\rho^2} \left(\frac{z+d}{R_2} - \frac{z}{R_1} \right) \right] \tag{4.37c}$$

where R_1 is distance between the dipole and observation point, and R_2 is distance from the image dipole to the observation point

$$R_1 = \sqrt{\rho^2 + z^2} \qquad R_2 = \sqrt{\rho^2 + (z+d)^2}. \tag{4.38}$$

It is well known that the magnetic vector potential in the air region for VED located on the surface of lossy half-space is given as

$$\mathbf{A}(\mathbf{r}) = A_z(\rho, z)\hat{\mathbf{z}} = \frac{\mu_0 Il}{4\pi} \left(\frac{e^{-jk_2 R_1}}{R_1} - \int_0^\infty \frac{e^{-u_2 z}}{u_2} \frac{\tau^2 u_1 - u_2}{\tau^2 u_1 + u_2} J_0(\lambda\rho)\lambda d\lambda \right) \hat{\mathbf{z}} \tag{4.39}$$

where

$$u_2 = \sqrt{\lambda^2 - k_2^2} \quad u_1 = \sqrt{\lambda^2 - k_1^2} \quad \tau = \frac{k_2}{k_1} \tag{4.40}$$

The integral in (4.39) characterizes the effect of the lossy ground; therefore, based on the finitely conducting half-space image theory, it can be approximated by the contribution of the image dipole located at the complex depth of d. So that, the quasi-static scalar electric potential can be approximated in the Lorenz gauge as

$$\varphi(\rho, z) = \frac{j\omega}{k_2^2} \frac{\partial A_z(\rho, z)}{\partial z} \simeq -\frac{jIl\zeta_0}{4\pi k_2} \left(\frac{z}{R_1^3} + \frac{z+d}{R_2^3} \right). \tag{4.41}$$

4.3.5   Conducted Interference in HBC Receivers

In addition to the HBC scenario mentioned previously, there is another promising application area of HBC where the receiving circuit is embedded externally in the surrounding environment of human body; and a closed circuit path is established when the subject wearing a transmitter touches or get very close to the receiver electrode. The receiver detects the signal from the potential difference between the contact electrode and the ground. For this case, in addition to the interference caused by fields in the vicinity of the body, there is also conducted interference due to the induced current in the body

(a) Cylinder with parallel load

(b) The corresponding equivalent circuit
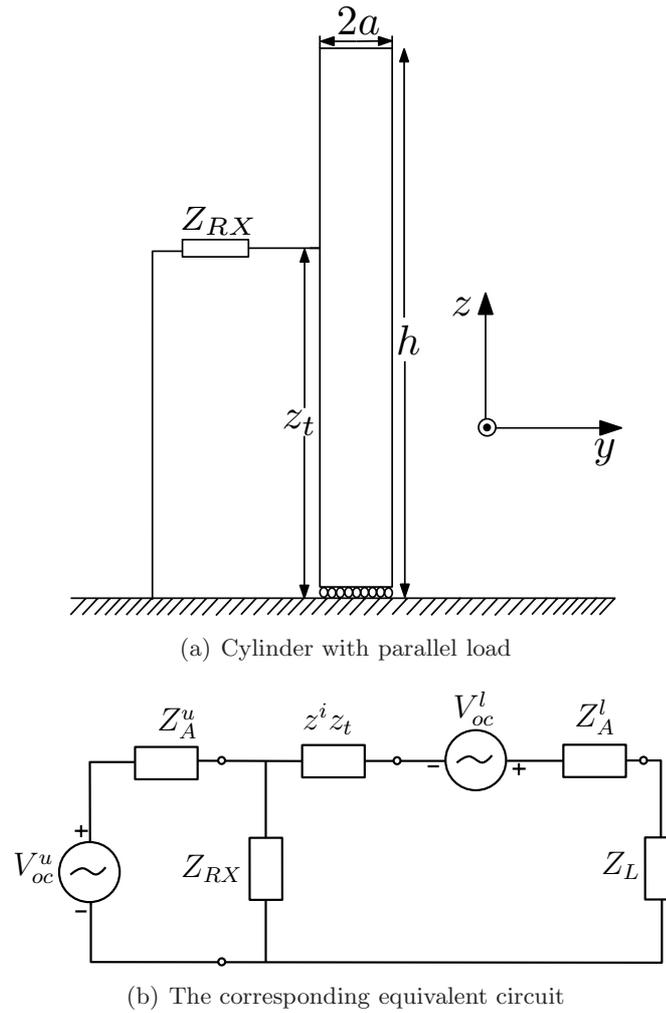
FIGURE 4.2: Human body cylinder model with externally embedded HBC receiver

- part of the current induced in the body from electromagnetic fields exposure gets grounded via the receiver circuit.

We analysed this problem by segmenting the cylinder into two parts, cutting it at $z=z_t$ as shown in Fig. 4.2. We treated the two segments as separate parasitic cylindrical antennas. The upper segment generates current at $z=z_t$ with source voltage of V_{oc}^u and output impedance of Z_A^u; and the lower segment and the receiver act like a load. The lower segment also generates current at the foot of the cylinder ($z=0$) with source voltage V_{oc}^l and output impedance of Z_A^l as shown in Fig. 4.2(b).

The upper segment source voltage V_{oc}^u is calculated by shorting the load as

$$V_{oc}^u = I_{sc}^u Z_A^u \tag{4.42}$$

where I_{sc}^u and Z_A^u are calculated based on the approach described in section 4.3.2, but taking the new height of the cylinder as $h_u = h - z_t$. The same applies for calculation of the lower source voltage V_{oc}^l and the corresponding impedance Z_A^l. Therefore, the current in the receiver load impedance I_{RX} can be calculated as

$$I_{RX} = \frac{Z_{eq}}{Z_{RX}} \left[\frac{V_{oc}^l Z_A^u + Z_{RX}(V_{oc}^l + V_{oc}^u)}{Z_A^u Z_{eq} + Z_{RX}(Z_{eq} + Z_A^u)} \right] - \frac{V_{oc}^l}{Z_{RX}} \tag{4.43}$$

where $Z_{eq} = z^i z_t + Z_A^l + Z_L$, and Z_L is impedance between the sole of the foot and the image.

4.4   Results and Discussion

The objective of this paper was to introduce the theoretical mechanism of interference in HBC as well as human body antenna effects on HBC operation, as little has progressed in the explanation of phenomena occurring in HBC. The complete characterization of HBC requires solving Maxwell's equation inside a high resolution voxel model of the human body as well as simulation of realistic near-field sources of interference that are more likely to be encountered in real-life. Such an approach calls for high computation time and complexity; therefore, we presented a simpler but useful approach to characterize HBC interference. The analytic solution derived for the total axial current, which is based on King's three-term approximation, is reasonably accurate for the cylindrical model of the body. But the actual human body has varying cross-sectional area due to different tissue layers, body parts and body postures; thus, the cylindrical model roughly approximates the case of a standing position with arms in contact with sides. Since the fields in the vicinity of the model are functions of the total axial current, we confine our discussion to the total axial current that can be easily related to the near-fields based on the relations outlined in the previous sections. The total axial current derived is a function of the dielectric property of the material forming the cylindrical model, the incident field, dimension of the model and the load at the foot. This is based on the implicit assumption that the ground is perfectly conductive and there are no nearby objects that rescatter the near-field.

The calculation of fields near the cylinder model in section 2.3 is valid for distances very close to the cylinder $\rho < 10a$ [56]. The total axial current for unloaded case ($Z_L = 0$),

as well as the magnetic field close to the cylinder, which does not involve a derivative of the total axial current, are excellent approximations. Nevertheless, the use of nonzero load and derivatives of the total axial current in the calculation of fields compromise the accuracy near the foot and edge of the cylinder, respectively. The accuracy of the axial electric field close to the cylinder can be improved by using a first-order iteration of the total axial current as pointed out in [60].

4.4.1 The Effect of h and Z_L on the Induced Total Axial Current

It is well known that a thin and perfectly conducting wire antenna has a narrowband frequency response. On the other hand, a thick and imperfectly conducting antenna, such as the cylinder model we used, has broadband frequency response within the HBC frequency range [61]. This implies that different radiation sources operating within the HBC frequency range, including nearby HBC users, have the potential to cause interference to HBC devices on which low power operation is intrinsic. For example, in typical healthcare settings, different devices use high frequency narrowband energy for their operation that falls within HBC frequency range; MRI uses 64 MHz sources, and lasers often use 13- or 27- MHz sources. Also other major sources of EMI include intentional radiators such as, telemetry and paging transmitters, and handheld radios.

The frequency response of the cylinder model also has a first resonance within the HBC frequency range, which shifts depending on the height of the cylinder h and the load at the foot Z_L. As the height increases from 1.5 m to 2 m, the resonance frequency shifts from 45 MHz to 35 MHz, as shown in Fig. 4.3(a), given that the impedance between the foot and the image is zero. The calculated resonance frequencies are in good agreement with the resonance frequencies of whole-body-averaged SAR predicted by other authors, such as Dimbylow [62], using FDTD algorithm on voxel-based models of real human anatomy. A good summary of related works by other authors is compiled in [19]. The presence of a load on the base of the cylinder has effect on the resonance frequency as well as the magnitude of the induced axial current. Assuming the load at the base of the cylinder is due to the impedance of rubber ($\epsilon = 3.5$) sole shoes, increasing the thickness of the sole introduces other resonances at higher frequencies while decreasing magnitude of the first resonance occurred due to the height of the cylinder, Fig. 4.3(b).
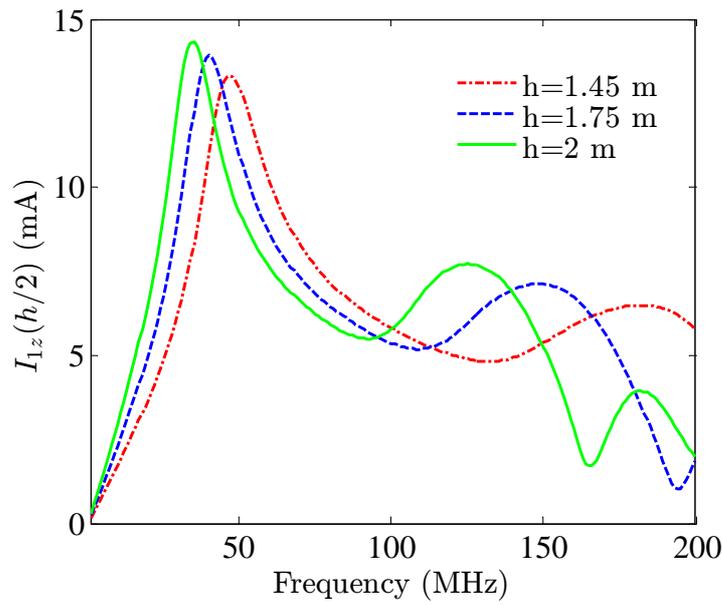
(a) $I_{1z}(h/2)$ for different height of cylinder
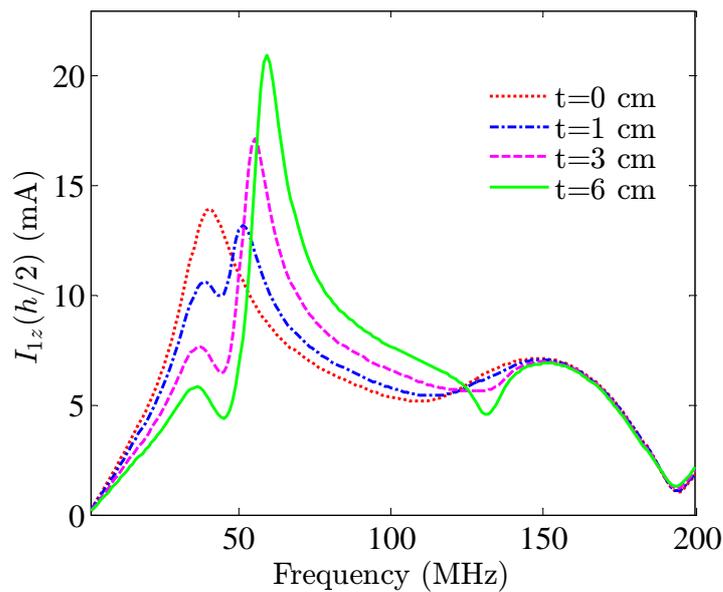
(b) $I_{1z}(h/2)$ for different thickness of the rubber sole

FIGURE 4.3: The effect of height h and load Z_L on the total axial current for E_0=1 V/m

4.4.2 Variations of the Potential Difference at the Electrodes of on-body HBC Receiver

As pointed out earlier, the HBC receiver detects the signal from the electric potential difference established between two points. In order to see how the received signal is
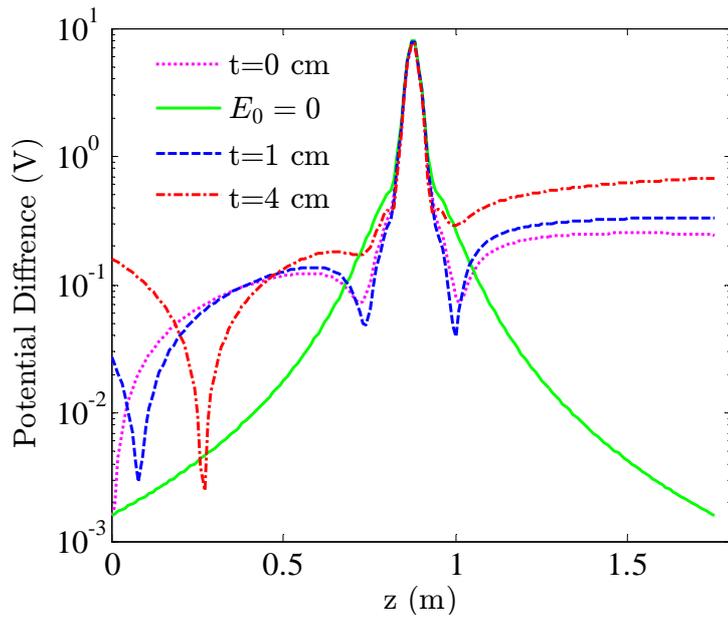
(a) Electric potential difference on the surface of the cylinder for different thickness of the rubber sole
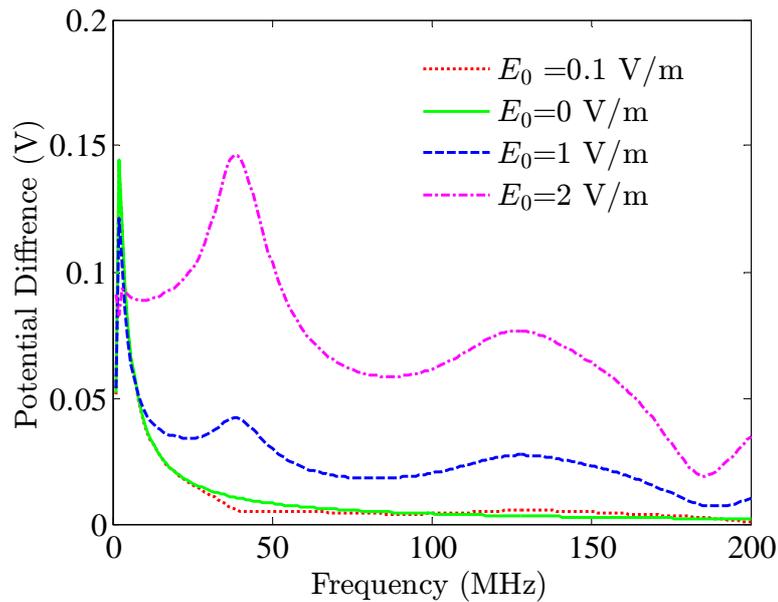
(b) Effect of $|E_0|$ on the potential difference at $z = h/2-0.3$ from the transmitter located at $z = h/2$

FIGURE 4.4: The effect of load and magnitude of the plane wave on the potential difference

affected by interference, we considered a transmitter and receiver that has 2 cm radius and 2 cm separation between their surface electrodes and circuit ground planes. We assumed that the transmitter feeds the electrode 1 mA current and is located on the surface of the cylinder at $(a,\ 0,\ h/2)$ in the coordinate system of the cylinder model.

Implementing quasistatic approximation, the signal detected by the receiver, which is located at $(a, 0, z)$, is calculated from the scalar potential difference between points on the surface of the cylinder and points 2 cm farther on the same radial line $(a + 0.02, 0, z)$. In reality, since the receiver is located in the reactive near-field of the transmitter and acts as a load to the transmitter, the current fed to the transmitter varies according to the location of the receiver. For the sake of simplicity, we assumed that the current remains constant and independent of the location of the receiver. The scalar potential in (4.36) is a function of first derivative of the current, which implies that the electric potential difference on the receiver, in the presence of a plane wave, is affected by location of the receiver, the load at the foot Z_L, and magnitude and frequency of the field E_0. As discussed previously, Z_L introduces resonance such that the potential difference is much more affected near the resonance frequency. Fig. 4.4(a) shows the effect of Z_L on the potential difference distribution along the length of the cylinder. The relationship between magnitude of E_0 and the calculated potential difference is obvious; the potential difference due to the plane wave is directly proportional to E_0 and its influence on the potential difference is shown in Fig. 4.4(b).

4.4.3 The Effect of the Human Body as Transmitting Antenna

The analysis in section 4.3.4 is based on the assumption that the human body is represented by infinite conductive half-space; but it does not take into account the characteristics of human body as a transmitting cylindrical antenna. Assuming that HBC transmitter acts like a source that drives current into the human body, the expression in (4.16) can be used to characterize the total induced axial current in the cylinder model for the particular case of the transmitter located at the base of the cylinder. The voltage at the base V_0^e, in this case, includes an additional term that represents the driving voltage of the HBC transmitter. This hypothesis is verified by a simple measurement using a battery powered vector network analyser (VNA) as shown in Fig. 4.5(a). In the literature, different theoretical HBC system models are validated using measurements on the arm. In order to complement the existing results in the literature, we carried out measurements on a human subject (1.73 m height) whose arm has length of 70 cm and average radius of 5 cm. The VNA is set to sweep a constant interval frequency of range 1-200 MHz with 0 dBm output power, which is well below the safety limit set by International Commission on Non-Ionizing Radiation Protection (ICNIRP) [22].
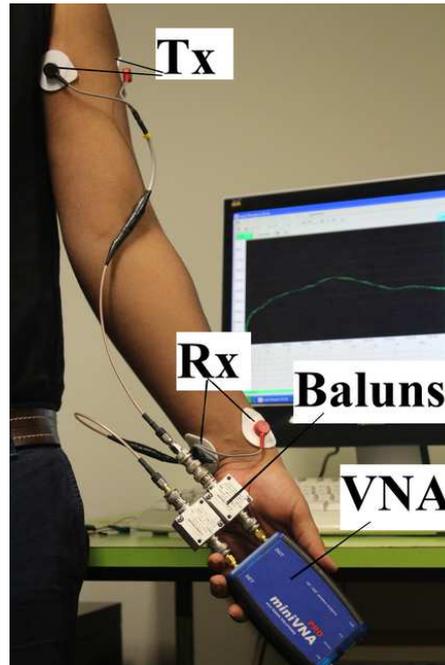
(a) Gain measurement setup
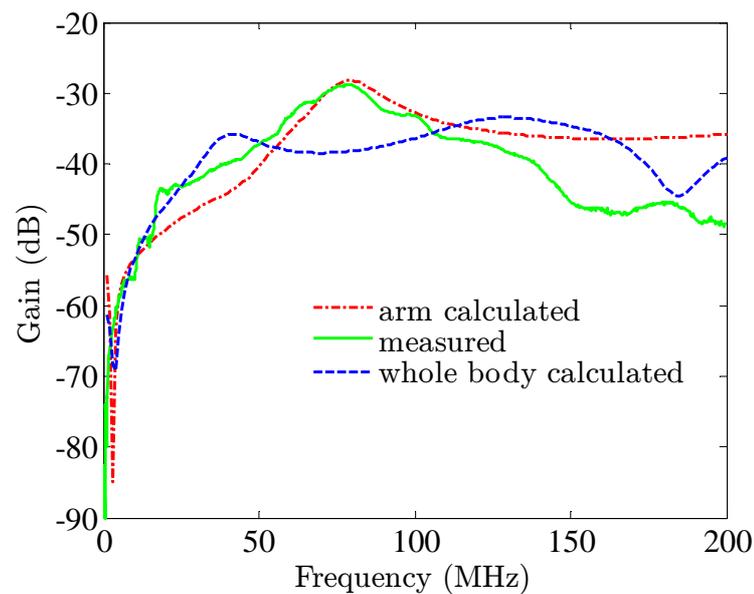
(b) Measured and calculated gain results

FIGURE 4.5: Gain measurement setup and gain measured and calculated results

The signal is coupled to the upper arm using a pair of Ag/AgCl electrodes; and the VNA detects the potential difference across a pair of Ag/AgCl electrodes located 40 cm farther on the lower arm. Baluns are used to isolate the common ground circuit plane of the transmitting and receiving ports of the VNA so that the return path through the VNA is avoided. The measured gain is maximum near 80 MHz as shown in Fig. 4.5(b).

A good approximation to the measurement result can be obtained by representing the arm by a cylindrical antenna of $h = 70$ cm and $a = 5$ cm, which is driven at its base and has resonance near 80 MHz, by assuming that the rest of the body acts like ground plane. The gain is calculated using the potential difference at $z = 2$ cm as the input voltage and the potential difference at $z = 40$ cm as the output voltage. The calculation result points to the possibility that the maximum gain near 80 MHz could be due to the resonance of the arm. Moreover, the measurement results show that the resonance frequency is not affected by the position of the electrodes; rather, only the gain is directly linked to the separation between the transmitting and the receiving electrodes. If the receiving electrodes are located at 30 cm farther from the transmitting electrodes, the gain increases by approximately 2 dB. In relation to this, some authors reported gain measurements that has maximum near 50 MHz. If we assume that the cylinder model has a dimension comparable to that of whole human body, the resonance occurs near 50 MHz for the case of $h = 1.75$ m as shown in Fig. 4.5(b), depending on the load at the foot. This suggests that the gain peak near 50 MHz could be due to the resonance of the whole body. Moreover, assuming that the ground is well insulated so that the image cylinder in the ground is not considered, the length of the antenna is halved resulting in a shift of the resonance frequency between 60-75 MHz, depending on the height of the cylindrical model.

4.4.4   The Current Conducted to Externally Embedded HBC Receiver

For the purpose of inspecting the validity of the approach we proposed in section 4.3.5 to calculate the conducted interference in externally embedded HBC receivers, a human subject of 1.73 m height is illuminated by electromagnetic field from a 60 cm monopole antenna located 3 m away as shown in Fig. 4.6(a). The monopole antenna is fed by a battery powered RF source tuned to generate from 1-200 MHz at 0 dBm. An AC-powered benchtop spectrum analyser measures the power in the electric current established when the subject touches a metallic electrode of 1.5 cm radius that is connected to the spectrum analyser port via a 3 cm coaxial cable. Even though it is known that, at the given distance, the incident electric field is not a perfect plane wave due to superposition of other components e.g. reflections, the proposed theoretical approach predicted the measured power to a reasonable accuracy as shown in Fig. 4.6(b). The value of the incident electric field is calculated based on the formula for vertical electric
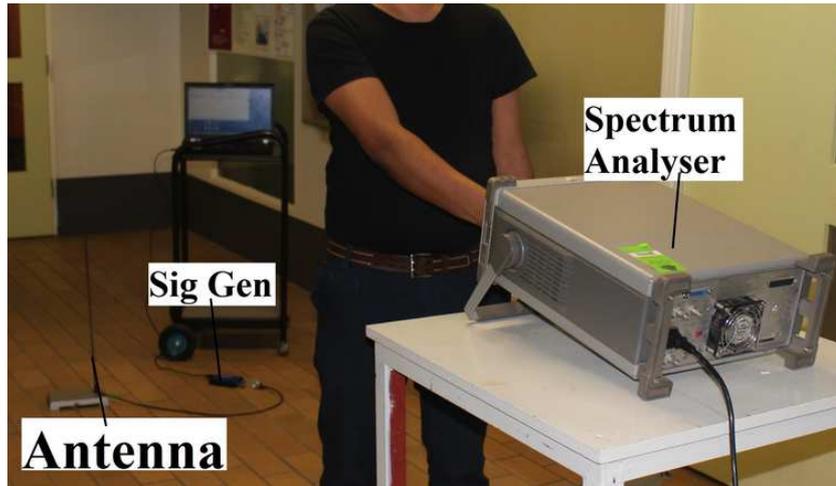
(a) Current measurement setup
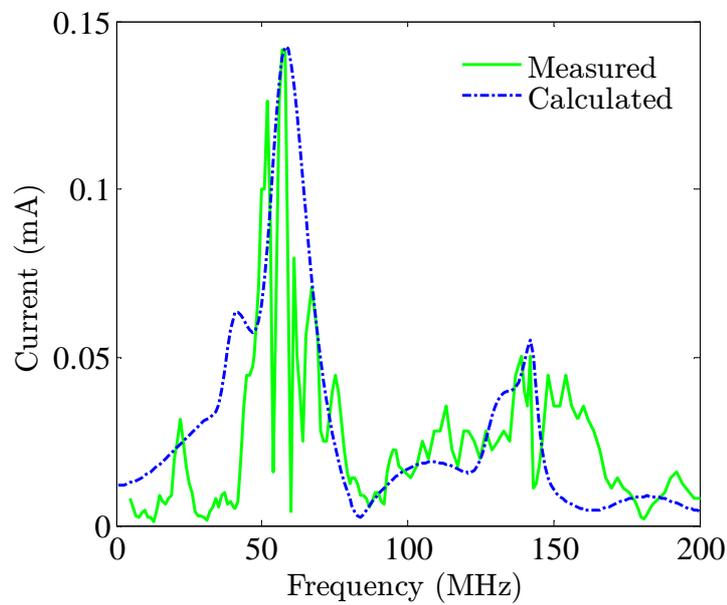
(b) Measured and calculated current in mA

FIGURE 4.6: Measurement setup and measured and calculated current in mA when a subject touches an electrode attached on spectrum analyser

near-field of a monopole antenna of height h and base current $I(0)$ as

$$E_0 \simeq \frac{jI(0)h}{4\pi\omega\epsilon_0\rho^3}(1 + jk_2\rho) \tag{4.44}$$

where $h = 0.6$ m and $\rho = 3$ m. The calculation result indicates that the resonance between 50 - 70 MHz occurred due to the load at the foot Z_L; the small resonance near 75 MHz could possibly be due to the resonance of the arm; and the receiver load Z_{RX}, which is the hand-electrode contact impedance and impedance of the network analyser

that acts like high pass filter suppressing the low frequency components.

4.4.5   General Remarks

The choice of operation frequency in HBC is a trade-off between gain and interference. For example, near 50 MHz a better gain performance can be obtained that leads to better communication performance but at the same time it might also increase the risk of interference to other HBC users or from nearby devices operating at the same frequency. For applications that the user is isolated from other users and electronic devices, the frequency near 50 MHz or 80 MHz gives a better gain performance. Also, for applications that require communication between nearby HBC users, center frequencies near 50 MHz might be promising with respect to low power requirement.

The interference due to RF exposure of the human body gets exacerbated by the dynamic nature of the human body. The human body is not stationary; it can get close to the proximity of EMI sources, which increases the level of induced current in the body. This implies that the design of HBC transceiver should take into account the mobility of human body as well as the likely EMI sources that can be encountered and their maximum field so that robust source, channel codings and modulation techniques can be deployed. Moreover, the HBC design should also consider EMI due to HBC devices on other body worn or implanted devices. In relation to this, HBC devices should also comply with Electromagnetic Compatibility (EMC) legislations. For example, the European Union EMC directive requires that a device should be immune to certain level of interference to work as intended. To get a quality label on an electronic device the directive imposes that the device should not dysfunction when exposed to an electric field of 3 V/m up to 1 GHz.

4.5   Conclusion

The effect of the human body as antenna on HBC is investigated. A homogenous cylindrical model of the human body is proposed, which has electrical property similar to muscle tissue. The induced total axial current in the model when it is exposed to plane wave is derived, which can be easily modified when the HBC transmitter is assumed to drive the human body as antenna. Expression for electromagnetic fields very close to

the cylinder are derived when the cylindrical model is illuminated by plane wave as well as when HBC transmitter is located on the surface of the cylinder. The effect of conducted interference, when the HBC receiver is located externally, is investigated using the cylindrical antenna model of the body. The calculation of potential difference revealed the cause of important phenomena in HBC gain measurements - the peaks occurring near 80 MHz and 50 MHz, which could be due to resonance of the arm or whole body, respectively. The selection of frequency in HBC transceiver design should not only rely on the gain performance; but it should also take into account the interference caused by the human body antenna effect.

Chapter 5

Cylindrical Antenna Theory for the Analysis of Whole-Body Averaged Specific Absorption Rate

BEHAILU KIBRET, ASSEFA K TESHOME, AND DANIEL T H LAI

5.1 Abstract

International guidelines and standards on whole-body radio-frequency (RF) dosimetry use the Whole-Body Averaged Specific Absorption Rate (WBA-SAR) as a surrogate metric to quantify the temperature rise in the body. This study proposes the analysis of whole-body RF dosimetry for far-field exposure of a grounded human body in the frequency range of 1-150 MHz based on a semi-analytic approach of cylindrical antenna theory. The human body is represented by a lossy homogeneous cylindrical monopole antenna. For the first time, an explicit model for the resonance frequency of a grounded human body is proposed. The model captures the effects of the human body weight, height and the dielectric properties. This study also addresses the effect of shoes on WBA-SAR. It is found that the resonance frequency for the WBA-SAR with shoe effect is higher than reported from using the bare-footed models, as confirmed by theory and measurement.

5.2 Introduction

One of the technological breakthroughs is the increasing use of electromagnetic fields for a broad spectrum of applications in day to day life. At the same time, the concern of the possible adverse effects of electromagnetic fields is also growing alongside in the society. Excessive whole-body exposure to the radio-frequency (RF) electromagnetic fields has the effect of increasing the human body core temperature. To address this issue, international standards [63] and guidelines [22] have been developed that use the whole-body averaged specific absorbtion rate (WBA-SAR) as a proxy metric to quantify the temperature rise in the body. WBA-SAR is the amount of RF power absorbed by the human body averaged over the whole-body. Since it is not suitable to measure the WBA-SAR inside the human body, computational results are often used to relate the WBA-SAR with external measurable quantities, such as, the incident electric field.

Prior RF dosimetry studies made use of simple human body models based on common geometrical shapes so that analytical solutions or simple numerical techniques could be applied [64, 65]. Currently, the most common way of computing the WBA-SAR is the finite-difference time-domain (FDTD) technique on realistic high resolution voxel models of the human body [62, 66, 67]. Through the whole-body RF dosimetry studies,

the analogy between the human body and a dipole or monopole antenna has been widely reported. But, not much has progressed in the analysis of the computation results from the antenna theory perspective. Among the few studies that focus on antenna theory, the similarity between a monopole antenna and a grounded human body has been reported in [16, 68, 69] from a statistical analysis of the FDTD computation results using the human body voxel models. Also, other earlier studies have employed the cylindrical antenna theory to calculate the induced current inside the human body when it is exposed to electromagnetic fields. The cylindrical antenna model of the human body was used in the analysis of the electromagnetic field exposure from power transmission lines by King *et al* [70] based on a semi-analytic approach. For similar power line frequency, Poljak *et al* [71] used the method of moments (MoM) to calculate the induced current in thick-wire model of the human body. Both approaches provided reasonably accurate results compared to the results found using the FDTD algorithm on voxel-based models of the human body [72]. A two-term approximation method was utilised by King [73] for higher frequency range of 50-200 MHz to calculate induced current in isolated or ungrounded cylindrical model of the human body in order to investigate the amount of current induced inside the body of amateur radio operators. Within this context, we propose a semi-analytic approach, based on the three-term approximation method, to analyse the WBA-SAR based on an equivalent cylindrical antenna representation of a grounded human body. The grounded cylinder represents a realistic case of a person standing on the ground, whereas an isolated or ungrounded cylinder represents a human body in free space.

In this study, a grounded human body is represented by an equivalent cylindrical antenna grounded on an infinite conductive plane as shown in Fig. 5.1. Early studies have used simple geometrical shapes, such as the cylinder, prolate spheroid or cuboid, to approximate the human body [64, 65]. Unlike previous studies, our study is not concerned with using the cylinder to approximate the physical attributes of the human body; rather, it is concerned with defining the parameters of a cylindrical antenna that produce equivalent WBA-SAR values compared to the FDTD computations on realistic voxel models of the human body. Also, the main objective of this study is not finding alternative analytic expressions for the WBA-SAR, since the state-of-the-art in electromagnetic computations allows a much better approach. Instead, we propose semi-analytic expressions that are used to analyse the whole-body RF dosimetry in a more convenient and flexible way
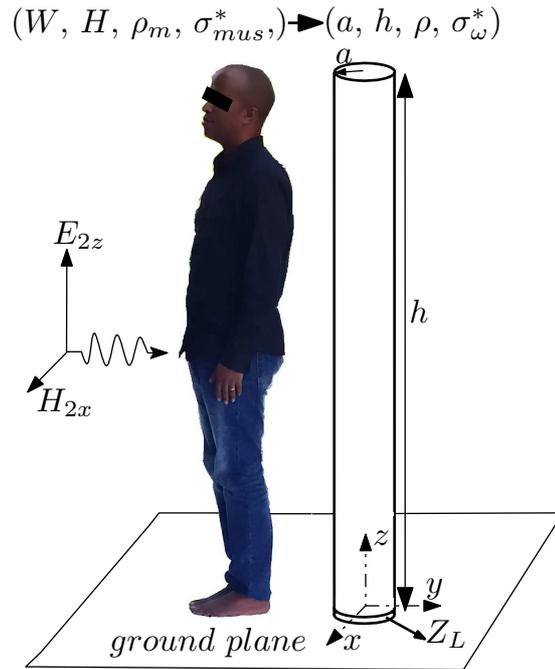
FIGURE 5.1: The equivalent cylindrical antenna representation of a grounded human body [53].

than can be achieved using FDTD. Moreover, the proposed model integrates the mechanism of how different parameters of the human body affect the WBA-SAR. The analysis focuses on the effect of human body attributes, such as, height, weight and the dielectric properties of the tissues with additional look at the effect of shoes. The approach is valid for the frequency range lower than 150 MHz, which is an important frequency range in whole-body RF dosimetry as it contains the resonance frequency of both the grounded and isolated human body. In RF dosimetry, the resonance frequency is defined as the frequency where the maximum WBA-SAR occurs. Recently, a similar approach was applied to analyse the WBA-SAR of an isolated or ungrounded human body [74] and to study the antenna effects of the human body on human body communications (HBC) [75]. Moreover, the practical application of the equivalent antenna representation of the human body has proved to be accurate at measuring the ankle current, as reported in [76].

In this paper, first, the expression for the total induced axial current and the WBA-SAR of the equivalent cylindrical monopole antenna are provided based on the three-term approach. Next, the parameters of the equivalent cylindrical antenna are related to the physical attributes of the human body. From the FDTD calculated WBA-SAR values of three voxel models, numerical values of the parameters of the cylinders representing the

adult males, adult females and children are defined. In order to demonstrate the validity of the approach, explicit formula for the resonance frequency is proposed and validated with FDTD based results of eleven different voxel models that represent different age groups, sex and race. Lastly, the effect of the height, weight, the dielectric properties of the body are discussed. More emphasis is given to the real life notion of WBA-SAR by analyzing the effect of shoes on the WBA-SAR and the resonance frequency, which is further supported by experimental results.

5.3   Theory

5.3.1   The Total Induced Axial Current

It was assumed that a time-harmonic vertically polarized plane wave induces a rotationally symmetric current density inside the equivalent cylindrical antenna representing a grounded human body as shown in Fig. 5.1. The approximate analytic expression for the total induced axial current inside the equivalent cylindrical antenna of height h, radius a, and complex conductivity σ_ω^* was driven based on the three-term approximation of the axial current in an imperfectly conducting and loaded receiving cylindrical antenna in [29, 30, 75] as

$$I_{1z}(z) = V_0^e v(z) + U_0 u(z). \tag{5.1}$$

V_0^e and U_0 are defined as

$$V_0^e = -I_{sc}(0)\frac{2Z_A Z_L}{2Z_A + Z_L} \qquad U^{inc} = \frac{E_0}{k_2} \tag{5.2}$$

and

$$v(z) = \frac{j2\pi k_2}{\zeta_0 \gamma \Psi_{dR} \cos(\gamma h)} \Big[\sin\gamma(h-|z|) + T_U(\cos\gamma z - \cos\gamma h)$$
$$+ T_D(\cos\tfrac{1}{2}k_2 z - \cos\tfrac{1}{2}k_2 h)\Big] \tag{5.3}$$

$$u(z) = \frac{j4\pi}{\zeta_0} \Big[H_U(\cos\gamma z - \cos\gamma h) + H_D(\cos\tfrac{1}{2}k_2 z - \cos\tfrac{1}{2}k_2 h)\Big] \tag{5.4}$$

where E_0 [Vm^{-1}] is the incident electric field at the surface of the cylinder, k_2 is the free space wave number, $Z_A = 1/(2v(0))$ [Ω] is the driving-point impedance of the same cylinder when driven at the base, Z_L [Ω] is the load impedance at the base of the cylinder,

and $I_{sc}(0) = U_0 u(0)$ is the current at the base when there is no load; and ζ_0 is the free space impedance. The expression of the frequency dependent coefficients Ψ_{dR}, T_U, T_D, H_U, and H_D are given in [75], which involve integrals that are solved numerically. Based on King [29], the imperfectly conducting nature of the equivalent cylindrical antenna was characterized by the complex propagation constant γ, which was defined as

$$\gamma = k_2 \sqrt{1 - j \frac{4\pi z^i}{k_2 \zeta_0 \Psi_{dR}}} \tag{5.5}$$

where z^i $[\Omega\text{m}^{-1}]$ is the impedance per unit length of the cylinder that was defined in [29] as

$$z^i = \frac{\kappa}{2\pi a \sigma_\omega^*} \frac{J_0(\kappa a)}{J_1(\kappa a)} = r^i + jx^i \tag{5.6}$$

where J_0 and J_1 are the zeroth and first-order Bessel functions. The term κ was also defined as

$$\kappa = -\sqrt{j\omega\mu_0\epsilon_0 \left(\frac{\sigma_\omega^*}{\epsilon_0} - j\omega - \frac{4\pi z^i}{\mu_0 \Psi_{dR}} \right)} \tag{5.7}$$

where μ_0 is permeability of free space, ϵ_0 is permittivity of free space, and ω is the angular frequency.

5.3.2 Total Power Dissipated Inside the Cylinder

The total average power dissipated P_{diss} inside the cylinder can be obtained as [77]

$$P_{diss} \simeq \frac{1}{2} \int_0^h r^i \, |I_{1z}(z)|^2 \, dz \tag{5.8}$$

where r^i is the real part of z^i (5.6). WBA-SAR is defined as the total average RF power absorbed by the human body divided by the total mass of the body [66]. Thus, for a homogenous cylinder of height h, radius a, density ρ and weight $W_c = \rho\pi a^2 h$, the total average absorbed power per unit mass $WSAR_{cyl}$ was defined as

$$WSAR_{cyl} = \frac{P_{diss}}{W_c} = \frac{r^i}{2\rho\pi a^2 h} \int_0^h |I_{1z}(z)|^2 \, dz. \tag{5.9}$$

5.3.3 Parameters of the Equivalent Cylindrical Antenna

In this study, the parameters of the equivalent cylindrical antenna were defined based on the anatomical parameters of the human body. The equivalent cylindrical antenna parameters taken were its radius a [m], density ρ [kgm^{-3}], height h [m], and the complex conductivity σ_ω^* [Sm^{-1}] of the material forming the cylinder. Also, the human body anatomical parameters used were the weight W [kg], height H [m], average density ρ_m [kgm^{-3}], and the complex conductivity of muscle σ_{mus}^* [Sm^{-1}], as shown in Fig. 5.1. The muscle tissue was chosen due to the fact that it is one of the major tissues in the body; and also, there is widespread use of the muscle tissue in homogenous models of the human body [16].

Using similar explanations given in our previous study on the analysis of the WBA-SAR of an isolated human body in [74], the parameters of the cylinder were defined as

$$a = L_1 \sqrt{\frac{W}{\pi \rho_m H}} \tag{5.10}$$

$$h = H \tag{5.11}$$

$$\sigma_\omega^* = L_2 \frac{2x}{3 - x} \sigma_{mus}^* \tag{5.12}$$

$$\rho = L_3 \frac{\rho_m}{x} \tag{5.13}$$

where L_1, L_2 and L_3 are the constants of proportionality; σ_{mus}^* was defined based on the 4-Cole-Cole dispersions [28]; $\rho_m \simeq 1050$ kgm^{-3} [78]; and x is a function of the lean-body-mass of the human subject, which was defined in [74]. The parameter x for males was defined as

$$x = 0.321 + \frac{1}{W} \left[33.92H - 29.53 \right] \tag{5.14}$$

and for females as

$$x = 0.295 + \frac{1}{W} \left[41.81H - 43.29 \right]. \tag{5.15}$$

As shown in (5.14) and (5.15), the subject specific parameter x is a function of the weight and height of the human subject. Thus, it was assumed that x correlates with the fat-to-muscle ratio of the human subject, which affects the value of WBA-SAR [79].

For a given frequency, height and weight of a human subject, the expression of $WSAR_{cyl}$ in (5.9) simplifies to a function of three unknowns, that are, L_1, L_2 and L_3. The value

TABLE 5.1: The constants of proportionality

	adult male	adult female	child
L_1	$\sqrt{5}$	$\sqrt{5}$	$\sqrt{5}$
L_2	0.25	0.21	0.16
L_3	0.38	0.44	0.60
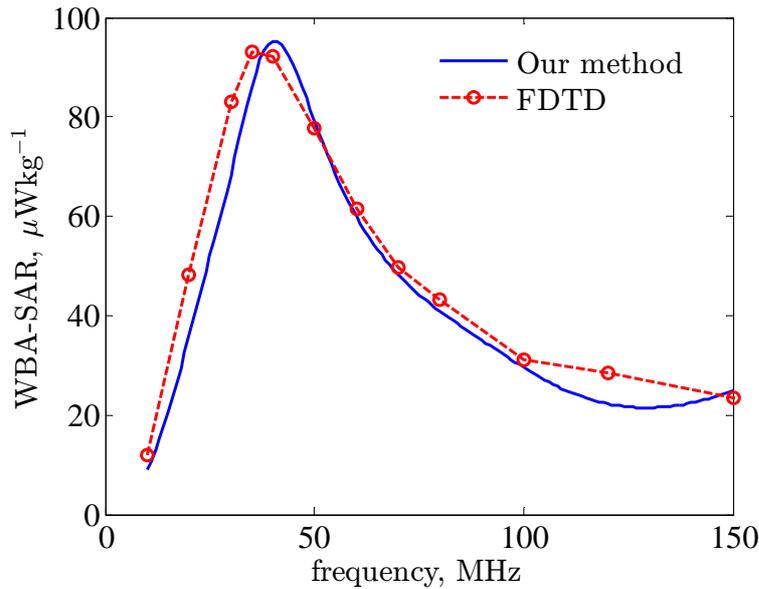
FIGURE 5.2: Comparison of the WBA-SAR calculated using the equivalent cylindrical antenna and using FDTD on the adultmale voxel model for $E_0 = 1$ Vm^{-1} r.m.s..

of these unknowns were evaluated by iteratively comparing the value of $WSAR_{cyl}$ with known FDTD computed WBA-SAR values of three voxel models representing an adult male, an adult female and a child. For the frequency range of 1 - 150 MHz, the values of the unknowns that produced the least average difference between the $WSAR_{cyl}$ and the known WBA-SAR were taken as the values of L_1, L_2 and L_3. The data for the FDTD based WBA-SAR values were taken from the literature [66, 79]. It was found that values of the constants of proportionality depend on the sex and age of the human subjects as shown in Table 5.1. The WBA-SAR calculated using (5.9) and the corresponding FDTD calculated WBA-SAR of the voxel models are shown in Fig. 5.2, Fig. 5.3 and Fig. 5.4.
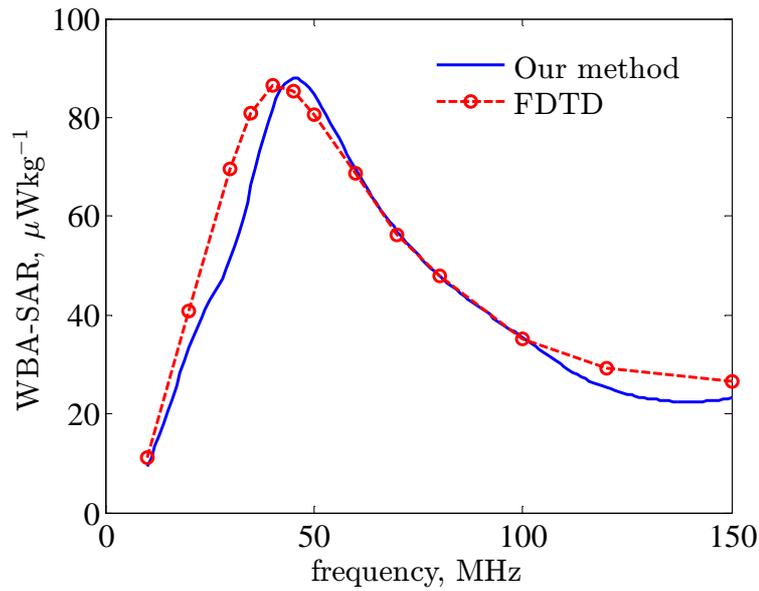
FIGURE 5.3: Comparison of the WBA-SAR calculated using the equivalent cylindrical antenna and using FDTD on the adult female voxel model for $E_0 = 1$ Vm^{-1} r.m.s..
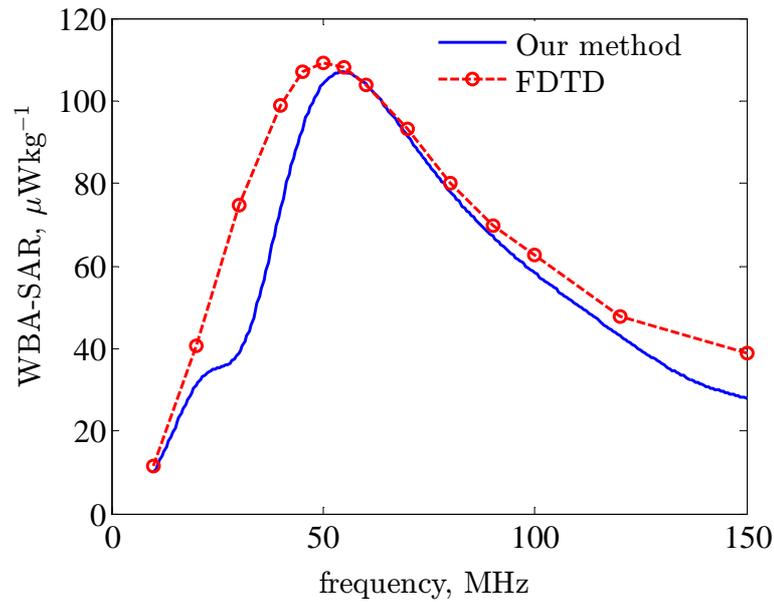
FIGURE 5.4: Comparison of the WBA-SAR calculated using the equivalent cylindrical antenna and using FDTD on the 10 years old child voxel model for $E_0 = 1$ Vm^{-1} r.m.s..

5.4 Results

The values of L_1, L_2 and L_3 were derived based on the FDTD computed results of three voxel models. Therefore, their validity to express the WBA-SAR of other human voxel

models, other than those used for their derivation, has to be assessed. This was done by deriving formulas for the resonance frequency.

Assuming the load impedance at the base of the cylinder $Z_L = 0$ in (5.1), the total axial current can be expressed as

$$I_{1z}(z) = U_0 u(z). \tag{5.16}$$

Replacing $I_{1z}(z)$ in (5.9) with the expression in (5.16), the maximum value of $WSAR_{cyl}$ with respect to frequency can be found by differentiating (5.9) with respect to the complex propagation constant γ (5.5). It was found that the maximum value occurs when

$$\gamma h = k_2 h \sqrt{1 - \left| \frac{j4\pi z^i}{k_2 \zeta_0 \Psi_{dR}} \right|} \simeq 1. \tag{5.17}$$

Since k_2 and h are real valued, the imaginary part of the expression in the square root is negligible; thus, the second term in the square root was approximated with its magnitude. The expression in (5.17) can be written in a quadratic form by replacing z^i with its expression in (5.6) as

$$k_2^2 - \left| \frac{j2}{\zeta_0 \Psi_{dR}} \frac{\kappa}{\sigma_\omega^*} \frac{J_0(\kappa a)}{J_1(\kappa a)} \right| \frac{k_2}{a} - \frac{1}{h^2} \simeq 0. \tag{5.18}$$

For the radius a and complex conductivity σ_ω^* of the three human body models used, when the expression in the absolute value in (5.18) is computed for the frequency range of interest, the result tends to approach the constant value of 0.12. The frequency dependent parameters inside the absolute value are functions of the complex conductivity of muscle, which has approximately constant magnitude in the frequency range of interest. Also, for the values of the radius a used, the values of the Bessel functions changes slightly. Therefore, replacing this term with its equivalent computed value 0.12, using the relation $k_2 = \omega\sqrt{\epsilon_0 \mu_0} = \omega/c = 2\pi f_{res}/c$, and replacing the radius a with (??), the quadratic equation can be solved for the resonance frequency f_{res} as

$$f_{res} \simeq \frac{c}{4\pi} \left[1.742 \left(\frac{\pi H}{W} \right)^{\frac{1}{2}} + \left(3.0345 \frac{\pi H}{W} + \frac{4}{H^2} \right)^{\frac{1}{2}} \right] \tag{5.19}$$

where c is the speed of light in free space.

The comparison of the resonance frequencies calculated using (5.19) to the FDTD based resonance frequencies of 11 voxel models that were developed by different authors and

TABLE 5.2: Comparison of the calculated resonance frequencies with that of the FDTD computed. The weight W is in kg, the height H in m, the resonance frequencies in MHz. Diff. is the percentage difference.

Voxel model	W	H	Sex	f_{res}	FDTD f_{res}	Diff. (%)
TARO	65	1.73	m	42.09	39	-7.92
HANAKO	53	1.60	f	45.13	45	-0.29
BAFB	105	1.88	m	37.08	38	2.42
Duke	70	1.74	m	41.38	40	-3.45
Ella	58	1.6	f	44.46	42	-5.86
Billie	34	1.48	f	51.07	51	-0.14
Thelonious	17	1.17	m	64.44	66	2.36
TARO 7 yr	23	1.2	m	59.99	61	1.66
TARO 5 yr	17	1.05	m	67.29	75	10.28
TARO 3 yr	13	0.90	m	75.83	83	9.46
Pregnant	58	1.61	f	44.34	46	3.61

reported in [16] is shown in Table 5.2. The formulation of the resonance frequency proposed (5.19) estimates the FDTD results of the 11 voxel models with an average percentage difference of 4.31 % as shown on the last column of the table.

5.5 Discussion

The semi-analytic approach followed here to analyse the equivalent cylindrical antenna and to calculate the total axial current has been proved to be accurate in cylindrical antenna analysis [80], provided that the condition $k_2 a \ll 1$ and $h \gg a$ is satisfied. For the equivalent cylindrical antennas used in this paper, the condition can be satisfied for the frequency range lower than 150 MHz, which is an important frequency range in the whole-body RF dosimetry as it contains the resonance frequency.

The formulation proposed in (5.19) is based on the three voxel models representing an adult male, adult female and a ten years old child; therefore, it became less accurate for very little children when comparing the predicted resonance frequency. For example, the percentage difference between the FDTD resonance frequency and the estimated resonance frequency for the five and three year old version of TARO is about 10%, which is much larger compared to the other models.

5.5.1 Effect of the Height and Weight

From the expression of the resonance frequency in (5.19), it can be seen that the resonance frequency depends on the weight and the height. The weight parameter in the formulation of the resonance frequency determines the radius of the cylindrical antennas or it represents how 'wide' a person is. For example, as shown in Table 5.2, the model Thelonious and TARO 5 yr have equal weight of 11 kg and height of 1.17 m and 1.05 m, respectively. Their resonance frequencies are 64.44 MHz and 67.29 MHz, respectively. This shows that a tall person has lower resonance frequency compared to a shorter person of the same weight. Similarly, from (5.19), it can be seen that a heavier person has a lower resonance frequency compared to a lighter person of the same height. For example, this can be seen by comparing two subjects of weight 30 and 40 kg and equal height of 1.4 m. Their corresponding resonance frequencies are 53.52 to 50.54 MHz, respectively.

5.5.2 Effect of the Dielectric Properties of Tissues

In order to observe the effect of the dielectric property on the WBA-SAR, the complex conductivity of the equivalent cylindrical antenna representing the adult male was doubled and halved. The predicted WBA-SAR is shown in Fig. 5.5. It can be seen that when the conductivity was doubled, the frequency characteristics of the WBA-SAR became narrower. This is expected from the perspective of antenna theory. It is well known that a thin and highly conductive wire antenna has a narrowband frequency response; but, a thick and imperfectly conducting cylindrical antenna has broadband response [61]. Also, when the conductivity was halved, the WBA-SAR got broader. This effect was also observed when comparing the WBA-SAR of the adult male and the adult female as shown in Fig. 5.2 and Fig. 5.3. The WBA-SAR of the female model is slightly broader than that of the male, which could be due to the smaller muscle mass percentage or higher fat in females. The conductivity of muscle is larger than muscle.

5.5.3 Effect of Shoes on Whole-body RF Dosimetry

Most studies on WBA-SAR were based on voxel models of a bare-footed human body. The effect of shoes on the WBA-SAR and the resonance frequency was reported in [62];
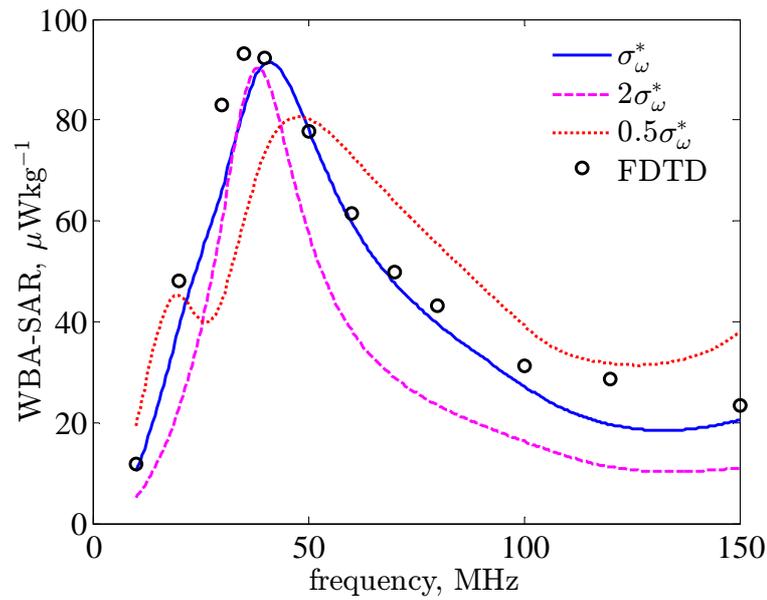
FIGURE 5.5: Comparison of the WBA-SAR calculated for different values of the complex conductivity.

but a detailed analysis was not given. All the preceding calculations were performed based on the assumption that the equivalent cylindrical antenna is grounded on a perfectly conducting plane; in other words, the load impedance was set to zero, $Z_L = 0$. But, in real life, people wear shoes; therefore, it is more relevant to see how a load at the base of the cylinder affects the WBA-SAR and the resonance frequency. Using the equivalent cylindrical antenna representation of the adult male, the load impedance of rubber (ϵ_r=3.5) with thickness of 1 and 2 cm is inserted at the base of the cylinder. Load insertion at the base has the effect of decreasing the value of WBA-SAR and shifting the resonance frequency to a higher band. For example, the insertion of 2 cm rubber at the base of the cylinder decreased the WBA-SAR by 16 μWkg^{-1} (for E^{inc}=1 Vm^{-1} r.m.s.) shifting the resonance frequency from 40 to 53 MHz as shown in Fig. 5.6. This prediction was supported by measurements carried out in our previous study on the antenna effects of the human body [75]. As described in our previous study, a human subject, who wore a pair of rubber-soled shoes and has an equivalent anatomical parameters with NORMAN, was illuminated with electromagnetic field generated from a monopole antenna located 3 meters away. It was found that the measured power due to the electric current established when the subject touches an electrode attached to a spectrum analyser has resonance near 55 MHz as shown in Fig. 5.7. This suggests that the WBA-SAR resonance frequency in a real scenario might be larger than the predicted
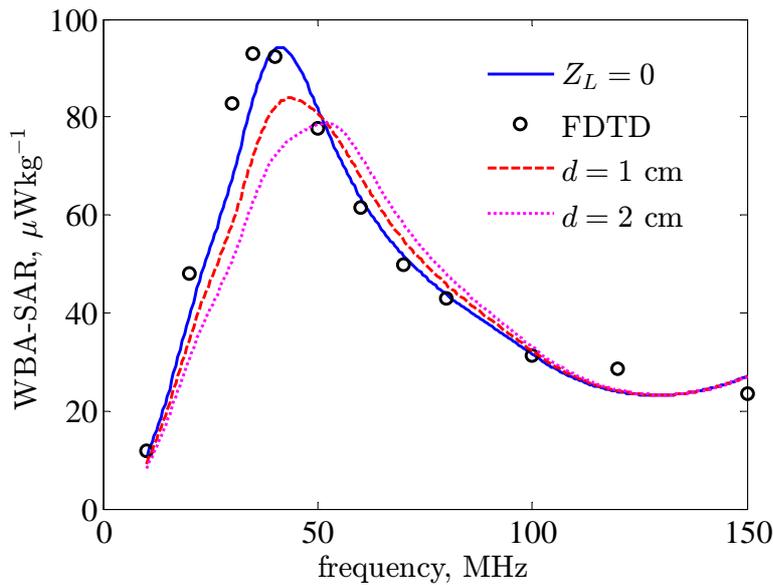
FIGURE 5.6: The effect of load due to inserting rubber of thickness d 1 and 2 cm at the base of the equivalent cylindrical antenna representing NORMAN.

value from using bare-footed voxel models. Our calculation and measurement suggest that, for an average size adult human with shoes on, the resonance frequency is between 50 to 60 MHz compared to the 35 to 45 MHz predicted for bare-footed voxel models.

Similarly, assuming that the load impedance is due to a gap (air) between the cylinder base and the ground, our calculation showed that a separation of 5 cm shifts the resonance frequency of the adult male to 65 MHz, which is equivalent to the resonance frequency of the isolated adult male. Also, a 1 cm cylinder base to ground separation shifts the resonance frequency to 56 MHz.

The proposed formulations can be used in the analysis of the WBA-SAR in the frequency range of 1- 150 MHZ, which contains the FM band. Moreover, the formulation of the resonance frequency and the analysis of the effect of shoes on the induced current have applications in the investigation of the electromagnetic phenomenon in HBC and in the survey of the possible application of the human body as antenna for implant wireless communications. For example, it has been explained how the minimum channel attenuation in HBC aligns with the resonance frequency of the induced currents in the human body exposed to electromagnetic fields [75]. In order to investigate the possible application of the human body as antenna for implant wireless communications, the
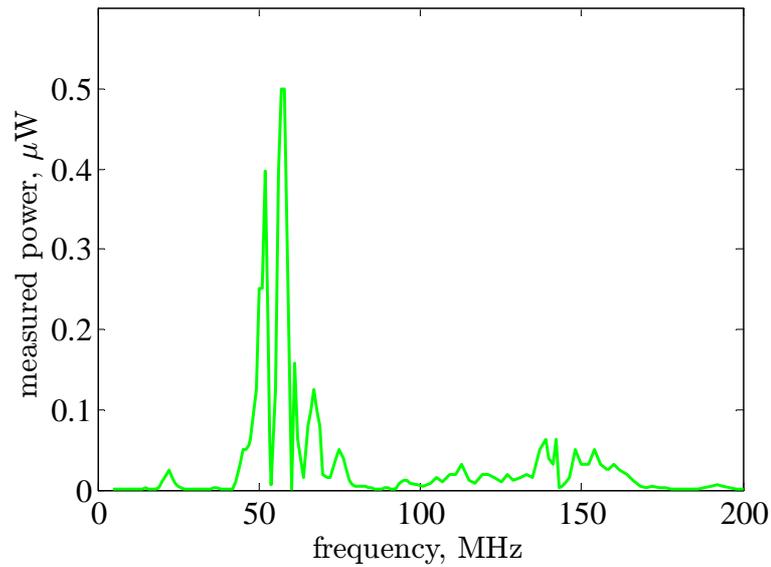
FIGURE 5.7: The measured power when a subject is illuminated by electromagnetic
field touching an electrode attached to spectrum analyzer.

formulation of the resonance frequency can also be useful to estimate the frequency at
which maximum RF power radiates out of the body.

5.6 Conclusion

The whole-body RF dosimetry is analysed based on the equivalent cylindrical antenna
representation of the human body of normal BMI in the frequency range lower than
150 MHz. The equivalent cylindrical antenna representation of the human body are
parameterized as adult males, adult females and children based on the FDTD computa-
tion results of three realistic voxel models. Explicit formula for the resonance frequency
was proposed, which was used to validate the proposed cylindrical antenna model. The
effect of the height, the weight and the dielectric properties of the body are discussed.
More importantly, the proposed equivalent cylindrical antenna suggests that the real
body resonance frequency could be higher than previous theoretical frequencies based
on bare-footed voxel models. The proposed approach can be applied to study the elec-
tromagnetics in human body communication, which has operation frequency less than
150 MHz.

Chapter 6

Characterizing the Human Body as a Monopole Antenna

BEHAILU KIBRET, ASSEFA K TESHOME, AND DANIEL T H LAI

6.1 Abstract

This paper, for the first time, fully characterizes the human body as a monopole antenna in the frequency range of 10 - 110 MHz, which contains the resonance frequency of the human body. The human body is represented by an equivalent cylindrical monopole antenna grounded on a highly conductive ground plane that is analysed based on the three-term approximation method. The reflection coefficient is measured using a human subject as a monopole antenna. Measurement results show that the theoretical predictions are in reasonable agreement. It is found that the human body resonates between 40 - 60 MHz depending on the posture of the body when it is fed by a 50 Ω impedance system at the base of the foot. A minimum reflection coefficient of -12 dB is measured that demonstrates that the human body can be potentially used as an antenna. Theoretically, it is predicted that the human body can be an efficient antenna with a maximum radiation efficiency reaching up to 70 %, which is supported by measurement results found in the literature.

6.2 Introduction

The interaction of radio frequency (RF) electromagnetic fields with the human body has been the main interest for a large number of research. Part of these studies centered on the use of this interaction for medical applications. Other studies focused on the effect of electromagnetic fields on the human body, which were primarily driven by the growing concern raised in the society about the possible adverse effects of electromagnetic fields. Additionally, other studies also paid particular attention on the effect of the human body on antennas that operate inside or in the vicinity of the human body, such as, implanted and wearable antennas. Aside from the brief mention of the analogy between the whole human body and a quarter wave monopole antenna in few of these studies, a comprehensive characterization of the human body as a monopole antenna is not available in the literature.

In the field of RF dosimetry, the mechanism of RF energy absorbtion inside the human body has been exhaustively studied. It has been reported that the frequency at which maximum RF energy dissipates inside the whole body, due to a vertically polarized plane wave, is close to the resonance frequency of a quarter wave monopole antenna

that has the same height as the human subject. This frequency, which is loosely termed as 'resonance frequency' in most RF dosimetry articles, not only depends on the height of the human subject, but also to the weight and gender of the subject [62].

Nowadays, the most common trend of computing the dissipated RF power inside the human body utilizes the finite-difference-time-domain (FDTD) algorithm based on computations of high resolution realistic voxel models of the human body [19]. Other prior studies used the cylindrical antenna model of the human body to study RF dosimetry. King applied a simplified form of the three-term approximation method to calculate the induced axial current inside the cylindrical antenna model of the human body [70], [81], [73]. In a related study, Poljak *et al.* implemented the method-of-moments (MoM) approach to calculate the axial current inside the thick-wire model of the human body [71]. Recently, we have applied the cylindrical antenna model of the human body using the three-term approximation to investigate the antenna effect of the human body on intrabody communication [75] and to analyse the whole-body averaged specific absorption rate [74].

Notable experiments, in attempt to characterize the human body as a monopole antenna, were carried out by Andresen *et al.* [21]. From the measured admittance of the human body as a monopole antenna, it was concluded that the human body does not resonate within the frequency range of 30-70 MHz. This contradicts the results in a large number of RF dosimetry computations and measurements that showed the whole-body resonance frequency of the human body is within the same frequency range. The reason for this could be the fact that the measured conductance is affected by the parasitic impedance between the foot and the ground. For the experimental setting used in [21], this parasitic impedance is so large that only a very weak resonance was observed between 30-70 MHz. By using a similar experimental setup, we were able to see a strong resonance at frequencies higher than 70 MHz. By decreasing the foot to ground separation, a strong resonance of the measured conductance can be observed within the frequency range 30-70 MHz. In [21], the authors also estimated the radiation efficiency of the human body as a monopole antenna by comparing gain measurements with that of thin-wire whip antennas. This second result is in reasonable agreement with our theoretical predications as shown later.

Other studies have made use of saline filled cylindrical models of the human body to measure the induced ankle current [15]. Similarly, a practical approach of using a monopole equivalent antenna of the human body was also proposed to measure the ankle current [76]. Despite the fact that all prior studies have focused on calculating or measuring the induced axial current inside the human body, none of them have fully characterized the human body with the essence of applying it as an antenna.

Presently, studies have demonstrated that the total axial induced RF current in the body, when the human body is irradiated by vertically polarized plane wave, is less affected by the change in cross-sectional size of the body, but behaves more like the axial current distribution in a cylindrical monopole antenna [15, 16]. These studies also showed that significant variations of the axial current density exist along the height of the body. This is due to the fact that large axial current density is developed in the cross-section of the body where there is small volume of conductive tissues, such as the knee and ankle. This is the basis of some studies that claim the local specific absorption rate (SAR) limit set by International Commission on Non-Ionising Radiation Protection (ICNIRP) [22] might be exceeded at the recommended exposure reference levels, at such parts of the body [62]. Therefore, the use of a homogenous cylindrical monopole antenna model of the human body is justifiable to characterize the whole human body in a standing posture. Such representation is more relevant to analyse the axial standing waves induced inside the human body that have wavelengths much larger than the body length. This is true for the frequency range we are interested in, which is lower than 110 MHz for a cylinder representing a human subject of height 1.76 m, as shown later. Moreover, such an approach has the advantage of simplicity and flexibility, to characterize the human body as antenna, compared to widely used methods, such as, the FDTD computations on realistic voxel models of the human body.

This paper characterizes the human body as a monopole antenna for the frequency range of 10 - 110 MHz. The human body is represented as a cylindrical monopole antenna that is analysed based on the three-term approximation method. The parameters of the cylindrical monopole antennas are defined based on the comparison with the FDTD based computation results of the total absorbed RF power inside the voxel models of the human body. Using these parameters, an expression for total induced axial current inside the human body is developed, which is used to characterize the human body as a receiving or transmitting antenna. The theoretical radiation efficiency and the reflection
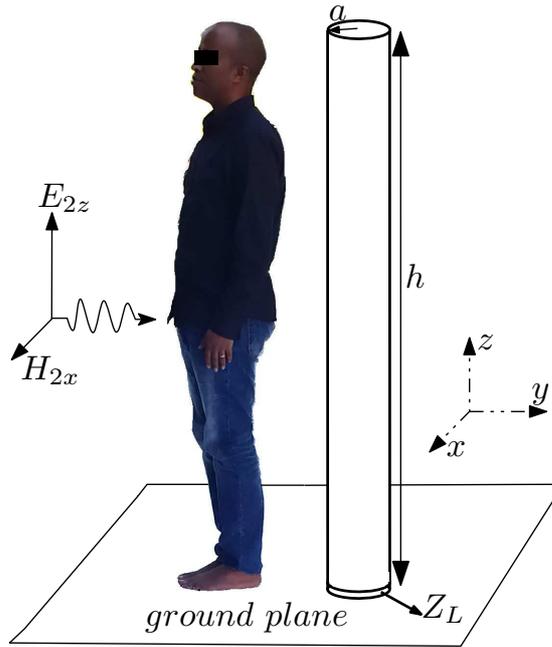
FIGURE 6.1: The equivalent cylindrical monopole antenna of a person standing on a highly conductive ground. Z_L is the load impedance due to the space (shoes) between the foot and the ground.

coefficient are used to determine the performance of the human body as a monopole antenna. The theoretically predicted results were compared against experiments that used a human subject to measure the reflection coefficient and radiation efficiency.

6.3 Theory

Due to the conductive nature of the body, at the frequency range of interest, the induced axial fields are not distributed uniformly at a given cross-section. In other words, the frequency range we are interested is high enough that skin-effects cannot be ignored. The skin-effect phenomenon is incorporated into the model by considering the field distribution in the cross-section of a very long conductive cylinder of radius a, complex conductivity σ_ω^* and permeability μ_0. Assuming, only the axial component of a rotationally symmetric magnetic vector potential $A_{1z}(\rho, z)$ is maintained along its axis, the resulting wave equation can be solved as

$$A_{1z}(\rho, z) = D J_0(\kappa \rho) \left(C_1 \cos \gamma z + C_2 \sin \gamma z \right) \tag{6.1}$$

where D, C_1, and C_2 are constants; J_0 is the zeroth-order Bessel function; $\kappa^2 = k_1^2 - \gamma^2$; $k_1 = \sqrt{j\omega\mu_0\sigma_\omega^*}$; and $\gamma = \beta$ - $j\alpha$ is the propagation constant along z-axis. From the boundary condition of the tangential magnetic fields at the surface of the cylinder, it can be shown that the total axial current $I(z)$ in the cylinder is

$$I(z) = C_1 \cos \gamma z + C_2 \sin \gamma z. \tag{6.2}$$

For the case of our equivalent cylindrical representation of the human body, the axial current should have a similar general form as the expression in (6.2) with additional terms to amend the effect of its finite length.

From the above expressions, the skin-effect can be expressed based on the axial current density $J_{1z}(\rho, z)$ as

$$J_{1z}(\rho, z) = \frac{I(z)\kappa}{2\pi a} \frac{J_0(\kappa\rho)}{J_1(\kappa a)} \tag{6.3}$$

where J_1 is the first-order Bessel function. Also, the surface impedance per unit length of the cylinder z^i can be defined as

$$z^i = \frac{\kappa}{2\pi a\sigma_\omega^*} \frac{J_0(\kappa a)}{J_1(\kappa a)}. \tag{6.4}$$

The expressions of the axial current density and the surface impedance per unit length of the equivalent cylindrical monopole antenna representing the human body were defined to be the same as the expressions in (6.3) and (6.4), respectively.

6.3.1 The Induced Axial Current

The human body can be completely characterized as a receiving or transmitting antenna from the induced currents in the body. The problem of computing the induced currents can be simplified by considering a typical scenario of a vertically polarized plane wave illuminating a human subject standing on a highly conductive ground, as shown in Fig. 6.1. For this specific case, we assumed that the axial current induced by the vertically polarized electric field is dominant. Other characteristics of the human body as a receiving or transmitting antenna, such as the antenna impedance, radiation efficiency and reflection coefficient, can be derived from the expressions of the axial current.

The problem is further simplified by using an equivalent cylindrical monopole antenna representation of the human body.

We assumed that a time-harmonic vertically polarized incident plane wave illuminated a cylindrical monopole antenna of height h and radius a, grounded on highly conductive infinite plane, that induced an axial current density of a form similar to the expression in (6.3). The surface axial magnetic vector potential $A_{2z}(a, z)$ due to the axial current density can be expressed as

$$A_{2z}(a, z) = \frac{\mu_0}{4\pi} \int_{V'} J_{1z}(\rho', z') \frac{e^{-jk_2 r}}{r} dv' \tag{6.5}$$

where $k_2 = \omega\sqrt{\mu_0 \epsilon_0}$ is the free space wave number. Applying the three-term approximation conditions ($k_2 a \ll 1$, $h \gg a$, and $k_2 h \leq \frac{5}{4}\pi$) [29], [30], the expression of r reduces to

$$r = \sqrt{(z - z')^2 + a^2} \tag{6.6}$$

so that the expression in (6.5) simplifies to

$$A_{2z}(a, z) = \frac{\mu_0}{4\pi} \int_{-h}^{h} I_{1z}(z') \frac{e^{-jk_2 r}}{r} dz' \tag{6.7}$$

where $I_{1z}(z')$ is the induced axial current.

The net axial electric field on the surface of the cylinder is related to $A_{2z}(a, z)$ as

$$\left(\frac{\partial^2}{\partial z^2} + k_2^2\right) A_{2z}(a, z) = j\frac{k_2^2}{\omega}\left[I_{1z}(z)z^i - V_0\delta(z) - E_0\right] \tag{6.8}$$

where E_0 is the incident axial electric field on the surface of the cylinder and V_0 is the voltage drop on a load at the base of the cylinder with the resulting electric field approximated by the delta-gap model.

An expression for $I_{1z}(z)$ can be derived from (6.8) using the three-term approximation method [75], [29], [30] as

$$I_{1z}(z) = V_0 v(z) + U_0 u(z) \tag{6.9}$$

where

$$V_0 = -I_{sc}(0)\frac{2Z_A Z_L}{2Z_A + Z_L} \tag{6.10}$$

$$U_0 = \frac{E_0}{k_2} \tag{6.11}$$

$$v(z) = \frac{j2\pi k_2}{\zeta_0 \gamma \Psi_{dR} \cos(\gamma h)} \left[\sin \gamma(h - |z|) + T_U(\cos \gamma z - \cos \gamma h) \right. $$
$$\left. + T_D(\cos \tfrac{1}{2}k_2 z - \cos \tfrac{1}{2}k_2 h) \right] \tag{6.12}$$

$$u(z) = \frac{j4\pi}{\zeta_0} \left[H_U(\cos \gamma z - \cos \gamma h) + H_D(\cos \tfrac{1}{2}k_2 z - \cos \tfrac{1}{2}k_2 h) \right] \tag{6.13}$$

Z_A is the input impedance of the monopole antenna; Z_L is load impedance at the base of the cylinder; $I_{sc}(0) = U_0 u(0)$ is the short-circuit current at the base of the cylinder when $Z_L = 0$; and $\zeta_0 = 120\pi \ \Omega$ is the free space impedance. The imperfectly conducting characteristics of the cylinder is defined by γ as

$$\gamma^2 = k_2^2 \left(1 - \frac{j4\pi z^i}{k_2 \zeta_0 \Psi_{dR}} \right). \tag{6.14}$$

The coefficients in the (6.12), (6.13) and (6.14) are calculated for each frequency by numerical computations of the integrals given in our previous paper [75].

The characteristics of the cylinder as a transmitting antenna can be easily derived from the expression of the total induced axial current of the receiving antenna when the cylinder is driven at the base with electromotive force V_0. Thus, the total induced axial current $I_{1z}(z)$ for the transmitting equivalent cylindrical monopole antenna can be expressed as

$$I_{1z}(z) = 2V_0 v(z). \tag{6.15}$$

6.3.2   The Cylindrical Antenna Parameters

In our previous studies [74], [82], we employed the equivalent cylindrical antenna representation of the human body to accurately predict the FDTD computed whole-body averaged specific absorption rate on 14 realistic high resolution voxel models that were reported in the literature. We found that the parameters of the equivalent cylindrical antenna (a, h, and σ_ω^*) depended on gender and age. In this study, since we used an adult male human subject for the experimental measurement, the parameters defined for the adult male voxel models were used to characterize the equivalent cylindrical antenna.

Accordingly, the expression for the radius a was derived as

$$a = \sqrt{\frac{5m}{\pi \rho_m h}} \tag{6.16}$$

where m (kg) is weight of the human subject, h (m) is height of the subject and $\rho_m = 1050$ kgm^{-3} is the average density of the human body. The complex conductivity of the cylinder was defined as

$$\sigma_\omega^* = 0.58 f_m \frac{2x}{3-x} \sigma_m^* \tag{6.17}$$

where f_m is the fraction of muscle tissue by mass that can be approximated as 0.43 for adult males with normal body-mass-index (18.5-24.9) and σ_m^* is the complex conductivity of muscle tissue calculated from the 4-Cole-Cole dispersions parameterized by Gabriel *et al.* [28]. The factor x is a function of the lean-body-mass that characterizes the total body water volume and it was defined for adult males as

$$x = 0.321 + \frac{1}{m}(33.92h - 29.53). \tag{6.18}$$

The height of the cylinder was defined to be the height of the human subject h.

In order to determine how well the equivalent cylindrical monopole antenna predicts the FDTD based computations results on realistic voxel models, the total absorbed RF power in a human subject calculated using the two methods was compared. The total absorbed power P_{abs} for an incident electric field E_0 illuminating a human subject grounded on a highly conductive ground is defined as

$$P_{abs} = \frac{1}{2} R_c \int_0^h |U_0 u(z)|^2 dz \tag{6.19}$$

where R_c is the real part of the total impedance per unit length Z_c of the cylinder that can be derived as

$$Z_c = \frac{1}{\pi a^2 \sigma_\omega^*}. \tag{6.20}$$

The comparison of the total absorbed power calculated using the FDTD computation on realistic voxel model of a male adult of height $h=$ 1.76 m and weight $m=$ 73 kg [62] and our three-term approximation approach (6.19) on its equivalent cylinder with parameters defined using (6.16) and (6.17) is shown in Fig. 6.2.
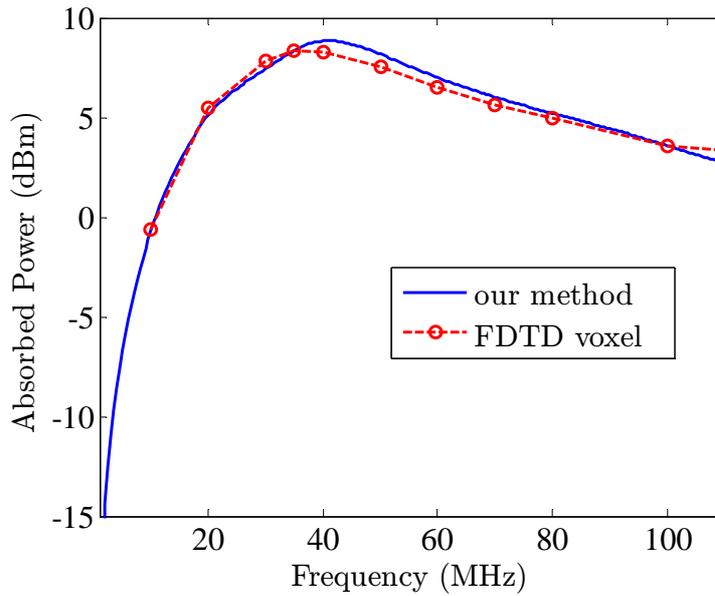
FIGURE 6.2: Comparison of the calculation results of the total absorbed RF power in the body of a grounded human subject of h=1.76 m and weight m=73 kg for an incident electric field E_0 of 1 V/m r.m.s.

6.3.3 Radiation Efficiency and Reflection Coefficient

The radiation efficiency η_r and reflection coefficient $|S_{11}|$ are important parameters that demonstrate the potential utilization of the human body as an antenna. The analysis of these parameters can be facilitated by the representation of the equivalent cylindrical monopole antenna with the corresponding equivalent circuit. We considered the specific case of a person standing bare foot on a dielectric slab of thickness d, area A and relative permittivity ϵ that is located on the surface of a highly conductive ground plane, as shown in Fig. 6.3. A thin Aluminium sheet is placed on top of the dielectric slab for the subject to rest the feet; and it is excited by an RF source via a 50 Ω transmission line that is grounded on the highly conductive ground plane. The reason such setting was chosen is, unlike conventional monopole antennas, the parasitic impedance Z_L due to the base of the foot and the ground cannot be ignored when considering the human body as a monopole antenna. This parasitic impedance is small due to the large surface area of the foot so that part of the RF current couples to the ground via this impedance. The parasitic impedance is related to the impedance due to the sole of shoes. Therefore, the equivalent circuit representation of the cylindrical antenna includes this parasitic impedance, as shown in Fig. 6.3.
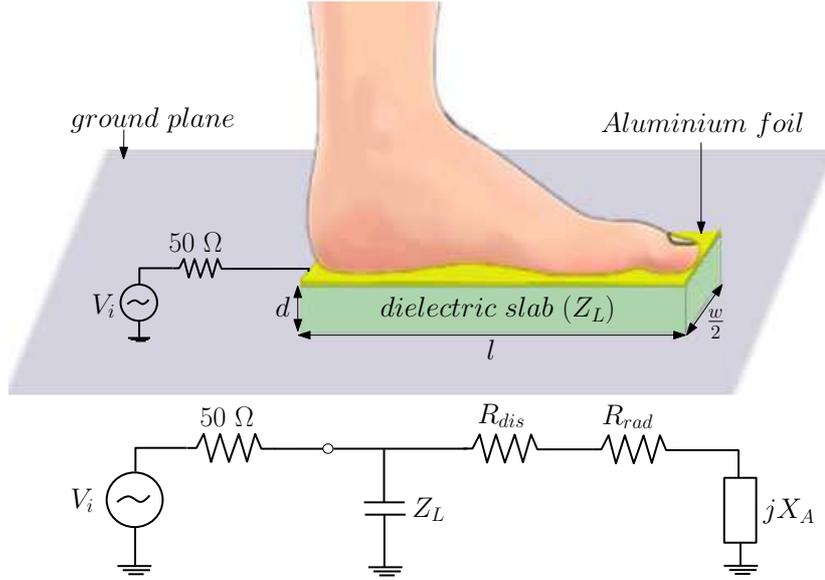
FIGURE 6.3: The diagram shows the typical setup of feeding the human body as a cylindrical monopole antenna and its corresponding equivalent circuit representation. A single foot is shown for clarity.

From Fig. 6.3, it can be seen that the human body antenna impedance Z_A was represented by its components as

$$Z_A = R_{dis} + R_{rad} + jX_A \qquad (6.21)$$

where R_{dis} represents the power dissipated P_{dis} in the human body due to conduction and dielectric loss of the human body, R_{rad} represents the radiated power P_{rad}, and X_A represents the power stored in the near fields of the human body. The antenna impedance Z_A can be easily calculated from the expression of the axial current (6.15) by assuming an input voltage V_0 at the terminals of the antenna. The antenna impedance Z_A is

$$Z_A = \frac{1}{2v(0)}. \qquad (6.22)$$

The antenna impedance calculated for an equivalent monopole antenna representing a human subject of height $h = 1.76$ m and weight $m = 73$ kg is shown in Fig. 6.4. Fig. 6.5 shows the relationship between the variation in the dimension of the equivalent cylindrical monopole antennas and the magnitude of the antenna impedance. The magnitude of the antenna impedance was calculated for different equivalent cylindrical monopole antennas representing human subjects of different height with similar body-mass-index of 23.56. Minimum of $|Z_A|$ shifts to lower frequencies as the height of the monopole antenna increases, suggesting that a tall human subject causes lower resonance frequency.
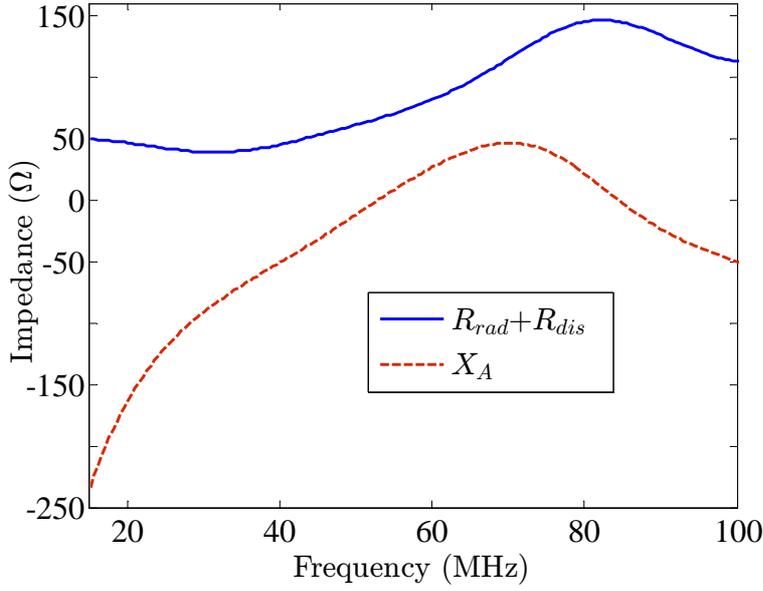
FIGURE 6.4: The antenna impedance Z_A calculated for a cylindrical monopole antenna representing a human subject of height h=1.76 cm and weight m=73 kg.
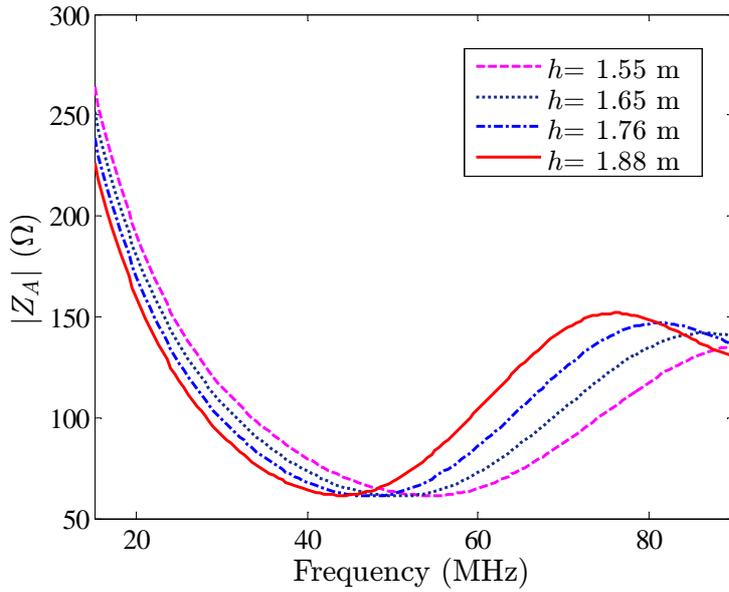
FIGURE 6.5: The magnitude of antenna impedance versus height of the cylindrical monopole antenna representing different human subjects that have the same body-mass-index of 23.56.

The radiation efficiency η_r is defined as the ratio of the power radiated to the total antenna input power P_{in} as

$$\eta_r = \frac{P_{rad}}{P_{in}} = 1 - \frac{P_{dis}}{P_{in}} = 1 - \frac{R_c}{R_{rad} + R_{dis}} \int\limits_0^h \frac{|v(z)|^2}{|v(0)|^2} dz \qquad (6.23)$$
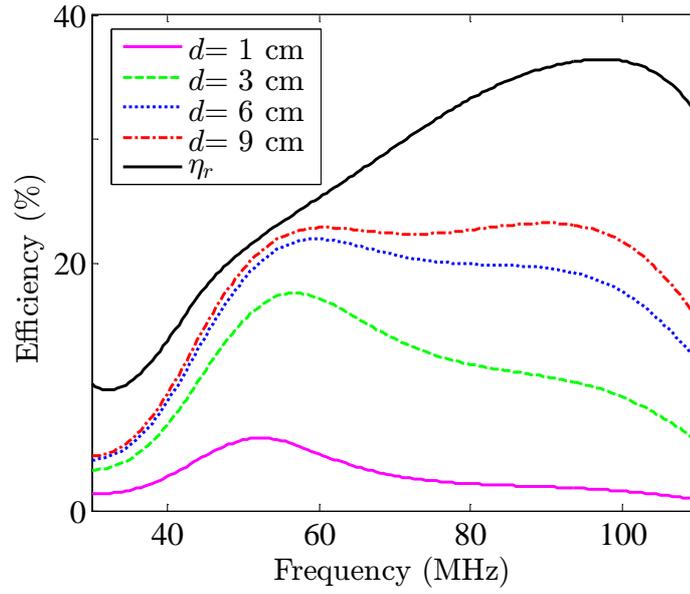
FIGURE 6.6: The theoretical radiation efficiency η_r and the total efficiency η_t for different thicknesses d of the dielectric slab (ϵ= 3, area= 22x30 cm^2) placed underneath the cylindrical monopole antenna representing a human subject of height h=1.76 m and weight m=73 kg.

where P_{in}= P_{rad}+P_{dis}. The effect of the impedance mismatch between the input circuit and the antenna can be characterized by the total efficiency η_t defined as

$$\eta_t = \eta_r \left(1 - |\Gamma|^2\right) \tag{6.24}$$

where Γ is the reflection coefficient. The reflection coefficient in the case of Fig. 6.3 is influenced by the parasitic impedance Z_L; therefore, it can be obtained as

$$\Gamma = \frac{Z_{eq} - Z_0}{Z_{eq} + Z_0} \tag{6.25}$$

where Z_0= 50 Ω is the output impedance of the feeding circuit and Z_{eq} is the equivalent impedance of Z_A and Z_L in parallel.

From Fig. 6.6 and Fig. 6.4, it can be seen that the theoretical radiation efficiency increases with frequency, which tends to follow the pattern of the real part of the antenna impedance $R_{rad} + R_{dis}$. This is because the real part of the total impedance of the cylinder per unit length R_c changes slowly within the frequency range of interest. The theoretical efficiency suggests that the human body has a high radiation efficiency, up to 70 %, for higher frequencies (between 90-100 MHz), provided the RF current is
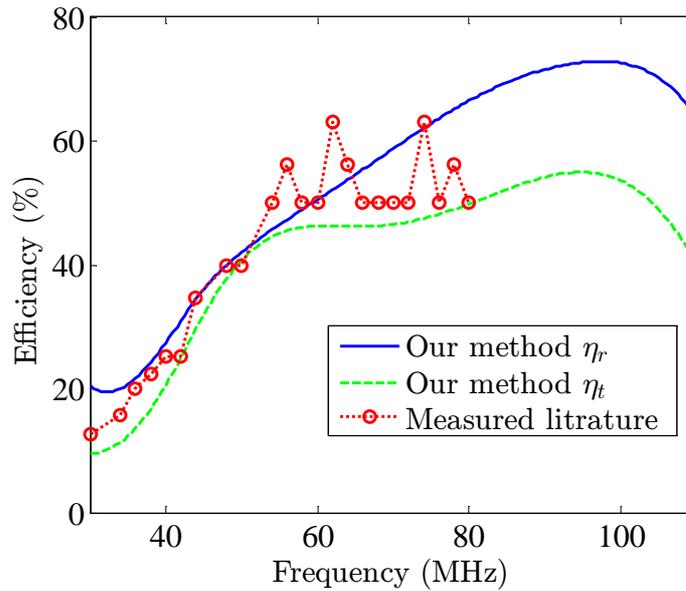
FIGURE 6.7: Comparison of η_r and η_t with the measured radiation efficiency found in [21]. η_t was calculated based on the experimental setting in the literature; $Z_0 = 50\ \Omega$, parameter for Z_L are $\epsilon = 1$, $A = \pi(0.15)^2\ \mathrm{m}^2$, and $d = 0.1\ \mathrm{m}$.

coupled to the base of the foot efficiently. For the particular scenario considered here, the total efficiency η_t is the appropriate parameter to characterize the performance of the human body as a monopole antenna, since it captures the effect of the dielectric slab (shoes) underneath the foot. Fig. 6.6 shows that as the thickness d of the dielectric slab increases, the parasitic impedance Z_L increases, causing more RF current to excite the base of the foot so that the total efficiency increases. Therefore, the parasitic impedance should be maximized to increase the total efficiency or gain. In practice, however, the radiation efficiency is smaller due to losses such as the power dissipated through the imperfectly conducting ground.

The calculated theoretical radiation efficiency of the human body is close to the measured radiation efficiency of a seawater monopole antenna, a maximum of 75 %, in the frequency range of 40-200 MHz [83]. In other studies [15], [84], measurements on saline based equivalent cylindrical monopole antennas of the human body were used to estimate the induced ankle current computed using a realistic voxel model of the human body. This suggests that the human body can be represented by a saline filled cylindrical monopole antenna. Therefore, the calculated theoretical radiation efficiency being close to the measured radiation efficiency of the seawater monopole antenna is a plausible estimate.
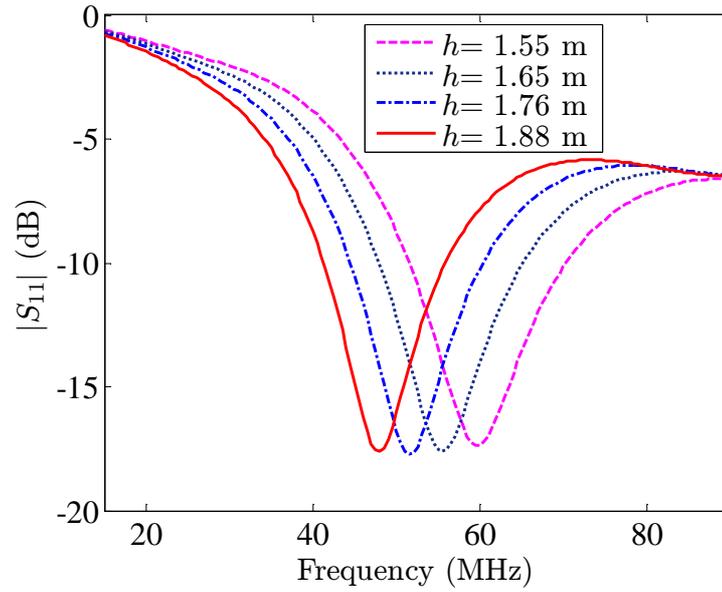
FIGURE 6.8: Comparison of the calculated reflection coefficients for cylindrical monopole antennas representing human subjects of different height and the same body-mass-index of 23.56.

In order to determine how accurate our predicted theoretical radiation efficiency is, η_r and η_t were compared to a measured radiation efficiency found in the literature. In [21], the radiation efficiency of a human body as a monopole antenna was estimated from gain measurements relative to whip antennas. By using the parameters used in the measurement, we predicted the measured radiation efficiency in a reasonable accuracy as shown in Fig 6.7. It can be seen that, at 60 MHz, half of the input power is dissipated inside the body. More interestingly, it can be inferred that the human body as a monopole antenna has a maximum theoretical radiation efficiency, about 70 %, in the FM radio band.

The other antenna performance indicator is the reflection coefficient that can be represented in the s-parameter form as

$$|S_{11}|(dB) = 20\log_{10}(|\Gamma|). \tag{6.26}$$

Fig. 6.8 shows the theoretical reflection coefficient for the equivalent cylindrical monopole antennas of different height representing human subjects of similar body-mass-index. The reflection coefficient was calculated ignoring the parasitic impedance Z_L and assuming the antenna was fed by a 50 Ω system. As expected, the resonance frequency
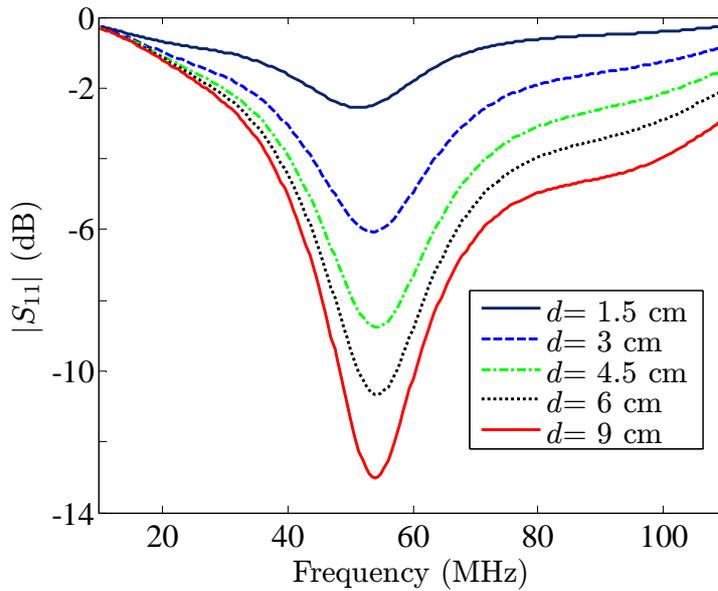
FIGURE 6.9: Comparison of the calculated reflection coefficients for different thicknesses d of the dielectric slab (ϵ= 3, area= 22x30 cm^2) placed underneath a cylindrical monopole antenna representing a human subject of height h= 1.76 m and weight m= 73 kg.

shifts downwards as the height of the antenna increases with a minimum reflection coefficient $|S_{11}|$ about -17 dB. The effect of the dielectric slab on the reflection coefficient is depicted in Fig. 6.9; it can be seen that as the thickness d of the dielectric increases the reflection coefficient decreases with the resonance frequency increasing slightly. The reflection coefficient also shows that a large value of the parasitic impedance improves the performance of the human body as antenna.

6.4   Experiment

In order to validate the theoretical predictions made about the performance of the human body as cylindrical monopole antenna, experimental characterization was carried out. The typical scenario considered in this study, which is shown in Fig. 6.3, was experimentally setup and important parameters were measured. A bare-foot human subject of height h= 1.76 m and weight m=73 kg stood on layers of rubber slabs (1.5 cm thick, 22 cm wide and 30 cm long each) with Aluminium foil placed on top, as shown in Fig. 6.10. The rubber layers were placed in the middle of a 4.5×5 m^2 Aluminium sheet that acted as the conductive ground plane. The signal was generated using a battery operating vector network analyser (VNA), which is capable of sweeping the
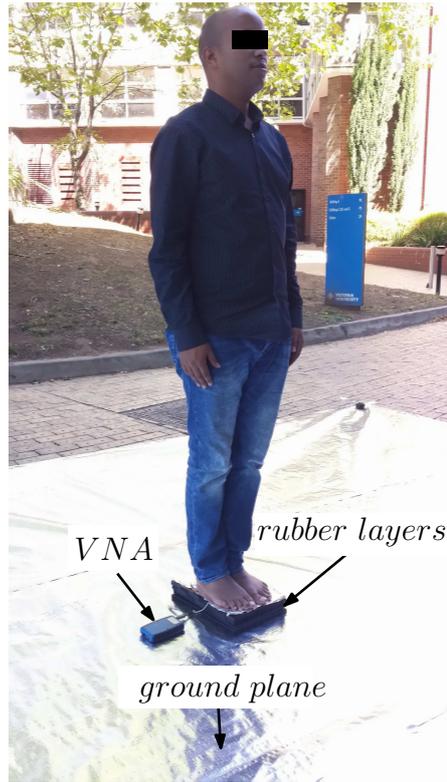
FIGURE 6.10: The experiment setup with a human subject of height h= 1.76 m and weight m= 73 kg.

frequency range of 1-200 MHz. The effect of radiating cables and human operator was eliminated by connecting the VNA and the measuring computer via a Bluetooth connection. The RF signal was fed to the Aluminium foil with a short coaxial cable with its shield attached to the ground plane. The rubber slabs were stacked to create a variable thickness dielectric in order to the see the effect of changing the values of the parasitic impedance.

The maximum output power of the VNA is 0 dBm, according to the specifications of the VNA, which is much smaller compared to the safety limit restricted by ICNIRP [22]. Taking the worst case, if we assumed all the power generated by the VNA is dissipated inside the body of the human subject, the Whole-Body Averaged Specific Absorbtion Rate (WBA-SAR) is $10^{-3}/73$= 137 μWkg^{-1}, which is much lower than the WBA-SAR limit set by ICNIRP, 0.4 Wkg^{-1} for occupational exposure. Even assuming the unlikely event that all the VNA output power is absorbed by 1 gm of the tissue of the human subject, the local SAR is equal to 137 mWkg^{-1}, which is still much smaller compared to the recommended limit for occupational exposure on the head and trunk, which is 10 Wkg^{-1}. For the frequency range of 100 kHz to 10 MHz, the ICNIRP limit is set based
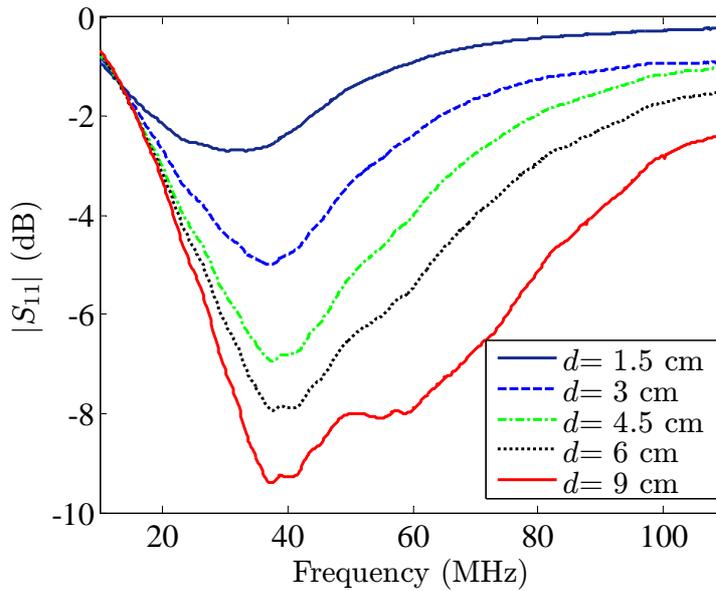
FIGURE 6.11: The measured reflection coefficient for different thicknesses of the rubber layers (ϵ= 3, area= 22x30 cm^2) placed underneath the human subject.

on the current density, which is defined as $f/100$ mA/m^2, where f is the frequency in Hz. At 1 MHz, taking the mean conductivity of muscle 0.5 Sm^{-1} and its density 1.06 kgm^{-3}, the power deposited in 1 gm of muscle due to the maximum permissible current density at this frequency is 100 mW, which is larger than the output power of the VNA. But, we know that it is unlikely that all the output power dissipates on a 1 gm tissue of the human subject; therefore, the experiment was safe to use a human subject.

The measured reflection coefficient for different thicknesses of the dielectric slab is shown in Fig. 6.11. Even though the theoretical reflection coefficient shown in Fig. 6.9 predicted the general behaviour of the experimental results, there are differences in the location of the resonance frequencies and the magnitude of the reflection coefficient. The resonance frequency predicted was near 50 MHz but the measurement results show resonance close to 40 MHz. One of the obvious causes of such differences is the fact that the human body is modeled by a cylindrical antenna that was analysed based on the three-term approximation. The other causes are experimental factors that were not included in the theoretical setup. One such factor is the effect of the Copper core of the coaxial cable used to connect the VNA to the Aluminium foil. In order to accommodate the variable thickness of the dielectric layers and secure a good ground connection, part of the Copper core, 7 cm long, was left unshielded. We observed that shortening the size of the unshielded core shifts the resonance frequency upwards as shown in Fig. 6.12,
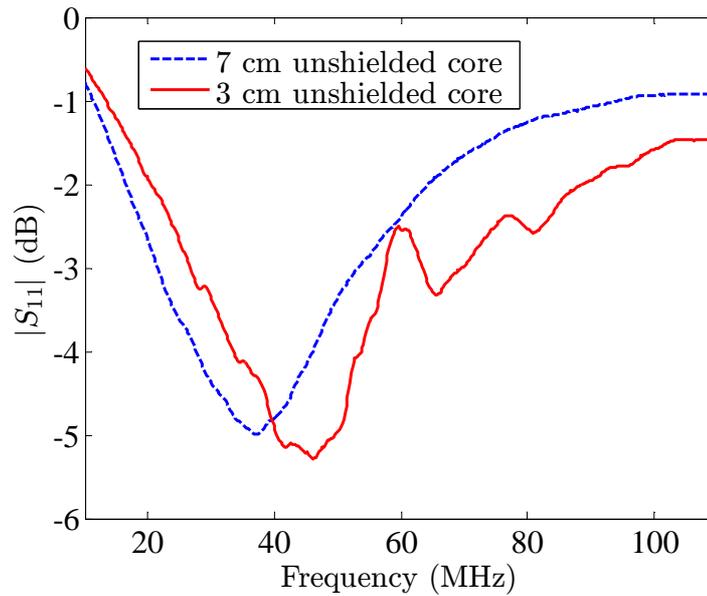
FIGURE 6.12: Comparison of the effect of varying the length of the unshielded Copper on the measured reflection coefficient. The thickness of the rubber layer used was 3 cm.

which illustrates the difference when using a 7 cm and a 3 cm long unshielded cores. This is expected as a longer unshielded Copper core increases the total height of the radiating element in addition to the human body; therefore, it has the effect of shifting the resonance frequency slightly downwards. Another experimental factor that was not included in the theoretical setup was the additional impedance due to the unshielded coaxial cable and its connection with the Aluminium foil. Incorporating this impedance as a series inductive reactance between the feeding circuit and the load Z_{eq} of the theoretical setup shown in Fig. 6.3, the measurement results can be predicted better as shown in Fig 6.13. Fig. 6.13 shows the addition of a series inductive reactance, which represents the effect of the unshielded core, reduces the capacitive reactance of the Z_{eq}; thus shifts the resonance frequency lower. Also, the theoretical axial current model is derived based on the assumption of a perfectly conducting infinite ground plane; however, the ground might have some effect on the experiment. Due to the ground loss, the measured radiation efficiency might smaller than theoretically predicted.

Another interesting observation is the human body retains its behaviour as a monopole antenna even for different postures. This was seen when the reflection coefficient was measured with the human subject in different postures as shown in Fig. 6.14. Lifting the arms high increases the total length of the radiating element, therefore the resonance
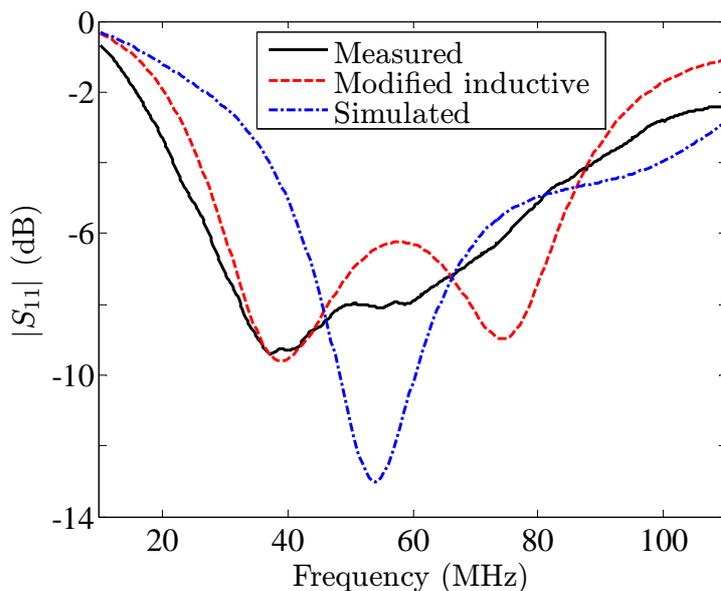
FIGURE 6.13: Comparison of the measured reflection coefficient with the simulation results. The modified simulation represents the reflection coefficient calculated after adding a series inductive reactance representing the unshielded Copper core. The thickness of rubber layer used was 9 cm.
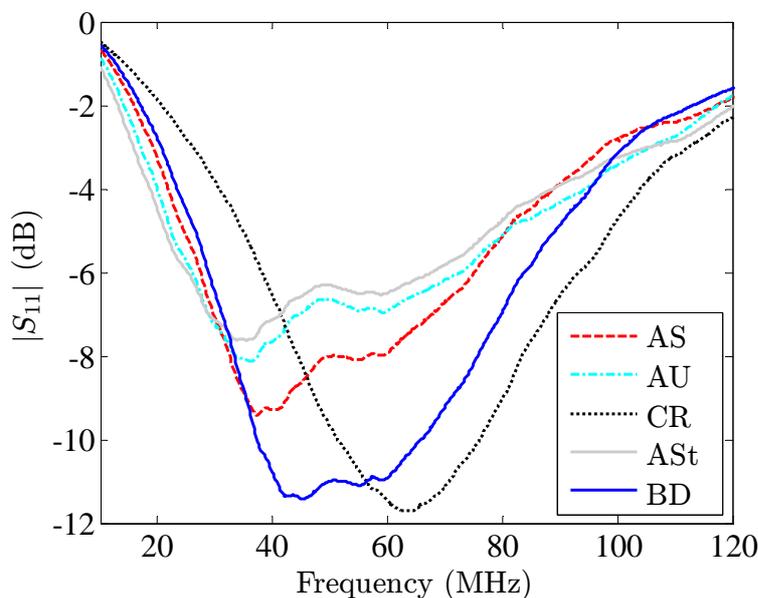
FIGURE 6.14: The measured reflection coefficient when the subject posed different postures. AS= arms by side, AU= arms raised up, CR= crouching, ASt= arms stretched out, and BD= bending down. The thickness of rubber layer used was 9 cm.

frequency shifts downwards as shown in the measurement results. The measured reflection coefficients for stretching the arms out and lifting them high are slightly different with the former case shifting the resonance frequency a little downwards. When the

subject crouched or bent down, the radiating length shortened; therefore, the resonance frequency shifted upwards. More interestingly, the reflection coefficient improved almost by 2 dB when crouching and bending down; this could be due to the increased surface area closer to the RF source.

Applying the human body as a transmitting antenna by coupling large RF power might not be ethical and also the power dissipated inside the human body might exceed the recommended limit. But, the human body can be used as a receiving monopole antenna for applications that involve low power electromagnetic fields or fields that are present in the environment. One such application is the use of the human body as a receiving antenna for RF energy harvesting. Currently, the interest in the area of RF energy harvesting is growing particularity in the field of self-sustained and autonomous sensor networks. Research focused on the ambient RF energy in the digital TV band because there is uninterrupted available broadcast power and also the antenna size required is relatively small. Several ambient RF energy surveys showed that the available power in the FM band is comparable or sometimes better than the available power in digital TV bands [85], [86], [87]. But the idea of designing an RF energy harvesting system in FM band has been abandoned for the primary reason that a larger antenna is required at this frequency band. By designing an optimal matching network, the human body might be used as antenna for RF energy harvesting in the FM band to power wearable or implanted antennas.

Another possible application of the human body as receiving antenna is in the area of far-field wireless power transfer to energize implants in the human body. As it known that the total axial current distribution in the human body, near the resonance frequency, has larger value close to the feet. It is also known that there is small amount of conductive tissue in the ankle; this implies that the current density in the vicinity of the ankle is very large compared to other parts of the body. The large current density at the ankle can be intercepted to power implants embedded in the lower legs. An implanted ferrite core toroidal transformer, in conjunction with a rectifying circuit, can be used to convert the RF current to a usable DC power. For such applications, the far-field power can be broadcasted from a source operating near the human body resonance frequency. The legal requirements of narrowband energy broadcasting can be met by employing the Industrial, Scientific and Medical (ISM) radio band at 40 MHz, which lies in the resonance frequency region of the human body.

6.5   Conclusion

In this paper, the human body as a cylindrical monopole antenna has been characterized by using the equivalent cylindrical antennas that were analysed using the three-term approximations. Theoretically, it was found out that the human body can be an efficient radiating antenna with theoretical radiation efficiency reaching up to 70 % for the frequency range of 90 - 100 MHz. But, the total efficiency deteriorates when the human body is coupled to a 50 Ω system due to impedance mismatch, which can be improved with the design of an optimal matching network. In practical scenario, the efficiency decreases further due to the losses in the ground and the small values of the parasitic impedance due to shoes. It was also found that the human body resonates between 40 - 60 MHz with the magnitude of the reflection coefficient not much affected with different postures. Measurement results showed that crouching and bending down improved the magnitude of the reflection coefficient by 2 dB. The human body as a monopole antenna can be used for applications that use low RF power, such as RF energy harvesting and far-field wireless power transfer.

Chapter 7

Analysis of the Human Body as an Antenna for Wireless Implant Communication

BEHAILU KIBRET, ASSEFA K TESHOME, AND DANIEL T H LAI

7.1 Abstract

Currently, the radio-frequency (RF) implant wireless communication is enabled by utilizing small antennas that radiate radio waves inside the human body. As an alternative technique for implant wireless communication, we propose to use the human body itself as an antenna by feeding an RF current into the tissues. In particular, this paper studies the scenario when the RF current is fed by a tiny toriodal inductor that is implanted and clamped around the tissues in the ankle. The frequency range of 1-70 MHz is considered, which includes the resonance frequency of the human body. Theoretical results, from applying small toroidal inductors, show that the system exhibits broadband characteristics with a maximum gain of -25 dB between 20 to 40 MHz, assuming an isotropic radiation from human body. However, for the case of the small toroidal inductors considered, the radiation resistance of the system is very small, which increases the power consumption. It is known that the radiation resistance can be further improved by choosing a magnetic core with high permeability and low loss, as well as, by optimizing the number of turns to reduce the parasitic capacitance and obtain a usable magnetizing inductance.

7.2 Introduction

The fast growth in the technology of wireless communication, low power microelectronics, and physiological sensors has enabled a new generation of wireless sensor networks for wearable computing devices based on the body area network (BAN) paradigm. BAN refers to the wireless communication of systems on, inside or in the immediate proximity of the human body [3]. Broadly, BAN devices are classified as wearable and implants. Currently, the wireless communication of implants with an external monitoring devices is enabled using magnetic induction or the radio-based Medical Implants Communications System (MICS) [24] that was later expanded and renamed to Medical Device Radiocommunications Service (MedRadio) by the Federal Communications Commission (FCC) [88].

The wireless implant communication using magnetic induction requires the external devices to be placed very close to or in contact with the surface of the body. Also, the communication efficiency is highly dependent on the orientation of the magnetic coils used. In addition to this, the commercially available implant devices, which employ

magnetic induction, usually operate in the low-MHz frequency range that requires large coils for efficient communication. At such frequency range, the magnetic link efficiency deteriorates if the implants are required to be smaller. However, recent studies found that an equivalently efficient magnetic link can be obtained by operating in the low GHz range and applying mm-sized coils [89, 90]. Moreover, the implant is usually powered by an external coil; thus, the implant cannot initiate communication [91].

In MedRadio, the frequency band 401-406 MHz is allocated for radio-frequency (RF) biomedical telemetry accommodating both implants and wearable medical devices. In addition to MedRadio, the Industrial, Scientific and Medical (ISM) bands have been used for wireless implant communications. The wireless implant communication in MedRadio or ISM bands employ high frequency radio waves that radiate from a miniaturized antenna embedded on the implants. The high frequency enables higher data-rate and antenna miniaturization; however, it also prompts a higher free-space path loss. Moreover, the human body is an unpredictable and hostile environment for high frequency radio-based communications. It causes high power consumption due to the power absorbed by tissues, impedance mismatch, and radiation pattern distortion [91].

Another technique that utilizes the conductive nature of the human body for implant-to-implant or implant-to-surface communication is galvanic coupling intra-body communication (IBC) [92, 93]. The transmitter in galvanic coupling IBC differentially applies a low-power and low frequency electric current using a pair of electrodes and the receiver detects the transmitted signal from the potential difference across a pair of receiver electrodes. This technique promises a low-power communication; however, it only allows a low data-rate applications since the operation frequency is lower than 1 MHz. Moreover, it does not allow a wireless communication between an implant and a receiver that is placed close to the body without making a contact.

As a bid to find an alternative wireless implant communication technique, in this paper, we explored the possibility of using the human body itself as antenna for implant wireless communication in the frequency range lower than 100 MHz. In particular, we considered the case when a toroidal inductor is clamped around a group of muscle fibers in the ankle in order to induce an electromotive force (emf) inside the body. It was hypothesised that the induced emf causes an RF current inside the body that dissipates in the tissues and also radiates out of the body using the human body as an antenna. Therefore,

the objective of this paper is exploring the feasibility of applying the radiated power to connect implants and external devices located in the proximity of the human body. Moreover, the same scenario was studied to analyse the amount of emf induced on the terminals of the implanted inductor when a human body is exposed to a vertically polarized electric field. This approach promises lower power consumption compared to higher frequency radio-wave based techniques, since the human body tissues absorbs less power as frequency decreases. It also promises the use of small size inductors when compared to the size required if the magnetic induction technique was employed at the same frequency range.

This study was motivated by our previous results on the characterization of the human body as a cylindrical monopole antenna [53]. From our previous study, for a human subject of height 1.76 m and weight 73 kg, we found out the human body behaves like a monopole antenna when fed on the foot, with a resonance frequency between 40-60 MHz depending on the posture of the body. We also found the human body behaved as a monopole antenna with a radiation efficiency reaching 70 % and a minimum reflection coefficient of -12 dB when it was coupled to a source of 50 Ω output impedance. This was supported by measurement and theoretical results. In addition to this, from the large number of RF dosimetry studies, such as [16], it is well known that the maximum axial RF current is induced near the foot when the human body is exposed to a vertically polarized electric field of frequency less 100 MHz. Thus, the maximum axial current near the foot causes a large axial current density in the ankle cross-section. This is because, in addition to the maximum axial current, the ankle cross-section has smaller mass of conductive tissues compared to other transverse cross-sections of the human body. Based on this context, this study aims to explore an implant wireless communication technique using a small implanted toriodal inductor as a means to collect or couple the induced axial current inside the ankle.

There are several studies in the literature that directly or indirectly support the validity of our proposed approach. For example, in a research undertaken by the US army in the 1970s [20], the human body was utilized as an antenna to transmit a radio signal that was coupled to the human body using a coil of wire wound around the chest. The study reported that a radio signal was transmitted for a distance of 1.5 km at 4.6 MHz from a 1 Watt transmitter. Though the transmitter power is high and the air-cored toroidal inductor was located on the chest, the underlying concept is similar to our

proposed approach. Moreover, in the area of RF dosimetry, there are several studies that strongly support our proposed concept. In these studies, similar to our proposed technique, toroidal inductors were used to measure the induced ankle current when the human body is exposed to electromagnetic fields. For example, in [94], the design and application of an ankle-worn RF current measuring device is discussed. The device uses a clamp-on and ferrite-cored toroidal inductor to measure the induced RF current in the ankle for the frequency range of 0.1-80 MHz. Similarly, in [95], an air-cored and ankle-worn toroidal inductor was used to measure the induced ankle current in the frequency range of 1-200 MHz. Additionally, in [96], a commercially available clamp-on current probe with a ferrite core was also utilized to measure induced ankle current.

In this study, the human body was represented by an equivalent cylindrical antenna. It is well known that the induced axial current inside a human body that is exposed to a vertically polarized plane wave has a similar axial distribution as that of a monopole cylindrical antenna [16]. Based on this, a practical equivalent monopole antenna was proposed to measure the induced ankle current in the human body [76]. It was also demonstrated that saline filled cylindrical antennas can be used to measure the induced ankle currents predicted based on finite-difference-finite-time (FDTD) computations using realistic voxel models of the human body [15]. Recently, the authors have successfully used the equivalent cylindrical antenna representation of the human body to characterize the human body as a monopole antenna [53], analyse the whole body averaged specific absorption rate (SAR) [74, 82] and investigate interference mechanism in Human Body Communications (HBC) [75].

The rest of the paper is organized as follows. Firstly, the axial current density calculated based on a realistic gray-scale image representation of the cross-section of the ankle joint is given, followed by the analytical expressions of the parameters of the toroidal inductor. Expressions for the gain of the system and the received power to a load connected to the terminals of the inductor are derived. Next, the scenarios of two toroidal inductors of different sizes are analyzed in order to understand the important factors that need to be considered in the design of such a system. Lastly, the results from a simple experiment using a saline filled cylinder are reported, that validates our proposed approach.
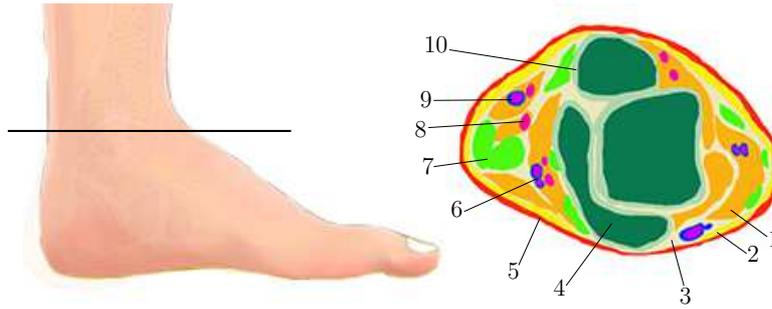
FIGURE 7.1: The cross-section of ankle joint with tissues assigned different colours. 1-muscle, 2-fat, 3-connective tissue, 4-cancellous bone, 5-skin, 6-blood vessel, 7-tendon, 8-nerve, 9-blood, 10-cortical bone.

7.3 The axial current density in the ankle

Since the cross-section of the ankle consists of different tissues, the axial current density is not uniformly distributed. The tissues have different dielectric properties; therefore, they interact differently to the axial RF electric field passing through them. Accordingly, we developed a model for the cross-section of the ankle based on a realistic anatomical atlas of the human body [97]. The tissues in the cross-section were assigned specific colours, as shown in Fig. 7.1; and from this, a grayscale image file was created that has specific intensity values for the pixels representing each tissues. The tissues that were classified in the cross-section were skin, muscle, fat, cortical bone, cancellous bone, blood vessel, blood, nerve, tendon, and connective tissues. Using the grayscale image, we had accurate representations of the size and location of the tissues; and it was also possible to read such information into computer programs. Moreover, the 4-Cole-Cole dispersions model was used to represent the dielectric properties of these tissues.

For the frequency range of interest, it was assumed that the axial electric field in the cross-section of the ankle is uniform. The total induced axial current I_z in the ankle, which includes both the conduction and displacement current in the cross-section of the ankle of area S, can be calculated from the axial current density distribution in the ankle J_z as

$$I_z = \int_S J_z ds = E_z \int_S \sigma_s^* ds \qquad (7.1)$$

where E_z is the axial electric field that is taken to be uniform and σ_s^* is the complex conductivity of 'points' in the cross-section. Considering the cross-section of the ankle

represented by the grayscale image, the expression in (7.1) can be approximated as

$$I_z \simeq 2E_z \sum_{m=1}^{M} \sigma_m^* A_{pixel} \tag{7.2}$$

where σ_m^* is the complex conductivity of the tissue represented by the mth grayscale pixel; M is the total number of pixels in the ankle cross-section and A_{pixel} is the area of a single pixel. A_{pixel} can be easily calculated by dividing the actual area of the ankle cross-section with M. Therefore, the axial current density J_z^n in the area represented by the nth pixel can be approximated as

$$J_z^n = \sigma_n^* E_z = \frac{0.5\sigma_n^* I_z}{A_{pixel} \sum\limits_{m=1}^{M} \sigma_m^*}. \tag{7.3}$$

Using (7.3), we can calculate the total axial current passing through any subsection of the ankle cross-section. Fig. 7.2 shows the magnitude of the axial current density calculated using (7.3) for an incident electric field $E_0 = 1$ V/m r.m.s. illuminating the adult male human subject that was discussed in our previous papers [53]. It can be seen that the highest current density occurred in the blood and muscle tissues, and the least occurring in the skin, fat, nerve, blood vessels, cortical bone and cancellous bone. Also, almost as much as half of the current density in the muscle tissue exists in the connective tissues and tendons.

7.4 The implanted toroidal inductor

In the preceding section, we showed that a large axial current density is induced inside the muscle tissue. In order to collect this current for the purpose of implant wireless communication, we propose to use a toroidal inductor that is clamped around a group of muscle fibers or a tendon in the ankle. We considered a toroid placed around the muscle tissue or tendons with the axis of toroid perpendicular to the cross-section of the ankle. Using such an arrangement, and with toroid thickness of several millimeters, it can be placed in the ankle without causing major tissue damage.

The mechanism of receiving the RF current flowing in the tissues that are encircled by the toroid is similar to the operation mechanism of current transformers. The RF
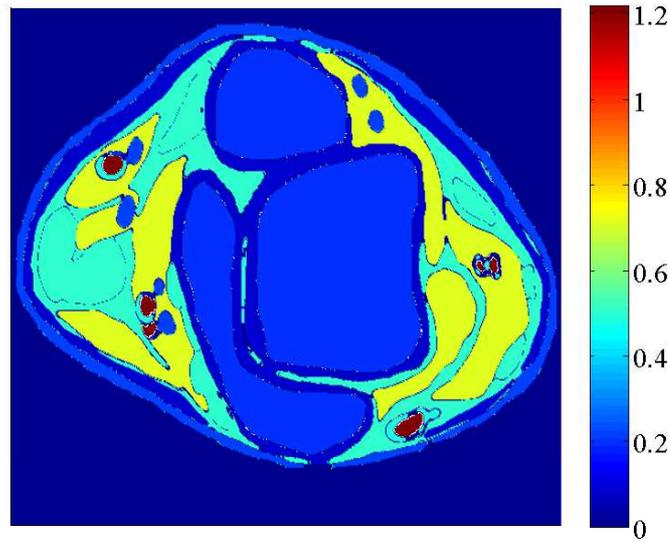
FIGURE 7.2: The magnitude of axial current density $|J_z^n|$ (A/m^2) in the cross-section of the ankle joint for an incident electric field $E_0 = 1$ V/m r.m.s and the total cross-section area of the ankle was taken as 0.0154 m^2.

current in the tissues induces a magnetic field inside the core of the toroid, in our case, which is assumed to be a ferrite core. The magnetic field in turn induces electromotive force on the copper winding that drives a current into the receiver load connected to its terminals.

The toroid has inner radius r_1, outer radius r_2, and height h_t, as shown in Fig.7.3. An enameled round copper wire of radius r_{cop} is wound around a ferrite core making N number of turns. In order to reduce the effect of leakage inductance, the inner wall of the toroid is completely covered by the copper windings. Thus, the number of turns was derived as

$$N \simeq \frac{\pi r_1}{r_{cop} + t_e} \tag{7.4}$$

where t_e is the thickness of the enamel layer of the copper wire. Also, the equivalent circuit representation of the toroid is shown in Fig. 7.4.

7.4.1 Magnetic core effects

It is well known that ferromagnetic materials dissipate power, due to magnetic hysteresis and eddy currents, when they are introduced into a changing magnetic field [98]. The eddy current loss can be reduced by using a laminated magnetic core that has high
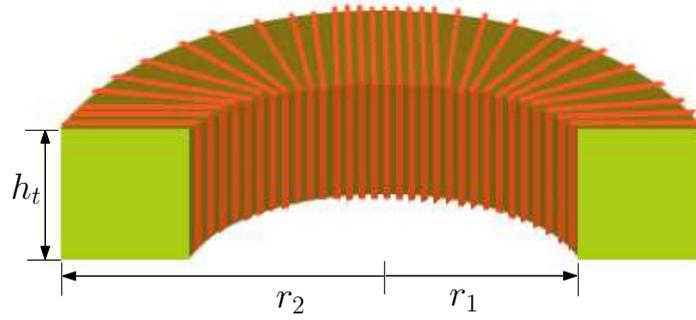
FIGURE 7.3: The half-section of the implanted toroidal inductor with ferrite core.
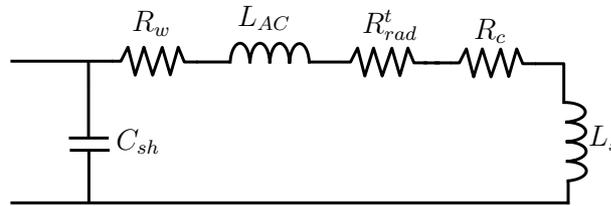
FIGURE 7.4: The equivalent circuit of the toroidal inductor. C_{sh} is the parasitic capacitance between turns; R_w represents the loss in winding wire; L_{AC} is the internal inductance of the wire; R_{rad}^t is the radiation resistance of the toroid; R_c represents the magnetic core loss; and L_s is the self-inductance.

electrical resistivity. The effect of hysteresis can be characterized by using the complex relative permeability μ^* of the magnetic core. The complex relative permeability is defined as

$$\mu^* = \mu' - j\mu'' \tag{7.5}$$

where μ' characterizes the stored energy and μ'' characterizes the power dissipated. The frequency characteristics of ferrites can be expressed using a theoretical dispersion model that includes magnetizing mechanisms, such as, domain-wall motion, magnetization rotation, and gyromagnetic spin rotation. Such a dispersion model is given in [99] as

$$\mu' = 1 + \frac{K_{spin}(f_{spin}^{res})^2}{(f_{spin}^{res})^2 + f^2} + \frac{K_{dw}(f_{spin}^{res})^2 \left[(f_{spin}^{res})^2 - f^2\right]}{\left[(f_{spin}^{res})^2 - f^2\right]^2 + \beta^2 f^2}, \tag{7.6}$$

$$\mu'' = \frac{K_{spin}f_{spin}^{res}f}{(f_{spin}^{res})^2 + f^2} + \frac{K_{dw}(f_{spin}^{res})^2 \beta f}{\left[(f_{spin}^{res})^2 - f^2\right]^2 + \beta^2 f^2} \tag{7.7}$$

where f is the operating frequency, K_{spin} is the static spin susceptibility; f_{spin}^{res} is the spin resonance frequency; K_{dw} is the static susceptibility of domain wall motion; f_{dw}^{res} is the domain wall resonance frequency; β is the damping factor of the domain wall motion.

In this study, it was assumed that the magnetic core used is a ferrite tape ESL 40012 that is manufactured using the Low Temperature Co-fired Ceramic (LTCC) processing and it is considered suitable for low power applications. The values of the coefficients in (7.6) and (7.7) for the initial complex permittivity of the ferrite tape ESL 40012 at 25 C° are given in [99] that were obtained by curve fitting experimental data.

From the conventional approach of calculating the inductance of a toroidal inductor [98], the core lose resistance R_c and self-inductance L_s can be calculated by replacing the relative permeability of the core with the complex relative permeability $\mu^* = \mu' - j\mu''$. Thus, for the inductor shown in Fig. 7.3,

$$L_s = \frac{N^2 \mu' \mu_0 h_t}{2\pi} \ln\left(\frac{r_2}{r_1}\right) \tag{7.8}$$

and

$$R_c = \omega \frac{\mu''}{\mu'} L_s \tag{7.9}$$

where ω is the radial frequency.

7.4.2 The skin-effect and proximity-effect in the copper winding

It is well known that, at high frequency, the effective resistance of copper wire increases due to the skin-effect phenomenon. For the case of inductors, the copper windings are placed close to each other; therefore, the magnetic field created due to the changing current in one conductor affects the current distribution in the neighbouring conductors, causing the proximity effect phenomenon. Thus, for RF inductors, the skin-effect as well as the proximity effect cause power loss in the winding conductor.

An analytic approximation for the AC resistance R_w of a round copper wire of conductivity σ in a single-layer winding inductor is given in [100] as

$$R_w = R_{dc} \upsilon \frac{e^{2\upsilon} - e^{-2\upsilon} + 2\sin(2\upsilon)}{e^{2\upsilon} + e^{-2\upsilon} - 2\cos(2\upsilon)} \tag{7.10}$$

where R_{dc} is the DC resistance defined as

$$R_{dc} = \frac{2N(h_t + r_2 - r_1)}{\sigma \pi r_{cop}^2}; \tag{7.11}$$

and

$$v = \left(\frac{\pi}{4}\right)^{\frac{3}{4}} 2r_{cop} \sqrt{\frac{r_{cop}}{r_{cop} + t_e}} \pi \sigma \mu_0 f. \tag{7.12}$$

The internal inductance of the wire was also expressed as

$$L_{AC} = R_{dc} \frac{v}{\omega} \frac{e^{2v} - e^{-2v} - 2\sin(2v)}{e^{2v} + e^{-2v} - 2\cos(2v)}. \tag{7.13}$$

7.4.3 The parasitic capacitance of the inductor

Another important factor in the high frequency application of inductors is the parasitic capacitance between turns. The parasitic capacitance determines the self-resonance frequency of the inductor; beyond this frequency the reactance of the inductor gets capacitive. The parasitic capacitance shunts the magnetizing current so that it causes a reduction in the performance of inductors. For a single layer inductor of N turns, the lumped parasitic capacitance referred to the terminals of the inductor was approximated in [101] as

$$C_{sh} = 2.732\epsilon_0 N(h_t + r_2 - r_1) \left[\epsilon_r \theta^* \left(\ln \frac{r_{cop} + t_e}{r_{cop}}\right)^{-1} + \cot\left(\frac{\theta^*}{2}\right) - \cot\left(\frac{\pi}{12}\right)\right] \tag{7.14}$$

where ϵ_r is the relative permittivity of the enamel layer and θ^* is defined as

$$\theta^* = \cos^{-1}\left(1 - \frac{1}{\epsilon_r} \ln \frac{r_{cop} + t_e}{r_{cop}}\right). \tag{7.15}$$

7.5 The Performance of the whole System

7.5.1 In transmission mode

The equivalent circuit of the ankle implant in transmission mode was approximated as shown in Fig. 7.5. As a loop antenna, a toroidal inductor by itself has poor radiation efficiency [61]; therefore, we ignored its radiation resistance R^t_{rad}. The operation of the system is similar to that of a current transformer; the toroid acts like the primary winding while the human body was approximated as a single turn secondary, as shown in Fig. 7.6. The representation of the human body as a single turn secondary describes more
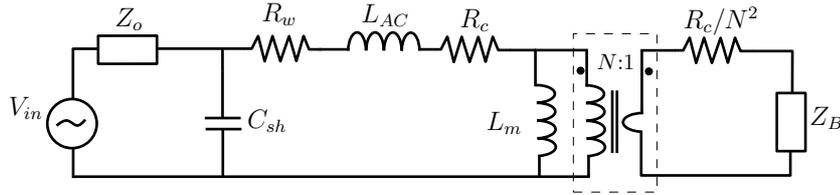
FIGURE 7.5: The equivalent circuit of the implanted toroidal inductor. V_{in} is the input voltage of the transmitter; Z_o is the output impedance of the transmitter; L_m is the magnetising inductance referred to the primary side; and Z_B is the impedance representing the effect of the human body and the surrounding.
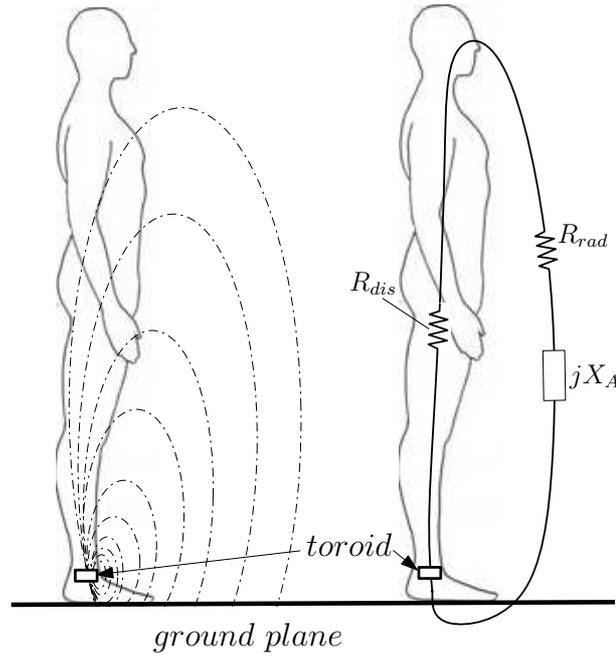
FIGURE 7.6: Visualisation of the lines of force in the human body forming the secondary loop, which is represented by the human antenna impedance, $Z_A = R_{rad} + R_{dis} + jX_A$, where R_{rad} characterizes the power radiated P_{rad} ; R_{dis} characterizes the power dissipated inside the human body due to ohmic and dielectric loss of tissues; and X_A characterizes the near-field reactive power oscillating in the vicinity of the human body.

accurately a toroidal inductor clamped to the exterior of the ankle. The approximation of this setup to an implanted toroidal inductor is based on the result from (7.3) that large axial current density exists in the muscle tissue which spans about 20% of the ankle joint cross-sectional area.

In Fig 7.5, Z_B is the sum of the impedances that represent the effects of the human body, the shoes, the ground and near-field coupling with nearby objects. Assuming the human subject is standing on a highly conductive ground plane and bare foot, Z_B can be approximated by the human body antenna impedance Z_A, which is expressed in [53].
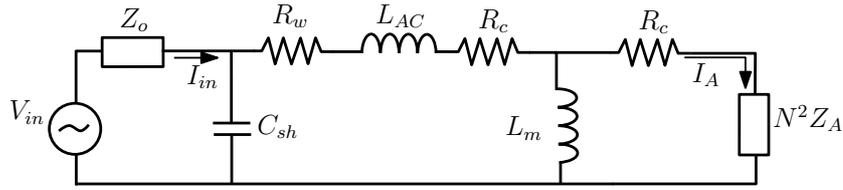
FIGURE 7.7: The simplified equivalent circuit of the implanted toroidal inductor in transmitting mode.

In our previous study [53], the human body was represented by a cylindrical monopole antenna to express the axial current inside the human body when it is excited by an RF source on the foot. Hence, Z_A is the antenna impedance of the human body when the human subject is excited by a delta-gap electromotive force (emf) placed between the feet and the ground. The delta-gap emf was assumed to be equal to the emf induced by the implanted inductor, which is approximated by a current-probe feeding model.

Based on the analysis in [53], Z_A can be expanded as

$$Z_A = R_{rad} + R_{dis} + jX_A \tag{7.16}$$

where R_{rad} characterizes the power radiated P_{rad} ; R_{dis} characterizes the power dissipated inside the human body due to ohmic and dielectric loss of tissues; and X_A characterizes the near-field reactive power oscillating in the vicinity of the human body. From the expression of the resistance per unit length of the equivalent cylindrical antenna and from the definition of the radiation efficiency in [53], the expression of R_{rad} and R_{dis} can be derived.

The circuit in Fig. 7.5 can be simplified by transferring the secondary impedance to the primary as shown in Fig. 7.7. Since we assumed that the winding completely covers the inner wall of the toroid, the magnetising inductance L_m was approximated by the self-inductance L_s of the toroid. The equivalent impedance seen by the transmitter Z_{eq} can be written as

$$Z_{eq} = \frac{Z_s}{j\omega C_{sh} Z_s + 1} \tag{7.17}$$

where

$$Z_s = \frac{j\omega L_m \left(N^2 Z_A + R_c\right)}{j\omega L_m + N^2 Z_A + R_c} + R_c + R_w + j\omega L_{\text{AC}}. \tag{7.18}$$

Therefore, referring Fig. 7.7, the radiation efficiency of the system η_r^t defined as the ratio of the radiated power P_{rad} to the input power P_{in} can be written as

$$\eta_r^t = \frac{P_{rad}}{P_{in}} = \frac{|I_A|^2 N^2 R_{rad}}{|I_{in}|^2 \operatorname{Re}(Z_{eq})} = F \frac{N^2 R_{rad}}{\operatorname{Re}(Z_{eq})} \tag{7.19}$$

where the factor F can be written as

$$F = \left| \frac{j\omega L_m}{(j\omega C_{sh} Z_s + 1)(R_c + N^2 Z_A + j\omega L_m)} \right|^2. \tag{7.20}$$

Moreover, Z_{eq} can be expanded as

$$Z_{eq} = R_{rad}^s + R_{dis}^s + jX^s \tag{7.21}$$

where R_{rad}^s characterizes the radiated power from the system; R_{dis}^s characterizes the power dissipated in the wire, the magnetic core and the human body; and X^s characterizes the power oscillating in the parasitic capacitance and in the near-field of the human body. From (7.19) and (7.20), the system radiation resistance can be derived as

$$R_{rad}^s = FN^2 R_{rad}. \tag{7.22}$$

The radiated power escapes into the surrounding using the human body as antenna. For simplicity, assuming the radiated power was emitted equally in all directions, the antenna gain of the system G can be approximated as

$$G(dB) = 10 \log_{10}(\eta_t). \tag{7.23}$$

In our previous study [53], the human body was represented by a monopole antenna based on measured and calculated values of the reflection coefficient and the radiation efficiency of the human body antenna. The definition of the gain of the human body antenna requires the knowledge of the directivity or radiation pattern; therefore, the gain in the direction of the maximum emission can be approximated by that of a quarter-wave monopole antenna by adding 5.19 dBi to the value obtained from (7.23).
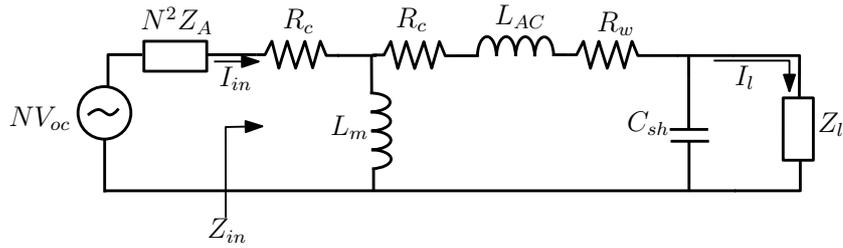
FIGURE 7.8: The simplified equivalent circuit of the implanted toroidal inductor in receiving mode. V_{oc} is the open-circuit voltage driving the current through the area enclosed by the toroid and Z_L is impedance of the load connected to the terminals of the toroid.

7.5.2 In reception mode

When a vertically polarized incident electric field impinges the human body, an axial current density is induced inside the cross-section of the ankle. From antenna theory, it is well known that an antenna in receiving mode can be represented by a Thevenin's equivalent circuit with a voltage source V_{oc} that is calculated by multiplying the short circuit current at the antenna terminals and the antenna impedance. Thus, assuming the human subject is standing bare foot on a conductive ground, V_{oc} can be written as

$$V_{oc} = I_z(0) Z_A \tag{7.24}$$

where $I_z(0)$ the axial foot current expressed in [53]. Therefore, the whole system in receiving mode was represented by the simplified equivalent circuit shown in Fig. 7.8.

For an incident electric field E_0 on the surface of the human body, the current $I_z(0)$ is defined in [53] as

$$I_z(0) = \frac{E_0}{k_2} u(0) \tag{7.25}$$

where $u(0)$ is a function of the parameters of the equivalent cylindrical antenna. Thus, the power delivered to the load P_{rec} can be calculated as

$$P_{rec} = 0.5 \left| I_l \right|^2 \mathrm{Re}\left(Z_l \right). \tag{7.26}$$

Using the relation between the incident electric field and the EIRP (equivalent isotropically radiated power) of a radiation source at a distance of d, $E_0 = \frac{\sqrt{60EIRP}}{d}$, and for a

free-space wavelength λ, the expression in (7.26) can written as

$$P_{rec} = 120 \left(\frac{\lambda}{4\pi d} \right)^2 EIRP \, |u(0)|^2 \, F_R \text{Re} \, (Z_l) \tag{7.27}$$

where

$$F_R = \left| \frac{j\omega N L_m Z_A}{(N^2 Z_A + Z_{in}) (j\omega L_m + Z_p) (j\omega C_{sh} Z_l + 1)} \right|^2 \tag{7.28}$$

$$Z_p = R_c + R_w + j\omega L_{\text{AC}} + \frac{Z_l}{j\omega C_{sh} Z_l + 1} \tag{7.29}$$

$$Z_{in} = R_c + \frac{j\omega L_m Z_p}{Z_p + j\omega L_m}. \tag{7.30}$$

Therefore, for a given radiation source at a distance d and with a known EIRP, the power received at the terminals of the toroidal inductor P_{rec} in dBm can be written as

$$P_{rec}(dBm) = 20.79 + EIRP(dBm) + 20 \log_{10} \left(\frac{\lambda}{4\pi d} \right)$$

$$+ 10 \log_{10} \left[F_R \text{Re} \, (Z_l) \right] + 20 \log_{10} \left[|u(0)| \right], \tag{7.31}$$

which is used to assess the received power in the illustrative scenario of the next section.

7.6 An Illustrative scenario

Considering the scenario of two implanted toroidal inductors with parameters shown in Table 7.1, the gain G calculated is shown in Fig. 7.9. As can be seen in the table, the two toroids have a core thickness $r_2 - r_1$ of 3 mm and a height h_t of 1 cm. The areas enclosed by the toroids are 0.64 % and 2.16 % of the cross-sectional area of the ankle joint considered in this study, which is indicated by the parameter $A\%$ in the table. The copper wire used was assumed to be 20 AWG (American Wire Gauge) copper wire with enamel thickness of $0.25r_1$. It can be seen that the gain exhibits a broadband feature with the maximum occurring between 20 - 45 MHz, which includes the resonance frequency of the human body. The resonance frequency of the human subject used for

TABLE 7.1: Parameters of the system

Parameters	Case1	Case2
r_1	6.59 mm	11.28 mm
r_2	9.59 mm	14.292 mm
h_t	1 cm	1 cm
d	$\lambda/2\pi$	$\lambda/2\pi$
r_{cop}	0.4 mm	0.4 mm
t_e	0.1 mm	0.1 mm
N	41	70
σ	5.592×10^7 Sm^{-1}	5.592×10^7 Sm^{-1}
H_m	1.76 m	1.76 m
m	73 kg	73 kg
$A\%$	0.64 %	2.16 %
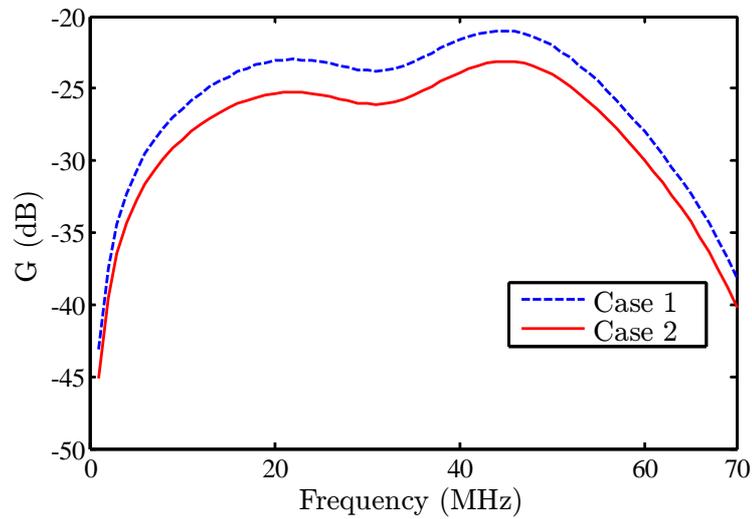
FIGURE 7.9: The calculated gain for the two cases.

the two scenarios, which has height H_m and weight m given in Table 7.1, is near 40 MHz [53, 82].

The gain calculated using (7.23) and shown in Fig. 7.9 was based on the assumption that only the human body impedance affect the current induced inside the human body. But, in reality, other factors, such as, the ground, shoes and nearby objects, affect the gain. When the impedance of 1 cm thick rubber shoes was added in series with the human body impedance Z_A, the calculated gain decreased by a maximum of 5 dB.

The given scenario can be further analysed by assuming an input current $|I_{in}|$ of constant magnitude. It was found that more than 99.5 % of the input current was shunted by the
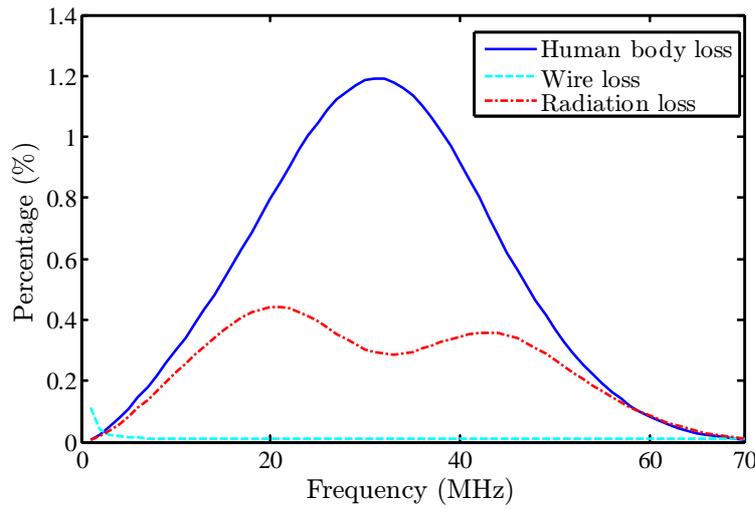
FIGURE 7.10: The power loss percentage in the human body, the wire and the radiated power.

parasitic capacitance, returning to the input terminal. The rest of the current dissipates power on the wire, the magnetic core, the human body, and also contributes to the radiated power. It was also found that more than 98.5 % of the power was dissipated inside the magnetic core and a maximum of 1 % of the power was absorbed inside the human body, with a negligible amount dissipating inside the wire, as shown in Fig. 7.10. Moreover, the radiated power was less than 0.5 %. This suggests that the two important factors that determine the performance of the toroid are the parasitic capacitance and the magnetic core losses. Reducing the effect of the parasitic capacitance as well as the magnetic core losses improve the efficiency of the system.

The magnetic core resistances R_c calculated for the two toroids is shown in Fig. 7.11. As shown in the figure, the value of this resistance is very large. The eddy currents induced inside the human body, due to the magnetic field inside the core, produce a magnetic flux that counteracts the original flux. In doing so, the eddy currents introduce additional loss in the magnetic core due to magnetic hysteresis, which otherwise would have been dissipated inside the body or radiated.

From (7.9), the expression of R_c can be rewritten as

$$R_c = \omega \mu'' \mu_0 N^2 h_t \ln \left(\frac{r_2}{r_1} \right). \tag{7.32}$$

From the above equation, it can be seen that the value of R_c is affected by the magnetic
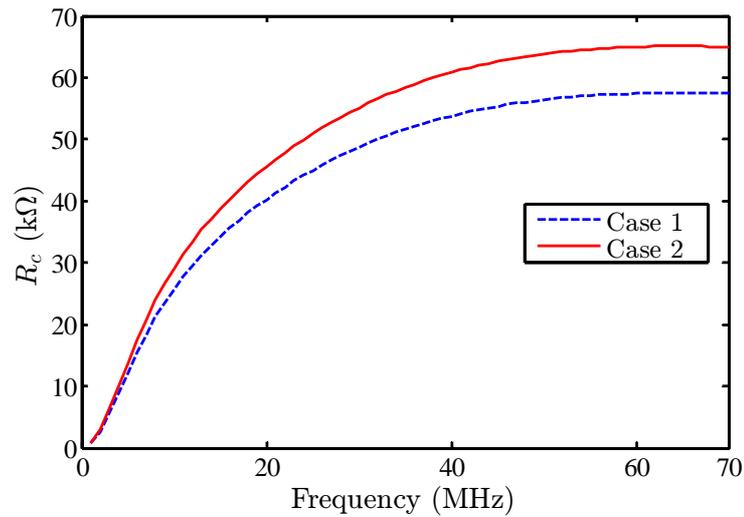
FIGURE 7.11: The magnetic core resistance R_c for the two cases. The toroid in Case 1 is smaller than that of Case 2.
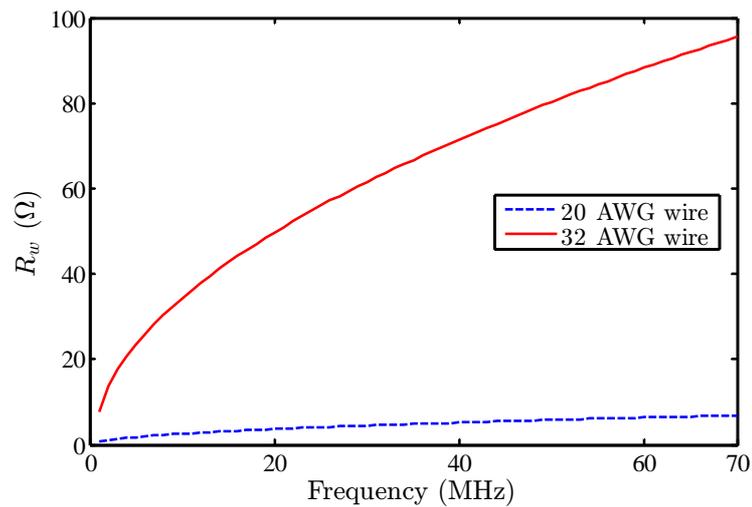
FIGURE 7.12: The wire resistance R_w for the case of two different wires of radius 0.1 mm (32 AWG) and 0.4 mm (20 AWG).

core material, the geometry of the toroid, number of turns, and frequency. Therefore, the magnetic core loss can be minimised by choosing a material that introduces less magnetic hysteresis and using a toroid that has less outer to inner radius ratio $\frac{r_2}{r_1}$ and less number of turns. As these parameters also determine the value of the self-inductance, which determines the emf induced in the human body, an optimization should be carried out to get a desirable value of the self-inductance.

The winding wire resistance introduces losses due to skin-effect and proximity-effect; but the value of this power loss is negligible when compared to other losses. This is because
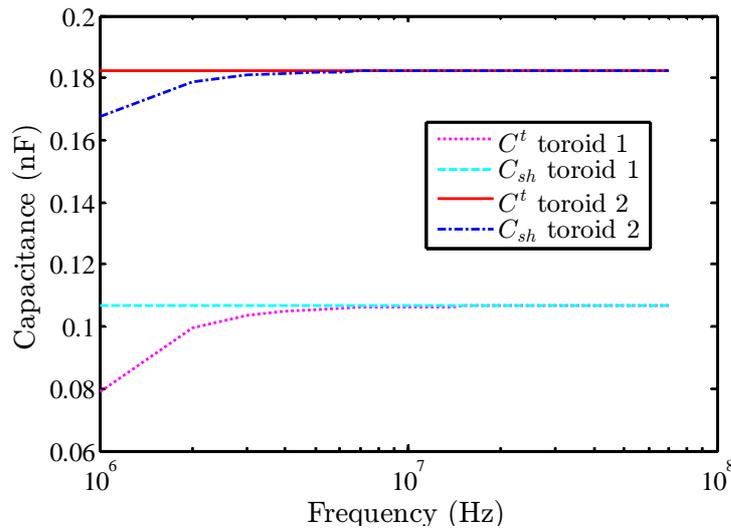
FIGURE 7.13: The parasitic capacitance C_{sh} and the equivalent capacitance C^t of the two cases.

the resistance due to the wire R_w is much smaller compared to R_c. Fig. 7.12 shows the calculated wire resistance R_w for 20 AWG and 32 AWG wires that have radius of 0.4 mm and 0.1 mm, respectively. The thinner wire caused a power loss of 10 dB higher than the thicker one; but in both cases, the power loss ratio due to the wire is negligible. The overall dissipated power in the case of the thinner wire is lower by almost 8 dB. This is because the number of turns N increases when the radius of the wire decreases in order to get a reduced leakage inductance.

From the calculation of the equivalent impedance Z_{eq} in (7.17), the parallel reactance due to the parasitic capacitance is much smaller than Z_s; therefore, only a very small fraction of the total current is used to setup the magnetic flux that is necessary to induce an emf in the body. The self-resonance frequency of the toroid is much less than the frequency range of interest; thus, the inductor acted like a capacitor. Fig. 7.13 shows the comparison of the parasitic capacitance C_{sh} and the equivalent series capacitance C^t of Z_{eq}, which shows that the reactance of Z_{eq} is dominated by C_{sh}. The design of a more efficient system requires the reduction of the parasitic capacitance. One way of reducing this capacitance is by increasing the separation of turns in the inductor. But this approach also introduces a leakage inductance that does not contribute to the axial current induced inside the enclosed tissue. For example, from Fig. 7.9, toroid 1 has a better gain than toroid 2, even though toroid 1 is smaller than toroid 2. This is because the number of turns in toroid 2 is larger than that of toroid 1, which increased
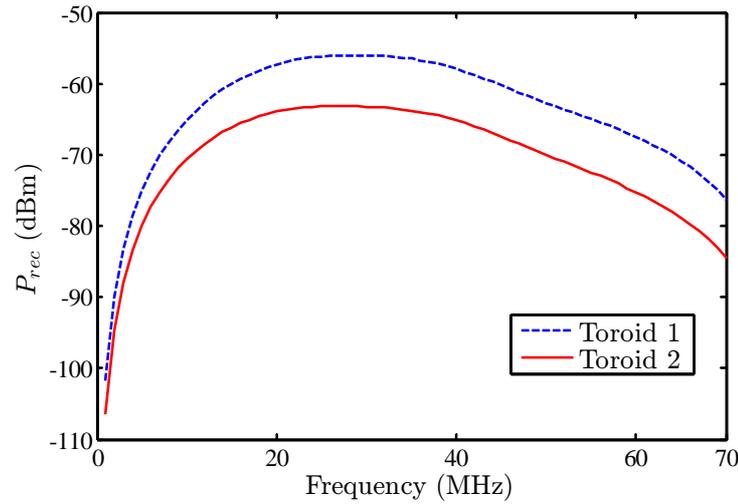
FIGURE 7.14: The calculated received power P_{rec} for the two cases for a source of 0 dBm EIRP located at a distance of $d = \lambda/2\pi$ m.

the parasitic capacitance. This suggests that a toroid that has a minimised leakage inductance and with smaller number of turns has a better performance than a toroid with larger number of turns. Therefore, the design of an efficient system calls for an optimized choice of the smallest number of turns that result in a reduced leakage inductance. In addition to this, in receiving mode, another important factor that puts a challenge when minimising the size of the toroid is: the current density inside the enclosed tissue area also decreases causing less magnetic flux induced inside the core.

Since the real part of the equivalent impedance $(R_{rad}^t + R_{dis}^t)$ is very small, the input current required to cause a usable radiated power is very large; this puts a challenge on low power requirements of implants that run on batteries. For example, at 40 MHz, for an input current $I_{in} = 10$ mA into toroid 1, the total radiated power from the body is about -80 dBm that falls down to -86 dBm at a distance of 2 m due to free space path loss, assuming isotropic radiation. Even though, the input power for this case is much smaller, about -55 dBm, the large input current might drain batteries quicker. Therefore, it is crucial to minimise the parasitic capacitance, which has the effect of increasing the real part of the Z_{eq}.

Assuming a transmitter of $EIRP = 0$ dBm is located a distance of $d = \frac{\lambda}{2\pi}$ from the body, the power received P_{rec} (7.31) on the load impedance $Z_L = 50$ Ω that is connected to the terminals of both inductors is shown in Fig. 7.14. As the received power is a function of the gain, the received power for toroid 1 is larger than that of toroid 2.

7.7 Validation

To show the validity of our proposed approach, we carried out a simple experiment using a saline-filled cylindrical antenna as a human body phantom. The idea is based on some studies, which demonstrated that saline-filled cylindrical antennas can be used to represent the human body in order to measure the induced foot current [15]. For our experiment, a transparent vinyl cylinder of height 1.2 m and diameter of 3 cm, with a conductive plate base, was used as shown in Fig. 7.15. A ferrite-core toriodal inductor of number of turns 36, height 1 cm and, inner diameter 1 cm and outer diameter of 2.8 cm, was inserted at the base of the cylinder leaving a 1 cm gap from the conductive plate. The inductor was connected to a battery powered Vector Network Analyzer (VNA) capable of sweeping 0.1-200 MHz via a 5 cm coaxial cable. The VNA was connected to the computer via bluetooth so the effect of measuring cables was eliminated. The reflection coefficient was measured, which agrees with our theoretical result that the parasitic capacitance shunts most of the current. Fig. 7.16 shows the measured reflection coefficient indicating about 85% of the current is reflected back, which agrees reasonably to the theoretical example discussed previously with 99% of the current shunted by the parasitic capacitance. It should be noted that the inductor considered for the theoretical case is much smaller. In practical design, the reflection coefficient can be improved by employing proper impedance matching to eliminate the large reactance. Also, the reflection coefficient can be improved by using a high quality magnetic core material and with optimized design of the inductor, which increases the radiation resistance. Additionally, in order to see the validity of our experiment, we also measured the impedance of the toroid to see the location of the self-resonance frequency. For the size of the toroid we used, the self-resonance frequency is expected to occur in the kHz range; the measured impedance in Fig. 7.17 supports this.

In the literature, a similar experiment applying a ferrite-cored toroidal inductor to induce RF current in a sea-water stream monopole antenna is reported in [102]. Also, a recent study [103] carried out similar experiments that used sea-water filled cylinder and a jet of sea-water pumped vertically into the air.
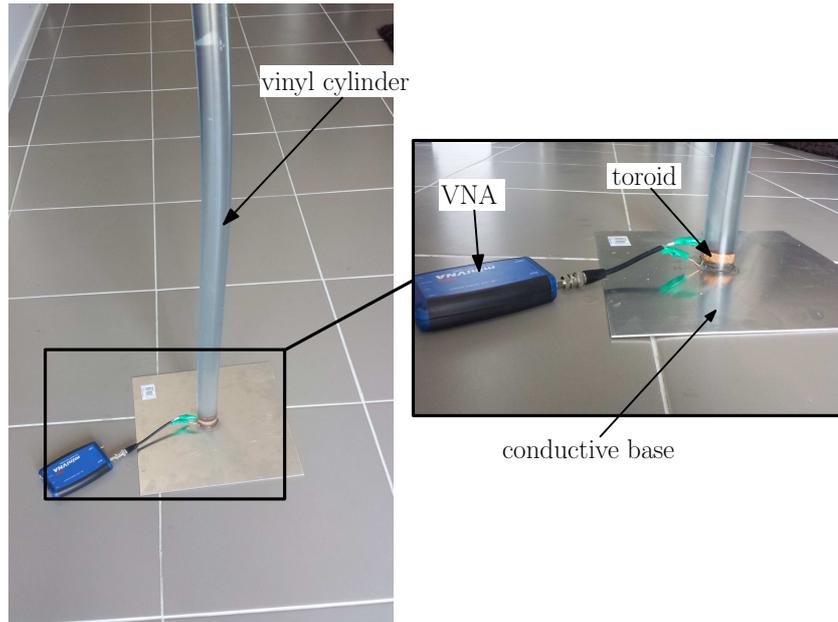
FIGURE 7.15: The experimental setup.
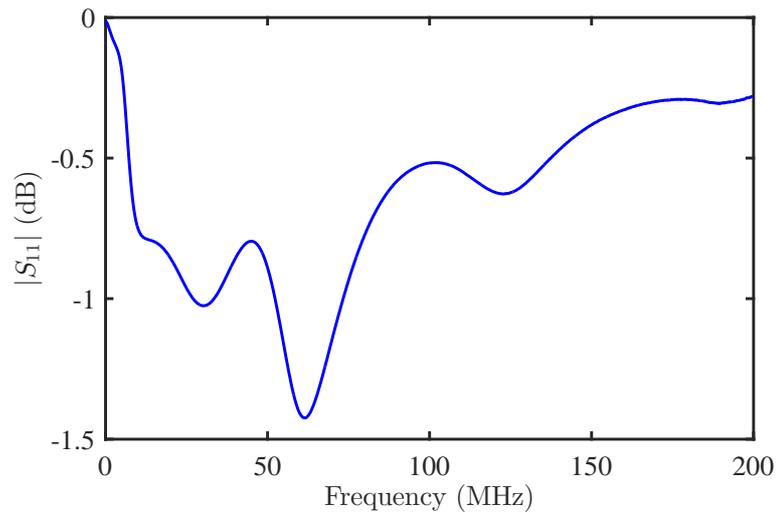
FIGURE 7.16: The measured reflection coefficient.

7.8 Remarks

The frequency range studied here aligns with the ISM radio bands at center frequency of 27.12 and 40.68 MHz, which are inside the range of frequency where the maximum gain occurs. The bandwidth allocated for the 40.68 MHz ISM band is about 100 kHz, which might be suitable for transmitting low bit rate biomedical signals that do not require a small duty cycle. The other ISM band at 27.12 MHz has relatively wider bandwidth, about 300 kHz. Another additional advantage of these bands is the maximum EIRP
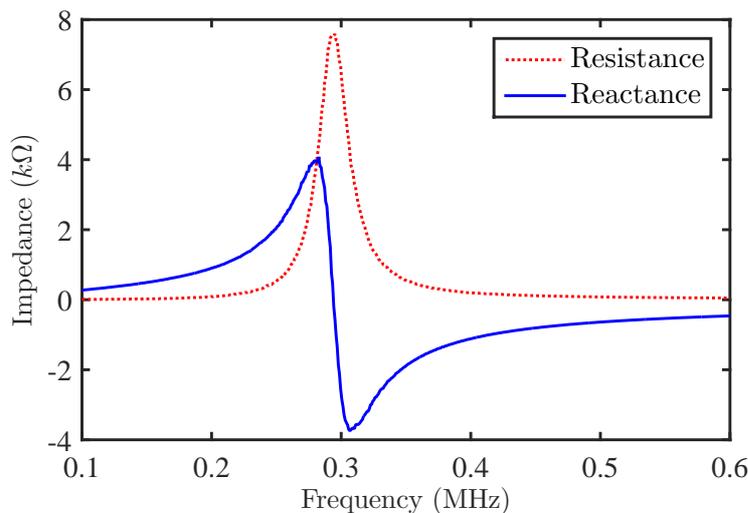
FIGURE 7.17: The measured impedance of the toroidal inductor.

allowed is relatively higher, for example, 1 W in Australia [104]. This suggests that the both ISM bands can be suitable to transmit signals downlink, from a transmitter located outside the body to an implant. Another important aspect of the frequency range used is it aligns with the frequency range of operation of human body communication (HBC) [38, 93], which is a technique that uses the human body as part of the communication channel. Thus, the wireless implant communication technique proposed can be used in conjunction with HBC, expanding the potential applications of body area networks.

Taking the gain in Case 1 at 40 MHz and taking a similar analysis as ITU-R SA 1346 [105], the performance of the system in a practical scenario is assessed. Assuming an input power of -2 dBm, the receiver located at a distance of $\lambda/2\pi = 1.2$ m that causes a free-space path loss of -6 dB, a fade margin and excess loss of -25 dB similar to the one given in ITU-R SA 1346, a radiation pattern of the human body similar to a quarter-wave monopole antenna that increases the gain by 5.16 dB, required signal-to-noise ratio (SNR) at the receiver is 14 dB, receiver antenna gain of 5.16 dBi, the power received at the receiver is -57 dBm. The received power is much larger than required for practical application. When the receiver is placed at a distance of 2 m, the free-space path loss is about -10 dB, which is much lower compared to the -30 dB loss in MedRadio at the same distance.

The amount of power dissipated inside the human body is approximately 1 % of the total dissipated power, as discussed earlier. For example, for an input current of 1 mA, at 40 MHz, the power dissipated inside the human body is close to -100 dBm.

This shows that current induced inside the human body from an implanted inductor for the purpose of low power wireless communication is less likely to cause harm. For the frequency range of interest, ICNIRP puts a whole-body averaged specific absorbtion rate of limit (WBA-SAR) of 0.4 W/kg for occupational exposure [22], which is much larger compared to the power levels calculated in this paper. Even considering the local SAR limit of ICNIRP, which is 10 Wkg^{-1}, the power dissipated inside the human body would be much smaller when considering a low power application of the proposed technique. For an input current of 1 mA, at 40 MHz, the power dissipated inside the magnetic core is approximately -77 dBm, which is too small to cause a significant temperature rise in the magnetic core.

7.9 Conclusion

A novel wireless implant communication technique using the human body as an antenna was investigated for the frequency range of 1-70 MHz when a ferrite-core toroidal inductor at the cross-section of the ankle is used to excite emf inside the human body. The case of using a similar inductor to receive the induced axial current at the cross-section of the ankle when the human body is exposed to plane electromagnetic wave was also explored. When using small inductors of size less than 2% of the cross-section of the ankle joint, a maximum isotropic gain of -25 dB was calculated for the frequency range of 20-40 MHz. It was also found that the parasitic capacitance and the magnetic properties of the core of the inductor are crucial in determining the radiation resistance of the system. The system is potentially feasible by reducing the parasitic capacitance and the loss due to the magnetic core. This can be done by choosing a magnetic material that has high permeability as well as low loss. Moreover, the number of turns of the inductor should be optimized in order to get low parasitic capacitance and usable magnetizing inductance.

Chapter 8

Conclusion and Future Works

8.1 Conclusion

In this thesis, the characteristics of the human body as an antenna were investigated and the results were applied to Human Body Communication and radio-frequency radiation dosimetry. Human Body Communication (HBC) is a wireless communication technique, applied to Body Area Networks, that uses the human body as part of the communication channel to connect wearable electronic devices. Radio-frequency (RF) radiation dosimetry is the science of quantifying the amount of absorbed RF radiation power inside the human body when it is exposed to RF electromagnetic fields. In addition to applying the human body antenna characteristics in HBC and RF dosimetry to analyse and interpret measured and computed results, the derived knowledge was studied with the objective of applying the human body antenna in wireless implant communication.

Broadly, HBC is classified as galvanic coupled and capacitive coupled HBC. In galvanic coupled HBC, low frequency electric current ($\leq$ 10 MHz) is applied differentially to the body using two electrodes; and the applied signal is detected from the potential difference between two electrodes on the receiver. In capacitive coupled HBC, a higher frequency signal ($\leq$ 150 MHz) is coupled to the body using a single electrode attached or placed close to the surface of the body with the transmitter circuit ground-plane acting as the ground electrode. The signals in capacitive coupled HBC are detected from the potential difference established between either two surface electrodes or a single electrode and the receiver circuit ground-plane. Due to the arrangement of the electrodes and the

higher frequency in capacitive coupled HBC, the near-field generated by the electrodes is affected by coupling to the environment such as nearby objects. Consequently, this causes the channel to be dynamic depending on the surrounding environment.

The thesis started by investigating the effect of the human body on signal propagation when low frequency (≤ 10 MHz) electric current is coupled to the body via two surface electrodes in galvanic coupled HBC. At this frequency range the wavelengths of the signals are very large compared to the dimension of the human body; therefore, the human body is electrically small and was assumed to radiate poorly. Consequently, a quasistatic approximation was applied to model the human arm using discrete circuit elements. The circuit model was developed based on the dielectric properties of tissues and the geometrical parameters of the human arm. Since the applied current is mainly affected by the dielectric properties of the tissues, a circuit model that incorporates the dielectric spectrum of tissues was proposed. Unfortunately, most previous models in the literature fail to include the dielectric spectrum; therefore, the models did not accurately predict the measured quantities, such as, the phase and gain. In addition to this, in order to consider the variation in size of different human subjects, the proposed circuit explicitly took anthropometric measures into account when calculating the specific tissue layer impedances. This helped to explain the variation of the measured results among the different human subjects used for the experiment. Another important factor that the circuit model had was the electrode-skin contact impedance, which was not modeled previously. The characterization of this impedance is very important since it affects the coupled current by acting like a high-pass filter. The model of the electrode-skin impedance was proposed based on the measured values of the human body impedance. From this study, it was found that the dielectric properties of tissues affect the signal depending on the distance between the transmitter electrodes and the distance between the transmitter and the receiver. When the distance between the transmitter electrodes is smaller than the distance between the transmitter and the receiver, the dielectric properties of muscle tissues tend to determine the characteristics of the received signal. In the other case, when such distance is larger, the dielectric properties of skin affect the detected signal.

The knowledge insufficiency in the literature about the human body antenna effect has led to the limitations in describing the mechanisms of signal propagation in HBC. Previously, there was an attempt to describe the signal propagation in capacitive coupled

HBC using a model developed to analyse the electromagnetic fields of a dipole source over a conductive and infinite plane. Unfortunately, this approach does not consider the antenna effect of the human body; thus, it was unable to explain the frequency where the maximum HBC gain occurred in the experiments. In this thesis, the antenna characteristics of the human body was incorporated into the HBC model to describe the mechanism of signal propagation and interference in capacitive coupled HBC, which have not been studied previously. The human body was modeled as an imperfectly conducting cylindrical antenna that was analysed using the three-term approximation technique. From this model, the potential difference on the surface of the cylinder was calculated assuming a vertically oriented dipole source over the surface of the cylinder. It was found that the frequency where the maximum gain occurred aligns with the resonance frequency of the human body.

Another ambiguous issue in capacitive coupled HBC is the widespread belief that capacitive coupling is less affected by interference form external electromagnetic sources. This is the result of taking the electrically small antenna properties of the electrodes in free space. Due to the large size of the signal wavelength compared to the size of the electrodes, the electrodes used can be considered as electrically small antennas, which radiate poorly when they are operated in free space. This led to the assumption that HBC was less affected by interference. In an experiment undertaken in this thesis, it was found that the human body radiates as a monopole antenna when an HBC transmitter operates on the body. This phenomenon was studied by considering a plane electromagnetic wave exposure to the cylinder model. It was found that the electric potential distribution in the vicinity of the body is affected by the electromagnetic interference and it depends on the antenna characteristics of the human body. It was also found that the maximum signal interference occurs at the resonance frequency of the human body, which is near 50 MHz for a human subject standing on a highly conductive ground. In connection to this, the effect of interference was investigated theoretically and experimentally when the HBC receiver is located externally. This represented the worst case scenario of HBC interference since the external HBC receiver establishes a current path to the ground for the RF current induced inside the human body from the interfering incident electromagnetic plane wave.

In the area of RF dosimetry, this thesis also analysed the whole-body RF power absorption from an antenna theory perspective. Since the human body is a lossy medium, the

tissues absorb part of the incident electromagnetic power and the rest is scattered in similar fashion as the imperfectly conducting monopole antennas do when it is illuminated by electromagnetic wave. The absorbed RF power is turned to heat, which can obstruct the normal function of the human body by raising the local or core temperature of the body. Therefore, the quantification of the safe levels of incident electromagnetic power is very important. The direct measurement or computing of temperature needs the translation from the thermal domain to the electromagnetic domain, which leads to a complicated problem. The common approach of simplifying this problem is using quantities, such as, the specific absorption rate (SAR), which can indirectly indicate the rise in temperature of the body. When the core temperature rise in the whole-body is required, the whole-body averaged specific absorption rate (WBA-SAR) is usually used as the proxy quantity. WBA-SAR is a surrogate metric used to determine the core temperature rise in the body from the exposure of electromagnetic fields. It is a quantity used by international guidelines and standards in order to limit the safe amount of electromagnetic field exposure. The WBA-SAR is defined as the amount of total RF power absorbed inside the body divided by the total body weight. The advantage of WBA-SAR is: it can be easily related to measurable field quantities, such as the incident electric field, so that it is easier to specify the safe levels of exposure. Since it is not convenient to measure WBA-SAR inside the human body, computational results using realistic numerical models of the human body are often used. Alternatively, physical human body phantoms are also used to experimentally determine WBA-SAR.

From the large number of studies in RF dosimetry, it was known that the WBA-SAR is maximum near the resonance frequency of the human body, in addition to other factors that affect it, such as the polarization of the incident wave and the surrounding environment. Little can be found in the literature about the detailed analysis of the WBA-SAR from the antenna theory point of view. From these studies, it is known that human body parameters, such as, the dielectric properties of tissues, the weight and height affect the WBA-SAR value. But, other than indicating such results from different computations, sufficient analysis has not been given on determining how such parameters affect the WBA-SAR. With the objective of filling this gap, in this thesis, the WBA-SAR was analysed based on the equivalent cylindrical antenna representation of the human body.

In this thesis, the equivalent cylindrical antenna representations of the human body

were developed based on the WBA-SAR values obtained from the finite-different time-domain (FDTD) computations on three numerical models representing an adult male, adult female and a child, which are found in the literature. From the proposed model a formula for the resonance frequency was derived, for the first time, based on the weight and height of the human body as parameters. Using this formulation the accuracy of the proposed models were validated by comparing the results to the resonance frequency obtained using the FDTD on 11 realistic numerical models found in the literature. Based on these models, it was found that as the effective conductivity of the body decreases the WBA-SAR spectrum tends to get wider. The decrease in conductivity implicitly implies the increase in fat percentage in the body. This points to the possible explanation of the observation made that the WBA-SAR spectrum of women is broader than that of men. Also, the model helped to determine the effect of height, which shifts the resonance frequency. It was found that a tall human subject has lower resonance frequency compared to a shorter person of equal weight.

In addition to this, most of the WBA-SAR results in the literature were presented from employing numerical models of the bare-footed human body. But, in reality, people wear shoes; yet, the effect of shoes was given little attention in the literature. From the results obtained from using the equivalent cylindrical model, it was found that the shoes affect the WBA-SAR by shifting the resonance frequency up and decreasing the WBA-SAR slightly. It was also found that the resonance frequency for a human subject who have shoes on is between 50 to 60 MHz, instead of the 35 to 45 MHz as predicted based on bare-footed realistic numerical models.

At this stage of the thesis, it was shown that the human body behaves like a monopole antenna, which has been given little attention previously. It was also shown that this property of the human body has impact in the explanations of some phenomena in the areas of HBC and RF dosimetry. Then, the natural question to follow is: if the human body behaved like an antenna, could it be used for wireless communication applications? To answer this question, in this thesis, the antenna characteristics of the human body were assessed based on the antenna performance indicator parameters, which are the reflection coefficient and the radiation efficiency. Among other parameters, these two parameters are the most important quantities that are used to determine how good an antenna is. The reflection coefficient expresses how good the antenna is matched to the signal transmitter or receiver. In other words, it used to express the amount of signal

reflected due to impedance mismatch. The radiation efficiency expresses the amount of power radiated from the antenna in comparison to the amount of power dissipated inside the antenna.

Therefore, in this thesis, the reflection coefficient of the human body as a monopole antenna was measured, for 10 to 110 MHz, by feeding an RF current on the sole of the foot using a signal generator of 50 Ω output impedance. It was found that the human body has a minimum reflection coefficient of approximately -12 dB resonating in the frequency range of 40 to 60 MHz, depending on the posture. This was also determined theoretically from applying the cylindrical model of the human that was developed previously. In addition to this, from the cylindrical antenna model of the human body, it was predicted that the radiation efficiency of the human body reaches 70 % in the frequency range of 90 to 100 MHz; this was supported by measurement results in the literature. These results demonstrated that the human body indeed can be used as antenna for low-power applications, such as, wireless implant communication.

Then, the viability of applying the human body as an antenna for wireless implant communication was investigated. This assessment stemmed from the fact that wireless implant communication is still a hot research topic as well as the current wireless techniques used have shortcomings. The wireless link between a nearby monitoring device and an implant is obtained using either a magnetic induction or radio-wave based links. In the magnetic induction approach, the external magnetic coil has to be placed very close to the surface of the body. In addition to this, the magnetic link is highly dependent on the orientation of the coil. Moreover, the performance of the magnetic link is highly dependant on the size of the coil used on the implant; larger coils have better performance. Unfortunately, implants have much limited size in order to minimise tissue damage. The radio-wave based link usually operates at higher frequencies, for example 402 to 405 MHz in MICS, that is affected due to the dielectric properties of the body. As frequency increases, the human body absorbs more power so that the penetration depth of radio-waves decreases. Also, the characteristics of antennas alter when they are operated inside the human body. In other words, an antenna specified for free space operates unpredictably inside the human body due to the dielectric properties of the tissues. Therefore, as an alternative wireless implant communication technique, the human body itself as an antenna was analysed theoretically by using an RF current instead of radio-waves.

From RF dosimetry, it is well known that large axial current density is established in the cross-section of the ankles when the human body is exposed to electromagnetic plane waves. Therefore, in this thesis, the performance of applying ferrite-core toroidal inductor in the cross-section of the ankle to collect or couple an RF current for the purpose of wireless implant communication was analysed theoretically. It was found that the system has a maximum broadband gain of -25 dB for the frequency range of 20 to 40 MHz when a toroidal inductor of size approximately 2 % of the ankle cross-section was considered. However, it was also found that the radiation resistance of the system is very small, only 0.5 % of the input power radiated for the given example. The small value in the radiation resistance requires a large amount of current to get a usable radiated power; therefore, the design of the system should increase the radiation resistance by taking into account factors that affect it. From this thesis, it was found that the parasitic capacitance and the magnetic core loss determine the value of the radiation resistance. Reducing these factors improve the amount of radiated power. The parasitic capacitance can be reduced by optimizing the number of turns with a tradeoff to obtain lower but usable magnetizing inductance. Also, a magnetic core that introduces less loss and with usable magnetizing inductance should be chosen. The previous results point to the possibility that this approach can be used as an alternative wireless implant communication technique for implants located in the ankle.

8.2   Future Works

- The application of the human body for wireless implant communication was studied theoretically; therefore, future research should support the theoretical results with experiments. The experiments can be carried out using the human body physical phantoms, such as, a saline-filled cylinders. Also, a more realistic numerical model of the human body with computational techniques like FDTD can be applied.

- The analysis of the human body antenna characteristics in this thesis was based on the implicit assumption that the human body is not moving. The movement of the body changes the antenna characteristics, such as, the antenna pattern and directivity, which have effects on the gain of the human body antenna. Therefore,

the future studies will also consider the effect of the body movement on the human body antenna.

- The human body antenna features can also be applied in areas, such as, the implementation of the human body antenna for RF energy harvesting in the FM band. Studies have shown that the ambient RF power in the FM band is mostly higher than other broadcast bands; additionally, it is continually present unlike other intermittent broadcast channels. But, most studies on RF energy harvesting focus on other higher frequency broadcast bands, due to the large antenna size requirement in the FM band that is not suitable to incorporate in wearable devices.

- The future researches can also focus on the prospective application of the human body antenna to connect wearable electronic devices to nearby monitoring devices. This application can be deployed in a network of HBC devices without the need to include a power-hungry central hub operating at a higher frequency to communicate with the nearby external monitoring devices.

Appendix A

A New Perspective on the Cylindrical Antenna Theory

BEHAILU KIBRET, ASSEFA K TESHOME, AND DANIEL T H LAI

A.1   Abstract

This paper presents a new perspective on the analysis of the cylindrical antenna theory. It applies the cylindrical surface waves on an infinitely-long cylindrical conductor, which are similar to the Sommerfeld axial cylindrical surface waves, to describe the conventional postulate of applying a sinusoidal current distribution on a cylindrical dipole antenna. This treatment leads to the derivation of simple expression for the current on a cylindrical dipole antenna of finite conductivity, which is in good agreement with the current obtained from the three-term approximations. Also, it proposes an expression for the current on an infinitely-long cylindrical dipole antenna of finite conductivity, which is also in good agreement to the current found from applying the Fourier transform technique. Moreover, the paper shows that the complex propagation constant used in the three-term approximation is similar to the complex propagation constant of the principal Sommerfeld wave on the surface of an infinitely-long cylindrical conductor. Therefore, a more accurate representation of the current near the feeding point is proposed based on the complex propagation constants of multiple Sommerfeld waves.

A.2   Introduction

The expression of the current on cylindrical antennas has a long history with notable early contributors, such as, Pocklington [106], Hallén [107] and R. W. P. King [108]. The knowledge of the current on the antenna simplifies the calculation of antenna parameters, such as, the input impedance and far-field components. The calculation of the current is usually carried out solving the Pocklington equation describing the surface vector magnetic potential, which is related to known source fields via boundary conditions. For a dipole cylindrical antennas of finite conductivity, King approximated the solution of this equation to express the current as the sum of three sinusoidal functions [29]. On the other hand, for infinitely-long and perfectly conducting dipole antenna, Hallén [109] transformed a similar equation to the Fourier domain and solved for the current as the sum of residues and a convergent integral equation, which has a form of outgoing traveling wave. As alternative, in this paper, the general form of the current on an infinitely-long cylindrical conductor, which is excited by a rotationally symmetric external electric field, is determined as a standing wave and travelling wave. Since the

electric field on the surface of a delta-gap and center-fed dipole antenna is rotationally symmetric, the general form of the current derived for the cylindrical conductor is used in the Pocklington equation. This approach leads to the expression of the vector magnetic potential as a product of the current and a constant, for both the finite and infinitely-long dipole antennas. The definition of the magnetic vector potential simplifies the solution of the Pocklington equation to derive simple expressions for the current. The simple expressions derived are in good agreement with the current obtained from the three-term approximation and from the Fourier transform technique for the case of infinitely-long dipole antennas.

The technique used in this paper also shows that the complex propagation constant used in the three-term method is similar to the complex propagation constant of the principal wave of the Sommerfeld axial cylindrical surface waves [110]. Moreover, it is known that the analytic approximation methods available today, such as the three-term approximation [29], are not accurate at describing the current near the feeding gap. As reported in [111], for conducting cylinders the higher order of the Sommerfeld surface waves attenuates rapidly. This suggests that the current near the feeding point can be more accurately described if multiple Sommerfeld waves are used. Consequently, we propose a more accurate form of the current near the feeding point.

The paper is organized as follows. Firstly, the fields on the surface of an infinitely-long cylindrical conductor, which is excited by an incident rotationally symmetric axial electric field, are expressed. Also, from the expression of the surface electric and magnetic fields, the surface impedance per unit length of the cylinder is defined. Applying the boundary conditions of the magnetic fields, the general form of the induced axial current is defined as a traveling wave and a standing wave. In the following section, the standing wave general form of the current is applied in the standard Pocklington equation of a finite size, imperfectly conducting, and delta-gap excited cylindrical dipole antenna. From this equation, the complex propagation and coefficients of the current are defined. Following this, the traveling wave general form of the current is applied to the Pocklington equation of a delta-gap excited and infinitely-long cylindrical dipole antenna of finite conductivity, which is also used to define the complex propagation constant and the coefficient of the exponential function used to express the current. Lastly, from the comparison of the complex propagation constants to Sommerfeld poles, an expression

of the current near the feeding point of a dipole antenna is proposed based on multiple Sommerfeld poles, for both types of dipole antennas.

A.3 Fields on An Infinitely-long Cylindrical Conductor

This section expresses the axial electric field, current density, surface impedance per unit length and the axial current on an infinitely-long cylindrical conductor of finite conductivity when it is excited by a rotationally symmetric electric field on its surface. These expressions are used to describe the axial current in a finite and infinitely-long cylindrical dipole antennas that are excited by delta-gap electric field source, in the following sections.

Assuming a rotationally symmetric and time harmonic $(e^{j\omega t})$ external electric field is maintained on the surface of an infinitely-long and circular conducting cylinder of radius a, conductivity σ, relative permittivity ϵ and permeability μ_0, which extends along the z-axis of a system of cylindrical coordinates (ρ, ϕ, z), the magnetic vector potential inside $\mathbf{A}_1 = A_{1z}(\rho, z)\,\hat{\mathbf{z}} + A_{1\rho}(\rho, z)\,\hat{\boldsymbol{\rho}}$ can be written, from the Maxwell's equations in Lorenz gauge, as

$$\nabla^2 \mathbf{A}_1 + k_1^2 \mathbf{A}_1 = 0 \tag{A.1}$$

where $k_1 = \sqrt{-j\omega\mu_0(\sigma + j\omega\epsilon_0\epsilon)}$. Since all the magnetic or electric field components can be obtained from either of the two components of $\mathbf{A}_{1z}(\rho, z)$, we assumed $A_{1\rho}(\rho, z) = 0$. Therefore, expanding the vector identity $\nabla^2 \mathbf{A}_1 = \nabla\nabla\cdot\mathbf{A}_1 - \nabla\times\nabla\times\mathbf{A}_1$ in cylindrical coordinates and substituting it into (A.1) gives the following equation:

$$\frac{\partial^2 A_{1z}(\rho, z)}{\partial z^2} + \frac{1}{\rho}\frac{\partial}{\partial\rho}\rho\frac{\partial A_{1z}(\rho, z)}{\partial\rho} + k_1^2 A_{1z}(\rho, z) = 0. \tag{A.2}$$

The solution for (A.2) can be obtained by the method of separation of variables, such that $A_{1z}(\rho, z)$ can be written as

$$A_{1z}(\rho, z) = g(z)G(\rho). \tag{A.3}$$

Substituting (A.3) in (A.2) yields the equation

$$\frac{1}{g(z)}\frac{\partial^2 g(z)}{\partial z^2} + k_1^2 = -\frac{1}{G(\rho)}\frac{1}{\rho}\frac{\partial}{\partial\rho}\rho\frac{\partial G(\rho)}{\partial\rho}. \tag{A.4}$$

It can be seen that the left side of the above equation is a function of z and the right side is a function of ρ; thus, the two sides can be equal if both of them are equal to a constant. Denoting the constant by v_1^2 and expressing it as $v_1^2 = k_1^2 - \gamma^2$ so that

$$\frac{\partial^2 g(z)}{\partial z^2} + \gamma^2 g(z) = 0 \tag{A.5}$$

and

$$\frac{1}{\rho}\frac{\partial}{\partial \rho}\rho\frac{\partial G(\rho)}{\partial \rho} + v_1^2 G(\rho) = 0. \tag{A.6}$$

The expression in (A.5) is the well known one dimensional wave equation that has a solution of a traveling wave in a lossy medium given as $g(z) = C_1 e^{\pm j\gamma z}$ or the standing wave representation as $g(z) = C_2 \left(\sin(\gamma z) + C_3 \cos(\gamma z)\right)$, where C_1, C_2 and C_3 are arbitrary constants. From the wave equation of $g(z)$, γ is the complex propagation constant that can be described as $\gamma = \beta - j\alpha$, where β is the phase constant and α is the attenuation constant.

Equation (A.6) can be written in terms of a new independent variable $x = v_1\rho$ as

$$\frac{\partial^2 G\left(\frac{x}{v_1}\right)}{\partial x^2} + \frac{1}{x}\frac{\partial G\left(\frac{x}{v_1}\right)}{\partial x} + G\left(\frac{x}{v_1}\right) = 0, \tag{A.7}$$

which is a Bessel equation with known solutions. One of the solution for the expression in (A.7) is $G(\rho) = C_4 J_0(v_1\rho)$, where J_0 is the zeroth-order Bessel function and C_4 is an arbitrary constant. The Bessel function was chosen so that the vector potential is non-zero at the center of the cylinder. Consequently, the magnetic vector potential can be written as

$$A_{1z}(\rho, z) = G(\rho) g(z) = C_4 J_0(v_1\rho) g(z). \tag{A.8}$$

Assuming the induced total axial current is $I(z)$, from Ampere's law, the magnetic flux density $B_{2\phi}(a, z)$ on the surface of the cylinder can be written as

$$B_{2\phi}(a, z) = \frac{\mu_0 I(z)}{2\pi a}. \tag{A.9}$$

From the expression of the magnetic vector potential, the magnetic flux density inside the cylinder can be expressed as

$$B_{1\phi}(\rho, z) = -\frac{\partial A_{1z}(\rho, z)}{\partial \rho} = C_4 v_1 J_1(v_1\rho) g(z) \tag{A.10}$$

where J_1 is the first-order Bessel function. Defining the arbitrary constant C_4 as

$$C_4 = \frac{\mu_0}{2\pi a \upsilon_1 J_1(\upsilon_1 a)} \tag{A.11}$$

and applying the magnetic field boundary conditions at the surface of the cylinder; the magnetic flux density at the surface of the cylinder can be written as

$$B_{1\phi}(a, z) = B_{2\phi}(a, z) = \frac{\mu_0 g(z)}{2\pi a} = \frac{\mu_0 I(z)}{2\pi a}, \tag{A.12}$$

which implies that

$$I(z) = g(z). \tag{A.13}$$

Equation (A.13) expresses the induced total axial current when the cylinder is excited by a rotationally symmetric electric field on the surface of the cylinder. Furthermore, if we are interested in a traveling wave current, it is expressed as

$$I(z) = C_1 e^{\pm j\gamma z}. \tag{A.14}$$

On the other hand, if we are interested in a standing wave form of the current, it can be expressed as

$$I(z) = C_2 \left(\sin(\gamma z) + C_3 \cos(\gamma z) \right). \tag{A.15}$$

The electric field inside the cylinder can be found from the vector magnetic potential using the relationship

$$\mathbf{E_1} = \frac{-j\omega}{k_1^2} \left(\nabla \nabla \cdot \mathbf{A_1} + k_1^2 \mathbf{A_1} \right). \tag{A.16}$$

From (A.16), the axial component of the electric field $E_{1z}(\rho, z)$ can be derived as

$$E_{1z}(\rho, z) = \frac{j\omega}{k_1^2} \frac{1}{\rho} \frac{\partial}{\partial \rho} \rho \left(\frac{\partial A_{1z}(\rho, z)}{\partial \rho} \right) = -j\omega \frac{\upsilon_1^2}{k_1^2} A_{1z}(\rho, z) = \frac{I(z)\upsilon_1}{2\pi a (\sigma + j\omega \epsilon_0 \epsilon)} \frac{J_0(\upsilon_1 \rho)}{J_1(\upsilon_1 a)}. \tag{A.17}$$

And the volume current density $J_{1z}(\rho, z)$ can be derived as

$$J_{1z}(\rho, z) = (\sigma + j\omega \epsilon_0 \epsilon) E_{1z}(\rho, z) = \frac{I(z)\upsilon_1}{2\pi a} \frac{J_0(\upsilon_1 \rho)}{J_1(\upsilon_1 a)}. \tag{A.18}$$

Thus, the surface impedance per unit length of the cylinder z^i can be defined as

$$z^i = \frac{E_{1z}(a,z)}{2\pi a H_{1\phi}(a,z)} = \frac{E_{1z}(a,z)}{I(z)} = \frac{v_1}{2\pi a(\sigma + j\omega\epsilon_0\epsilon)} \frac{J_0(v_1 a)}{J_1(v_1 a)} \tag{A.19}$$

where $H_{1\phi}(a,z)$ is the magnetic field intensity on the surface of the cylinder.

A.4 Delta-gap Excited Finite Cylindrical Dipole Antenna

When we consider a finite length cylindrical dipole antenna of height $2h$, radius a, conductivity σ, relative permittivity ϵ, permeability μ_0, with axis aligned along the z-axis, and center-fed by a delta-gap electric field source located at $z = 0$, the current at the ends of the cylinder has to be zero. Consequently, we expect the current to be even symmetric with respect to $z = 0$ and form a standing wave with a general expression similar to (A.15). Therefore, since the current vanishes at $z = \pm h$ and evenly symmetric with respect to $z = 0$, for $0 < |z| \leq h$, it can be expressed as

$$I(z) = C_2 \left[\sin(\gamma|z|) - \sin(\gamma h) + C_3(\cos(\gamma z) - \cos(\gamma h))\right]. \tag{A.20}$$

The axial surface electric field at $z = 0$ is the delta-gap electric field source that is defined as

$$E_{1z}(a,z) = -V_0\delta(z) \tag{A.21}$$

where V_0 is the electromotive force (emf) applied on the infinitesimal gap at $z = 0$. Since the electric field source at $z = 0$ is rotationally symmetric, we expect the surface axial electric field on the rest of the cylinder is also rotationally symmetric. Therefore, from the expression in (A.19), the surface axial electric field can be expressed as

$$E_{1z}(a,z) = z^i I(z), \quad 0 < |z| \leq h. \tag{A.22}$$

As a result, the axial magnetic vector potential on the surface of the cylinder $A_{2z}(z)$ due to the surface axial electric field can be related as

$$z^i I(z) - V_0\delta(z) = \frac{-j\omega}{k_2^2}\left(\frac{\partial^2}{\partial z^2} + k_2^2\right) A_{2z}(z) \tag{A.23}$$

where $k_2 = \omega\sqrt{\epsilon_0\mu_0}$ is the free space wave number. Also, the vector magnetic potential $A_{2z}(a, z)$ can be related to the volume axial current density $J_{1z}(\rho, z)$ expressed in (A.18) as

$$A_{2z}(a, z) = \frac{\mu_0}{4\pi}\int_{-h}^{h}\int_{0}^{a}2\pi J_{1z}(\rho', z')K(z - z')\rho'd\rho'dz' = \frac{\mu_0}{4\pi}\int_{-h}^{h}I(z')K(z - z')dz' \quad \text{(A.24)}$$

where $K(z - z')$ is the thin-wire approximate kernel defined as

$$K_{ap}(z - z') = \frac{e^{-jk_2\sqrt{(z-z')^2+a^2}}}{\sqrt{(z - z')^2 + a^2}}. \quad \text{(A.25)}$$

From the above expressions, the standard Pocklington equation can be written as

$$\left(\frac{\partial^2}{\partial z^2} + k_2^2\right)\int_{-h}^{h}I(z')K(z - z')dz' = \frac{j4\pi k_2}{\eta_0}\left(I(z)z^i - V_0\delta(z)\right) \quad \text{(A.26)}$$

where $\eta_0 = 120\pi$ is the free space impedance.

For $|z| > 0$, from the boundary conditions of the electric field and the magnetic field on the surface of the cylinder, and from the expression of the vector magnetic potential in (A.8), the boundary conditions for the vector magnetic potential can be written as

$$A_{2z}(a, z) = -\frac{k_2^2}{v_2^2}\frac{v_1^2}{k_1^2}A_{1z}(a, z) = \frac{1}{j\omega}\frac{k_2^2}{v_2^2}z^iI(z) \quad \text{(A.27)}$$

where $v_2^2 = \gamma^2 - k_2^2$. From the expressions in (A.24) and (A.27), the following relation can be obtained

$$\int_{-h}^{h}I(z')K_{ap}(z - z')dz' = \Psi I(z), \quad 0 < |z| \leq h \quad \text{(A.28)}$$

where Ψ is a constant, which is defined as

$$\Psi = \frac{j4\pi k_2}{k_2^2 - \gamma^2}\frac{z^i}{\eta_0}. \quad \text{(A.29)}$$

The relationship in (A.28), implies that the thin-wire kernel can be approximated as

$$K_{ap}(z) \sim \Psi\delta(z), \quad \text{(A.30)}$$

which also implies that Ψ can be approximately computed as

$$\Psi \sim \int_{-h}^{h} K_{ap}(z)\, dz. \tag{A.31}$$

Therefore, the left-hand side expression in (A.26) can be simplified, replacing the expression of the current in (A.20), as

$$2\gamma \Psi C_2 \delta(z) + \left(k_2^2 - \gamma^2\right) \Psi I(z) - \gamma^2 \Psi C_2 \left(\sin(\gamma h) + C_3 \cos(\gamma h)\right). \tag{A.32}$$

Equating the terms in the above expression with that of the right-hand side of (A.26), the complex propagation constant γ can be obtained as

$$\gamma = k_2 \sqrt{1 - \frac{j4\pi z^i}{k_2 \Psi \eta_0}}, \tag{A.33}$$

which can also be determined from (A.29). The complex propagation constant γ (A.33) can be calculated by applying the iteration procedure. First, the iteration is initialized by setting $\gamma = k_2$ and calculating z^i, which is used to calculate γ iteratively until it converges. We have seen that such iteration converges after a few cycles.

Similarly, the constants C_2 and C_3 can be calculated as

$$C_2 = \frac{-j2\pi k_2}{\gamma \Psi} \frac{V_0}{\eta_0} \tag{A.34}$$

and

$$C_3 = -\tan(\gamma h). \tag{A.35}$$

Therefore, the axial current $I(z)$ can be written as

$$I(z) = \frac{j2\pi k_2}{\gamma \Psi \cos(\gamma h)} \frac{V_0}{\eta_0} \sin(\gamma(h - |z|)) \tag{A.36}$$

The accuracy of the expression for the current in (A.36) is validated by comparison with the current obtained from the three-term approximation, which is obtained by approximately solving the expression in (A.26) and involves an approximation of the thin-wire kernel integral shown in (A.28). King *et al* [29] derived the three-term expression of the

axial current as

$$I_{1z}(z) = \frac{j2\pi k_2}{\gamma \Psi_{dR} \cos(\gamma h)} \frac{V_0}{\eta_0} \Big[\sin \gamma(h - |z|) + T_U(\cos \gamma z - \cos \gamma h)$$

$$+ T_D(\cos \tfrac{1}{2}k_2 z - \cos \tfrac{1}{2}k_2 h) \Big] \tag{A.37}$$

and

$$\gamma = k_2 \sqrt{1 - \frac{j4\pi z^i}{k_2 \Psi_{dR} \eta_0}} \tag{A.38}$$

where the factor Ψ_{dR} and the coefficients T_U and T_D involve the numerical computations of eight integrals. The calculation of γ also applies the iteration procedure; the iteration is initialized by setting $\gamma = k_2$ to calculate the initial values of z^i and Ψ_{dR}. For very thin-wire dipole antennas, the expression in (A.36) is a good approximation to the three-term expression given in (A.37), as shown in Fig. A.1. The three-term expression is valid for $0 \le k_2 h \le 5\pi/4$; thus, the values of h within this range are used for comparison. As shown in Fig. A.1(a), the two expressions are in good agreement with differences start to appear as the height decreases. Fig. A.1(b) shows that the contributions of the two cosine terms in the three-term equation is insignificant, which supports the agreement between the proposed expression in (A.36) and the three-term expression (A.37).

A.5 Delta-gap Excited Infinitely-Long Cylindrical Dipole Antenna

When we consider an infinitely-long cylindrical dipole antenna of radius a, with similar dielectric properties as the finite one, that is excited with a delta-gap electric field source at $z = 0$, the general form of the current is expected to be an outgoing travelling wave similar to the one given in (A.14), but with a little modification to take into account the presence of infinitesimal gap at $z = 0$. Thus, the current can be defined as

$$I(z) = I_{z0} e^{-j\gamma|z|}, \quad |z| > 0, \tag{A.39}$$
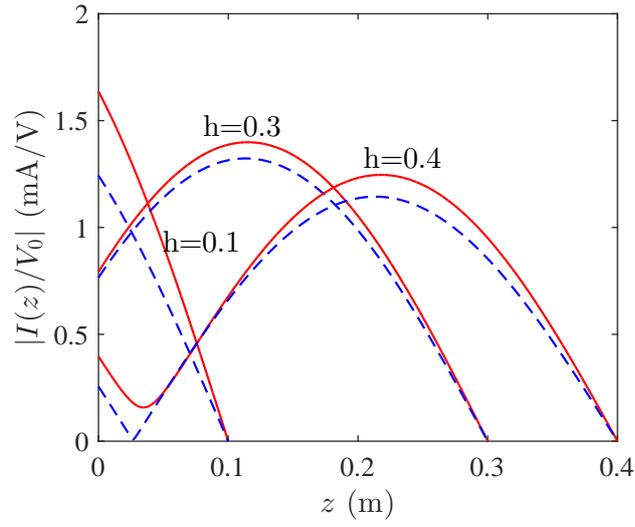
(a)
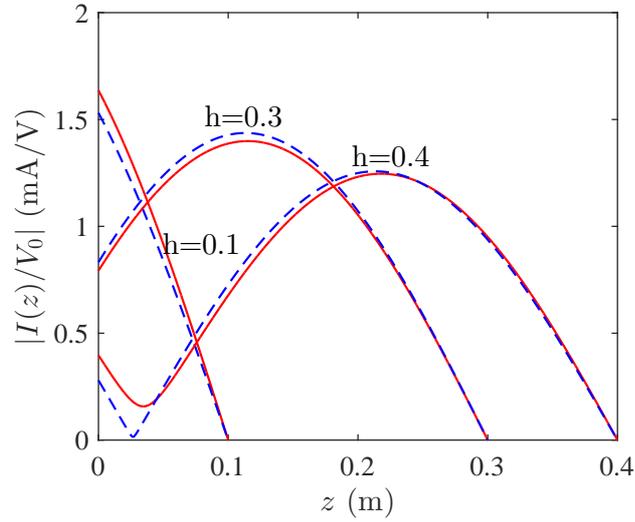
(b)

FIGURE A.1: Comparison of the proposed current expression with that of the three-term expression for a cylindrical dipole of radius $a = 0.001$ cm and skin-depth to radius ratio of 0.1 at 400 MHz. (a) Compares the current in (A.36) (broken line) to the three-term expression (A.37) (solid line) for the half-length h of 0.4, 0.3 and 0.1 m. (b) Compares the first sinusoidal term (broken line) and the complete three-terms (solid line) in (A.37).

where I_{z0} is the current near the infinitesimal gap. Similar to the finite case, the vector magnetic potential $A_{2z}(a, z)$ on the surface of the cylinder can be described as

$$A_{2z}(a, z) = \frac{\mu_o}{4\pi} \int\limits_{-\infty}^{\infty} I(z') K(z - z') \, dz' \tag{A.40}$$

where the kernel $K(z - z')$ can either take the exact form, which is given as

$$K_{ex}(z - z') = \frac{1}{2\pi} \int_{-\pi}^{\pi} \frac{e^{-jk_2\sqrt{(z-z')^2 + 4a^2 \sin^2(\phi'/2)}}}{\sqrt{(z - z')^2 + 4a^2 \sin^2(\phi'/2)}} d\phi' \tag{A.41}$$

or the approximate form given in (A.25).

Replacing the expression of the current into the integral in (A.40), for $z > 0$, the vector magnetic potential can be obtained as

$$A_{2z}(a, z) = \frac{\mu_o}{4\pi} I(z) \int_{-\infty}^{\infty} K(x) e^{j\gamma x} dx = \frac{\mu_o}{4\pi} I(z) \bar{K}(\gamma) \tag{A.42}$$

where x is a dummy variable used for the integration and $\bar{K}(\gamma)$ is the Fourier transform of the kernel evaluated at the complex propagation constant γ. For $|\gamma| > k_2$, the Fourier-transform of the exact kernel is given in [112] as

$$\bar{K}_{ex}(\gamma) = 2I_0(v_2 a) K_0(v_2 a) \tag{A.43}$$

and for the approximate kernel as

$$\bar{K}_{ap}(\gamma) = 2K_0(v_2 a) \tag{A.44}$$

where K_0 and I_0 are the modified Bessel functions; and $v_2 = \sqrt{\gamma^2 - k_2^2}$ is defined previously in (A.27). Moreover, for $z < 0$, $A_{2z}(a, z)$ has the same expression as (A.42) since $\bar{K}(\gamma)$ is an even function. Consequently, for $|z| > 0$, applying the boundary condition of the vector magnetic potential on the surface of the cylinder given in (A.27), the complex propagation constant can be expressed as

$$\gamma = k_2 \sqrt{1 - \frac{j4\pi z^i}{k_2 \bar{K}(\gamma) \eta_0}}, \tag{A.45}$$

which can be computed applying a similar iteration procedure as the finite case. The iteration can be initialized by setting $\gamma = k_2 + \varepsilon$ to compute z^i and $\bar{K}(\gamma)$, where ε is a very small number. Then, the value of z^i and $\bar{K}(\gamma)$ is used to calculate γ. This continues until the value of γ converges. As shown in an example below, this iteration is highly convergent.

In order to express the axial current completely, we need to determine I_{z0}. The differential equation relating the vector magnetic potential and the axial electric field on the surface of the cylinder, which is given in (A.23), can be solved by applying Green's function $F(z)$ satisfying the relation

$$\left(\frac{\partial^2}{\partial z^2} + k_2^2\right) F(z) = 2k_2\delta(z). \tag{A.46}$$

Thus, the vector magnetic potential can be expressed as

$$A_{2z}(a, z) = -j\frac{k_2}{2\omega}\left[C_4\cos(k_2 z) + V_0\sin(k_2|z|) - z^i\int\limits_{-\infty}^{\infty} I(q) F(z - q)\, dq\right] \tag{A.47}$$

where C_4 is an arbitrary constant and q is a dummy variable used for integration. By choosing the Green's function $F(z) = 2\sin(k2z)u(z)$ with the unit step function $u(z)$, the $A_{2z}(a, z)$ can be expressed for $z > 0$. Also, taking the limit of (A.47) as z approaches zero from the right side, C_4 can obtained as

$$C_4 = \frac{2k_2 z^i I_{z0}}{\gamma^2 - k_2^2}. \tag{A.48}$$

Replacing the expression of $A_{2z}(a, z)$ in (A.42) in (A.47), taking the Laplace transform on both sides, and evaluating it at the Laplace domain variable $s = 0$, it can be simplified as

$$\frac{V_0}{k_2} - \frac{2z^i I_{z0}}{j\gamma k_2} = \frac{\eta_0 \bar{K}(\gamma) I_{z0}}{2\pi\gamma}, \tag{A.49}$$

which can be used to obtain I_{z0} as

$$I_{z0} = \frac{2\pi k_2}{\gamma \bar{K}(\gamma)}\frac{V_0}{\eta_0}. \tag{A.50}$$

Then, the current on an infinitely-long cylindrical dipole antenna can be expressed as

$$I(z) = \frac{2\pi k_2}{\gamma \bar{K}(\gamma)}\frac{V_0}{\eta_0}e^{-j\gamma|z|}. \tag{A.51}$$

In order to validate the accuracy of the axial current expression in (A.51), we compared it to the current obtained from the Fourier transform method. The Pocklington equation

for the infinite case can be written as

$$\left(\frac{\partial^2}{\partial z^2} + k_2^2 \right) \int_{-\infty}^{\infty} I(z') K(z - z') \, dz' = \frac{j4\pi k_2}{\eta_0} \left(I(z) z^i - V_0 \delta(z) \right). \tag{A.52}$$

Taking the Fourier transform of both sides, the above equation can be written as

$$\left(k_2^2 - \xi^2 \right) \bar{I}(\xi) \bar{K}(\xi) = \frac{j4\pi k_2}{\eta_0} \left(\bar{I}(\xi) z^i - V_0 \right) \tag{A.53}$$

where $\bar{I}(\xi)$ is the Fourier transform of the current. Taking the Inverse-Fourier transform of the above expression, the current can be obtained as

$$I(z) = \frac{j4\pi k_2}{2\pi} \frac{V_0}{\eta_0} \int_{-\infty}^{\infty} \frac{e^{-j\xi|z|}}{Z(\xi)} d\xi \tag{A.54}$$

where

$$Z(\xi) = \left(\xi^2 - k_2^2 \right) \bar{K}(\xi) + j4\pi k_2 \frac{z^i}{\eta_0}. \tag{A.55}$$

Following the technique proposed by Hallén [113, p. 451], the integral in (A.54) is simplified to a form suitable for computation as the sum of a convergent branch cut integral and a sum of residues

$$I(z) = \sum_n I_n(z) + I_{bc}(z) \tag{A.56}$$

where

$$I_n(z) = 4\pi k_2 \frac{V_0}{\eta_0} \frac{e^{-j\xi_n|z|}}{Z'(\xi_n)} \tag{A.57}$$

where $Z' = \partial Z/\partial \xi$ and ξ_n is the nth root of Z when z^i in (A.19) is defined with $\upsilon_1 = \sqrt{k_1^2 - \xi^2}$. Also, the branch cut integral, taking the exact kernel, can be written as

$$I_{bc}(z) = \frac{2k_2^2}{j\pi} \frac{V_0}{\eta_0} \int_0^{\infty} \left\{ dt \frac{t}{\sqrt{t^2 - 1}} \left[\frac{e^{-k_2\sqrt{t^2-1}|z|}}{-k_2^2 t^2 J_0(ak_2 t) H_0^{(1)}(ak_2 t) + 4\omega\epsilon_0 z^i} \right. \right.$$
$$\left. \left. - \frac{e^{-k_2\sqrt{t^2-1}|z|}}{k_2^2 t^2 J_0(ak_2 t) H_0^{(2)}(ak_2 t) + 4\omega\epsilon_0 z^i} \right] \right\} \tag{A.58}$$

where $H_0^{(1)}$ and $H_0^{(2)}$ are the Hankel functions.

The integrand in (A.54) has poles at ξ_n, which are sometimes called Sommerfeld poles.

TABLE A.1: Comparison the propagation constant γ to ξ_1 given in [114] for the frequency of 300 MHz and radius $a = 0.01$ *cm*. δ_s/a is the skin-depth to radius ratio.

δ_s/a	γ	ξ_1 [114]
1	$6.3564 - j0.3762$	$6.3580 - j0.3765$
0.5	$6.3556 - j0.1122$	$6.3572 - j0.1122$
0.25	$6.3247 - j0.0488$	$6.3262 - j0.0488$

Note that the surface field components described in section A.3, which are directly proportional to the axial current, are similar to the axial cylindrical surface waves discussed by Sommerfeld. According to Stratton [111, p. 530], the function (A.55) has multiple roots that represent the propagation constants of multiple Sommerfeld waves. Also, for conducting cylinders, the higher order waves attenuates rapidly; therefore, it is sufficient to keep the principal wave, which is represented by the first pole ξ_1. From solving the first root ξ_1 of (A.55), it can be seen that ξ_1 is equal to the propagation constant γ we derived in (A.45). Therefore, the current can be written as

$$I\left(z\right) = I_{res}\left(z\right) + I_{bc}\left(z\right) \tag{A.59}$$

where

$$I_{res}\left(z\right) = 4\pi k_2 \frac{V_0}{\eta_0} \frac{e^{-j\xi_1|z|}}{Z'\left(\xi_1\right)} = 4\pi k_2 \frac{V_0}{\eta_0} \frac{e^{-j\gamma|z|}}{Z'\left(\gamma\right)}. \tag{A.60}$$

Table A.1 shows a comparison of the propagation γ constant we calculated using (A.45) to the first root ξ_1 of (A.55) that is given in [114] that describes the admittance of infinitely-long cylindrical dipole antenna with magnetic frill excitation. The iteration used to calculate γ converged at the fourth cycle.

Figure A.2 shows the comparison of the current calculated using (A.51) to the one obtained by applying the Fourier transform technique in (A.59), for an infinitely-long cylindrical dipole of radius $a = 0.01$ cm at the frequency of 400 MHz. Different conductivities of the dipole are compared by taking different skin-depth to radius ratio $b = \delta_s/a$; the conductivity can be obtained as $\sigma = 2/(\omega\mu_0\delta_s^2)$. As shown in Fig. A.2(a), the two expressions tends to be different near the gap or $z = 0$ due to the contribution of the branch cut integral for small z. But they are in good agreement for larger values of z. Moreover, it also shows that the two expressions are in excellent agreement for lower conductivities. From looking at the expression of I_{res} in (A.60) and the current
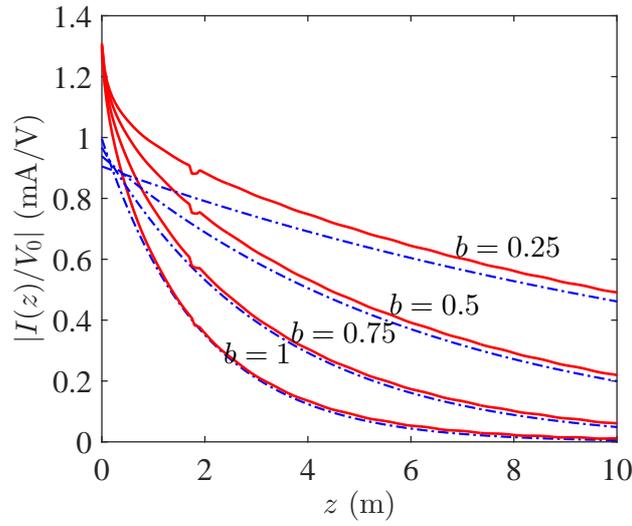
(a)
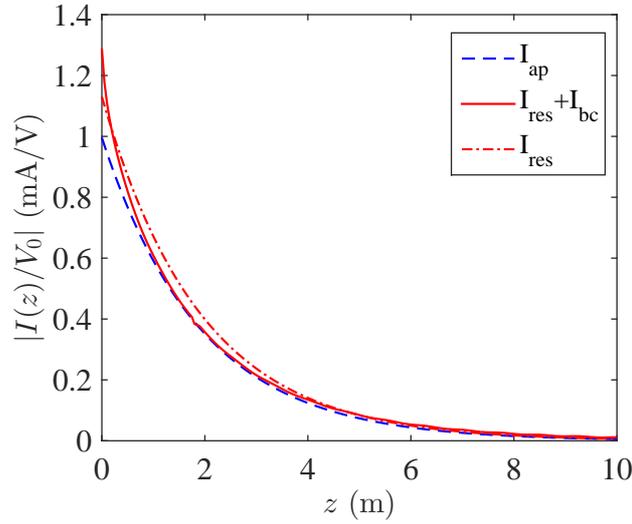
(b)

FIGURE A.2: The current calculated on infinitely long dipole of radius $a = 0.01$ cm and at 400 MHz, (a) Comparison of the current calculated from (A.51), the broken line, to from (A.59), the solid line, for case of different skin-depth to radius ratios represented by b (b) Comparison of the current I_{ap} from (A.51) to the currents in (A.59)

.

in (A.51), it might look like our derived current approximates the residual current I_{res}. But, from the comparison of these expressions in Fig. A.2(b), it can be seen that (A.51) is more closer to the total current (A.59) than the residual current.

The three-term expression in (A.37) is derived based on the condition that $0 \leq k_2 h \leq 5\pi/4$. This implies that, for large h, the three-term expression is not accurate. The accuracy of the expression proposed for finite cylindrical dipole in (A.36) is assessed
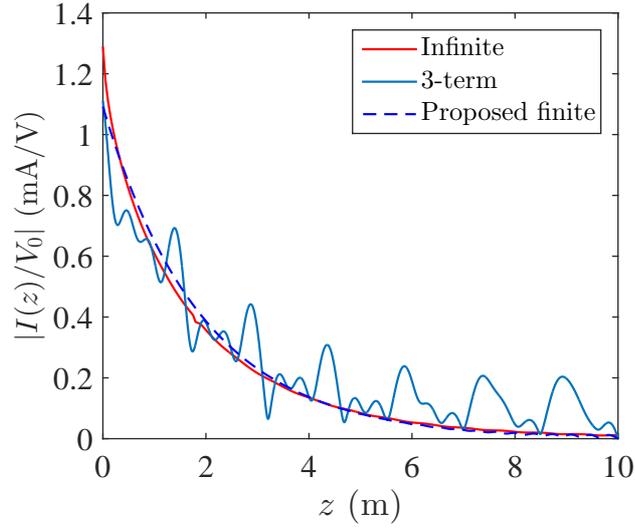
FIGURE A.3: Comparison of the proposed current for finite dipole (A.36), the three-term approximation (A.37) and the infinitely-long dipole (A.59). The finite dipole has a height $h = 10$ m, radius $a = 0.01$ cm and $b = \delta_s/a = 1$; and the infinite dipole has the same radius and conductivity.

by comparing the current in long cylindrical dipole antennas to the current on a lossy infinite cylindrical dipole antenna. Fig. A.3 compares the current on a dipole antenna of half-length $h = 10$ m computed with (A.36) and (A.37) to the current computed using (A.59), for $b = \delta_s/a = 1$ and radius of 0.01 cm. As expected the current from the three-term approximation has ripples due to the numerical integrals involved. But, the current from (A.36) and (A.59) are in excellent agreement suggesting that the expression in (A.36) is valid for electrically long lossy cylindrical dipole antennas.

From the comparison of the complex propagation constant for the case of the proposed current on finite cylindrical dipole antenna (A.33), the three-term (A.38), and the infinitely-long dipole antenna (A.45) shown in Table A.2, it can be seen that the complex propagation constants used for the finite cylindrical dipole antennas are similar to the complex propagation constant of the principal Sommerfeld surface wave. It is known that one of the limitations of the analytical expressions of the current, such as the three-term approximations, is they are not accurate near the feeding point of the dipole antenna. One of the factors of these limitations is the use of a single propagation constant of the principal wave in the expression of the current. But, very close to the feeding point (the gap), the higher-order waves also contribute. Therefore, a better approximation of the current near the feeding point should include all the propagation constants of the multiple Sommerfeld surface waves. Thus, the current near the feeding

point I_{z0} for the finite dipole antenna can be expressed as

$$I_{z0} = \lim_{z \to 0} I(z) = \frac{V_0}{\eta_0} \frac{j2\pi k_2}{\Psi} \sum_n \frac{\tan(\xi_n h)}{\xi_n} \tag{A.61}$$

and for the infinitely-long dipole antenna

$$I_{z0} = \lim_{z \to 0} I(z) = \frac{V_0}{\eta_0} 2\pi k_2 \sum_n \frac{1}{\xi_n \bar{K}(\xi_n)} \tag{A.62}$$

where ξ_n is the nth Sommerfeld pole calculated as the nth root of the expression $Z(\xi) = 0$ in (A.55). The above expressions can be applied to calculate the antenna admittance. Alternatively, the expression of $Z(\xi) = 0$ can be rewritten as

$$\xi^2 - k_2^2 \left(1 - \frac{1}{ak_1^2} P(\xi)\right) = 0 \tag{A.63}$$

where

$$P(\xi) = \frac{\upsilon_1 I_0(\upsilon_1 a)}{I_1(\upsilon_1 a) I_0(\upsilon_2 a) K_0(\upsilon_2 a)}, \tag{A.64}$$

which was derived based on the identity of the Bessel functions that $I_n(x) = (j)^{-n} J_n(jx)$. In this case, the variables υ_1 and υ_2 are defined as

$$\upsilon_1 = \sqrt{\xi^2 - k_1^2} \quad \text{and} \quad \upsilon_2 = \sqrt{\xi^2 - k_2^2}. \tag{A.65}$$

A method to find the multiple Sommerfeld poles is discussed in [111, p. 527]. The the fields of a transverse magnetic mode discussed in [111] are similar to those discussed in section A.3 of this paper. According to the discussion in [111], from the boundary conditions of the transverse magnetic modes, the following relation can be obtained

$$\frac{k_1^2}{\upsilon_1 a} \frac{I_1(\upsilon_1 a)}{I_0(\upsilon_1 a)} = -\frac{k_2^2}{\upsilon_2 a} \frac{K_1(\upsilon_2 a)}{K_0(\upsilon_2 a)}, \tag{A.66}$$

which can be used to rewrite the expression in (A.63) as

$$I_0(u) K_1(u) u - 1 = 0 \tag{A.67}$$

where $u = \upsilon_2 a$ is a complex argument. The roots obtained ξ_n must satisfy (A.67). For example, for highly conductive cylinders, the principal root ξ_1 is close to k_2; this implies that the first root u is very small. Therefore, taking the asymptotic expression $I_0(u) \sim 1$

TABLE A.2: Comparison of γ/k_2 for the case of proposed current on a finite cylindrical dipole antenna, the three-term, and for the infinitely-long dipole antenna, for the frequency of 300 MHz and radius $a = 0.01\ cm$. For the finite antennas, the half-length $h = 0.4\ m$ is taken.

δ_s/a	γ/k_2 (A.45)	γ/k_2 (A.33)	γ/k_2 (A.38)
0.1	$1.0024 - j0.0027$	$1.0038 - j0.0025$	$1.0034 - j0.0036$
0.25	$1.0062 - j0.0075$	$1.0095 - j0.0069$	$1.0083 - j0.0096$
0.5	$1.0111 - j0.0179$	$1.0177 - j0.0160$	$1.0148 - j0.0212$
1	$1.0112 - j0.0599$	$1.0306 - j0.0570$	$1.0182 - j0.0682$
1.5	$1.0114 - j0.1376$	$1.0536 - j0.1277$	$1.0242 - j0.1498$

and $K_1(u) \sim 1/u$, the above equation can be satisfied. Moreover, the propagation constants calculated from (A.33), (A.38) and (A.45) satisfy (A.67). For metallic conductors, the value of the higher order roots ξ_n are very large so that their contributions in (A.61) and (A.62) are negligible. But, as conductivity of the cylinder decreases, the higher order roots start to take over and with contribution of the principal wave vanishes for the case of dielectrics. For example, for an infinitely-long cylinder of radius $a = 0.01$ cm and conductivity of 100 S/m, at 300 MHz, $\xi_1 = 52.6365 - j62.4109$, which is much larger than obtained for metallic conductors.

A.6   Conclusion

The fields on the surface of an infinitely-long cylindrical conductor, when it is excited by a rotationally symmetric incident electric, were used to analyse imperfectly conducting cylindrical dipole antennas of finite and infinite lengths. General forms of the induced current derived from the infinitely-long conductor were used to simplify the solutions of the Pocklington equations involved. Consequently, simple expression of the current for both finite and infinite cylindrical dipole antennas were proposed. The proposed expressions for the current were validated by comparison with the current obtained from the three-term approximation method, for the case of the finite dipole antenna, and the current obtained from applying the Fourier method, for the case of the infinite one. The results showed that the currents are in good agreement. Moreover, from the comparison of the complex propagation constants, an expression for the current near the feeding gap was proposed based on multiple Sommerfeld poles.

Appendix B

Analysis of the Whole-Body Averaged Specific Absorption Rate (SAR) for Far-Field Exposure of an Isolated Human Body using Cylindrical Antenna Theory

BEHAILU KIBRET, ASSEFA K TESHOME, AND DANIEL T H LAI

B.1   Abstract

This study proposes an accurate estimation of whole-body averaged specific absorption rate (WBA-SAR) for far-field exposure of an isolated human body in the frequency range of 10-200 MHz based on a lossy homogenous cylindrical antenna model of the human body. Equations are derived for the total induced axial current and the whole-body averaged SAR based on a rigorous treatment of cylindrical antenna theory. An explicit formula for the resonance frequency in terms of the anatomical parameters and the dielectric properties of the body is proposed for the first time. Moreover, important phenomena in far-field radio frequency (RF) dosimetry, such as, the cause of resonance and the SAR frequency characteristics are discussed from an antenna theory perspective.

B.2   Introduction

As the application of electromagnetic fields increases along with the progress of technology, there is also a growing concern in the society about its possible adverse effects. As a prevention from excessive heating due to electromagnetic exposure of the human body, the International Commission on Non-Ionizing Radiation Protection (ICNIRP) and the Institute of Electrical and Electronic Engineers (IEEE) have developed safety guideline [22] and standard [63], respectively, that use the whole-body averaged specific absorption rate (WBA-SAR) as a proxy metric for temperature rise in the body. The ICNIRP guideline limits a WBA-SAR of 0.4 Wkg^{-1} for occupational exposure and 0.08 Wkg^{-1} for public exposure. Since it is inconvenient to measure SAR inside the human body, calculations are used to associate the SAR with measurable external electromagnetic field quantities, such as, the incident electric field; thus, an exposure restriction can be imposed.

Early studies in electromagnetic dosimetry made use of simple geometrical shapes to model the human body so that analytical or simple numerical techniques can be applied [64, 115]. Utilising the progress in computational electromagnetics and computing power in the last two decades, several studies have investigated SAR based on anatomically realistic voxel models of the human body [62, 66, 67]. Also, complementing such studies, other studies have used the cylindrical antenna model of the human body to calculate the induced currents inside the human body when it is exposed to the extremely low

frequency (ELF), very low frequency (VLF) and radio frequency (RF) electromagnetic fields. King *et al* [70] proposed an analytic method based on a two-term approximation of the current in a cylindrical antenna for the case of ELF and VLF exposure, in order to investigate electromagnetic field exposure from power transmission lines. Poljak *et al* [71] utilized the method of moments (MoM) to compute currents in a thick-wire model of human body in ELF exposure by employing the exact kernel of the Pocklington integro-differential equation. Both approaches provided reasonably accurate results compared to the results found using the finite-difference time-domain (FDTD) algorithm on voxel-based models of the human body [72]. King extended his studies to 150 MHz [73] using similar analytic approaches; but the results were not much accurate compared to the measured values and results reported by other authors. For example, the whole-body resonance frequency predicted by King for a grounded human body of height 1.75 m is near 53 MHz, which is different from the measured and calculated resonance frequency, near 40 MHz, reported by other authors [116]. One of the reasons for such large deviation could be King's oversimplified assumption using a single-term sinusoidal current in order to solve the two integral expressions inside the Hallén's type equation involved. In general, the ongoing acceptable trend of computing electromagnetic fields inside the human body makes use of the FDTD algorithm on realistic voxel-based models of the human body. In relation to this, though the analogy between the dipole antenna and the human body has been extensively reported, little has progressed in RF dosimetry analysis from an antenna theory perspective. This paper presents a simple but accurate technique to calculate the whole-body averaged SAR for far-field RF exposure based on the cylindrical antenna theory, which complements the results obtained through the FDTD.

It is known that the human body is anatomically more complicated than a homogenous cylinder. Therefore, unlike most of the previous papers, this paper does not attempt to approximate the human body with a cylinder; rather, it defines parameters of a cylindrical antenna based on the anatomical parameters of the human body so that the calculated WBA-SAR of the cylinder approximates that of the FDTD based WBA-SAR of the human body voxel models.

The results in this paper, from the representation of the human body as a cylindrical antenna, are validated by comparing them to the results from other authors who used the FDTD on the voxel models of two adult males (NORMAN and TARO), two adult

females (NAOMI and HANAKO) and two children (NORMAN 10 Year and TARO 7 Year) that are described in [62, 67, 117, 118].

In this paper, firstly, the cylindrical antenna theory is applied to derive expressions for the total induced axial current and the WBA-SAR for a cylindrical antenna model of the human body. Then, the cylindrical antenna model is parameterised based on comparisons with the FDTD based results reported by other authors who used anatomically realistic voxel models. Furthermore, an explicit expression for the resonance frequency is derived. Finally, the effect of anatomy on the resonance frequency and the WBA-SAR is discussed.

B.3 Whole-Body Averaged SAR for an Isolated Cylinder

The human body in standing position is represented by a homogenous cylindrical antenna that comprises muscle like tissue as shown in Fig. B.1. The dielectric property of muscle is calculated based on the 4-Cole-Cole dispersions that are parameterised by Gabriel *et al* [28]. Therefore, the complex conductivity of muscle σ_{mus}^* as a function of the excitation angular frequency ω can be calculated as

$$\sigma_{mus}^* = j\omega\epsilon_0\epsilon_{mus}^* = \sigma_{eff} + j\omega\epsilon_0\epsilon \tag{B.1}$$

where ϵ_{mus}^* is the complex permittivity of muscle defined in [28], σ_{eff} is the effective conductivity and ϵ is the relative permittivity. The permeability of the cylinder is taken to be equal to that of free space μ_0.

In this paper, it is assumed that a time-harmonic vertically polarized incident plane wave induces a rotationally symmetric current density in the cylinder of height $2h$ and radius a as shown in Fig. B.1. Working in a cylindrical coordinate system (ρ, ϕ, z) with the origin on the axis and at the midsection of the cylindrical antenna model, based on Taylor *et al* [30], an approximate analytic expression for the total axial current can be derived as

$$I_{1z}(z) = \frac{j4\pi E^{inc}}{k_2\zeta_0}\left[H_U(\cos\gamma z - \cos\gamma h) + H_D(\cos\tfrac{1}{2}k_2z - \cos\tfrac{1}{2}k_2h)\right] \tag{B.2}$$
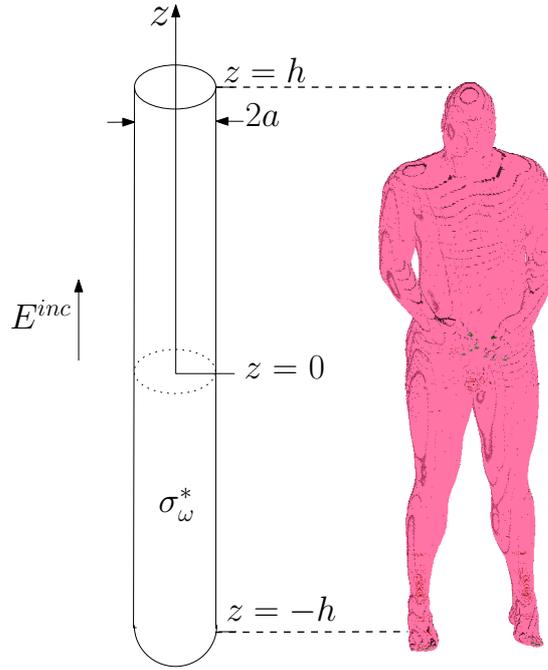
FIGURE B.1: The cylindrical antenna model of the human body exposed to vertically polarised plane wave.

where $k_2 = \omega\sqrt{\epsilon_0\mu_0}$ is the free space wave number, $\zeta_0 = 120\pi\ \Omega$ is free space impedance and E^{inc} is the incident electric field at the surface of the cylinder. The imperfectly conducting nature of the cylinder is characterized by the parameter $\gamma = \beta - j\alpha$,

$$\gamma^2 = k_2^2 \left(1 - \frac{j4\pi z^i}{k_2\zeta_0\Psi_{dR}}\right) \tag{B.3}$$

where z^i is impedance per unit length of the cylinder. According to King [54], z^i can be calculated as

$$z^i = \frac{\kappa}{2\pi a\sigma_\omega^*} \frac{J_0(\kappa a)}{J_1(\kappa a)} \tag{B.4}$$

where J_0 and J_1 are zeroth and first-order Bessel function, $\kappa^2 = k_1^2 - \gamma^2$, σ_ω^* is the complex conductivity of the cylinder, and $k_1 = \sqrt{j\omega\mu_0\sigma_\omega^*}$. The coefficients in (B.2) involve integrals that are computed numerically,

$$H_U = \frac{C_D - E_D}{C_U E_D - C_D E_U} \qquad H_D = \frac{E_U - C_U}{C_U E_D - C_D E_U} \tag{B.5}$$

where

$$C_U = \left(1 - \frac{\gamma^2}{k_2^2}\right)(\Psi_{dUR} - \Psi_{dR})(1 - \cos\gamma h) - \frac{\gamma^2}{k_2^2}\Psi_{dUR}\cos\gamma h$$
$$+ j\Psi_{dUI}\left(\frac{3}{4} - \cos\frac{1}{2}k_2h\right) + \Psi_U(h) \tag{B.6a}$$

$$C_D = \Psi_{dD}\left(\frac{3}{4} - \cos\frac{1}{2}k_2h\right) - \left(1 - \frac{\gamma^2}{k_2^2}\right)\Psi_{dR}\left(1 - \cos\frac{1}{2}k_2h\right) + \Psi_D(h) \qquad \text{(B.6b)}$$

$$E_U = -\frac{\gamma^2}{k_2^2}\Psi_{dUR}\cos\gamma h - j\frac{1}{4}\Psi_{dUI}\cos\frac{1}{2}k_2h + \Psi_U(h) \qquad \text{(B.6c)}$$

$$E_D = -\frac{1}{4}\Psi_{dD}\cos\frac{1}{2}k_2h + \Psi_D(h) \qquad \text{(B.6d)}$$

$$\Psi_U(h) = \int_{-h}^{h} \left(\cos\gamma z' - \cos\gamma h\right)\frac{e^{-jk_2R_h}}{R_h}dz' \qquad \text{(B.7a)}$$

$$\Psi_D(h) = \int_{-h}^{h} \left(\cos\frac{1}{2}k_2z' - \cos\frac{1}{2}k_2h\right)\frac{e^{-jk_2R_h}}{R_h}dz' \qquad \text{(B.7b)}$$

$$\Psi_{dR} = \Psi_{dR}(z_m), \quad \begin{cases} z_m = 0, & k_2h \le \pi/2 \\ z_m = h - \lambda/4, & k_2h > \pi/2 \end{cases} \qquad \text{(B.8a)}$$

$$\Psi_{dR}(z) = \csc\gamma(h - |z|)\int_{-h}^{h}\sin\gamma(h - |z'|)\left[\frac{\cos k_2R}{R} - \frac{\cos k_2R_h}{R_h}\right]dz' \qquad \text{(B.8b)}$$

$$\Psi_{dUR} = [1 - \cos\gamma h]^{-1}\int_{-h}^{h}[\cos\gamma z' - \cos\gamma h]\left[\frac{\cos k_2R_0}{R_0} - \frac{\cos k_2R_h}{R_h}\right]dz' \qquad \text{(B.8c)}$$

$$\Psi_{dD} = \left[1 - \cos\frac{1}{2}k_2h\right]^{-1}\int_{-h}^{h}\left[\cos\frac{1}{2}k_2z' - \cos\frac{1}{2}k_2h\right]\left[\frac{e^{-jk_2R_0}}{R_0} - \frac{e^{-jk_2R_h}}{R_h}\right]dz' \qquad \text{(B.8d)}$$

$$\Psi_{dUI} = -\left[1 - \cos\frac{1}{2}k_2h\right]^{-1}\int_{-h}^{h}[\cos\gamma z' - \cos\gamma h]\left[\frac{\sin k_2R_0}{R_0} - \frac{\sin k_2R_h}{R_h}\right]dz' \qquad \text{(B.8e)}$$

$$R = \left[(z - z')^2 + a^2\right]^{\frac{1}{2}} \qquad R_0 = \left[z'^2 + a^2\right]^{\frac{1}{2}} \qquad \text{(B.8f)}$$

$$R_h = \left[(h - z')^2 + a^2\right]^{\frac{1}{2}} \qquad \text{(B.8g)}$$

The value of γ is calculated by the process of iteration that is initialised by $\gamma = k_2$ to calculate z^i and Ψ_{dR}, which are in turn used to calculate γ. The iteration is found to be highly convergent; thus, the results after several iteration steps suffice to provide

accurate approximation.

The time average power per unit length dissipated in the cylinder cross-section at z is

$$P_{av}(z) = \frac{1}{2}\text{Re}\left(z^i\right)|I_{1z}(z)|^2. \tag{B.9}$$

Therefore, the whole-body averaged SAR of the cylinder ($WBASAR_{cyl}$) can be calculated as

$$WBASAR_{cyl} = \frac{\int\limits_{-h}^{h} P_{av}(z)dz}{W_{cyl}} = \frac{1}{2}\frac{\text{Re}(z^i)}{W_{cyl}}\int\limits_{-h}^{h}|I_{1z}(z)|^2dz \tag{B.10}$$

where W_{cyl} [kg] is the weight of the cylinder and it is related to the physical parameters of the human subject that is represented by the cylindrical antenna model. Since the current is directly proportional to the incident electric field in (B.2), for a given WBA-SAR, the root-mean-squared (r.m.s.) incident electric field E^{inc} can be calculated as

$$E^{inc} = \left[\frac{(WBASAR)W_{cyl}}{\text{Re}(z^i)\int\limits_{-h}^{h}|I_{1z}^e(z)|^2dz}\right]^{\frac{1}{2}} \tag{B.11}$$

where $WBASAR$ [Wkg^{-1}] is the whole-body averaged SAR given, and the $I_{1z}^e(z)$ [A/Vm^{-1}] is the total induced axial current per unit incident electric field field, defined as

$$I_{1z}^e(z) = \frac{j4\pi}{k_2\zeta_0}\left[H_U(\cos\gamma z - \cos\gamma h) + H_D(\cos\tfrac{1}{2}k_2 z - \cos\tfrac{1}{2}k_2 h)\right]. \tag{B.12}$$

B.4 Parameters of the Cylindrical Antenna Model

The radius of the cylinder is calculated by comparing the body-mass-index ($BMI = W/H^2$) of the human subject with that of a homogenous cylinder [119] comprising muscle like tissue as

$$a \propto \sqrt{\frac{W}{\pi\rho_m H}} \tag{B.13}$$

where ρ_m [kgm^{-3}] is the average density of the human body, W [kg] is the weight of the human subject and H [m] is the height of the human subject. The dielectric property of the cylinder is characterized by assuming it consists of a suspension of spherical

particles (cells) with complex conductivity σ_s^* in a medium of complex conductivity σ_m^*; furthermore, it is assumed that $\sigma_s^* \ll \sigma_m^*$. Based on the Maxwell-Wagner effective medium theory [120], the effective complex conductivity of the cylinder σ_ω^* can be related by

$$\frac{\sigma_\omega^* - \sigma_m^*}{\sigma_\omega^* + 2\sigma_m^*} = (1-x)\frac{\sigma_s^* - \sigma_m^*}{\sigma_s^* + 2\sigma_m^*} \tag{B.14}$$

that can be simplified as

$$\sigma_\omega^* = \frac{2x}{3-x}\sigma_m^* \tag{B.15}$$

where x is the volume fraction of the medium. It is assumed that the volume of the medium is equivalent to that of the total body water inside the human body, which is associated with the lean-body-mass, LBM, or fat free mass of the body. Therefore, assuming a unity density, the volume fraction of the medium is approximated as

$$x \simeq \frac{LBM}{W} \tag{B.16}$$

where the lean-body-mass for males is computed as [121]

$$LBM = 0.3210W + 33.92H - 29.5336 \tag{B.17}$$

and for females

$$LBM = 0.29569W + 41.813H - 43.2933. \tag{B.18}$$

Generally, the fraction of total body water is between 0.71-0.74 for human subjects of normal BMI. When the complex conductivity of the medium is equal to that of muscle ($\sigma_m^* = \sigma_{mus}^*$), the complex conductivity of the cylinder becomes $\sigma_\omega^* \approx \frac{2}{3}\sigma_{mus}^*$, which is the same value used extensively for the dielectric property of a homogenous human body model [68]. This paper points to the possible explanation of the basis of using the 2/3 constant of proportionality.

B.5 Results

It has been widely reported that WBA-SAR depends on the height, the dielectric properties of the body, the anatomy and the shape of the body. Therefore, in order for the cylindrical antenna model to predict the WBA-SAR value obtained from the FDTD

analysis of voxel-based models of actual human bodies, the parameters of the cylinder (H, σ_ω^*, a and W_{cyl}) should be defined based on the parameters of the voxel models. So that, from the comparison of the six voxel models, best accuracy can be obtained if the following parametrisation is performed on the cylinder models.

The calculated WBA-SAR is in excellent agreement with the FDTD results if the constant of proportionality in the expression of the radius (B.13) is equal to $\sqrt{5}$. Moreover, as the human anatomy depends on sex, the dielectric property is defined with additional sex dependent factor, such that,

$$\sigma_\omega^* \simeq \frac{\%mus}{2} \frac{2x}{3-x} \sigma_{mus}^* \tag{B.19}$$

where $\%mus$ is fraction of muscle by mass; and it can be approximated as 0.43 for the male models and 0.33 for the females [122]. Similarly, the weight of the cylinder is also sex dependent; for the adult male models,

$$W_{cyl} = \frac{W}{x} = \frac{W^2}{0.321W + 33.92H - 29.5336} \tag{B.20}$$

for the adult females,

$$W_{cyl} = 1.12\frac{W}{x} = \frac{1.12W^2}{0.29569W + 41.813H - 43.2933} \tag{B.21}$$

and for the children,

$$W_{cyl} = 1.4\frac{W}{x} = \frac{1.4W^2}{0.321W + 33.92H - 29.5336}. \tag{B.22}$$

Applying the previous parametrisation on the cylindrical antenna models, the maximum induced total axial current $|I_{1z}(z)|$ occurs when

$$k_2 \left(1 - \left|\frac{j4\pi z^i}{k_2\zeta_0\Psi_{dR}}\right|\right)^{\frac{1}{2}} h \simeq \frac{\pi}{8}. \tag{B.23}$$

Equation (B.23) can be written in a quadratic form by replacing z^i with the expression in (B.4) as

$$k_2^2 - \left|\frac{j2}{\zeta_0\Psi_{dR}} \frac{\kappa}{\sigma_\omega^*} \frac{J_0(\kappa a)}{J_1(\kappa a)}\right| \frac{k_2}{a} - \frac{1}{16}\left(\frac{\pi}{H}\right)^2 = 0 \tag{B.24}$$

TABLE B.1: Calculated resonance frequencies. Weight W is in kg, Height H in m, resonance freuency f_{res} in MHz.

Voxel Model	H	W	f_{res}	f_{res} FDTD	% error	H/λ_{res}
Norman	1.76	73	65.85	65	1.31	0.3866
Naomi	1.63	60	70.15	70	0.21	0.3814
Taro	1.73	65	68.88	70	1.6	0.3974
Hanako	1.60	53	73.47	74	0.72	0.3921
Norman10yr	1.38	33	86.24	85	1.46	0.3969
Taro7yr	1.20	23	96.85	95	1.95	0.3876

where $H = 2h$ is the height of the cylinder. The term in the absolute value in (B.24) tends to remain constant irrespective of frequency and the complex conductivity and radii that are used as parameters for the six cylindrical antenna models; therefore, approximating it with a constant T and using $k_2 = \omega\sqrt{\epsilon_0\mu_0} = \omega/c = 2\pi f_{res}/c$, the quadratic equation can be solved for the resonant frequency f_{res} as

$$f_{res} \simeq \frac{c}{4\pi}\left[\frac{T}{a} + \sqrt{\left(\frac{T}{a}\right)^2 + \frac{1}{4}\left(\frac{\pi}{H}\right)^2}\right] \tag{B.25}$$

where c is the speed of light in free space. The expression in (B.25) has a form similar to the resonance frequency expression of the resonant cylindrical dielectric cavity antenna [123]; and it implies that the resonance frequency depends on the height H, the dielectric property of the body T and the anatomy a. When the parameters of the six cylindrical antenna models are applied, T gets very close to 0.31. Therefore, the expression for the resonance frequency can be rewritten as

$$f_{res} \simeq \frac{c}{4\pi}\left[4.4923\sqrt{\frac{\pi H}{W}} + \sqrt{20.181\frac{\pi H}{W} + 0.25\left(\frac{\pi}{H}\right)^2}\right] \tag{B.26}$$

where ρ_m in (B.13) is approximated as 1050 kgm^{-3}. The comparison of the resonance frequencies calculated from (B.26) to the FDTD based resonance frequencies calculated for the six voxel models is shown in Table B.1. It is to be noted that the value of T is different for little children and adults with large BMI. Particularly, the expression in (B.26) is very accurate for the normal BMI range, for which, the muscle percentage can be approximated by 43% for the males and 33% for the females.

In the literature, it has been largely reported that the height to wavelength ratio (H/λ_{res})
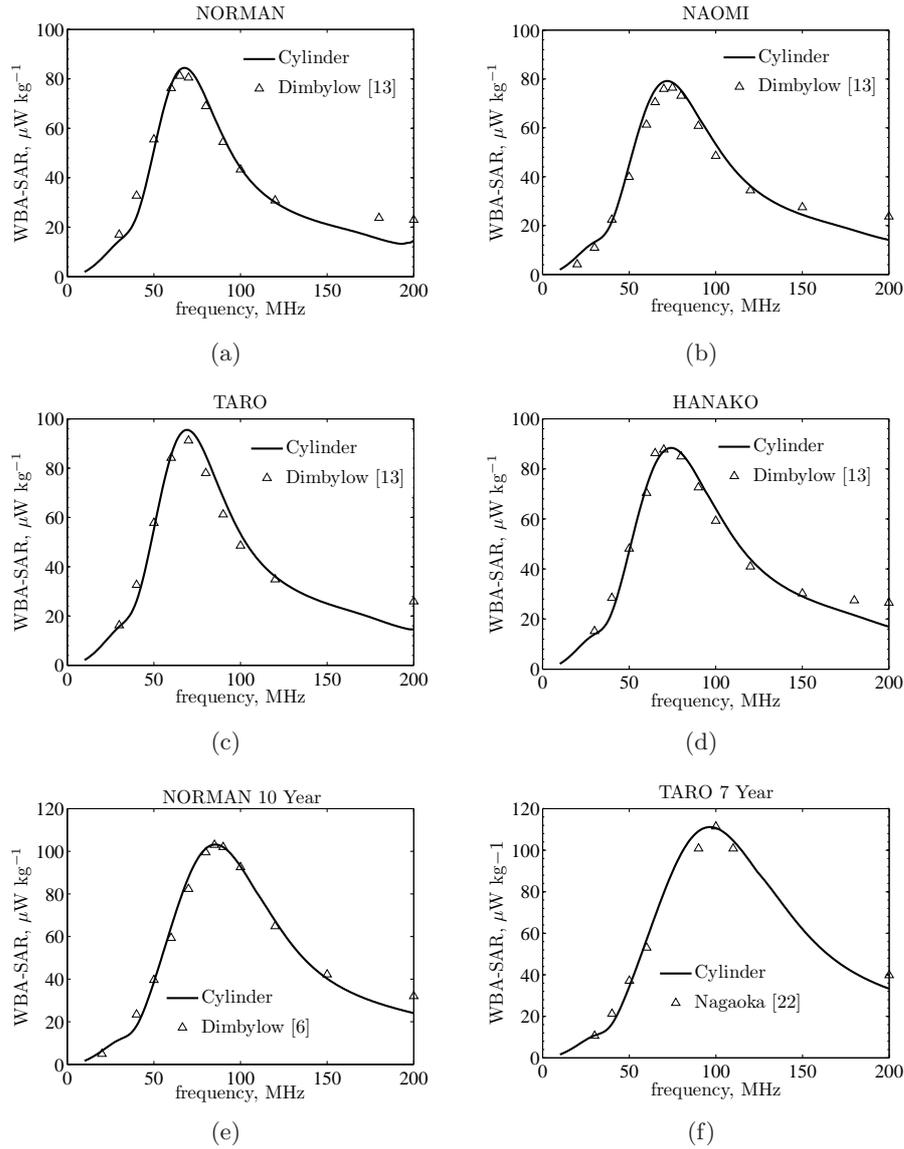
FIGURE B.2: WBA-SAR from the cylindrical model (solid line) and the FDTD computed on voxel models by other authors (triangle markers) for an incident field $E^{inc} = \sqrt{2}$ Vm^{-1} (1 Vm^{-1} r.m.s.).

at the resonance frequency approaches 0.4 [62, 67, 68, 115]; but, an adequate rationale has not been reported that sheds light on the phenomenon. Since the accurate formulation of the resonance frequency (B.26) proposed in this paper is a function of anatomical parameters and the dielectric properties of the body, it points to the possible explanation of the phenomenon observed.

The whole-body averaged SAR calculated using (B.10) is compared to the FDTD based results reported in [62, 117, 124] as shown in Fig. B.2. Moreover, the calculated incident electric field (B.11) required to produce the International Commission on Non-Ionising Radiation Protection (ICNIRP) occupational (0.4 Wkg^{-1}) and public (0.08 Wkg^{-1})
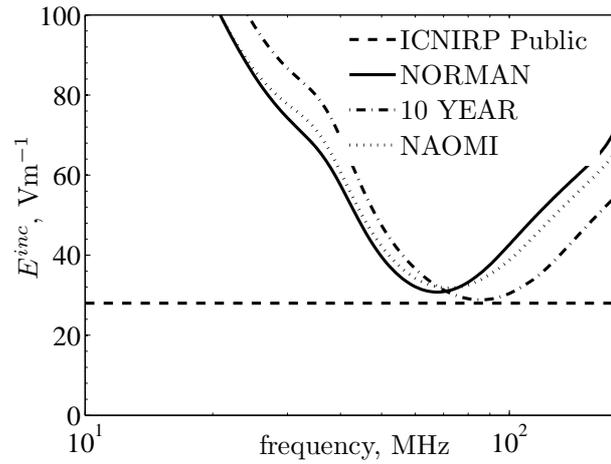
(a)
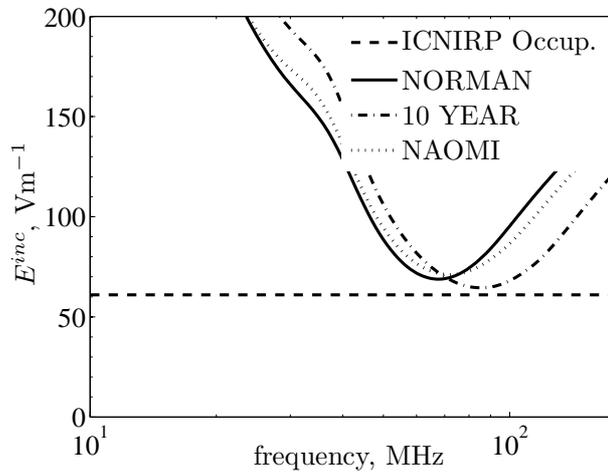
(b)

FIGURE B.3: Calculated electric field values (r.m.s.) required to produce the ICNIRP public (a) and occupational (b) exposure restrictions on the WBA-SAR

WBA-SAR restrictions are shown in Fig. B.3. From Fig. B.3, it can be seen that the incident electric field calculated for the 10 year old child model is too close to the ICNIRP reference level (28 Vm^{-1} for public exposure and 61 Vm^{-1} for occupational exposure) [22], indicating that the proposed reference level may not provide a conservative estimate of WBA-SAR in children as reported by other studies [62].

B.6   Discussion

The expression for the total induced axial current in (B.2) is derived based on the thin-wire approximation that puts the condition $k_2 a \ll 1$ and $h \gg a$, which is loosely
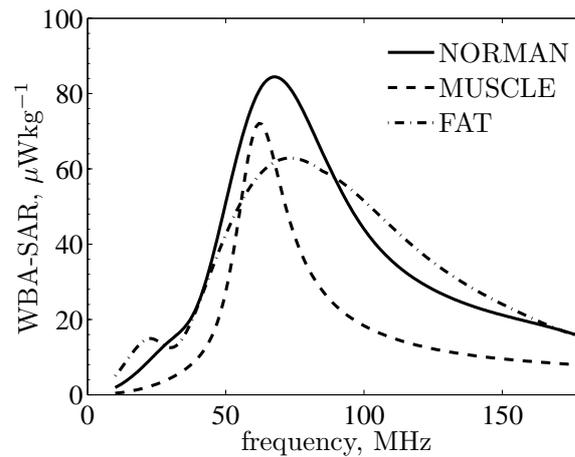
FIGURE B.4: Comparison of different dielectric properties for the cylindrical model

satisfied by the frequency range 10-200 MHz. This implies that the calculated axial current for higher frequencies becomes less accurate; as a result, the calculated WBA-SAR starts to diverge from the FDTD results for frequencies higher than 150 MHz as shown in Fig. B.2. In short, the technique discussed here is more appropriate for the whole-body resonance frequency range. For the adult models, the WBA-SAR tends to remain constant for the frequencies higher than 200 MHz up to 3 GHz [117]; therefore, the frequency range considered in this study is relevant, as the WBA-SAR for the higher frequencies can be roughly approximated by the WBA-SAR value close to 200 MHz. In addition to this, it should be noted that the equation for the total axial current (B.2) is valid for vertically polarized incident electric field.

The expression for the total induced axial current (B.2) involves integrals that are computed numerically. When the computation is carried out using Matlab running on an ordinary PC, the computation time required to compute the WBA-SAR for 10 - 200 MHz is less than 10 seconds. This is a large time improvement over FDTD computations for voxel models that require extensive computing power. In addition, our approach is comparable in accuracy.

From the explicit expression of the resonance frequency in (B.25), interesting connections of the resonance frequency and a person's anatomy can be predicted. For example, assuming the adult male model, NORMAN, gained 7 kg of weight and also assuming the weight gain is not due to an increase in muscle mass, the value of the constant T in (B.25) changes slightly from 0.31 to 0.32. This causes the resonance frequency to shift from 65.8 MHz to 64.9 MHz. On the other hand, if NORMAN is 6 cm shorter

TABLE B.2: Relationship between the anatomy and the resonance frequency based on NORMAN

Height H (m)	Weight (kg)	f_{res} (MHz)
1.76	73	65.85
1.76	80	64.9
1.70	73	66.8

with the same weight and $T = 0.32$, the resonance frequency shifts to 66.8 MHz. This implies that the resonance frequency for a person with high percentage fat is slightly smaller compared to that of a slender person of the same height. It also implies that a tall person has lower resonance frequencies compared to that of a shorter person of equivalent weight assuming that both have equal muscle mass. Overall, the effect of height is more pronounced than that of weight. These predictions are summarized in Table B.2. In relation to this, the weight increase in NORMAN caused the WBA-SAR to decrease by approximately 6.5 μWkg^{-1} for the frequencies higher than the resonance frequency and with insignificant change for the frequencies lower than the resonance frequency. This implies that the weight gain due to body fat might decrease the WBA-SAR for frequencies higher than the resonance frequency. But, the height difference in NORMAN modestly and uniformly decreased the WBA-SAR by approximately 1.47 μWkg^{-1}.

From antenna theory, it is known that a lossy and thick cylindrical antenna has a broadband frequency response [61]. A similar effect is also exhibited in the frequency characteristics of the WBA-SAR. If the cylindrical antenna model representing NORMAN is allowed to have a complex conductivity equal to that of the muscle tissue ($\sigma_\omega^* = \sigma_{mus}^*$), the calculated WBA-SAR has a narrower frequency characteristics compared with that of the FDTD based result, as shown in Fig B.4. On the other hand, if the complex conductivity of the cylindrical antenna model is equal to that of fat tissue, the WBA-SAR has a broader frequency characteristics. This explains the narrower frequency characteristics of the adult male models compared to that of the females, as the females have lower muscle percentage by mass.

B.7   Conclusion

The cylindrical antenna theory is applied to formulate the total induced axial current and the WBA-SAR inside a cylindrical antenna model of the human body. The cylindrical antenna model is parameterised based on the anatomical parameters of six voxel models. From this, we propose a mathematical model for the resonance frequency, which points to the possible explanation of the relation between the height and the resonance wavelength, $H/\lambda_{res} \approx 0.4$. Moreover, important characteristics of the WBA-SAR, such as, the effect of weight, height and dielectric properties of the body are discussed. In general, this paper complements the results obtained through FDTD on realistic voxel model of the human body, by interpreting the results from antenna theory perspective. Future work will investigate models of WBA-SAR with a grounded human body.

Bibliography

[1] E T Whittaker. *A History of the Theories of Aether and Electricity from the Age of Descartes to the Close of the Nineteenth Century.* Longmans, Green and Company, 1910.

[2] L Guo, N J Kubat, and R A Isenberg. Pulsed radio frequency energy (prfe) use in human medical applications. *Electromagn Biol Med*, 30(1):21–45, 2011.

[3] A Astrin et al. Ieee standard for local and metropolitan area networks part 15.6: Wireless body area networks: Ieee std 802.15. 6-2012. *IEEE Xplore*, 2012.

[4] A Fort, J Ryckaert, C Desset, P De Doncker, P Wambacq, and L Van Biesen. Ultra-wideband channel model for communication around the human body. *IEEE J. Sel. Area. Comm. on*, 24(4):927–933, 2006.

[5] R Xu, H Zhu, and J Yuan. Electric-field intrabody communication channel modeling with finite-element method. *IEEE Trans. Biomed. Eng.*, 58(3):705–712, 2011.

[6] M S Wegmueller, A Kuhn, J Froehlich, M Oberle, N Felber, N Kuster, and W Fichtner. An attempt to model the human body as a communication channel. *IEEE Trans. Biomed. Eng.*, 54(10):1851–1857, 2007.

[7] K Fujii, M Takahashi, and K Ito. Electric field distributions of wearable devices using the human body as a transmission channel. *IEEE Trans. Antennas. Propag.*, 55(7):2080–2087, 2007.

[8] S H Pun, Y M Gao, P U Mak, M I Vai, and M Du. Quasi-static multilayer electrical modeling of human limb for ibc. In *The 4th International Symposium on Bio-and Medical Informatics and Cybernetics (BMIC 2010), Orlando, Florida, USA*, 2010.

[9] Y Gao, S H Pun, M Du, M I Vai, and P U Mak. A preliminary two dimensional model for intra-body communication of body sensor networks. In *Intelligent Sensors, Sensor Networks and Information Processing, 2008. ISSNIP 2008. International Conference on*, pages 273–278. IEEE, 2008.

[10] Y Song, Q Hao, K Zhang, M Wang, Y Chu, and B Kang. The simulation method of the galvanic coupling intrabody communication with different signal transmission paths. *IEEE Trans. Instrum. Meas.*, 60(4):1257–1266, 2011.

[11] M S Wegmueller, M Oberle, N Kuster, and W Fichtner. From dielectrical properties of human tissue to intra-body communications. In *World Congress on Medical Physics and Biomedical Engineering 2006*, pages 613–617. Springer, 2007.

[12] M A Callejon, L M Roa, J Reina-Tosina, and D Naranjo-Hernandez. Study of attenuation and dispersion through the skin in intrabody communications systems. *IEEE Trans Inf Technol Biomed.*, 16(1):159–165, 2012.

[13] J Wang and Q Wang. *Body Area Communications: Channel Modeling, Communication Systems, and EMC*. John Wiley & Sons, 2012.

[14] N Cho, J Yoo, S J Song, J Lee, S Jeon, and H Yoo. The human body characteristics as a signal transmission medium for intrabody communication. *IEEE Trans. Microw. Theory Techn.*, 55(5):1080–1086, 2007.

[15] A Y Simba, A Itou, L Hamada, S Watanabe, T Arima, and T Uno. Development of liquid-type human-body equivalent antennas for induced ankle current measurements at vhf band. *IEEE Trans. Electromagn. Compat*, 54(3):565–573, 2012.

[16] A Hirata, K Yanase, I Laakso, K H Chan, O Fujiwara, T Nagaoka, S Watanabe, E Conil, and J Wiart. Estimation of the whole-body averaged sar of grounded human models for plane wave exposure at respective resonance frequencies. *Phys Med Biol.*, 57(24):8427, 2012.

[17] European Telecommunications Standards Institute (ETSI). Electromagnetic compatibilityand radio spectrum matters (erm); improvement of radiated methods of measurement (using test sites) and evaluation of the corresponding measurement uncertainties; part 7: Artificial human beings. *ETSI Technical Report*, 1998.

[18] J Bae, H Cho, K Song, H Lee, and H J Yoo. The signal transmission mechanism on the surface of human body for body channel communication. *IEEE Trans. Microw. Theory Techn.*, 60(3):582–593, 2012.

[19] J W Hand. Modelling the interaction of electromagnetic fields (10 mhz–10 ghz) with the human body: methods and applications. *Phys Med Biol.*, 53(16):R243, 2008.

[20] K Ikrath, K J Murphy, and W Kennebeck. Development of camouflaged body coupled radio transmitters. Technical report, DTIC Document, 1973.

[21] J B Andersen and P Balling. Admittance and radiation efficiency of the human body in the resonance region. *Proc. IEEE*, 60(7):900–901, 1972.

[22] International Commission on Non-Ionizing Radiation Protection et al. Guidelines for limiting exposure to time-varying electric and magnetic fields (1 hz to 100 khz). *Health Physics*, 99(6):818–836, 2010.

[23] P S Hall and Y Hao. Antennas and propagation for body centric communications. In *Antennas and Propagation, 2006. EuCAP 2006. First European Conference on*, pages 1–7. IEEE, 2006.

[24] ETSI EN ETSI. 301 839–1 v1. 3.1 (2009–10): Electromagnetic compatibility and radio spectrum matters (erm); short range devices (srd); ultra low power active medical implants (ulp-ami) and peripherals (ulp-ami-p) operating in the frequency range 402 mhz to 405 mhz; part 1: technical characteristics and test methods.(2009), 2014.

[25] S Gabriel, R W Lau, and C Gabriel. The dielectric properties of biological tissues: Iii. parametric models for the dielectric spectrum of tissues. *Phys Med Biol.*, 41(11):2271, 1996.

[26] J C Maxwell. A dynamical theory of the electromagnetic field. *Philos Trans R Soc Lond*, pages 459–512, 1865.

[27] K R Foster and H P Schwan. Dielectric properties of tissues and biological materials: a critical review. *Crit Rev Biomed Eng.*, 17(1):25–104, 1988.

[28] S Gabriel, R W Lau, and C Gabriel. The dielectric properties of biological tissues: Iii. parametric models for the dielectric spectrum of tissues. *Phys Med Biol.*, 41(11):2271, 1996.

[29] R W P King and T T Wu. The imperfectly conducting cylindrical transmitting antenna. *IEEE Trans. Antennas. Propag.*, 14(5):524–534, 1966.

[30] C D Taylor, C W Harrison, and E A Aronson. Resistive receiving and scattering antenna. *IEEE Trans. Antennas. Propag.*, 15(3):371–376, 1967.

[31] U Varshney. Pervasive healthcare and wireless health monitoring. *Mobile Networks and Applications*, 12(2-3):113–127, 2007.

[32] Ž Lučev, I Krois, and M Cifrek. Intrabody communication in biotelemetry. In *Wearable and Autonomous Biomedical Devices and Systems for Smart Environment*, pages 351–368. Springer, 2010.

[33] M A Estudillo, D Naranjo, L M Roa, and J Reina-Tosina. Intrabody communications (ibc) as an alternative proposal for biomedical wearable systems. *Handbook of Research on Developments in E-Health and Telemedicine: Technological and Social Perspectives*, 1:1, 2009.

[34] T G Zimmerman. Personal area networks: near-field intrabody communication. *IBM Syst J*, 35(3.4):609–617, 1996.

[35] Z Lucev, I Krois, and M Cifrek. A capacitive intrabody communication channel from 100 khz to 100 mhz. *IEEE Trans. Instrum. Meas.*, 61(12):3280–3289, 2012.

[36] M S Wegmueller, M Oberle, N Felber, N Kuster, and W Fichtner. Signal transmission by galvanic coupling through the human body. *IEEE Tran. Instrum. Meas.*, 59(4):963–969, 2010.

[37] K Hachisuka, T Takeda, Y Terauchi, H Sasaki, Kand Hosaka, and K Itao. Intrabody data transmission for the personal area network. *Microsystem Technologies*, 11(8-10):1020–1027, 2005.

[38] M Seyedi, B Kibret, D T H Lai, and M Faulkner. A survey on intrabody communications for body area network applications. *IEEE Trans. Biomed. Eng.*, 60(8):2067–2079, 2013.

[39] O G Martinsen and S Grimnes. *Bioimpedance and bioelectricity basics.* Academic press, 2011.

[40] M Makhsous, F Lin, A Cichowski, I Cheng, C Fasanati, T Grant, and R W Hendrix. Use of mri images to measure tissue thickness over the ischial tuberosity at different hip flexion. *Clinical Anatomy*, 24(5):638–645, 2011.

[41] V Brodar. Observations on skin thickness and subcutaneous tissue in man. *Zeitschrift für Morphologie und Anthropologie*, pages 386–395, 1960.

[42] S H Goldberg, R Omid, A N Nassr, R Beck, and M S Cohen. Osseous anatomy of the distal humerus and proximal ulna: implications for total elbow arthroplasty. *J Shoulder Elbow Surg*, 16(3):S39–S46, 2007.

[43] International Commission on Non-Ionizing Radiation Protection et al. Guidelines for limiting exposure to time-varying electric and magnetic fields (1 hz to 100 khz). *Health Physics*, 99(6):818–836, 2010.

[44] J Rosell, J Colominas, P Riu, R Pallas-Areny, and J G Webster. Skin impedance from 1 hz to 1 mhz. *IEEE Trans. Biomed. Eng.*, 35(8):649–651, 1988.

[45] N Cho, J Lee, L Yan, J Bae, S Kim, and H Yoo. A 60kb/s-to-10mb/s 0.37 nj/b adaptive-frequency-hopping transceiver for body-area network. In *2008 IEEE International Solid-State Circuits Conference-Digest of Technical Papers*, pages 132–602, 2008.

[46] Q Wang, T Sanpei, J Wang, and D Plettemeier. Emi modeling for cardiac pace-maker in human body communication. In *Proc. Int. Symp. on EMC*, pages 629–632, 2009.

[47] H Park, I Lim, S Kang, and W Kim. Human body communication system with fsbt. In *Consumer Electronics (ISCE), 2010 IEEE 14th International Symposium on*, pages 1–5. IEEE, 2010.

[48] Jaume Anguera P, D Aguilar, J Vergés, M Ribó, and C Puente Baliarda. Handset antenna design for fm reception. In *Antennas and Porpagation Society International Symposium, 2008 IEEE*, pages 1–4. IEEE, 2008.

[49] D Aguilar, J Anguera, C Puente, and M Ribó. Small handset antenna for fm reception. *Microw Opt Tecg Let*, 50(10):2677–2683, 2008.

[50] J Vergés, J Anguera, C Puente, and D Aguilar. Analysis of the human body on the radiation of fm handset antenna. *Microw Opt Tecg Let*, 51(11):2588–2590, 2009.

[51] A Pladevall, C Picher, A Andujar, and J Anguera. Some thoughts on human body effects on handset antenna at the fm band. *Prog Electromagn Res M*, 19:121–132, 2011.

[52] D Poljak. Human exposure to electromagnetic fields. *Advanced Modeling in Computational Electromagnetic Compatibility*, pages 453–491, 2006.

[53] B Kibret, A K Teshome, and D T H Lai. Characterizing the human body as a monopole antenna. *IEEE Trans. Antennas. Propag.*, 63(10):4384–4392, 2015.

[54] R W P King and S Prasad. *Fundamental electromagnetic theory and applications.* Prentice-Hall Englewood Cliffs, USA, 1986.

[55] R W P King and T T Wu. Currents, charges, and near fields of cylindrical antennas. *Currents*, 69(3), 1965.

[56] R W P King and T T Wu. Electromagnetic field near a parasitic cylindrical antenna. In *Proc. Inst. Electr. Eng*, volume 113, pages 35–40. IET, 1966.

[57] J R Wait and K P Spies. On the image representation of the quasi-static fields of a line current source above the ground. *Can. J. Phy.*, 47(23):2731–2733, 1969.

[58] J R Wait. Image theory of a quasistatic magnetic dipole over a dissipative half-space. *Electron. Lett.*, 5(13):281–282, 1969.

[59] P R Bannister. Summary of image theory expressions for the quasi-static fields of antennas at or above the earth's surface. *Proc. IEEE*, 67(7):1001–1008, 1979.

[60] R W P King and T T Wu. Currents, charges, and near fields of cylindrical receiving and scattering antennas. *IEEE Trans. Antennas. Propag.*, 13(6):978–979, 1965.

[61] C A Balanis. *Antenna theory: analysis and design.* John Wiley & Sons, 2012.

[62] P J Dimbylow. Fine resolution calculations of sar in the human body for frequencies up to 3 ghz. *Phys Med Biol.*, 47(16):2835, 2002.

[63] on Non-Ionizing Radiation Hazards IEEE Standards Coordinating Committee 28. *IEEE Standard for Safety Levels with Respect to Human Exposure to Radio Frequency Electromagnetic Fields, 3kHz to 300 GHz.* Institute of Electrical and Electonics Engineers, Incorporated, 2005.

[64] C H Durney. Electromagnetic dosimetry for models of humans and animals: A review of theoretical and numerical techniques. *Proc. IEEE*, 68(1):33–40, 1980.

[65] O P Gandhi. State of the knowledge for electromagnetic absorbed dose in man and animals. *Proc. IEEE*, 68(1):24–32, 1980.

[66] P J Dimbylow. Fdtd calculations of the whole-body averaged sar in an anatomically realistic voxel model of the human body from 1 mhz to 1 ghz. *Phys Med Biol.*, 42(3):479, 1997.

[67] J Wang, O Fujiwara, S Kodera, and S Watanabe. Fdtd calculation of whole-body average sar in adult and child models for frequencies from 30 mhz to 3 ghz. *Phys Med Biol.*, 51(17):4119, 2006.

[68] A Hirata, O Fujiwara, T Nagaoka, and S Watanabe. Estimation of whole-body average sar in human models due to plane-wave exposure at resonance frequency. *IEEE Trans. Electromagn. Compat*, 52(1):41–48, 2010.

[69] K Yanase and A Hirata. Effective resistance of grounded humans for whole-body averaged sar estimation at resonance frequencies. *Prog Electromagn Res B*, 35:15–27, 2011.

[70] R W P King and S S Sandler. Electric fields and currents induced in organs of the human body when exposed to elf and vlf electromagnetic fields. *Radio Science*, 31(5):1153–1167, 1996.

[71] D Poljak and V Roje. Currents induced in human body exposed to the power line electromagnetic field. In *Engineering in Medicine and Biology Society, 1998. Proceedings of the 20th Annual International Conference of the IEEE*, volume 6, pages 3281–3284. IEEE, 1998.

[72] O P Gandhi and J Chen. Numerical dosimetry at power-line frequencies using anatomically based models. *Bioelectromagnetics*, 13(S1):43–60, 1992.

[73] R W P King. Electric current and electric field induced in the human body when exposed to an incident electric field near the resonant frequency. *IEEE Trans. Microw. Theory Techn.*, 48(9):1537–1543, 2000.

[74] B Kibret, A K Teshome, and D T H Lai. Analysis of the whole-body averaged specific absorption rate (sar) for far-field exposure of an isolated human body using cylindrical antenna theory. *Prog Electromagn Res M*, 38:103–112, 2014.

[75] B Kibret, A K Teshome, and D T H Lai. Human body as antenna and its effect on human body communications. *Prog Electromagn Res*, 148:193–207, 2014.

[76] O P Gandhi and E E Aslan. Human-equivalent antenna for electromagnetic fields, February 28 1995. US Patent 5,394,164.

[77] R W P King, C Harrison Jr, and E Aronson. The imperfectly conducting cylindrical transmitting antenna: Numerical results. *IEEE Trans. Antennas. Propag.*, 14(5):535–542, 1966.

[78] H J Krzywicki and K SK Chinn. Human body density and fat of an adult male population as measured by water displacement. *Am. J. Clin. Nutr.*, 20(4):305–310, 1967.

[79] P Dimbylow. Resonance behaviour of whole-body averaged specific energy absorption rate (sar) in the female voxel model, naomi. *Phys Med Biol.*, 50(17):4053, 2005.

[80] R W P King. The linear antenna—eighty years of prograss. *Proc. IEEE*, 55(1):2–16, 1967.

[81] R W P King. The electric field induced in the human body when exposed to electromagnetic fields at 1-30 mhz on shipboard. *IEEE Trans. Biomed. Eng.*, 46(6):747–751, 1999.

[82] B Kibret, A K Teshome, and D T H Lai. Cylindrical antenna theory for the analysis of whole-body averaged specific absorption rate. *IEEE Trans. Antennas. Propag.*, 63(11):5224–5229, 2015.

[83] C Hua, Z Shen, and J Lu. High-efficiency sea-water monopole antenna for maritime wireless communications. *IEEE Trans. Antennas. Propag.*, 62(12):5968–5973, 2013.

[84] Y Takahashi, T Arima, P Pongpaibool, S Watanabe, and T Uno. Development of a liquid-type human-body equivalent antenna using nacl solution. In *Electromagnetic Compatibility, 2007. EMC Zurich 2007. 18th International Zurich Symposium on*, pages 151–154. IEEE, 2007.

[85] R J Vyas, B B Cook, Y Kawahara, and M M Tentzeris. E-wehp: A batteryless embedded sensor-platform wirelessly powered from ambient digital-tv signals. *IEEE Trans. Microw. Theory Techn.*, 61(6):2491–2505, 2013.

[86] N Shariati M, W Rowe, and K Ghorbani. Rf field investigation and maximum available power analysis for enhanced rf energy scavenging. In *42nd European Microwave Conference, EuMC*, pages 329–332. IEEE, 2012.

[87] N Barroca, J M Ferro, L M Borges, J Tavares, and F J Velez. Electromagnetic energy harvesting for wireless body area networks with cognitive radio capabilities. In *Proceedings of URSI Seminar of the Portuguese Committee, Lisbon, Portugal*, 2012.

[88] US Federal Communications Commission (FCC). Medrradio approval. *Rep. FCC 09-23-A1*, 2009.

[89] A S Y Poon, S O'Driscoll, and T H Meng. Optimal frequency for wireless power transmission into dispersive tissue. *Antennas and Propagation, IEEE Transactions on*, 58(5):1739–1750, 2010.

[90] T Bjorninen, R Muller, P Ledochowitsch, L Sydanheimo, L Ukkonen, M M Maharbiz, and J M Rabaey. Design of wireless links to implanted brain–machine interface microelectronic systems. *Antennas and Wireless Propagation Letters, IEEE*, 11:1663–1666, 2012.

[91] G Z Yang and M Yacoub. *Body sensor networks*. Springer, 2006.

[92] J E Ferguson and A D Redish. Wireless communication with implanted medical devices using the conductive properties of the body. *Expert review of medical devices*, 8(4):427–433, 2011.

[93] B Kibret, M Seyedi, D T H Lai, and M Faulkner. Investigation of galvanic coupled intrabody communication using human body circuit model. *IEEE J Biomed Health Inform*, 18(4):1196–1206, 2014.

[94] R P Blackwell. The personal current meter-a novel ankle-worn device for the measurement of rf body current in a mobile subject. *Journal of Radiological Protection*, 10(2):109, 1990.

[95] M J Hagmann and T M Babij. Noninvasive measurement of current in the human body for electromagnetic dosimetry. *Biomedical Engineering, IEEE Transactions on*, 40(5):418–423, 1993.

[96] J Wilen, K H Mild, L E Paulsson, and G Anger. Induced current measurements in whole body exposure condition to radio frequency electric fields. *Bioelectromagnetics*, 22(8):560–567, 2001.

[97] F H Netter. *Atlas of human anatomy*. Elsevier Health Sciences, 2014.

[98] M K Kazimierczuk. *High-frequency magnetic components*. John Wiley & Sons, 2009.

[99] N Blaz, A Maric, G Radosavljevic, L Zivanov, G Stojanovic, I Atassi, and W Smetana. Modeling and characterization of frequency and temperature variation of complex permeability of ferrite ltcc material. *Prog Electromagn Res B*, 23:131–146, 2010.

[100] P L Dowell. Effects of eddy currents in transformer windings. *Proc. Inst. Electr. Eng*, 113(8):1387–1394, 1966.

[101] A Massarini and M K Kazimierczuk. Self-capacitance of inductors. *IEEE T Power Electr*, 12(4):671–676, 1997.

[102] Online. Sea water antenna system. url link.

[103] C Hua and Z Shen. Shunt-excited sea-water monopole antenna of high efficiency. *Antennas and Propagation, IEEE Transactions on*, 63(11):5185–5190, 2015.

[104] Radiocommunications Act 1992. Radiocommunications (low interference potential devices) class licence 2000. *Australian Communications and Media Authority*, 2014.

[105] International Telecommunications Union. Sharing between the meteorological aids service and medical implant communication systems (mics) operating in the mobile service in the frequency band 401 – 406 mhz. *ITU-R SA.1346*, 63, 1998.

[106] H C Pocklington. Electrical oscillations in wires. In *Proc. Camb. Phil. Soc*, volume 9, pages 324–332, 1897.

[107] E Hallén. *Theoretical investigations into the transmitting and receiving qualities of antennae*. Almqvist & Wiksells, 1938.

[108] R W P King. *The theory of linear antennas: with charts and tables for practical applications*. Harvard Univ Pr, 1956.

[109] E Hallén. Properties of a long antenna. *J APPL PHYS*, 19(12):1140–1147, 1948.

[110] A Sommerfeld. Ueber die fortpflanzung elektrodynamischer wellen längs eines drahtes. *Annalen der Physik*, 303(2):233–290, 1899.

[111] J A Stratton. *Electromagnetic theory*. New York: McGraw-Hill, 1941.

[112] G Fikioris and T T Wu. On the application of numerical methods to hallen's equation. *IEEE Trans. Antennas. Propag.*, 49(3):383–392, 2001.

[113] E Hallén and R Gåsström. *Electromagnetic theory*, volume 43. Chapman & Hall London, 1962.

[114] J H Richmond. Admittance of infinitely long cylindrical wire and finite conductivity and magnetic-frill excitation. *IEEE Trans. Antennas. Propag.*, 27(2):264–266, 1979.

[115] O P Gandhi. State of the knowledge for electromagnetic absorbed dose in man and animals. *Proc. IEEE*, 68(1):24–32, 1980.

[116] O P Gandhi, J Chen, and A Riazi. Currents induced in a human being for plane-wave exposure conditions 0-50 mhz and for rf sealers. *IEEE Trans. Biomed. Eng.*, 33(8):757–767, 1986.

[117] P J Dimbylow, A Hirata, and T Nagaoka. Intercomparison of whole-body averaged sar in european and japanese voxel phantoms. *Phys Med Biol.*, 53(20):5883, 2008.

[118] T Nagaoka, S Watanabe, K Sakurai, S Kunieda, Eand Watanabe, M Taki, and Y Yamanaka. Development of realistic high-resolution whole-body voxel models of japanese adult males and females of average height and weight, and application of models to radio-frequency electromagnetic-field dosimetry. *Phys Med Biol.*, 49(1):1, 2004.

[119] S B Heymsfield, A Martin-Nguyen, T M Fong, D Gallagher, and A Pietrobelli. Body circumferences: clinical implications emerging from a new geometric model. *Nutr Metab (Lond)*, 5:24, 2008.

[120] S Grimnes, O Rikshospitalet, and H P Schwan. Interface phenomena and dielectric properties of biological tissue. *Encyclopedia of surface and colloid science*, 20:2643–2653, 2002.

[121] R Hume. Prediction of lean body mass from height and weight. *J Clin Pathol*, 19(4):389–391, 1966.

[122] A El Habachi, E Conil, A Hadjem, E Vazquez, M F Wong, A Gati, G Fleury, and J Wiart. Statistical analysis of whole-body absorption depending on anatomical human characteristics at a frequency of 2.1 ghz. *Phys Med Biol.*, 55(7):1875, 2010.

[123] S A Long, M W McAllister, and L C Shen. The resonant cylindrical dielectric cavity antenna. *IEEE Trans. Antennas. Propag*, 31:406–412, 1983.

[124] T Nagaoka, E Kunieda, and S Watanabe. Proportion-corrected scaled voxel models for japanese children and their application to the numerical dosimetry of specific absorption rate for frequencies from 30 mhz to 3 ghz. *Phys Med Biol.*, 53(23):6695, 2008.